Development of microfluidic methods for the determination of products of nitrosative and oxidative stress

By

Kelci M. Schilly
B.S., University of North Carolina at Chapel Hill, 2015

Submitted to the graduate degree program in Chemistry and the Graduate Faculty of the University of Kansas in partial fulfillment of the requirements for the degree of Doctor of Philosophy.

Chair: Dr. Susan M. Lunte

Dr. Robert C. Dunn

Dr. Michael A. Johnson

Dr. James D. Blakemore

Dr. Karen J. Nordheden

Date Defended: 23 February 2021

The dissertation committee for Kelci M. Schilly certifies that this is the approved version of the following dissertation:

Development of microfluidic methods for the determination of products of nitrosative and oxidative stress

Chair: Dr. Susan M. Lunte

Date Approved: 03 March 2021

Abstract

When the pro-inflammatory and anti-inflammatory immune responses become imbalanced, an excess of pro-inflammatory reactive nitrogen and oxygen species (RNOS) may be produced, which in turn can react with biomolecules such as proteins, lipids, and DNA. These reactions result in structural modifications that can ultimately lead to functional alterations, cell damage, or even cell death. As RNOS are highly reactive and short-lived at physiological pH ($t_{1/2}$ < 1 s), rapid microfluidic methods allow for near real-time measurement of these species in biological samples. Additionally, electrophoretic separation techniques such as capillary electrophoresis (CE) and microchip electrophoresis (ME) are useful for the efficient separation of small, ionic species such as RNOS. In this dissertation, several novel microfluidic and electrophoretic approaches for studying cellular nitrosative and oxidative stress *via* monitoring of RNOS (*e.g.,* nitric oxide, peroxynitrite), their metabolites (*e.g.,* nitrite), and their reactive products (*e.g.*, 3-nitrotyrosine) are described. First, a method using ME with electrochemical detection (EC) was developed to detect nitrite in cell lysates isolated from stimulated macrophages as an indicator of nitric oxide production. This method features transient isotachophoresis stacking and a platinum black working electrode for enhanced signal and sensitivity for nitrite. Additionally, progress towards a second ME-EC method with dual electrochemical detection is reported that is selective for nitrotyrosine and nitrotyrosine-containing peptides. A complementary CE-UV method for the separation of several nitrated and non-nitrated peptides was also developed and has been applied to the identification of reaction products of tyrosine under acidic and oxidizing conditions. Finally, stereolithographic 3D printing was used to develop a low-volume module for boronate affinity enrichment that will ultimately be integrated with other modules and used in a plug-and-play system for capture and detection of derivatized, nitrated peptides. Together, these methods provide a suite of approaches for investigating nitrosative and oxidative stress in cellular systems.

Acknowledgements

First and foremost, I would like to thank my advisor, Dr. Sue Lunte. I have grown so much during graduate school, both personally and professionally, thanks to her mentorship and support. She has built a more supportive, collaborative research group than I could have ever asked for, and from the moment I joined the group in 2015 I felt welcomed into the Lunte Lab family. Not many advisors would allow their second-year student to go on a summer internship in the months leading up to orals, but Sue not only allowed it but encouraged it. Even fewer advisors would, in their "welcome back" meeting with that student, ask if they were interested in going on a second research rotation the next year, but Sue did. Sue always puts her students first and for that I am eternally grateful – I have had so many amazing formational experiences in graduate school that go beyond the science we did in MRB, from meetings with collaborators, to my JPL internship and my rotation in the Netherlands, to attending exciting conferences, to building up the Graduate Student Organization, and finally to mentoring my incredible team of undergraduate students. Sue has been endlessly encouraging and supportive of all these endeavors, and because of each of these opportunities I am a better scientist, leader, and communicator. Thank you Sue!

I would also like to thank the rest of my committee, Dr. Robert Dunn, Dr. Michael Johnson, Dr. James Blakemore, and Dr. Karen Nordheden, for serving on my defense committee and reading my dissertation. I would also like to thank the KU Chemistry Department in general for their support during graduate school, especially all those who assisted the GSO in becoming registered – I have seen so much growth in KU Chemistry during my time here and am excited to see that trajectory continue! I would also like to acknowledge the NIH Training Grant in Dynamic Aspects of Chemical Biology that funded me during my PhD. I am very grateful to all those faculty and staff involved in that training program, and in particular Dr. Audrey Lamb, for not only teaching me about chemical biology but also helping me prepare for my career.

Next, I would like to thank all past and present members of the Sue Lunte research group for all the support they have given me over the years, including Dr. Rachel Saylor, Dr. Abdullah Al-Hossaini, Dr. Nate Oborny, Sonia Schoeneich, Dr. Ebru Buyuktuncel, Anton Barybin, and Dr. Sara Thomas. I would also like to thank Dr. Giuseppe Caruso and Claudia Fresta for their support of cell work and Dr. Michael Hogard for always being up for a coffee break. I would especially like to thank Dr. Joe Siegel for being my mentor in the group. Thank you for making research fun, even in the last stretches of late nights in lab before Pittcon, and for helping me gain the confidence I needed to succeed as a researcher and mentor.

Dr. Manjula Wijesinghe and Dr. Shamal Gunawardhana, my Sri Lankan big brothers, I have so much to thank you for. Manjula Aiya, thank you for all the time you have spent discussing electrochemistry with me, even after you graduated. Thank you also for all our early morning chats in the office and for being a great friend to me all throughout graduate school. Shamal Aiya, thank you for being a mentor to me and for always being happy to answer all my questions. I learned so much about mentoring from watching you put so much care and patience into working with your undergrads, and I am equally thankful to you for putting up with all my talking (and I am also grateful to you and Mihiri for friendship and all the delicious food)! You have both taught me so much and I am so lucky I had the opportunity to work with both of you for so long.

Galina Bulgakova, thank you for being such a big part of my support system (both in and out of lab) ever since you joined the group. Thank you for all our research brainstorming sessions, for being my go-to CE expert, and for being the sounding board to all of my research ideas and project plans. Outside of the lab, thank you for Thai Diner nights with Sasha and coffee dates and for helping me endlessly stalk the Humane Society page until Zeke finally got a cat. Emily Kurfman, thank you so much for your friendship and support – I am so appreciative of you for always being willing to help me, whether it was editing five chapters in one week or going above

and beyond answering all my mass spec questions. I am so lucky to have found friends like both of you in my group! Dhanushka Weerasekara, thank you for sharing your biology, figure-making, and photography skills and for helping to edit my chapters. It has been great working with you for so long – I enjoyed all our chats in lab and on trips to conferences. Indika Warnakula, thank you also for helpful discussions and for fun conversations in lab. I will miss working with you all.

I also must thank the incredible undergraduate students I have had the chance to work with over the last several years – Garet Melton, Lexie Paige, Geldon Sherifi, and Riley Stegmaier. Garet, thank you for coming into lab every day with a smile, even when you were frustrated with your project, and for entertaining us all with your pickle juice obsession. Lexie, thank you for putting in so many hours learning the ins and outs of microchips, for sending me last-minute data while I was already at a conference, and for always being such a fun presence in the lab. Riley, thank you for being so flexible in your first (very unconventional) year of research. I would not have been able to accomplish nearly as much this year if it were not for your hard work, and I have really enjoyed your company in lab! I have learned so much from the opportunity Sue gave me to mentor these students and am so grateful for everything they have taught me, everything they have helped me accomplish, and all the good times we have had.

Cady Bush, where would any of us be without you?! Thank you for 5.5 years of checking schedules, dealing with all the group logistics, and for always brightening my day when I would pop by your desk to say hi! You are an amazingly organized and amazingly supportive person and made every administrative email and transaction fun and I am so thankful that I was able to work with you during grad school. I also have many people outside the Lunte Group to thank for their role my research, including Ryan Grigsby for microfabrication support, Dr. Chamani Perera for synthesis and characterization support, the MAI Core for helpful discussions, and Dr. Christian Schoeneich, Dr. Maggie Witek, Dr. Russell Swerdlow for collaboration on the KU Alzheimer's

Disease Center Pilot Grant and for helping me to define the scope of the project. I learned so much from each of you and am appreciative of your training, support and helpful discussions. Additionally, I would like to thank Chelsea Comadoll for helpful discussions regarding synthetic chemistry and organic reaction mechanisms and Dr. Tom Field for letting me talk electrochemistry with him at the softball fields twice a week.

I was lucky enough to work in not just one but three great research groups during graduate school. I would like to thank Dr. Peter Willis and his group at the NASA Jet Propulsion Laboratory for welcoming me into their lab in Summer 2017. I learned so much about astrobiology, device miniaturization, and the space program from working with this group. I would especially like to thank Dr. Jessica Creamer and Dr. Fernanda Mora for being excellent mentors during this time. I would also like to thank the Society for Lab Automation and Screening for funding my research rotation in the Pharmaceutical Analysis Group at the University of Groningen in Fall 2018. I am appreciative to Dr. Sabeth Verpoorte for welcoming me into her group and for being a mentor for me during that time, and to the entire lab for being so kind and helpful as I was getting used to life in the Netherlands and learning my way around the lab. I would especially like to thank my officemates and collaborators, Dr. Maciej Grajewski and Pim de Haan, for challenging me to think about my research in new ways, for showing me the best places to buy coffee during work (and a beer after work) and for being excellent friends and colleagues during my stay in Groningen. I would also like to thank Daan Zillen for assistance with Solidworks designs.

I was so lucky to have made so many close friends during graduate school within my research group; however, there were countless other people in the Chemistry Department who made my time in Lawrence wonderful and helped support me through my time at KU. Thank you to everyone who stayed up late grading and finishing assignments with me in our first years of grad school, to everyone who listened to me talk about my research problems and helped me

through orals, and to everyone who was always up for fun. In particular, I would like to thank Brittany Sanders and Dr. Tal Aharon – both of you have been there for me since my first summer at KU and I am so grateful for your support and friendship.

Finally, I have to thank my family. My fiancé, Zeke, always pushes me to be a better scientist and has mastered the art of critiquing my research while still being supportive. Thank you for always being able to brighten my day, for keeping me well-fed during long days in the lab, and especially for impulsively adopting a cat during orals. Late nights writing would have been a lot rougher without Lirael sitting right next to me! This last year of graduate school hasn't exactly gone as we'd planned, but I'm so glad I've had you by my side and I'm looking forward to what comes next for us. My parents have never questioned my decisions, even when I said I was going to move to Kansas and start a PhD program in chemistry three weeks after graduating from an undergraduate program I had found very challenging. Mom and Dad, thank you for supporting me unconditionally and for always reminding me that I can do it, and for keeping track of my jargon so I could tell you all about my research. I would not have been able to make it through the last several years without your support. I would also like to thank my siblings, Tyler, Haley, Colin, and Caleb for supporting me and for always being up for a chat about how grad school was going. To everyone who has played a role in my life for the past six years, thank you!

Abbreviations

Reactive nitrogen and oxygen species – RNOS

Capillary electrophoresis – CE

Microchip electrophoresis – ME

Electrochemical detection – EC

Alzheimer's disease – AD

Polydimethylsiloxane – PDMS

Background electrolyte – BGE

3-nitrotyrosine – NT, 3-NT, NO_2Y, 3-NO_2Y

Diode array detection – DAD

3-morpholinosydnonimine hydrochloride – SIN-1

Nitric oxide synthase – NOS

Superoxide dismutase – SOD

Lipopolysaccharide – LPS

Fluorescence detection – FL

Mass spectrometry – MS

Liquid chromatography – LC

Limit of detection – LOD

L-3,4-dihydroxyphenylalanine – L-DOPA

Cyclodextrin – CD

Electroosmotic flow – EOF

Critical micelle concentration – CMC

Polymethylmethacrylate – PMMA

Working electrode – WE

Reference electrode – RE

Counter electrode – CE

Ground – GND

Sodium dodecyl sulfate – SDS

Tetradecyltrimethylammonium chloride – TTAC

Isoelectric point – pI

Carbon fiber – CF

Nitric oxide – NO

Table of Contents

1 Chapter 1: Research Objectives and Summaries 2

1.1 Research Objectives 2

1.2 Chapter Summaries 2

1.2.1 Chapter 2 2

1.2.2 Chapter 3 3

1.2.3 Chapter 4 3

1.2.4 Chapter 5 3

1.2.5 Chapter 6 4

1.2.6 Chapter 7 4

1.2.7 Chapter 8 5

2 Chapter 2: Introduction to cellular nitrosative and oxidative stress and protein nitration 7

2.1 Production of RNOS in cells and their effects 7

2.1.1 Biochemistry of peroxynitrite and tyrosine nitration 7

2.1.2 Effects of tyrosine nitration 10

2.1.3 Prevalence of tyrosine nitration 11

2.1.4 RNOS and Alzheimer's disease 13

2.2 Analytical methods for the investigation of nitrosative and oxidative stress 17

2.2.1 Methods for studying RNOS and related compounds 17

2.2.1.1 Assays and sensors 17

2.2.1.2 Electrophoretic methods 17

2.2.2 Methods for studying protein and peptide nitration 21

2.2.2.1 Considerations for detection of 3-nitrotyrosine 21

2.2.2.2 Chromatographic methods for studying protein nitration 22

2.2.2.3 Electrochemical methods for studying protein nitration 24

2.2.2.4 Controversies regarding the detection of NT and methods to address artifactual formation 27

2.3 Conclusions 28

2.4 References 28

3 Chapter 3: Introduction to electrophoretic separations and microchip electrophoresis with electrochemical detection 35

3.1 Electrophoretic separations 35

3.2 Microchip electrophoresis with electrochemical detection 39

3.2.1 Microchip electrophoresis 39

3.2.2 Material and fabrication methods 42

3.2.2.1 Microchip substrates 42

3.2.2.2 Microelectrode fabrication 44

3.2.2.3 Electrode modifications 46

3.2.3 ME-EC configurations 47

3.2.3.1 Electrode alignments 47
3.2.3.1.1 End-channel alignment 49
3.2.3.1.2 In-channel alignment 49
3.2.3.1.3 Off-channel alignment 50
3.2.3.2 Dual channels and/or electrodes 51
3.2.3.2.1 Dual-series electrode configuration 51
3.2.3.2.2 Dual-channel, dual-parallel electrode configuration 55
3.3 Conclusions 58
3.4 References 58
4 Chapter 4: Improved detection of intracellular nitrite in macrophage cells .. 67
4.1 Abstract 67
4.2 Introduction 67
4.3 Materials and methods 70
4.3.1 Reagents and materials 70
4.3.2 PDMS microchip fabrication 71
4.3.3 Electrode fabrication 72
4.3.4 Electrophoresis procedure 73
4.3.5 Electrochemical detection and data analysis 73
4.3.6 Pt black deposition 74
4.3.7 Cell culture and sample preparation 74

4.4 Results and discussion 77

4.4.1 Separation optimization and stacking of nitrite 77

4.4.2 Electrode deposition optimization 82

4.4.3 Signal enhancement 85

4.4.4 Nitrite in biological samples 88

4.5 Conclusions 91

4.6 Acknowledgements 91

4.7 References 92

5 Chapter 5: Capillary electrophoresis with diode array detection as a tool for .. study of oxidative modifications of tyrosine-containing species 97

5.1 Abstract 97

5.2 Introduction 97

5.3 Materials and methods 99

5.3.1 Reagents and materials 99

5.3.2 Electrophoresis procedure 99

5.3.3 Peroxynitrite synthesis 100

5.3.4 Data analysis 100

5.3.5 LC-MS protocol 100

5.4 Results and discussion 104

5.4.1 Separation optimization 104

5.4.1.1 Analyte selection 104

5.4.1.2 Effect of BGE pH on separation 104

5.4.1.3 Effect of BGE concentration on separation 105

5.4.1.4 Effect of surfactant concentration on separation 105

5.4.1.5 Addition of cyclodextrins to improve separation 109

5.4.1.6 Optimal CE separations of analytes of interest 109

5.4.2 Oxidation and nitration of tyrosine-containing species 112

5.4.2.1 Generation of a highly reactive, oxidizing environment 112

5.4.2.2 Exposure of tyrosine to the peroxynitrite reaction mixture 113

5.4.2.3 Identification of reaction products using CE-DAD 117

5.4.2.4 Reactions of peroxynitrite with other tyrosine-containing analytes 126

5.4.3 Additional uses of the optimized CE-DAD method 129

5.4.3.1 Evaluation of the formation of artifactual 3-nitrotyrosine during sample storage 129

5.4.3.2 Detection of tyrosine reaction products in the presence of SIN-1 133

5.4.3.3 Observation of the reduction of 3-nitrotyrosine *via* sodium dithionite 135

5.4.3.4 Evaluation of extraction conditions for further analysis of complex samples 137

5.4.4 Confirmation of peak identities using mass spectrometry 139

5.5 Concluding remarks 139

5.6 References 140

6 Chapter 6: Microchip electrophoresis with dual electrode amperometric detection for the selective study of tyrosine nitration 142

6.1 Introduction 142

6.2 Material and methods 144

6.2.1 Reagents and materials 144

6.2.2 Microchip fabrication 144

6.2.3 ME-EC procedure 145

6.2.4 Cyclic voltammetry procedure 145

6.2.5 Peroxynitrite synthesis 145

6.3 Results and discussion 146

6.3.1 Single electrode detection of tyrosine and nitrotyrosine 146

6.3.2 Premise for dual electrode electrochemical detection of 3-NT 148

6.3.3 Conditions attempted for dual electrode ME-EC of 3-NT 151

6.3.3.1 Buffer composition 151

6.3.3.2 Electrode characteristics 155

6.3.3.3 Consistency of electrode configuration 158

6.3.4 Peak identification 161

6.3.4.1 Sample blanks and comparison to other nitrated species 161

6.3.4.2 Electrochemistry of peaks 167

6.3.4.3 Calibration curves 169

6.3.5 Evaluation of dual electrode detection system performance using model analytes 171

6.4 Conclusions 176

6.5 References 176

7 Chapter 7: Development of a 3D printed scaffold for boronate affinity enrichment of cis-diol-containing species 180

7.1 Introduction 180

7.2 Materials and methods 187

7.2.1 Reagents and materials 187

7.2.2 3D printing procedures 187

7.2.3 Monolith polymerization procedure 188

7.2.4 Offline and online detection procedures 188

7.3 Results and discussion 190

7.3.1 Development of a 3D printed scaffold for boronate enrichment of cis-diol-containing analytes 190

7.3.2 Polymerization conditions optimization 196

7.3.3 Column use optimization 199

7.3.3.1 Model analyte 199

7.3.3.2 Experimental set-up 202

7.3.3.3 Sample introduction 202

7.3.3.4 Analyte loading 206

7.3.3.5 Analyte elution 208

7.3.4 Exploration of possible techniques for eluent detection 212

7.3.4.1 Off-line detection 212

7.3.4.2 On-line detection 216

7.4 Conclusions and outlook for 3D printing in relation to this work 224

7.5 References 224

8 Chapter 8: Summary and Future Directions 227

8.1 Summary 227

8.2 Future directions 228

8.2.1 Electrophoretic separations for the analysis of 3-nitrotyrosine in biological systems 228

8.2.2 Development of a modular, 3D-printed device to detect protein nitration in the blood 231

List of Figures

Figure 2.1. Tyrosine oxidation pathways. Purple text indicates enzymes important to the pathway; Blue text indicates antioxidants that may reverse oxidation of tyrosine; Red text indicates species capable of oxidizing tyrosine; Green text indicates final products of tyrosine oxidation reaction. Abbreviations: nitric oxide synthase (NOS), superoxide dismutase (SOD), NADPH oxidase (NOX), myeloperoxidase (MPO), glutathione (GSH), ascorbic acid (AA), electron transfer (ET), lipid (L). Based on information found in references.[2, 4-11] 9

Figure 2.2 Aβ-induced oxidative stress in a cell of an AD brain. 4-HNE = 4-hydroxynonenal. Orange star indicates oxidative damages. Reproduced from reference[1] with permission from Elsevier. 15

Figure 2.3. (A) Monitoring the production of peroxynitrite from SIN-1 using ME-EC in reverse polarity. Reprinted with permission from reference[29]. Copyright (2010) American Chemical Society. (B) Monitoring the acid hydrolysis of PROLI/NO at pH 7.2-7.4 using ME-EC in reverse polarity. Triangle nitrite; solid circle PROLI/NO; open circle NO. The arrows indicate sample injections. Reproduced from reference[30] with permission from Springer Nature..... 19

Figure 2.4. (A) Comparison of LPS-stimulated (top) and native (bottom) RAW 264.7 macrophage cell lysates using ME-EC in reverse polarity (B) Comparison of the ME-EC method and the Griess assay for determining the increase in nitrite concentration resulting from a 24 h LPS stimulation relative to the nitrite concentration produced from native cells. Reproduced from reference[31] with permission from The Royal Society of Chemistry..... 20

Figure 2.5. Diagram of a HPLC-electrochemical system. Reproduced from reference[50] with permission from Taylor & Francis. 26

Figure 3.1. (A) Schematic of a capillary electrophoresis instrument; (B) separation mechanism for capillary electrophoresis in normal polarity; (C) sample electropherogram for three

analytes: one cation, one neutral species, and one anion, in normal polarity. EOF: electroosmotic flow. 38

Figure 3.2. Comparison of experimental set-up for (A) capillary and (B) microchip electrophoresis. 41

Figure 3.3. Microfabrication methods used in this dissertation (A) Fabrication of a silicon master and PDMS microchip; (B) fabrication of a metal working electrode in a glass substrate; (C) fabrication of a carbon fiber working electrode in a PDMS substrate topped with a PDMS 5-cm simple-T microchip (D). 43

Figure 3.4. Electrode alignments used with ME-EC with a single working electrode; arrows indicate the path of the separation current. (A) End-channel detection (B) In-channel detection (C) Off-channel detection; B: buffer, S: sample waste, W: waste, GND: ground, WE: working electrode, HV: high voltage. Adapted from reference[96]. 48

Figure 3.5. (a) Dual-series electrode configuration for ME-EC (b) Dual-electrode detection of tyrosine, 5-hydroxyindoleacetic acid (HIAA), and catechol; E_1 = +750 mV, E_2 = -100 mV. Reprinted with permission from reference[110]. Copyright (2000) American Chemical Society (c) Dual-electrode detection used to identify comigrating ascorbic acid (AA) and homovanillic acid (HVA) peaks with E_1 = +400 mV and E_2 = +1000 mV. Reproduced from reference[114]. B: buffer, S: sample waste, W: waste, GND: ground, WE: working electrode, HV: high voltage. 54

Figure 3.6. Comparison of two dual-channel, dual-parallel electrode configurations (a) Schematic of a dual-channel microchip with one separation channel and one reference channel. Adapted with permission from [115] Copyright (2007) American Chemical Society (b) Comparison of approximate baseline noise and background currents when different reference electrodes were employed in dual- and single-channel microchips operated in reverse polarity. Reproduced from [118] with permission (c) Schematic of a dual-channel microchip with two separation channels.

Adapted from [113] with permission from The Royal Society of Chemistry. (d) Electropherogram obtained using the dual-channel, dual-parallel configuration for (1) nitrite, (2) azide, (3) iodide, (4) tyrosine, and (5) hydrogen peroxide standards using reverse polarity. Reproduced from [113] with permission from The Royal Society of Chemistry. B: buffer, S: sample waste, W: waste, GND: ground, WE: working electrode, HV: high voltage. 57

Figure 4.1. Protocol for the analysis of LPS-stimulated macrophage cells. (A) Native cells are incubated with LPS for 24 h to induce stimulation. (B) Cells are harvested and centrifuged to produce a cell pellet. (C) The cell pellet is washed once with PBS to remove excess medium and once with water to remove any remaining salt. (D) The cell pellet is resuspended in borate buffer at pH 10 with 5.5 mM TTAC to lyse the cells, and the lysate is centrifuged through a molecular weight cutoff filter to remove any proteins and large insoluble species. (E) Filtered cell lysate is placed in the sample well of a PDMS/glass microchip for ME-EC analysis. 76

Figure 4.2. Migration times of nitrite (■), azide (●), ascorbic acid (▲), and hydrogen peroxide (▼) by ME-EC with a BGE consisting of 10 mM borate at pH 10 with varying concentration of TTAC. 79

Figure 4.3. Electropherograms illustrating a standard solution of 50 μM nitrite (1), 20 μM azide (2), 40 μM ascorbic acid (3), and 100 μM hydrogen peroxide (4) using (a) a run buffer and sample buffer consisting of 10 mM borate and 5.5 mM TTAC at pH 10, and the effect of adding 10 mM NaCl (b) to the sample buffer, (c) to both the run buffer and sample buffer, and (d) to only the run buffer. System peaks are denoted by *. 79

Figure 4.4. (A) Electropherograms depicting the change in nitrite stacking due to transient isotachophoresis as a result of adding NaCl to the run buffer at a concentration of (a) 0 mM, (b) 2.5 mM, (c) 5 mM, (d) 10 mM, and (e) 15 mM. (B) Effect of increasing NaCl concentration on

peak efficiency (N) of each analyte (n = 3). Legend: nitrite (1, ■), azide (2, ●), ascorbic acid (3, ▲), hydrogen peroxide (4, ▼). System peaks are denoted by *. 81

Figure 4.5. SEM images of a (A) non-activated and (B) activated Pt black-modified working electrode. 84

Figure 4.6. (A) Electropherograms of 100 μM nitrite (1), 40 μM AA (2), and 100 μM hydrogen peroxide (3) standards (a) before and (b) after Pt black modification. (B) Comparison of the noise at (a) a bare Pt electrode versus (b) a Pt black electrode during a ME separation. 87

Figure 4.7. Calibration curves generated for nitrite using (a) bare Pt and (b) Pt black as the working electrode. 87

Figure 4.8. Electropherograms of an LPS-stimulated RAW 264.7 macrophage cell lysate sample obtained using (a) bare Pt and (b) Pt black. 90

Figure 5.1. Protocol for synthesis of peroxynitrite and subsequent (A,B) stabilization with NaOH or (C) reaction with tyrosine. 102

Figure 5.2. Effect of buffer pH on separation of analytes of interest (n = 3). 106

Figure 5.3. Effect of buffer concentration on separation of analytes at (A) pH 8.2 borate and (B) pH 9.2 borate (n = 3) 107

Figure 5.4. Effect of SDS concentration on separation of analytes, visualized with (A) electropherograms and (B) plot of migration times with varied concentration (n = 3). 108

Figure 5.5. Effect of cyclodextrins on analyte separation (A) electropherograms demonstrating effects of different cyclodextrins, (B) migration times of analytes with different cyclodextrins at the same concentration (n = 3), (C) effect of varied SBE-β-CD concentration on separation (n = 3). *Abbreviations: HDM-β-CD = Heptakis(2,6-di-o-methyl)-β-CD; SBE-β-CD = sulfobutylether-β-CD; 2-HP-β-CD = 2-hydroxypropyl-β-CD.* 110

Figure 5.6. Optimal separations obtained (A) without and (B) with addition of cyclodextrin. 111

Figure 5.7. (A) Electropherogram of the products of peroxynitrite synthesis reaction at 302 nm after 1, 7, or 15 s degradation time between synthesis and stabilization with NaOH. (B) Average normalized peak height of peroxynitrite at 302 nm with varied degradation time (n = 3). 115

Figure 5.8. (A) Electropherograms of the peroxynitrite/tyrosine reaction product mixture at 1, 7, and 15 s degradation times; (B) the average peak height of each of the products and of unreacted tyrosine at varied degradation time under these reaction conditions (n = 4). 116

Figure 5.9. Ratio of peak heights at varied wavelengths for (A) tyrosine and 3-NT standards, (B) the product peak identified as 3-NT, (C) Product A, and (D) Product B. (n = 3)119

Figure 5.10. Result of reacting peroxynitrite (tdeg = 1s) with tyrosine (bottom) vs reacting it with 3-nitrotyrosine (top). 120

Figure 5.11. Reaction scheme of the synthesis of peroxynitrite.[7] 122

Figure 5.12. (A) comparison of a typical reaction (green) with exposure of (blue) water, (red) tyrosine, and (black) nitrotyrosine to acidified hydrogen peroxide. (B) results of nitrotyrosine exposure to acidified hydrogen peroxide over 4 h, (C) spectra of reaction peaks (blue) and exposure peaks (red). “X” denotes peaks A/B. (n = 1) 124

Figure 5.13. Proposed reaction scheme for the production of 3-nitrotyrosine and Product A. 125

Figure 5.14. Comparison of products of the reaction of various tyrosine-containing species with peroxynitrite reaction mixture with standard solutions of (A) Y and 3-NO_2Y, (B) AY and A(NO_2Y), (C) AYL and A(NO_2Y)L, (D) FSAYLER and FSA(NO_2Y)LER, (E) NH_2Y and ClY,, and (F) DiY. Reaction with L-DOPA is unpictured but results in a loss of the L-DOPA peak. 128

Figure 5.15. (A) Scheme for exposure of tyrosine to acidified nitrite, (B) Conversion of tyrosine to nitrotyrosine upon exposure to acidified nitrite (n = 1). 130

Figure 5.16. Conversion of tyrosine to 3-nitrotyrosine upon exposure to nitrite under acidic conditions at a variety of temperature (n=3)..... 132

Figure 5.17. SIN-1 with (A) tyrosine or (B) water at 10 timepoints (t1 → t10). Peak 3 can be identified as tyrosine, and peaks 4, 6, and 7 could be oxidative modifications of tyrosine. (n = 1) 134

Figure 5.18. Use of sodium dithionite to reduce (A) 3-NT standard solution and (B) tyrosine/peroxynitrite reaction mixture (t_{deg} = 1 s); (C) comparison of DAD data of the peak at approximately 2.9 min before and after the sodium dithionite reduction with DAD data. 136

Figure 5.19. (A) Effect of varying pH on the extraction efficiency of reaction product peaks and (B) Result of extraction step on reaction samples. 138

Figure 6.1. ME-EC with a single CF WE aligned pseudo-in-channel of tyrosine (Y) and 3-NT (NO_2Y) at two WE potentials, 0.8 V and 1.0 V *vs*. Ag/AgCl RE. BGE: 10 mM sodium phosphate at pH 6.5, 2 mM SDS. (A) standards (B) products of the reaction of tyrosine and peroxynitrous acid at low pH, (C) products of the reaction of tyrosine with largely degraded peroxynitrous acid (HCl, NO_2^-, NO_3^-). Peak 1 corresponds to unreacted tyrosine and Peak 2 likely corresponds to nitrated tyrosine. 147

Figure 6.2. (A) Cyclic voltammograms of tyrosine, 3-NT, and 3-AT at pH 6.4; (B) Effect of increasing pH on increasing the absolute potential necessary to reduce 3-NT (i). (C) Effect of increasing pH on decreasing potential necessary to re-oxidize the reduced 3-NT (ii) and to oxidize non-reduced 3-NT (iii). GC WE, Ag/AgCl RE, Pt wire CE, 50 mV/s, 50 mM phosphate buffer at varied pH. 150

Figure 6.3. Dual electrode ME-EC at dual 15 µm wide Pt working electrodes with a 10 µm gap. WE1 was aligned 0 µm in-channel and the BGE was 15 mM phosphate at pH 7.4 with 15 mM SDS and 2.5 mM boric acid. (A) sample: 3-NT, day A; (B) sample: tyrosine and 3-NT, day B; (C) effect of WE1 potential on reduction peaks (no potential applied to WE2), sample: tyrosine and 3-NT, day B. 152

Figure 6.4. Dual electrode ME-EC of (A) 3-NT in 10 mM acetate buffer at pH 4.64 with 2 mM SDS, 10 µm Pt, WE1 0 µm in-channel, WE2 ~20 µm end-channel (B) Tyr and 3-NT in 10 mM phosphate buffer at pH 6.4 with 2 mM SDS, 33 µm CF, WE1 0 µm in-channel, WE2 ~63 µm end-channel. 154

Figure 6.5. Effect of electrode alignment and WE1 potential on background current stability and system peak intensity for a sample of 3-NT and 3-AT injected 3 times (70 s run time), BGE 10 mM phosphate at pH 6.4, 2 mM SDS. Dual 33 µm CF WE, 33 µm gap with indicated WE1 potential and alignment and WE2 +400 mV *vs*. Ag/AgCl, aligned ~63 µm end-channel relative to WE1. 157

Figure 6.6. A and B depict two different configurations of the ground, counter, and reference electrodes relative to the end of the separation channel and the working electrodes. C and D depict top and side views, respectively, of a 3D-printed electrode holder. 160

Figure 6.7. Effect of sample matrix on system peaks with a dual 33 µm CF WE, 30 µm gap; WE1 ~63 µm in-channel, -400 mV *vs.* Ag/AgCl; WE2: ~0 µm in-channel, +900 mV *vs.* Ag/AgCl; (A) 3-NT diluted into 10 mM phosphate buffer – conductivity of sample lower than that of BGE; (B) water diluted into 10 mM phosphate to match conductivity of 3-NT sample from A is both sample and BGE – conductivity of sample matches that of BGE; (C) 3-NT diluted into 10 mM phosphate buffer and BGE consists of water diluted into 10 mM phosphate – conductivity of sample matches that of BGE..... 163

Figure 6.8. Growth of a system peak over time when BGE is matched to the sample matrix. Each subsequent pair of electropherograms depicts an injection immediately following the previous pair. Dual 33 μm CF WE, 30 μm gap; WE1 ~63 μm in-channel, -400 mV *vs.* Ag/AgCl; WE2: ~0 μm in-channel, +900 mV *vs.* Ag/AgCl. 164

Figure 6.9. Dual electrode ME-EC at 33 μm CF WE, 30 μm gap; BGE: 10 mM phosphate at pH 6.4, 2 mM SDS; Samples: indicated solution diluted into BGE; detection at (A) WE1: -200 mV *vs.* Ag/AgCl, 63 μm in-channel, (B) WE2: +600 mV *vs.* Ag/AgCl/0 μm in-channel. Peaks 1 and 3 are system peaks, Peak 2 is dependent on nitration. 166

Figure 6.10. (A) Reductive HDVs of the system peak (peak 1) and the peak that comigrates with 3-NT (peak 2) at WE1 aligned 33 μm in-channel; (B) oxidative HDVs of Tyr, 3-NT, 3-AT, and the oxidation peak 2 observed in the dual system at WE2 aligned 0 μm in-channel; (C) oxidative HDVs of the oxidation peak 2 observed in this dual system (WE2 Peak 2) and in the LC-EC system reported by Kissinger, *et al.* (Kissinger WE2 Peak 2) at 3 mm glassy carbon electrodes, WE1 -750 mV *vs*. Ag/AgCl, WE2 varied, and a LC mobile phase of 90 mM sodium acetate – 35 mM citric acid buffer (pH 4.4), 3 mM SOS, 1.0 mM EDTA, 3% (v/v) MeOH.[12] Additional ME-EC parameters: Dual 33 μm CF WE, 30 μm gap, BGE: 10 mM phosphate at pH 6.4, 2 mM SDS. 168

Figure 6.11. Calibration curves for (A) reduction peaks 1 (system peak) and 2 (3-NT-dependent peak) at WE1: -400 mV *vs*. Ag/AgCl, 63 μm in-channel and (B) oxidation peaks 1 (system peak, not observed) and 2 (3-NT) at WE2: +900 mV *vs*. Ag/AgCl, 0 μm in-channel. BGE: 10 mM phosphate at pH 6.4, 2 mM SDS..... 170

Figure 6.12. Dual electrode ME-EC at 33 μm dual CF WE (30 μm gap, WE1: 0 μm in-channel, WE2: 63 μm end-channel), BGE: 20 mM borate at pH 8.2 with 5 mM SDS of (A) 3-NT, (B) resazurin, and (C) dopamine. * denotes likely system peaks. 173

Figure 6.13. HDV of dopamine at different electrode alignments (A) for oxidation to the orthoquinone at WE1, (B) for reduction of the orthoquinone WE2, and (C) for oxidation of dopamine at a single WE. (D) Single WE aligned 63 μm in-channel, (E) Single WE aligned 33 μm in-channel. 175

Figure 7.1. (A) Conventional workflow for analysis of nitrated peptides; (B) Tagging of nitrated peptides via sodium dithionite reduction followed by selective derivatization with (3R, 4S)-1-(4-(aminomethyl)phenylsulfonyl)pyrrolidine-3,4-diol (APPD); (C) Trapping of tagged peptides via boronate affinity chromatography at high pH followed by elution in an enriched, purified fraction at low pH. 183

Figure 7.2. Possible layout of an integrated microfluidic device for profiling mitochondrial protein nitration from whole blood..... 183

Figure 7.3. All-glass microchip containing a boronate affinity monolith (BAM) with a steel pin secured at the inlet via a piece of PDMS. 186

Figure 7.4. (A) Generic scaffold for monolith polymerization containing a central polymerization chamber; (B) Cross-section of the scaffold sealed against a base to form a sealed well; (C) Sealed scaffold containing polymerization solution being exposed to UV light for polymerization; (D) Sealed scaffold containing boronate polymer; (E) Scaffold containing boronate polymer removed from its base so the outlet is open for flow of solution. 191

Figure 7.5. Scaffold designs explored during device optimization. (A) PDMS well; (B) 3D-printed disk scaffold; (C) 3D-printed plug for 3D-printed disk scaffold; (D) 3D printed cylinder; (E) 3D printed female portion of a luer-lock (FLL); (D) 3D printed female portion of a luer-lock with a rim around the outlet (FLLR); (E) 3D printed cylinder that can be screwed into connectors (integratable cylinder, IC); (F) 3D printed male luer-lock (MLL) connection cap for the IC scaffold. 192

Figure 7.6. Schematic of how uncured PDMS can be used as a base during polymerization. (A) To polymerize a monolith within the scaffold, the scaffold is placed into uncured PDMS such that it sinks slightly into the PDMS layer, forming a seal so the well can be filled with polymerization solution; (B) After polymerization, the scaffold is peeled off the PDMS base, resulting in a scaffold that contains a boronate monolith open on both ends. 195

Figure 7.7. Polymerization optimization. (A) Effect of increasing UV exposure time on extent of polymerization; (B) Effect of increasing distance from the UV source on extent of polymerization; (C) Polymerization set-up with UV spot source and PDMS well scaffold; (D) Comparison of i. FLLR scaffold (45 µL polymerization solution (P.S.), 30 min), ii. IC scaffold (45 µL P.S., 30 min), iii. IC scaffold (90 µL P.S., 45 min), iv. IC scaffold (45 µL P.S., 15 min + 45 µL P.S., 45 min)..... 198

Figure 7.8. (A) Model analyte Alizarin Red S (ARS); (B) Absorbance spectrum of 10^{-4} M ARS in 0.1 M phosphate buffer at pH 7.4 (i) unbound, (ii) after addition of 10^{-3} M phenylboronic acid (PBA) to bind the ARS, and (iii) after addition of 10^{-1} M fructose to preferentially bind to the PBA and displace the bound ARS, reproduced from Ref.[17] with permission from The Royal Society of Chemistry; (C) 1 mg/4 mL ARS at varied pH; (D) Color shift of 100 µM ARS upon exposure to non-boronated (-VPBA) or boronated (+VPBA) polymer..... 200

Figure 7.9. (A) Integration of scaffold F with a syringe and syringe pump; (B) Addition of a tube for collection of eluent. 201

Figure 7.10. Sample reproducibility of spotting varied volumes of 1 mM ARS on Scaffold F columns using a syringe. 205

Figure 7.11. Column use protocol for loading of exact volumes of sample. (A) A piece of tubing is loaded with a known volume of analyte; (B) Once the analyte is in the tubing, loading buffer is pumped into the syringe to push the analyte into the column to bind; (C) Once the analyte

has passed through the column, loading buffer continues to rinse the column to remove any nonspecifically bound analyte; (D) When elution buffer is pumped through the column, the analyte is released from the column and collected in the eluent. 205

Figure 7.12. Demonstration of efficacy of 50 mM phosphate at pH 7.74 as a loading buffer. (A) The eluent from the +VPBA column is largely colorless, while the eluent from the -VPBA column is the same color as the ARS solution being perfused, demonstrating the ARS being bound to the +VPBA column. (B) No ARS is observed eluting from the +VPBA column, while the ARS is being observed flushing out of the -VPBA column; (C) After loading with ARS, the color difference between ARS bound to the +VPBA column versus unbound to the -VPBA column is observed; (D) After rinsing with pH 7.74, the +VPBA column has retained the ARS, while the -VPBA column has not. 207

Figure 7.13. (A) Comparison of boronated (+VPBA) and nonboronated (-VPBA) columns (i) loaded with ARS, (ii) rinsed with pH 7.74 phosphate, and (iii) rinsed with pH 2.1 phosphate. (B) Comparison of eluent from each of those steps demonstrating the change in color and color intensity with each condition. 210

Figure 7.14. Effect of increasing percent acetone (v/v) with pH 2.1 phosphate as elution buffer..... 211

Figure 7.15. (A) Absorbance spectra of ARS at pH 2.0 and pH 7.5 (spectrophotometer); (B) calibration curves of ARS at the λ_{max} for pH 2.0 and 7.5 (spectrophotometer); (C) calibration curves of ARS at the λ_{max} for pH 2.0 and 7.5 and the effect of the addition of acetone on the pH 2.0 calibration curve (plate reader). 213

Figure 7.16. Approximate nmol ARS detected in each eluent fraction from boronated and nonboronated columns with (A) varied flow rate and (B) varied loading pH. These plots demonstrate the irreproducibility of this method..... 215

Figure 7.17. Result of using three different MS-compatible solvents as elution “buffer.” Images depict the amount of ARS eluted in the first elution fraction *vs*. the ARS that remained bound on the column after elution when using (A) 0.1% formic acid, (B) 100% acetonitrile, and (C) 0.1% formic acid + 50% acetonitrile as the elution solution..... 217

Figure 7.18. Integration of column with mass spectrometer. 219

Figure 7.19. MS data obtained when a boronated column was loaded with DA and rinsed off-line and then perfused with elution buffer directly into the instrument as shown in Figure 7.18. (A) Total ion chromatogram during elution from column; (B) sample mass spectrum during elution in region 1; (C) extracted ion chromatogram at dopamine's m/z 154; (D) zoomed in mass spectrum during elution in region 2. “A” indicates a point when perfusion was paused and “B” indicates the point when perfusion was restarted. 220

Figure 7.20. Integration of column with UV detector using a syringe pump and Uniswitch device. 222

Figure 7.21. Sample preliminary data using LC UV detector for (A) calibration with ARS; (B) loading/rinsing/eluting ARS on a non-boronated column; (C) the same experiment on a boronated column. 223

Figure 8.1. (A) Schematic of the mechanical homogenizer that was used for bulk cell lysis; (B) Photographs of a 3D printed version of this homogenizer in development. 232

Chapter 1

Research Objectives and Chapter Summaries

1 Chapter 1: Research Objectives and Summaries

1.1 Research Objectives

Although nitrosative and oxidative stress has been associated with a wide variety of disease states, very little is still understood concerning the detailed mechanisms involved in the development of nitrosative and oxidative stress and how it impacts disease progression. Therefore, there is a need for improved analytical methods for monitoring the production of reactive nitrogen and oxygen species (RNOS) under conditions of cellular and physiological stress, as well as the reactions of these RNOS with biomolecules. The goal of this dissertation is to develop a suite of methods capable of monitoring RNOS, their metabolites, and their reactive products with biomolecules, in particular protein nitration, in biological samples. In order to accomplish this goal, several novel electrophoretic-based separation methods have been developed. Particular focus has been on the use of microchip electrophoresis due to its low sample volume requirements and its ability to perform efficient, rapid separations of transient species. Future work is focused on the development of 3D printed devices for sample preparation prior to analysis.

1.2 Chapter Summaries

1.2.1 Chapter 2

This dissertation focuses on the development of analytical methods capable of probing conditions of nitrosative and oxidative stress in biological samples. This chapter reviews the biochemical origins of nitrosative and oxidative stress, including mechanisms of the formation of reactive nitrogen and oxygen species (RNOS) *in vivo.* The modification of protein-bound tyrosine by RNOS as a biomarker of oxidative stress is also discussed. Lastly, a review of analytical methods used to detect both RNOS and protein nitration is presented and important considerations for the quantification of biological 3-nitrotyrosine content are discussed.

1.2.2 Chapter 3

Much of the work described in this dissertation for monitoring RNOS and tyrosine nitration takes advantage of electrophoretic separations. This chapter introduces the principles of capillary electrophoresis separations and then compares capillary electrophoresis with its miniaturized form, microchip electrophoresis. The coupling of microchip electrophoresis to electrochemical detection for fast, miniaturizable, sensitive, and selective detection of electroactive analytes is then discussed, with emphasis placed on the different electrode configurations possible and on important considerations for coupling electrochemical detection with a separation field.

1.2.3 Chapter 4

Nitrite is one of the products of nitric oxide degradation and is often used as an indirect measure of the amount of nitric oxide produced during proinflammatory conditions such as those found in an imbalanced immune response, which results in oxidative and nitrosative stress. Our group previously had described a ME-EC method for the detection of nitrite in macrophage cell lysates. In this chapter, a more sensitive method for the detection of nitrite in macrophage cell lysates is described. Nitrite was separated from other intercellular components, and a transient isotachophoresis method for enhancing the nitrite peak height was developed. A method for depositing Pt black on a bare Pt band working electrode was developed and the effect of this modification on the electrochemical signal was assessed. The optimized method was used to detect nitrite in the bulk cell lysates of macrophage cells stimulated with lipopolysaccharides.

1.2.4 Chapter 5

In order to gain a complete picture of the biological impacts of oxidative stress, it is important to be able to monitor all possible oxidative products of a biomolecule of interest simultaneously. Therefore, in this chapter, a capillary electrophoresis separation with UV detection is optimized that is capable of resolving several oxidative modifications of free tyrosine

as well as the nitrated and non-nitrated forms of three tyrosine-containing peptides. As a proof-of-concept, this method is then applied to the identification of reaction products upon exposure of tyrosine to peroxynitrite as well as acidified nitrite. These applications demonstrate this method's utility for studying oxidative tyrosine modifications formed both biologically and during sample preparation.

1.2.5 Chapter 6

Even under conditions of nitrosative and oxidative stress, non-nitrated tyrosine is always present in a significant excess versus nitrated tyrosine residues in proteins. As a result, it is of interest to develop analytical methods capable of the selective detection of 3-nitrotyrosine. To this end, this chapter describes progress towards the development of a microchip electrophoresis method with dual electrode electrochemical detection for selective detection of nitrated tyrosine and nitrated tyrosine-containing peptides in the presence of non-nitrated species. Factors that impact the reproducibility of the system are discussed and peaks in the dual electrode electropherograms are identified. The impact of electrode alignment on the electrochemical response is then evaluated using dopamine a model analyte that exhibits a more stable electrochemical background than 3-nitrotyrosine.

1.2.6 Chapter 7

This chapter discusses available 3D printing technology, current uses of 3D printing for analytical applications, and the benefits and challenges to adapting 3D printing technology to the fabrication of microfluidic devices. The development of a 3D printed scaffold for a miniaturized boronate affinity column is then discussed. Scaffold design as well as polymerization, loading, and elution conditions were optimized and several detection strategies were explored. This column will ultimately be integrated with other modules for the capture of derivatized nitrated peptides from the blood of Alzheimer's disease patients.

1.2.7 Chapter 8

This chapter summarizes the work described in the rest of this dissertation and discusses some possible future directions, most notably the improvement of the electrode configurations and materials for dual electrode electrochemical detection of reducible species and the development of additional 3D printed sample preparation modules.

Chapter 2

Introduction to cellular nitrosative and oxidative stress and protein nitration

Parts of this chapter are reproduced from the following publication:

Schilly, K.M., Gunawardhana, S.M., Wijesinghe, M.B., Lunte, S.M. "Biological applications of microchip electrophoresis with electrochemical detection: *in vivo* monitoring and cell analysis." *Anal. Bioanal. Chem.* **2020**; 412: 6101-6119, Springer Nature.

2 Chapter 2: Introduction to cellular nitrosative and oxidative stress and protein nitration

2.1 Production of RNOS in cells and their effects

2.1.1 Biochemistry of peroxynitrite and tyrosine nitration

Reactive nitrogen and oxygen species (RNOS) include peroxynitrite ($ONOO^-$ and ONOOH, pK_a 6.8), nitric oxide ($^{\bullet}NO$), and superoxide ($O_2^{\bullet-}$), which undergo a whole suite of biochemical reactions.[1] RNOS are naturally produced by the body as by-products of the respiratory electron transport chain, as well as enzymatically during the inflammatory immune response.[1] Under normal physiological conditions, RNOS production and elimination is highly controlled such that these species cannot accumulate.[1] However, under pathological conditions, RNOS begin to accumulate, leading to oxidative and nitrosative stress.[1] Under such conditions, biomolecules such as proteins, lipids, and DNA are often modified *via* reaction with these RNOS, leading to structural and functional changes that have been associated with cell injury that can be found in many disease states.

Peroxynitrite is produced *in vivo* from the reaction of superoxide and nitric oxide (second order rate constant, 1.9×10^{10} $M^{-1}s^{-1}$).[2, 3] The physiological half-life of nitric oxide is approximately 1 s, far greater than that of superoxide (which is approximately 1 μs) and that of peroxynitrite (around 5 – 20 ms). Therefore, the diffusion of nitric oxide to sites of superoxide production is an important step in the production of peroxynitrite, and the reactions of peroxynitrite with biomolecules largely occur in the vicinity of superoxide's production.[1, 4] Peroxynitrite is a strong one and two-electron oxidant that can react with biomolecules, transition metal centers, and thiols either directly or indirectly *via* production of free radical intermediate species that in turn may react with these species.[2] While many amino acids are susceptible to oxidation, including cysteine, methionine, arginine, histidine, lysine, phenylalanine, and tryptophan, tyrosine nitration is one of the most common indicators of the presence of peroxynitrite and RNOS *in vivo*.[1, 2]

In order for a tyrosine residue to be nitrated, it must first be oxidized to a tyrosyl radical (Tyr$^{\bullet}$) by an oxidant such as $^{\bullet}OH$, $^{\bullet}NO_2$, or $CO_3^{\bullet-}$. These species may be generated from peroxynitrite when it complexes with CO_2 (physiological concentration, 1.3 mM) to form the nitroso-peroxocarboxylate adduct ($ONOOCO_2^-$), which can then dissociate to form these nitrogen dioxide and carbonate radicals.[2, 3] Tyr$^{\bullet}$ may then either react with any of the other radicals in the system to produce modified residues such as nitrotyrosine ($^{\bullet}NO_2$), chlorotyrosine (HOCl), dityrosine ($^{\bullet}$Tyr), or hydroxytyrosine (*i.e.* dihydroxyphenylalanine, DOPA) ($^{\bullet}OH$) (Figure 2.1).[2] During inflammatory conditions, activated leukocytes produce many reactive species that can induce these modifications, including superoxide, hydrogen peroxide, hypobromous acid (HOBr), and hypochlorous acid (HOCl).[5]

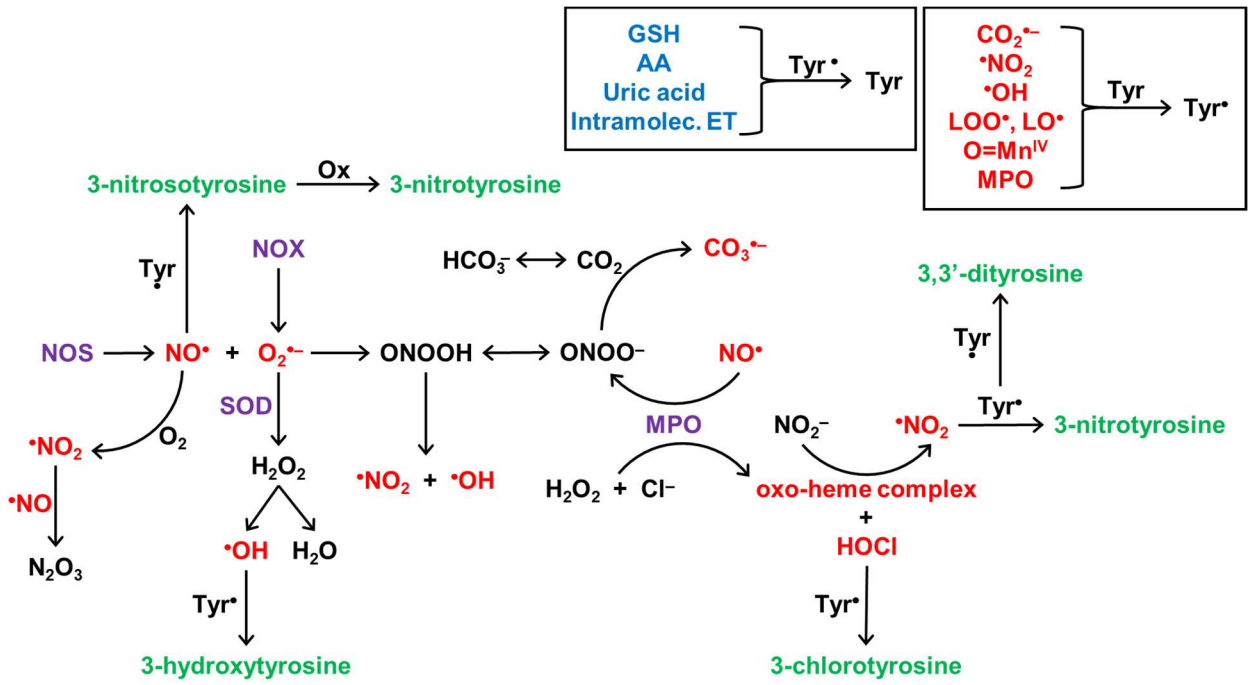

Figure 2.1. Tyrosine oxidation pathways. Purple text indicates enzymes important to the pathway; Blue text indicates antioxidants that may reverse oxidation of tyrosine; Red text indicates species capable of oxidizing tyrosine; Green text indicates final products of tyrosine oxidation reaction. Abbreviations: nitric oxide synthase (NOS), superoxide dismutase (SOD), NADPH oxidase (NOX), myeloperoxidase (MPO), glutathione (GSH), ascorbic acid (AA), electron transfer (ET), lipid (L). Based on information found in references.[2, 4-11]

2.1.2 Effects of tyrosine nitration

The addition of the nitro-group to a tyrosine in a protein results in several changes to the chemical behavior of that residue. Nitration results in a shift of the phenolic pK_a of free tyrosine molecules from 10.2 to 7.2, an increase in molecular size of around 30 Å, the appearance of an absorbance band at 360 nm in acidic media (420 nm in basic media), and an increase in the hydrophobicity of tyrosine-containing peptides.[6] Additionally, nitration can affect the ionization efficiency of the peptide for MS analysis.[6] With regards to the redox potential, nitration causes a positive shift in $E^{\circ'}$ of 200-300 mV versus the tyrosine/tyrosyl radical, thereby affecting tyrosine-dependent intramolecular electron transfer in proteins.[4] Because of these alterations to the chemical and physical properties of tyrosine, nitration can result in significant changes to protein structure.[4] These changes can cause biological effects due either to a loss- or gain-of-function or by altering the processes of protein assembly and polymerization, protein degradation, protein aggregation, and tyrosine-kinase-dependent pathways.[4] It has also been reported that nitrated proteins are degraded by the proteasome significantly faster than non-nitrated proteins, with half-lives of hours versus days. [3, 12, 13]

A notable example of a loss-of-function is the peroxynitrite-mediated nitration of Mn-SOD at Tyr34.[6] This minor modification results in a loss-of-function that then leads to less consumption of $O_2^{\bullet-}$, a greater production of peroxynitrite, and more Mn-SOD nitration so that the effect grows and becomes significant over time.[6] Overall, this Tyr34 nitration significantly alters the redox homeostasis of the mitochondria and perpetuates the production of peroxynitrite; this cascade ultimately leads to mitochondrial dysfunction.[4] Another protein that is often nitrated *in vivo* is cytochrome c.[4] When cytochrome c is exposed to peroxynitrite, the solvent-exposed tyrosine residues Tyr74 and Tyr97 are nitrated preferentially.[4] When cytochrome c is exposed to H_2O_2-dependent nitrating conditions, the heme-adjacent Tyr67 is nitrated instead.[4] Tyr74 nitration

induces a conformational change that interrupts the normal electron transport capacity of the protein and induces peroxidatic activity. This conformational change is observed in non-nitrated tyrosine at pH 9.4.[4] These examples illustrate the possible effects of nitration with regard to loss-of-function and gain-of-function and show that the conditions of nitration affect the modifications observed in a given protein.[4]

2.1.3 Prevalence of tyrosine nitration

Although it is well established that nitration is a marker of many disease states, much is still unknown about the specific sites that are nitrated, with estimates indicating that only 1 in 10^5 tyrosine residues are modified endogenously under inflammatory conditions.[13] There is evidence that tyrosine nitration is a selective process that results in only specific tyrosine residues within a protein being nitrated, as demonstrated in the MnO_2 and cytochrome c examples above.[4, 6] Much work is being done to identify which residues are nitrated under different conditions in order to gain an understanding of how nitrosative and oxidative stress is playing a role in disease pathogenesis.[6] In most proteomic analyses of nitration, relatively few nitrated proteins are able to be identified, with only a few specific residues nitrated on each one.[6] Assuming tyrosine residues make up between 3-4% of the amino acids in a protein, this relatively low incidence has led some to question the biological impact of tyrosine nitration. However, since the nitration is focused on specific residues, it is possible that loss- or gain-of-function may occur even with this low fraction of nitration in a biological system.[6] It is of note that while a large number of the same residue must be nitrated in order to result in a significant loss-of-function, a gain-of-function requires a relatively small fraction of the total amount of protein to be nitrated to observe this new function.[6]

It is evident that both the amount of oxidant/nitrating agent and the duration of the dose are important factors in determining the extent of nitration and which sites are nitrated, in addition to the identity of the oxidizing and nitrating agents.[6] The tyrosine nitration reaction is pH-

dependent, and pH is a significant factor in determining which RNOS are present in the system and what degradation/reaction pathways they follow, so the pH of the tyrosine microenvironment plays a role in the extent of its nitration.[4] The propagation of lipid peroxidation likely plays a role in the nitration of tyrosine in membrane proteins where lipid-derived radicals act as an oxidant to produce the tyrosyl radical.[4] Due to the increased production of peroxynitrite in mitochondria, where superoxide is produced as a byproduct of the electron transport chain, mitochondrial proteins are often more extensively nitrated than proteins in other cellular locations.[4]

Seeley and Stevens reported in 2011 a systematic study on factors that determine the extent of tyrosine nitration that can occur in a protein.[13] They observed that tyrosine residues surrounded by basic and/or uncharged polar residues exhibit greater degrees of nitration than tyrosine residues surrounded by hydrophobic and acidic residues.[13] They also correlated a higher degree of charge asymmetry around the tyrosine residue with increased nitration.[13] Other factors affecting nitration include amino acid side chain flexibility and bulkiness around the tyrosine site and the pH of the microenvironment, which could impact peroxynitrite stability.[13] A challenge to interpreting experiments designed to study the site-specificity of tyrosine nitration is that the use of large amounts of nitrating agent tends to oxidize all susceptible amino acid residues, while reactions with small amounts of nitrating agent exhibit the proper selectivity but to such a low degree, with respect to the total protein present in the system, that it is difficult to identify any functional changes of the nitrated proteins in the mixture.[4]

In 2011, Bayden *et al.* published a paper on structure-based predictive models for identifying the factors influencing protein tyrosine nitration.[14] While 85% of tyrosine residues are surface exposed, there is clearly some selectivity in determining which of these easily accessible tyrosine residues are nitrated.[14] Studies have been done to determine the conditions (*e.g.* location in the protein, hydrophobicity and pH of the environment, adjacent amino acids, *etc.*) that promote

nitration, and in this paper, they reported the first comprehensive and quantitative investigation of protein structural features that influence tyrosine nitration.[14] They built quantitative structure-based models to evaluate the role of secondary structure, steric effects, backbone and polar/non-polar sidechains, acidic and basic residues, sulfur, conjugated ring systems, ionization states, and hydrophobic interactions on tyrosine nitration.[14] It has been observed that steric effects and the presence of heteroatoms or unsaturated centers to stabilize the reactive radicals both play a strong role in directing tyrosine nitration. Additionally, both acidic and basic neighboring residues have been suggested to promote nitration. While these studies have generated substantial data regarding the conditions that promote nitration, at this time it is not possible to predict every preferentially-nitrated site in every protein or to predict the impact of these nitrated sites on the propagation of disease states, as these nitrating species are capable of inducing additional oxidative modifications that can also affect protein structure and function.[15]

2.1.4 RNOS and Alzheimer's disease

A devastating disease that has been associated with nitrosative and oxidative stress is Alzheimer's disease (AD). AD results in both cognitive decline due to neuronal degeneration in the hippocampus, entorhinal and frontal cortices and changes to emotional behavior due to similar degeneration in the amygdala, prefrontal cortex, and hypothalamus.[16] During AD, plaques of amyloid-beta (Aβ) and neurofibrillary tangles of hyperphosphorylated tau protein form and chronic neuroinflammation, neuronal injury, and synapse loss occur.[1, 16] The development of Aβ plaques has also been associated with the condition of oxidative stress.[1] The Aβ peptides that form these plaques are a byproduct of the cleavage of amyloid protein precursor (APP). When these oligomers enter the lipid bilayer, they induce the formation of RNOS that can then lead to lipid peroxidation as well as oxidation of proteins and nucleic acids.[16] It is also important to note that

Aβ plaques consist not only of aggregated peptides but they also contain metal ions including copper, iron, and zinc that can catalyze the production of RNOS.[1] The oxidation of lipids, proteins, and nucleic acids by RNOS can cause damage to neuronal membranes and has been implicated in the development of AD (Figure 2.2).[1] Evidence of oxidative stress caused by both Aβ peptides and mitochondrial dysfunction has been found in the brains of AD patients in the early stages of the disease, indicating that oxidative stress may have a role in the pathogenesis of the disease.[1] The oxidation of proteins in the brain can lead to a wide variety of structural modifications, including dissociation of subunits, unfolding, exposure of hydrophobic residues, aggregation, and backbone fragmentation.[16] Each of these modifications can then affect the protein's function.[16] In particular, tyrosine nitration is known to induce steric constraints to protein phosphorylation, thereby interrupting signaling mechanisms.[16] Mitochondrial dysfunction can also lead to an excess production of RNOS, which in turn has been linked with the pathogenesis of AD and is discussed below.[16]

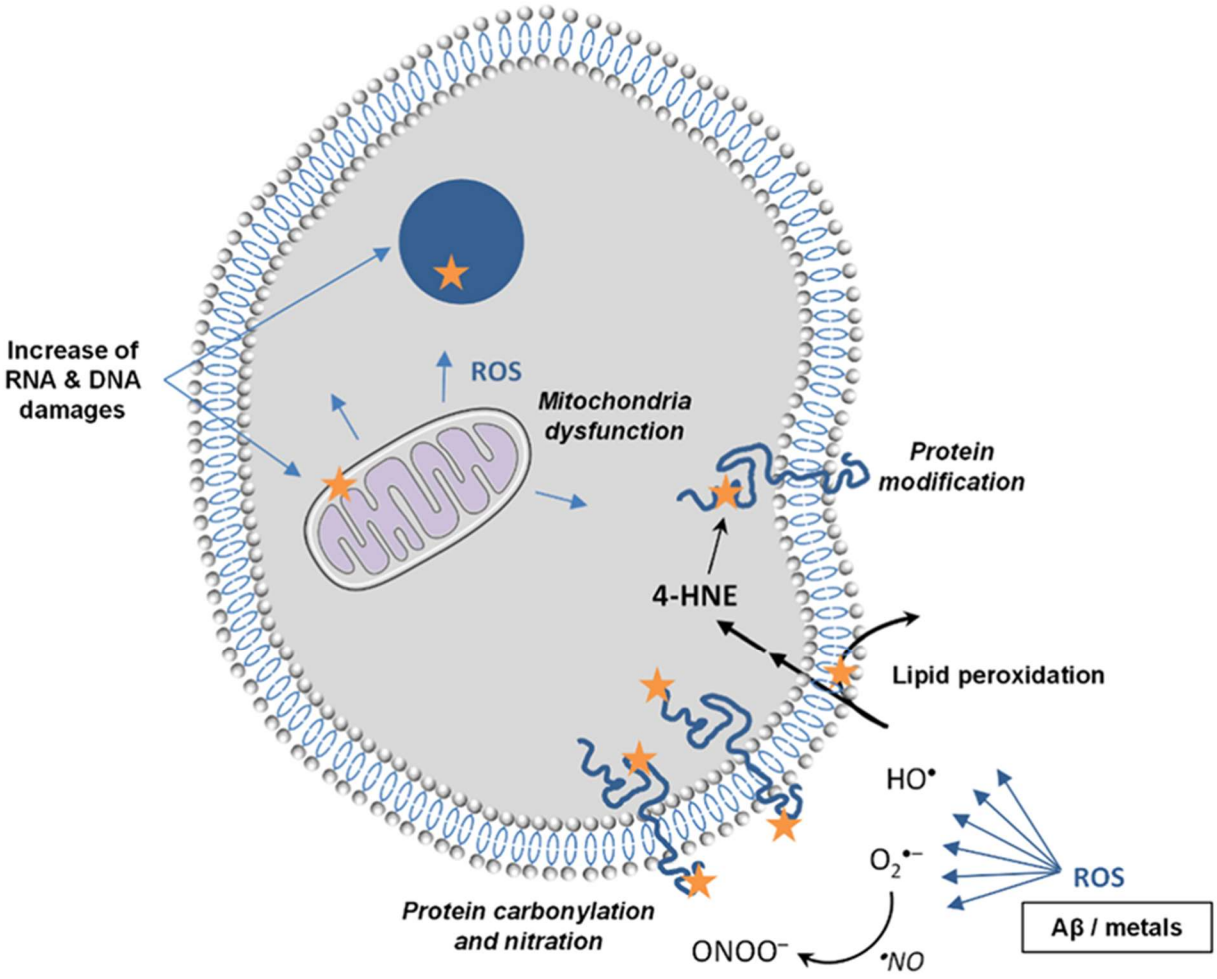

Figure 2.2 Aβ-induced oxidative stress in a cell of an AD brain. 4-HNE = 4-hydroxynonenal. Orange star indicates oxidative damages. Reproduced from reference[1] with permission from Elsevier.

Markers of nitrosative and oxidative stress have been found in both the brains and the blood of AD patients, with many of these studies utilizing redox proteomics to identify the proteins prone to oxidation.[16] Damage related to RNOS has been reported in AD and Parkinson's disease patients in the areas of the brain that undergo selective neurodegeneration.[17] In particular, protein nitration has been shown to be elevated in the hippocampus and neocortex of AD patients and nitrated tau may play a role in tauopathy.[17] As discussed above, RNOS production and oxidative stress are intimately linked with mitochondrial dysfunction, as RNOS are regularly produced as part of the electron transport chain and when processes become imbalanced mitochondrial DNA can become susceptible to oxidative attack, resulting in further disruption of the electron transport chain and out of control RNOS production.[17]

Mitochondrial dysfunction has been implicated in the progression of AD by resulting in production of excess RNOS and causing Aβ or tau-induced neurotoxicity.[17] Additionally, the formation of 3,3'-dityrosine has been shown to stabilize tau filaments and nitration of tau inhibits the ability of monomeric tau to promote tubulin assembly. Overall, these modifications result in a promotion of tau aggregation during oxidative conditions.[3] Possible biomarkers for Alzheimer's disease fall into several categories and include specific markers of AD neuropathology (*e.g.* tau, Aβ variations), non-specific markers of neurodegeneration, markers of oxidative stress, and markers of neural inflammation.[18] More information on the mechanisms of the production of oxidative stress that influences AD pathogenesis and a discussion on the potential for antioxidants as therapies for AD may be found in the work of Kamat *et al.*[19] However, there are still many unknowns regarding the exact role RNOS play in AD progression. In order to gain a greater understanding this relationship, the development of methods to study biochemical markers of oxidative and nitrosative stress is integral.

2.2 Analytical methods for the investigation of nitrosative and oxidative stress

2.2.1 Methods for studying RNOS and related compounds

2.2.1.1 Assays and sensors

Because of the short half-lives of RNOS, they are often detected *via* either their more stable metabolites or their reactive products with biomolecules such as 3-nitrotyrosine, which will be discussed in more detail below. Nitric oxide may be oxidized to form nitrite and nitrate and so these more stable species are often detected together using the Griess assay, which yields a fluorescent or colorimetric indication of the total nitrite content in the sample.[20] While the Griess assay is able to provide an indirect measure of the amount of nitric oxide produced in a biological system, it lacks specificity. Amatore *et al.* have developed various amperometric techniques for the sensitive detection of RNOS such as H_2O_2, $ONOO^-$, and $NO^\bullet$ from single stimulated RAW 264.7 macrophages. By integrating their electrodes within microfluidic devices they have been able to detect very low concentrations of these species simultaneously in separate channels for each species of interest.[21-25]

2.2.1.2 Electrophoretic methods

The sub-minute separation times of microchip electrophoresis (ME) are ideal for measuring reactive and labile species before they disappear. Additionally, the small sample volume requirements of microfluidic methods and the ability to integrate multiple processes onto one device are well-suited to cell analysis[26]. In particular, it is of interest to detect RNOS in macrophage and microglial cells, which are known to produce these cytotoxic species during the proinflammatory immune response. By measuring the concentrations of RNOS and the antioxidants that oppose them in cells under different conditions, the biochemical consequences of these imbalances can be better understood. Electrochemical detection (EC) is an attractive, low-cost, direct detection method for analysis of many biological compounds, including reactive

nitrogen and oxygen species, antioxidants, neurotransmitters, neuromodulators, and nucleobases[27, 28]. Rapid and timely monitoring of these chemicals is crucial for understanding many disease processes, early diagnoses, and the development of improved therapeutics. In this regard, development of analytical methods for continuous monitoring of biomarkers of disease *in vivo* has been of great interest during the last few decades.

Initial work the Lunte group on this topic focused on developing ME-EC methods to analyze standard solutions of peroxynitrite and nitric oxide, two important RNOS. A PDMS/glass hybrid microchip with a palladium working electrode aligned end-channel was used to separate peroxynitrite from its degradative product nitrite and detect it in its anionic form at pH 11. The peroxynitrite peak was identified based on voltammetric characterization and its degradation over time with an LOD of 2.4 μM. SIN-1 (3-morpholiniosydnonimine) was then used to generate nitric oxide and superoxide, which react to produce peroxynitrite, and the resulting samples were analyzed by ME-EC as shown in Figure 2.3a[29]. A similar approach was used for the detection of nitric oxide generated from two different NONOate salts (Figure 2.3b)[30].

Because nitric oxide and peroxynitrite are difficult to detect under physiological conditions, initial cell experiments focused on measuring nitrite in macrophage cell lysates as an indicator of the amount of nitric oxide production. Macrophage cells were stimulated with lipopolysaccharide (LPS) to induce nitric oxide synthase to produce nitric oxide, which was then oxidized to nitrite *in vivo*. A separation of nitrite, azide (an interference from cell filters), iodide (internal standard), tyrosine, glutathione, and hydrogen peroxide was optimized, and nitrite and glutathione were detected in the lysates using a PDMS/glass hybrid microchip with an integrated Pt working electrode (Figure 2.4a, b)[31].

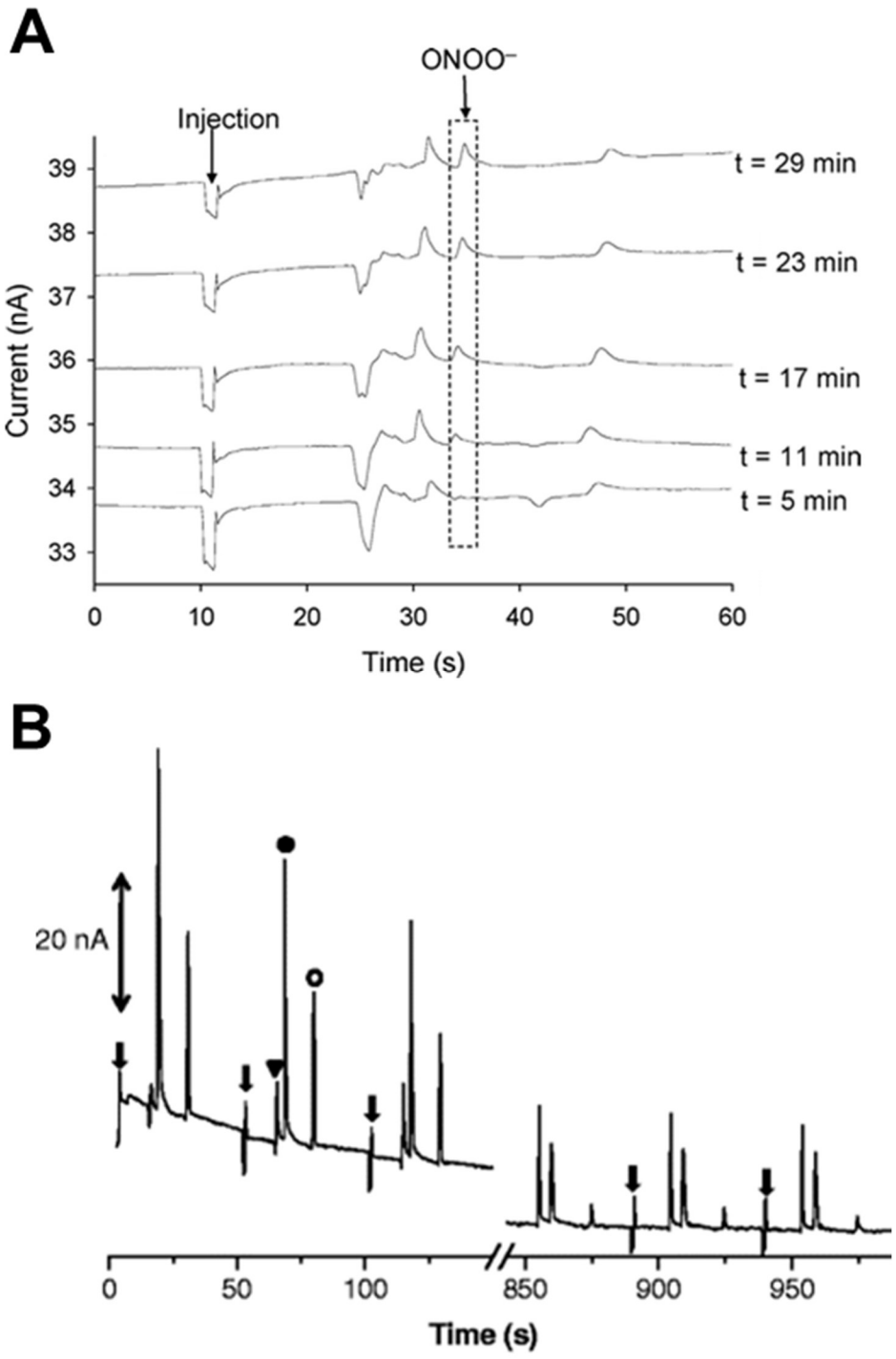

Figure 2.3. (A) Monitoring the production of peroxynitrite from SIN-1 using ME-EC in reverse polarity. Reprinted with permission from reference[29]. Copyright (2010) American Chemical Society. (B) Monitoring the acid hydrolysis of PROLI/NO at pH 7.2-7.4 using ME-EC in reverse polarity. Triangle nitrite; solid circle PROLI/NO; open circle NO. The arrows indicate sample injections. Reproduced from reference[30] with permission from Springer Nature.

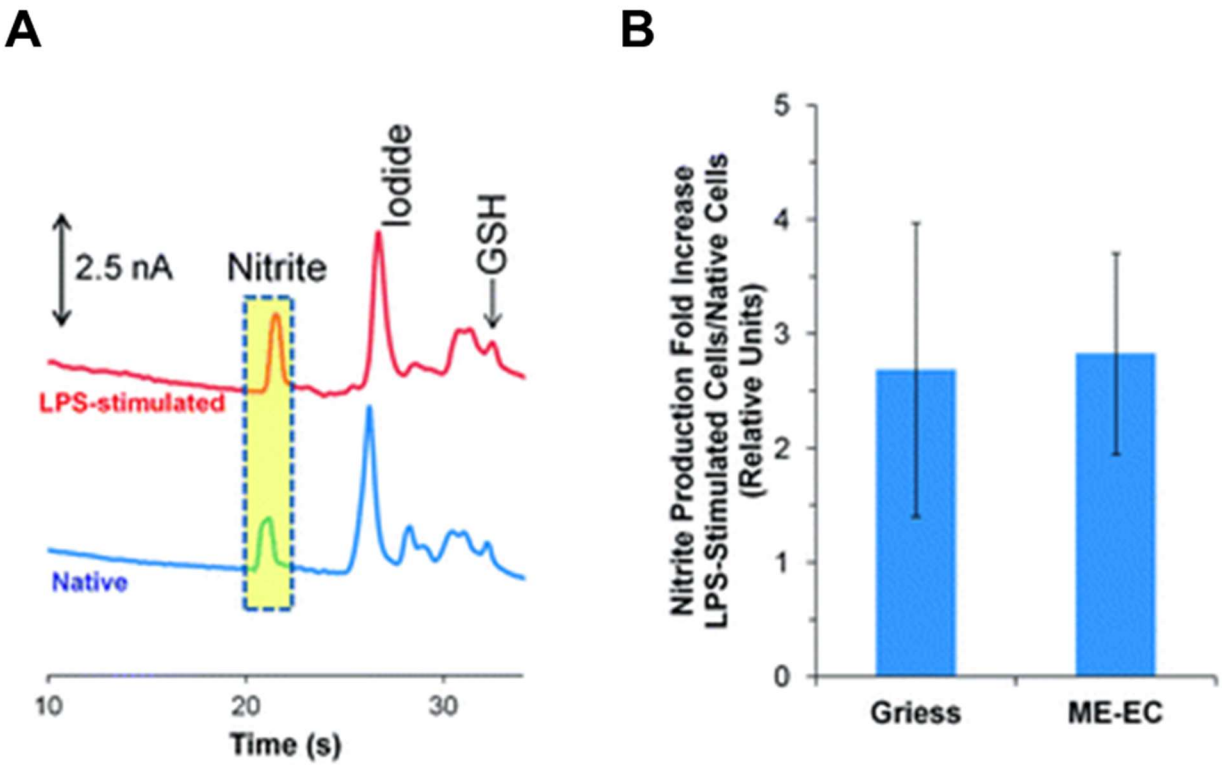

Figure 2.4. (A) Comparison of LPS-stimulated (top) and native (bottom) RAW 264.7 macrophage cell lysates using ME-EC in reverse polarity (B) Comparison of the ME-EC method and the Griess assay for determining the increase in nitrite concentration resulting from a 24 h LPS stimulation relative to the nitrite concentration produced from native cells. Reproduced from reference[31] with permission from The Royal Society of Chemistry.

More recent applications of ME-EC for RNOS detection include the use of the dual-channel, dual-electrode method to discriminate between the nitrite and azide signals in a cell lysate sample via their current ratios at 1100 and 950 mV versus Ag/AgCl[32]. The recent development of an integrated ME-EC system for the determination of low molecular weight S-nitrosothiols (RSNOs) by the metal catalyzed decomposition of RSNOs and amperometric detection of the nitrite produced is also noteworthy[33].

Electrophoresis has also been used with spectroscopic detection methods for the study of RNOS, including capillary electrophoresis (CE) with UV detection of peroxynitrite and its metabolites[34] and ME with fluorescence (FL) detection for the study of RNOS. Metto *et al.* reported a microfluidic system that couples cell transport and lysis with a microchip electrophoresis separation and fluorescence detection of nitric oxide in LPS-stimulated Jurkat cells *via* derivatization with 4-amino-6-methylamino-2',7'-difluorofluorescein diacetate (DAF-FM DA).[35] ME-FL has also been used to indirectly detect superoxide in phorbol 12-myristate 13-acetate (PMA)-stimulated RAW 264.7 macrophage cells *via* MitoHE, a fluorescent probe that reacts with superoxide to produce 2-OH-MitoE^+ for detection.[36] More recently, this method has been modified to detect not only superoxide but also nitric oxide and determine the nitric oxide to superoxide ratio in stimulated cells.[37] Finally, CE-UV has been used to detect peroxynitrite and its metabolites.[34]

2.2.2 Methods for studying protein and peptide nitration

2.2.2.1 Considerations for detection of 3-nitrotyrosine

A wide range of techniques have been used to measure 3-nitrotyrosine (3-NT) in biological samples, including immunological methods, liquid chromatography with UV/Vis, diode array detection (DAD), electrochemical detection (EC), mass spectrometry (MS), or MS/MS detection, and gas chromatography with MS or MS/MS detection.[8, 38] The main concerns with qualifying

methodologies for quantification of biological 3-NT are the avoidance of artifactual acid-catalyzed 3-NT formation (especially prevalent in derivatization and sample processing), specificity (especially relevant in GC derivatization reactions), and sensitivity (most methods are not able to detect the low levels of biological 3-NT).[39] Although the earliest methods for 3-NT quantification employed immunological techniques, lately it has been shown that enzyme-linked immunosorbent assays (ELISA) can suffer from poor reliability due to the low concentrations of endogenous NT present in the sample, nonspecific antibody binding, the presence of NT sites that are inaccessible to the antibody, and cross-reactivity.[8, 9] Another factor in the discrepancy in reported NT levels can be that ELISA results are based on equivalents of nitrated bovine serum albumin, not actual nitrated tyrosine residues in the sample.[9] To obviate some of these problems, antibodies have been used in combination with other techniques. One example is the use of immunoaffinity chromatography to isolate nitrated peptides prior to NanoLC-ESI-MS/MS peptide sequencing.[40] Another is the use of an electrochemiluminsescence-based ELISA method with improved sensitivity to detect protein nitration in serum after a surgery-induced inflammatory response.[41] Overall, ELISA-based methods have the advantage of being easier to apply in a clinical setting where cost-effective, high-throughput methods are ideal.[41]

2.2.2.2 Chromatographic methods for studying protein nitration

According to a 2016 review by Teixeira *et al.*, chromatographic methods coupled to UV or MS detection exhibit the most promising sensitivity and specificity. LC-UV is capable of detection of NT in both free and protein-bound form, but it is less specific than other detection methods. Detection is typically performed at the wavelength of maximum absorbance for tyrosine and NT at pH 3.5, 280 nm, although 357 nm (selective absorbance of NT) and 430 nm (maximum absorbance of NT at pH 9.5) have also been used.[8] When a diode array detector (DAD) is employed, the simultaneous detection at multiple wavelengths improves the selectivity for NT

without compromising the signal of the wavelength of maximum absorbance. However, all absorbance-based measurement lacks the sensitivity necessary for detecting nanomolar levels of NT *in vivo*.[8] To improve the limits of detection, Dremina *et al*. derivatized NT with a cis-diol-containing fluorophore to enable capture on a boronate affinity column and analysis using LC with fluorescence detection.[42] LC-FL has the requisite LOD necessary for detecting biological concentrations of NT; however, the formation of fluorescent side products as well as the specificity of the derivatization reaction for NT can be a concern.[8, 43] The application of LC-EC for NT analysis will be discussed in greater detail in 2.2.2.3.

LC-MS is the gold standard for measuring NT in biological fluids, as it does not require sample derivatization and features low detection limits.[8] However, tandem mass spectrometry (MS/MS) is necessary in order to obtain the selectivity required for NT and any MS method is inherently expensive. [8, 43] GS-MS has also been used for the highly sensitive detection of NT after derivatization; however, there is concern that artifactual NT may be formed during the derivatization procedure which may skew results.[8, 43] Tyrosine nitration has been studied using LC-MS and LC-MS/MS with both positive and negative ESI modes[6] and MALDI-TOF MS has also been used for peptide mapping of nitrated sites after exposure of a protein to peroxynitrite.[6] Several groups have expanded upon conventional LC-MS methods to impart more selectivity and sensitivity for NT. For example, Sacksteder *et al.* used LC/LC-MS/MS to identify nitration sites in the proteins isolated from whole mouse brain and correlate these nitration sites with neurodegenerative diseases.[44] They also characterized these sites to determine any trends in which protein sites are readily nitrated.[44]

Guo and Prokai *et al.* previously reported a method to enrich nitrated peptides and identify sites of nitration by first performing a specific reductive methylation of the aliphatic amines and then converting nitrotyrosine residues to aminotyrosine prior to selective capture and enrichment

via a solid-phase ester reagent on glass beads.[45] The peptides were then released from the beads via acid hydrolysis.[45] By using isotopic variants of formaldehyde in the reductive methylation step, they are able to perform relative quantitation of nitrated peptides via nano-LC-MS/MS.

2.2.2.3 Electrochemical methods for studying protein nitration

While MS detection is the gold standard for the study of tyrosine nitration due to its selectivity, sensitivity, and ability to identify specific sites of nitration, much attention has also been paid to the electrochemical detection of NT, due largely to its interesting electrochemical properties. There are a few instances of electrochemical sensors designed specifically for the detection of NT. Martins *et al.* developed the first paper-based electrochemical sensor for the detection of 3-NT utilizing carbon and silver screen-printed electrodes to create a 3-electrode sensor for square wave voltammetric detection of 3-NT over a linear concentration range of 500 nM to 1 mM with an LOD of 49.2 nM.[46] They were able to selectively detect 3-NT in a mixture of tyrosine, ascorbic acid, uric acid, and creatinine by applying their optimized waveform.[46] Additionally, Chen *et al.* utilized copper ferrite nanodots entrapped by porous reduced graphene oxide nanosheets in an electrochemical sensing platform (cyclic voltammetry and amperometry) for quantification of 3-NT with a LOD of 25.14 pM due to the electrocatalytic activity of the composite electrodes.[47] They spiked human urine and blood serum samples with 5 and 10 μM 3-NT and were able to accurately quantify it with 97.4-99.6% recovery and 1.26-3.24% RSD.[47]

Liquid chromatography has also been coupled to electrochemical detection (LC-EC) for selective detection of NT. In particular, dual mode EC detection has the advantages of decreasing the potential necessary for the detector electrode, which enhances selectivity and sensitivity by lowering the background current.[48] LC-EC can be more selective than UV or FL detection by taking advantage of the reduction of NT at a potential of -800 to -1000 mV followed by oxidation at 250 to 1000 mV.[43] Photolysis has also been used to generate L-DOPA that may be selectively

detected at an the oxidation electrode.[49] Figure 2.5 shows the instrumental schematic for such experiments and the general electrochemical process being detected.[50]

Such LC-EC methods have been used to detect both free and protein-bound NT in a variety of biological samples representing a wide range of stimulation conditions and disease states[50-63], including NT in the cerebrospinal fluid of AD patients[64, 65], as well as the artifactual formation of NT during freezing of biological samples[66] and NT in atmospheric bio-aerosol proteins.[67] Additional variations on the conventional LC-EC techniques include the incorporation of an acetylation/deacetylation/reduction sample preparation protocol to improve chromatographic properties and generate a more easily-oxidized species[68] and a biotin-tagging strategy to enrich NT-containing peptides.[69]

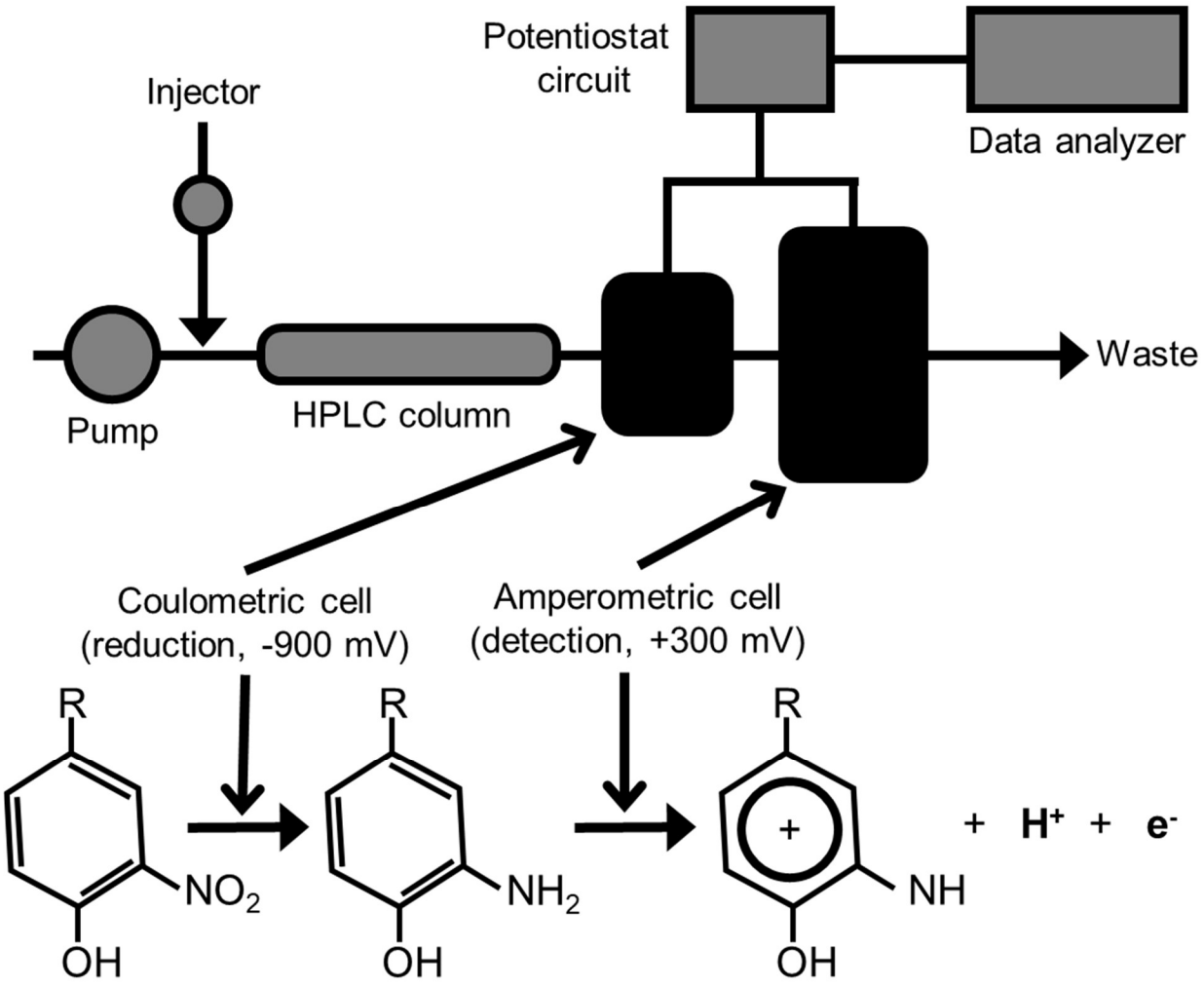

Figure 2.5. Diagram of a HPLC-electrochemical system. Reproduced from reference[50] with permission from Taylor & Francis.

2.2.2.4 Controversies regarding the detection of NT and methods to address artifactual formation

Although nitrotyrosine is a widely accepted biomarker of nitrosative stress, since its first connection as a biomarker of endogenous protein nitration in 1990 by Ohshima, its detection *in vivo* has not been without controversy.[70] One recent review by Tsikas suggests that the actual biological concentration of nitrotyrosine is in the pM to nM range and that works that report higher concentrations (*i.e.* μM) of 3-NT likely failed to adequately consider artificial formation of 3-NT during sample preparation.[70] Although the reported values vary widely, it is proposed in this review that the concentration of NT in healthy plasma is on the high pM/low nM threshold and that the ratio of NT to Tyr is around $1:10^6$.[70] Therefore, in order to accurately quantify NT in human plasma, the LOQ of a method must be below 1 nM.[70] LC-FL and LC-MS/MS are both capable of operating in this concentration range, while papers that report LC-UV/Vis and LC-EC values in the low μM range may be suspect.[70]

Several strategies have been proposed to minimize formation of artifactual NT and/or account for it in the analysis.[8] When attempting to quantify NT, it is often desired to first completely digest the protein into its component amino acids *via* either acid hydrolysis or enzymatic digestion.[8] While acid hydrolysis has been used extensively in the literature and has been shown to yield reliable results, there is much concern over artifactual NT formation during acid hydrolysis, while enzymatic digestion appears to be less prone to artifactual NT formation.[8] To account for this formation, NT can be isolated by solid phase extraction (SPE) and HPLC, reduced to 3-aminotyrosine before sample derivatization, processed in the presence of high concentrations of other reactive aromatic compounds that would be preferentially nitrated in its place (*e.g.* phenol), or quantified with stable-isotope labeling of Tyr.[6, 8] Additionally, artifactual

nitrotyrosine formation may be mitigated through removal of nitrite before sample processing, using alkaline hydrolysis, or using deuterated tyrosine as an internal standard in order to assess artifactual nitration.[71] Yi *et al.* used isotopomer standards to account for artifactual formation of 3-NT in quantification in biological samples via LC-MS/MS or GC-MS.[72] It is also important to account for the autohydrolysis of the digesting enzyme in these studies. Artifactual formation has been shown to be dependent on the concentration of nitrating agents in the system, the content of buffer (*i.e.* sodium phosphate versus potassium phosphate), and the rate of freezing of a biological sample.[56, 66]

Overall, these studies demonstrate the importance of developing reliable, sensitive, selective techniques for the detection of biological NT with minimal sample preparation. Without careful accounting of artifactual NT, it is easy to come to incorrect conclusions as to the total NT in a system or its source.

2.3 Conclusions

The development of methods capable of monitoring both RNOS production and protein nitration under conditions of oxidative and nitrosative stress is essential if we are to gain a greater understanding of complex disease states such as Alzheimer's disease. In this dissertation, RNOS and their products will be detected on rapid timescales after electrophoretic separations and the biochemistry of these reactions that are so important to the redox homeostasis of cells will be explored.

2.4 References

1. Cheignon, C.; Tomas, M.; Bonnefont-Rousselot, D.; Faller, P.; Hureau, C.; Collin, F., Oxidative stress and the amyloid beta peptide in Alzheimer's disease. *Redox Biology* **2018,** *14*, 450-464.
2. Bartesaghi, S.; Radi, R., Fundamentals on the biochemistry of peroxynitrite and protein tyrosine nitration. *Redox Biology* **2018,** *14*, 618-625.
3. Souza, J. M.; Peluffo, G.; Radi, R., Protein tyrosine nitration—functional alteration or just a biomarker? *Free Radical Biol. Med.* **2008,** *45* (4), 357-366.

4. Radi, R., Protein tyrosine nitration: biochemical mechanisms and structural basis of functional effects. *Acc. Chem. Res.* **2012,** *46* (2), 550-559.
5. Curtis, M. P.; Hicks, A. J.; Neidigh, J. W., Kinetics of 3-chlorotyrosine formation and loss due to hypochlorous acid and chloramines. *Chem. Res. Toxicol.* **2011,** *24* (3), 418-428.
6. Batthyány, C.; Bartesaghi, S.; Mastrogiovanni, M.; Lima, A.; Demicheli, V.; Radi, R., Tyrosine-nitrated proteins: Proteomic and bioanalytical aspects. *Antioxidants & Redox Signaling* **2017,** *26* (7), 313-328.
7. Whiteman, M.; Spencer, J. P., Loss of 3-chlorotyrosine by inflammatory oxidants: implications for the use of 3-chlorotyrosine as a bio-marker in vivo. *Biochem. Biophys. Res. Commun.* **2008,** *371* (1), 50-53.
8. Teixeira, D.; Fernandes, R.; Prudencio, C.; Vieira, M., 3-Nitrotyrosine quantification methods: Current concepts and future challenges. *Biochimie* **2016,** *125*, 1-11.
9. Frijhoff, J.; Winyard, P. G.; Zarkovic, N.; Davies, S. S.; Stocker, R.; Cheng, D.; Knight, A. R.; Taylor, E. L.; Oettrich, J.; Ruskovska, T., Clinical relevance of biomarkers of oxidative stress. *Antioxidants & redox signaling* **2015,** *23* (14), 1144-1170.
10. Bartesaghi, S.; Ferrer-Sueta, G.; Peluffo, G.; Valez, V.; Zhang, H.; Kalyanaraman, B.; Radi, R., Protein tyrosine nitration in hydrophilic and hydrophobic environments. *Amino Acids* **2007,** *32* (4), 501-515.
11. Mohiuddin, I.; Chai, H.; Lin, P. H.; Lumsden, A. B.; Yao, Q.; Chen, C., Nitrotyrosine and chlorotyrosine: clinical significance and biological functions in the vascular system. *J. Surg. Res.* **2006,** *133* (2), 143-149.
12. Souza, J. M.; Choi, I.; Chen, Q.; Weisse, M.; Daikhin, E.; Yudkoff, M.; Obin, M.; Ara, J.; Horwitz, J.; Ischiropoulos, H., Proteolytic degradation of tyrosine nitrated proteins. *Arch. Biochem. Biophys.* **2000,** *380* (2), 360-366.
13. Seeley, K. W.; Stevens Jr, S. M., Investigation of local primary structure effects on peroxynitrite-mediated tyrosine nitration using targeted mass spectrometry. *Journal of Proteomics* **2012,** *75* (6), 1691-1700.
14. Bayden, A. S.; Yakovlev, V. A.; Graves, P. R.; Mikkelsen, R. B.; Kellogg, G. E., Factors influencing protein tyrosine nitration—structure-based predictive models. *Free Radical Biol. Med.* **2011,** *50* (6), 749-762.
15. Campolo, N.; Issoglio, F. M.; Estrin, D. A.; Bartesaghi, S.; Radi, R., 3-Nitrotyrosine and related derivatives in proteins: precursors, radical intermediates and impact in function. *Essays in Biochemistry* **2020,** *64* (1), 111-133.
16. Tramutola, A.; Lanzillotta, C.; Perluigi, M.; Butterfield, D. A., Oxidative stress, protein modification and Alzheimer disease. *Brain Res. Bull.* **2017,** *133*, 88-96.
17. Bhat, A. H.; Dar, K. B.; Anees, S.; Zargar, M. A.; Masood, A.; Sofi, M. A.; Ganie, S. A., Oxidative stress, mitochondrial dysfunction and neurodegenerative diseases; a mechanistic insight. *Biomedicine & Pharmacotherapy* **2015,** *74*, 101-110.
18. Bailey, P., Biological markers in Alzheimer's disease. *Can. J. Neurol. Sci.* **2007,** *34* (S1), S72-S76.
19. Kamat, P. K.; Kalani, A.; Rai, S.; Swarnkar, S.; Tota, S.; Nath, C.; Tyagi, N., Mechanism of oxidative stress and synapse dysfunction in the pathogenesis of Alzheimer's disease: understanding the therapeutics strategies. *Mol. Neurobiol.* **2016,** *53* (1), 648-661.
20. Hensley, K.; Mou, S.; Pye, Q. N., Nitrite determination by colorimetric and fluorometric griess diazotization assays. In *Methods in Biological Oxidative Stress*, Springer: **2003**; pp 185-193.

21. Li, Y.; Sella, C.; Lemaître, F.; Guille Collignon, M.; Amatore, C.; Thouin, L., Downstream Simultaneous Electrochemical Detection of Primary Reactive Oxygen and Nitrogen Species Released by Cell Populations in an Integrated Microfluidic Device. *Anal. Chem.* **2018**, *90* (15), 9386-9394.
22. Amatore, C.; Arbault, S. p.; Koh, A. C., Simultaneous detection of reactive oxygen and nitrogen species released by a single macrophage by triple potential-step chronoamperometry. *Anal. Chem.* **2010,** *82* (4), 1411-1419.
23. Li, Y.; Meunier, A.; Fulcrand, R.; Sella, C.; Amatore, C.; Thouin, L.; Lemaître, F.; Guille-Collignon, M., Multi-chambers Microsystem for Simultaneous and Direct Electrochemical Detection of Reactive Oxygen and Nitrogen Species Released by Cell Populations. *Electroanalysis* **2016,** *28* (8), 1865-1872.
24. Li, Y.; Sella, C.; Lemaître, F.; Guille Collignon, M.; Thouin, L.; Amatore, C., Highly Sensitive Platinum-Black Coated Platinum Electrodes for Electrochemical Detection of Hydrogen Peroxide and Nitrite in Microchannel. *Electroanalysis* **2013,** *25* (4), 895-902.
25. Li, Y.; Hu, K.; Yu, Y.; Rotenberg, S. A.; Amatore, C.; Mirkin, M. V., Direct electrochemical measurements of reactive oxygen and nitrogen species in nontransformed and metastatic human breast cells. *Journal of the American Chemical Society* **2017,** *139* (37), 13055-13062.
26. Johnson, A. S.; Selimovic, A.; Martin, R. S., Microchip-based electrochemical detection for monitoring cellular systems. *Anal. Bioanal. Chem.* **2013,** *405* (10), 3013-3020.
27. Bucher, E. S.; Wightman, R. M., Electrochemical analysis of neurotransmitters. *Annual review of analytical chemistry* **2015,** *8*, 239-261.
28. Hasanzadeh, M.; Shadjou, N.; de la Guardia, M., Current advancement in electrochemical analysis of neurotransmitters in biological fluids. *TrAC, Trends Anal. Chem.* **2017,** *86*, 107-121.
29. Hulvey, M. K.; Frankenfeld, C. N.; Lunte, S. M., Separation and detection of peroxynitrite using microchip electrophoresis with amperometric detection. *Anal. Chem.* **2010,** *82* (5), 1608-1611.
30. Gunasekara, D. B.; Hulvey, M. K.; Lunte, S. M.; da Silva, J. A. F., Microchip electrophoresis with amperometric detection for the study of the generation of nitric oxide by NONOate salts. *Anal. Bioanal. Chem.* **2012,** *403* (8), 2377-2384.
31. Gunasekara, D. B.; Siegel, J. M.; Caruso, G.; Hulvey, M. K.; Lunte, S. M., Microchip electrophoresis with amperometric detection method for profiling cellular nitrosative stress markers. *Analyst* **2014,** *139* (13), 3265-3273.
32. Gunasekara, D. B.; Wijesinghe, M. B.; Pichetsurnthorn, P.; Lunte, S. M., Evaluation of Dual Electrode Configurations for Microchip Electrophoresis Used for Voltammetric Characterization of Electroactive Species. *Analyst* **2020,** *145*, 865-872.
33. Duarte-Junior, G. F.; Ismail, A.; Griveau, S.; d'Orlyé, F.; da Silva, J. A. F.; Coltro, W. K.; Bedioui, F.; Varenne, A., Integrated microfluidic device for the separation, decomposition and detection of low molecular weight S-nitrosothiols. *Analyst* **2019,** *144* (1), 180-185.
34. Frankenfeld, C. N.; Rosenbaugh, M. R.; Fogarty, B. A.; Lunte, S. M., Separation and detection of peroxynitrite and its metabolites by capillary electrophoresis with UV detection. *Journal of Chromatography A* **2006,** *1111* (2), 147-152.
35. Metto, E. C.; Evans, K.; Barney, P.; Culbertson, A. H.; Gunasekara, D. B.; Caruso, G.; Hulvey, M. K.; Fracassi da Silva, J. A.; Lunte, S. M.; Culbertson, C. T., An integrated microfluidic device for monitoring changes in nitric oxide production in single T-lymphocyte (Jurkat) cells. *Anal. Chem.* **2013,** *85* (21), 10188-10195.

36. de Campos, R. P.; Siegel, J. M.; Fresta, C. G.; Caruso, G.; da Silva, J. A.; Lunte, S. M., Indirect detection of superoxide in RAW 264.7 macrophage cells using microchip electrophoresis coupled to laser-induced fluorescence. *Anal. Bioanal. Chem.* **2015,** *407* (23), 7003-7012.
37. Caruso, G.; Fresta, C. G.; Siegel, J. M.; Wijesinghe, M. B.; Lunte, S. M., Microchip electrophoresis with laser-induced fluorescence detection for the determination of the ratio of nitric oxide to superoxide production in macrophages during inflammation. *Anal. Bioanal. Chem.* **2017,** *409* (19), 4529-4538.
38. Herce-Pagliai, C.; Kotecha, S.; Shuker, D. E., Analytical methods for 3-nitrotyrosine as a marker of exposure to reactive nitrogen species: a review. *Nitric Oxide* **1998,** *2* (5), 324-336.
39. Tsikas, D.; Caidahl, K., Recent methodological advances in the mass spectrometric analysis of free and protein-associated 3-nitrotyrosine in human plasma. *J. Chromatogr. B* **2005,** *814* (1), 1-9.
40. Abdelmegeed, M. A.; Jang, S.; Banerjee, A.; Hardwick, J. P.; Song, B.-J., Robust protein nitration contributes to acetaminophen-induced mitochondrial dysfunction and acute liver injury. *Free Radical Biol. Med.* **2013,** *60*, 211-222.
41. Knight, A. R.; Taylor, E. L.; Lukaszewski, R.; Jensen, K. T.; Jones, H. E.; Carré, J. E.; Isupov, M. N.; Littlechild, J. A.; Bailey, S. J.; Brewer, E., A high-sensitivity electrochemiluminescence-based ELISA for the measurement of the oxidative stress biomarker, 3-nitrotyrosine, in human blood serum and cells. *Free Radical Biol. Med.* **2018,** *120*, 246-254.
42. Dremina, E. S.; Li, X.; Galeva, N. A.; Sharov, V. S.; Stobaugh, J. F.; Schöneich, C., A methodology for simultaneous fluorogenic derivatization and boronate affinity enrichment of 3-nitrotyrosine-containing peptides. *Anal. Biochem.* **2011,** *418* (2), 184-196.
43. Ryberg, H.; Caidahl, K., Chromatographic and mass spectrometric methods for quantitative determination of 3-nitrotyrosine in biological samples and their application to human samples. *J. Chromatogr. B* **2007,** *851* (1-2), 160-171.
44. Sacksteder, C. A.; Qian, W.-J.; Knyushko, T. V.; Wang, H.; Chin, M. H.; Lacan, G.; Melega, W. P.; Camp, D. G.; Smith, R. D.; Smith, D. J., Endogenously nitrated proteins in mouse brain: links to neurodegenerative disease. *Biochemistry* **2006,** *45* (26), 8009-8022.
45. Guo, J.; Prokai-Tatrai, K.; Prokai, L., Relative quantitation of protein nitration by liquid chromatography–mass spectrometry using isotope-coded dimethyl labeling and chemoprecipitation. *Journal of Chromatography A* **2012,** *1232*, 266-275.
46. Martins, G. V.; Marques, A. C.; Fortunato, E.; Sales, M. G. F., Wax-printed paper-based device for direct electrochemical detection of 3-nitrotyrosine. *Electrochim. Acta* **2018,** *284*, 60-68.
47. Chen, S.-M.; Umamaheswari, R.; Mani, G.; Chen, T.-W.; Ali, M. A.; Fahad, A.-H.; Elshikh, M.; Farah, M. A., Hierarchically structured CuFe 2 O 4 ND@ RGO composite for the detection of oxidative stress biomarker in biological fluids. *Inorganic Chemistry Frontiers* **2018,** *5* (4), 944-950.
48. Honeychurch, K. C.; Hart, J. P., Voltammetric Behavior of p-Nitrophenol and Its Trace Determination in Human Urine by Liquid Chromatography with a Dual Reductive Mode Electrochemical Detection System. *Electroanalysis: An International Journal Devoted to Fundamental and Practical Aspects of Electroanalysis* **2007,** *19* (21), 2176-2184.
49. Liu, H.; Huang, T.; Kissinger, C. B.; Kissinger, P. T., Comparison of detection methods for liquid chromatographic determination of 3-nitro-L-tyrosine. *Journal of Chromatography B: Biomedical Sciences and Applications* **1998,** *713* (2), 289-295.
50. Sugiura, H.; Ichinose, M.; Tomaki, M.; Ogawa, H.; Koarai, A.; Kitamuro, T.; Komaki, Y.; Akita, T.; Nishino, H.; Okamoto, S., Quantitative assessment of protein-bound tyrosine

nitration in airway secretions from patients with inflammatory airway disease. *Free Radical Res.* **2004,** *38* (1), 49-57.
51. Hensley, K.; Williamson, K. S.; Maidt, M. L.; Prasad Gabbita, S.; Grammas, P.; Floyd, R. A., Determination of biological oxidative stress using high performance liquid chromatography with electrochemical detection (HPLC-ECD). *J. High. Resolut. Chromatogr.* **1999,** *22* (8), 429-437.
52. Kanski, J.; Schöneich, C., Protein nitration in biological aging: proteomic and tandem mass spectrometric characterization of nitrated sites. *Methods Enzymol.* **2005,** *396*, 160-171.
53. Crow, J. P., [16] Measurement and significance of free and protein-bound 3-nitrotyrosine, 3-chlorotyrosine, and free 3-nitro-4-hydroxyphenylacetic acid in biologic samples: A high-performance liquid chromatography method using electrochemical detection. In *Methods Enzymol.*, Elsevier: **1999**; Vol. 301, pp 151-160.
54. Hensley, K.; Maidt, M.; Pye, Q.; Stewart, C.; Wack, M.; Tabatabaie, T.; Floyd, R., Quantitation of protein-bound 3-nitrotyrosine and 3, 4-dihydroxyphenylalanine by high-performance liquid chromatography with electrochemical array detection. *Anal. Biochem.* **1997,** *251* (2), 187-195.
55. Liu, Y.; Zhou, P.; Da, H.; Jia, H.; Bai, F.; Hu, G.; Zhang, B.; Fang, J., Azo Coupling Strategy for Protein 3-Nitrotyrosine Derivatization. *Chemistry–A European Journal* **2019**.
56. Sodum, R. S.; Akerkar, S. A.; Fiala, E. S., Determination of 3-nitrotyrosine by high-pressure liquid chromatography with a dual-mode electrochemical detector. *Anal. Biochem.* **2000,** *280* (2), 278-285.
57. Ohshima, H.; Celan, I.; Chazotte, L.; Pignatelli, B.; Mower, H. F., Analysis of 3-nitrotyrosine in biological fluids and protein hydrolyzates by high-performance liquid chromatography using a postseparation, on-line reduction column and electrochemical detection: results with various nitrating agents. *Nitric Oxide* **1999,** *3* (2), 132-141.
58. Ishida, N.; Hasegawa, T.; Mukai, K.; Watanabe, M.; Nishino, H., Determination of nitrotyrosine by HPLC-ECD and its application. *J. Vet. Med. Sci.* **2002,** *64* (5), 401-404.
59. Ueshima, K.; Minakata, Y.; Sugiura, H.; Yanagisawa, S.; Ichikawa, T.; Akamatsu, K.; Hirano, T.; Nakanishi, M.; Matsunaga, K.; Yamagata, T., The influence of free 3-nitrotyrosine and saliva on the quantitative analysis of protein-bound 3-nitrotyrosine in sputum. *Analytical chemistry insights* **2007,** *2*, 1-7.
60. Williamson, K. S.; Hensley, K.; Floyd, R. A., HPLC With Electrochemical Detection Analysis of 3-Nitrotyrosine in Human Plasma. In *Methods in Biological Oxidative Stress*, Springer: **2003**; pp 151-157.
61. Richards, D. A.; Silva, M. A.; Devall, A. J., Electrochemical detection of free 3-nitrotyrosine: application to microdialysis studies. *Anal. Biochem.* **2006,** *351* (1), 77-83.
62. Hitomi, Y. H.; Okuda, J.; Nishino, H.; Kambayashi, Y.; Hibino, Y.; Takemoto, K.; Takigawa, T.; Ohno, H.; Taniguchi, N.; Ogino, K., Disposition of Protein-bound 3-nitrotyrosine in Rat Plasma Analysed by a Novel Protocol for HPLC–ECD. *J. Biochem.* **2007,** *141* (4), 495-502.
63. Bircan, F. S.; Balabanli, B.; Turkozkan, N.; Ozan, G., Effects of taurine on nitric oxide and 3-nitrotyrosine levels in spleen during endotoxemia. *Neurochem. Res.* **2011,** *36* (11), 1978-1983.
64. Tohgi, H.; Abe, T.; Yamazaki, K.; Murata, T.; Ishizaki, E.; Isobe, C., Alterations of 3-nitrotyrosine concentration in the cerebrospinal fluid during aging and in patients with Alzheimer's disease. *Neurosci. Lett.* **1999,** *269* (1), 52-54.

65. Murata, T. A., Takashi; Sato, Chigumi, The concentrations of 3-nitrotyrosine in the cerebrospinal fluid in patients with dementia of Alzheimer's type and vascular dementia. *Iwate Igaku Zasshi* **2001,** *53* (1), 11-18.
66. Daiber, A.; Bachschmid, M.; Kavaklí, C.; Frein, D.; Wendt, M.; Ullrich, V.; Munzel, T., A new pitfall in detecting biological end products of nitric oxide—nitration, nitros (yl) ation and nitrite/nitrate artefacts during freezing. *Nitric Oxide* **2003,** *9* (1), 44-52.
67. Ito, T.; Ogino, K.; Nagaoka, K.; Takemoto, K.; Nishiyama, R.; Shimizu, Y., Detection of 3-Nitrotyrosine in Atmospheric Environments via a High-performance Liquid Chromatography-electrochemical Detector System. *JoVE (Journal of Visualized Experiments)* **2019,** (143), e58371.
68. Shigenaga, M. K., [4] Quantitation of protein-bound 3-nitrotyrosine by high-performance liquid chromatography with electrochemical detection. In *Methods Enzymol.*, Elsevier: **1999**; Vol. 301, pp 27-40.
69. Nuriel, T.; Deeb, R. S.; Hajjar, D. P.; Gross, S. S., Protein 3-nitrotyrosine in complex biological samples: quantification by high-pressure liquid chromatography/electrochemical detection and emergence of proteomic approaches for unbiased identification of modification sites. In *Methods Enzymol.*, Elsevier: **2008**; Vol. 441, pp 1-17.
70. Tsikas, D., What we—authors, reviewers and editors of scientific work—can learn from the analytical history of biological 3-nitrotyrosine. *J. Chromatogr. B* **2017,** *1058*, 68-72.
71. Moore, K. P.; Mani, A. R., Measurement of protein nitration and S-nitrosothiol formation in biology and medicine. In *Methods Enzymol.*, Elsevier: **2002**; Vol. 359, pp 256-268.
72. Yi, D.; Ingelse, B. A.; Duncan, M. W.; Smythe, G. A., Quantification of 3-nitrotyrosine in biological tissues and fluids: generating valid results by eliminating artifactual formation. *Journal of the American Society for Mass Spectrometry* **2000,** *11* (6), 578-586.

Chapter 3

Introduction to electrophoretic separations and microchip electrophoresis with electrochemical detection

Parts of this chapter are reproduced from the following publication:

Schilly, K.M., Gunawardhana, S.M., Wijesinghe, M.B., Lunte, S.M. "Biological applications of microchip electrophoresis with electrochemical detection: *in vivo* monitoring and cell analysis." *Anal. Bioanal. Chem.* **2020**; 412: 6101-6119, Springer Nature.

3 Chapter 3: Introduction to electrophoretic separations and microchip electrophoresis with electrochemical detection

3.1 Electrophoretic separations

Since CE in its modern form was first introduced in 1981 by Jorgenson and Lukacs[1], it has been used to approach a variety of analytical problems in the bioanalytical[2, 3], pharmaceutical[4, 5], forensic[6, 7], and environmental fields[8, 9]. Capillary zone electrophoresis (CZE) is an analytical method that separates analytes based on their charge and hydrodynamic radius. In conventional CZE, the ends of a fused silica capillary containing an electrolyte solution are placed into two buffer reservoirs and a potential is applied across the capillary (Figure 3.1a). When analytes are injected into the capillary and the separation potential is applied, negatively-charged analytes experience attraction towards the positively-charged anode, positively-charged analytes experience attraction towards the negatively-charged cathode, and neutral analytes do not experience attraction to either end. Due to this attraction, each analyte exhibits an electrophoretic mobility directed towards the appropriate electrode. This magnitude of the electrophoretic mobility (μ_{ep}) is dependent on the charge of the analyte (q), and inversely dependent on the viscosity of the buffer (η) and the hydrodynamic radius of the analyte (r). The electrophoretic velocity (v_{ep}) of an analyte is dependent on the electrophoretic mobility and the magnitude of the electric field applied across the capillary ($E:V/L$) (*Equation 1*).

$$\mu_{ep} = \frac{q}{6\pi\eta r};\ v_{ep} = \mu_{ep}E$$

Equation 1

A second factor that influences the separation is the presence of electroosmotic flow ($\mu_{eo,}$ EOF), which pulls all analytes towards one end of the capillary. The magnitude of the EOF is dependent on the electric field strength (E), dielectric constant (ϵ) of the buffer, the zeta potential

at the capillary surface (ζ), and the viscosity of the buffer (*Equation 2*). The electroosmotic flow is produced due to hydrated cations that are attracted via Coulomb's force to the negatively charged silanol groups on the capillary surface. When a positive external potential is applied to the system, these cations are attracted to the cathode, and as the outer layer of hydrated cations at the slipping plane migrates towards the cathode, they pull the rest of the bulk solution along with them. This phenomenon results in analytes being carried towards the cathode in normal polarity separations (Figure 3.1b,c), so a detector is then placed at this end.

$$\mu_{eo} = \frac{\epsilon\zeta}{4\pi\eta};\ v_{eo} = \mu_{eo}E$$

Equation 2

The actual velocity at which an analyte travels through the capillary is dependent on its intrinsic electrophoretic mobility, the electroosmotic flow in the capillary, and the electric field strength across the capillary. The apparent observed mobility (μ_{app}) of an analyte is the sum of its electrophoretic mobility and the electroosmotic mobility (*Equation 3*). The μ_{app} determines the direction of the migration of each analyte, with a positive value resulting in net movement towards the cathode and a negative value resulting in net movement towards the anode under normal polarity conditions. As the electric field strength increases, the magnitudes of the electroosmotic and electrophoretic velocities both increase, impacting the net movement and velocity of the analytes.

$$\mu_{app} = \mu_{ep} + \mu_{eo}; v_{app} = E(\mu_{ep} + \mu_{eo})$$

Equation 3

For the analysis of mixtures of anions that exhibit large negative electrophoretic mobilities, a negative electric field may be applied, and the electroosmotic flow may be reversed by adding a positively charged surfactant to the run buffer to coat the capillary. The surfactant generates a

positive surface charge at the wall and the formation of an electric double layer with negatively charged ions in the diffuse layer, leading to a bulk flow towards the positively charged anode.

CZE has several advantages for bioanalysis. These include the low sample volume requirements and capability of obtaining fast, highly efficient separations of charged analytes. When it is desirable to separate analytes that have a similar charge-to-size ratio, buffer additives may be used to impart an extra degree to the separation. When a surfactant is added in excess of its critical micelle concentration (CMC), the separation mechanism shifts from CZE to micellar electrokinetic chromatography (MEKC). In MEKC, both ionic and neutral species may be separated, as analytes are then separated based on their partitioning between the charged micelles and the aqueous buffer phase. Neutral species with different affinities for the micelles may be resolved based on this property. When the chemical and physical properties of analytes of interest are too similar for them to be resolved with either CZE or MEKC, other additives such as cyclodextrins may be incorporated into the buffer to help separate difficult-to-resolve species. Cyclodextrins are cyclic oligosaccharides that contain certain numbers of glucose monomers bonded in a ring. This structure forms a hydrophobic “pocket” for analytes to partition in and out of during the separation. Additionally, the chiral centers on the glucose monomers will interact differently with enantiomers of the same compound, thereby enabling separation of chiral molecules. These interactions act to shift the migration times of analytes and thereby impact the separation.

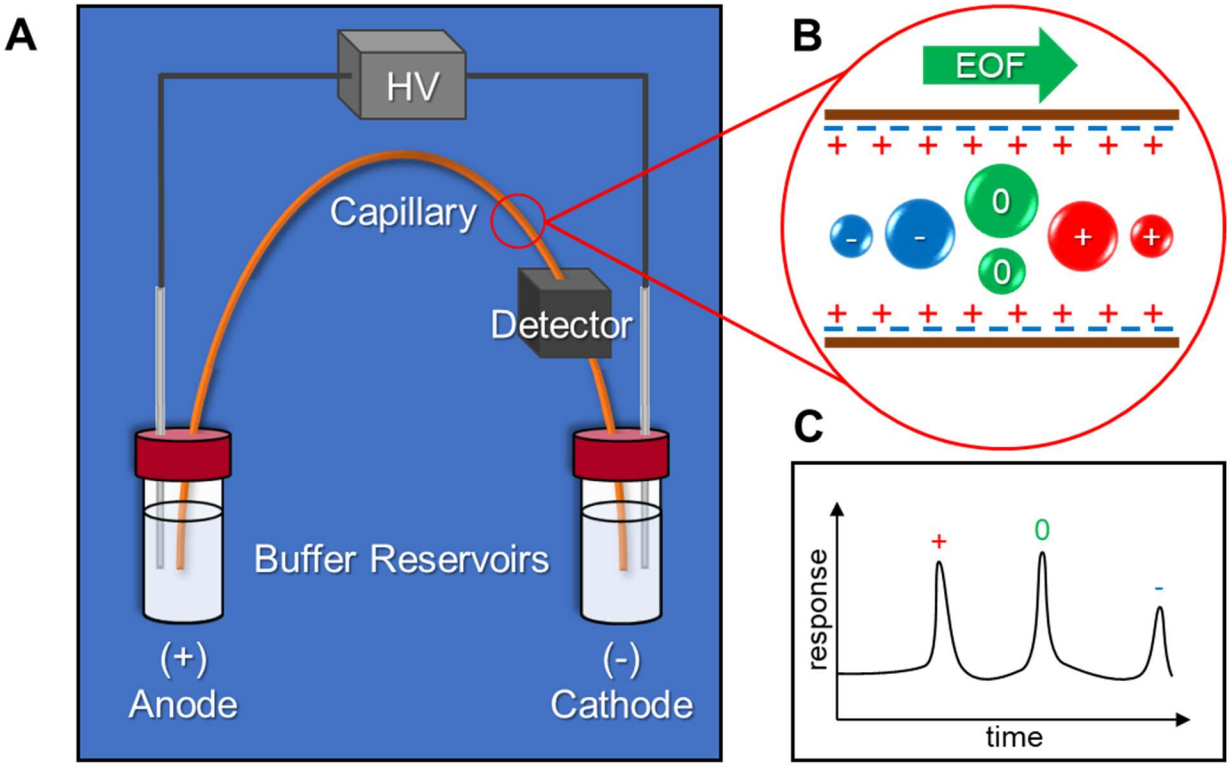

Figure 3.1. (A) Schematic of a capillary electrophoresis instrument; (B) separation mechanism for capillary electrophoresis in normal polarity; (C) sample electropherogram for three analytes: one cation, one neutral species, and one anion, in normal polarity. EOF: electroosmotic flow.

3.2 Microchip electrophoresis with electrochemical detection

3.2.1 Microchip electrophoresis

The first microchip electrophoresis (ME) system was reported by Manz *et al.* almost thirty years ago[10]. ME operates under the same principles as CE and has many of the same advantages, including low sample volume requirements, fast analysis times, and efficient separations (Figure 3.2A). However, whereas a typical CE system is a large, bench-top instrument featuring a capillary for separation, a typical ME system consists of a planar microchip that can fit in the palm of a hand with external power supplies to apply the separation field and a microchannel for the separation instead of a capillary (Figure 3.2B). The smaller dimensions of a ME device versus a CE instrument result in even more rapid separations, as a high separation potential can be applied over a much shorter separation length (typically 5-15 cm), as well as even lower sample volume requirements that makes it ideal for analysis of volume-limited biological samples. In addition, the use of micro- and nanofabrication methods to produce ME devices in a variety of materials such as glass, polydimethylsiloxane (PDMS), or thermoplastics makes it possible to vary the surface properties of the channel to suit the application and to select a fabrication method suited to the production scale. Finally, the planar format makes ME highly amenable to integration of sample preparation and detection steps directly on the chip, which lends itself to applications of portable and automated on-site analysis[11-13].

In the years since its introduction in the form of a glass microchip with fluorescence (FL) detection, a wide variety of detection methods have been incorporated with ME[14-16]. An important consideration for transfer of a method from a conventional system to the microscale is the compatibility of the materials and detection equipment with miniaturization. Several detection methods have been incorporated with ME, including fluorescence (FL), mass spectrometry (MS), and electrochemistry (EC)[16]. In particular, FL detection has been used extensively with ME for

highly sensitive detection of a variety of analytes; however, derivatization is typically required to make the analytes of interest fluorescent[17-19]. MS has also been coupled to ME and can provide definitive identification of an analyte; however, it is expensive[20-24]. Additionally, both FL and MS detectors are difficult to miniaturize to take full advantage of the compact nature of ME. EC detection, including potentiometry, conductimetry, voltammetry, and amperometry, is an alternative detection method that can be readily miniaturized for point-of-measurement applications. Electrodes can be fabricated directly on-chip, and miniature portable, isolated potentiostats are commercially available. The use of EC detection does not typically require derivatization, and it is a selective and sensitive method for detecting redox active compounds[25-29].

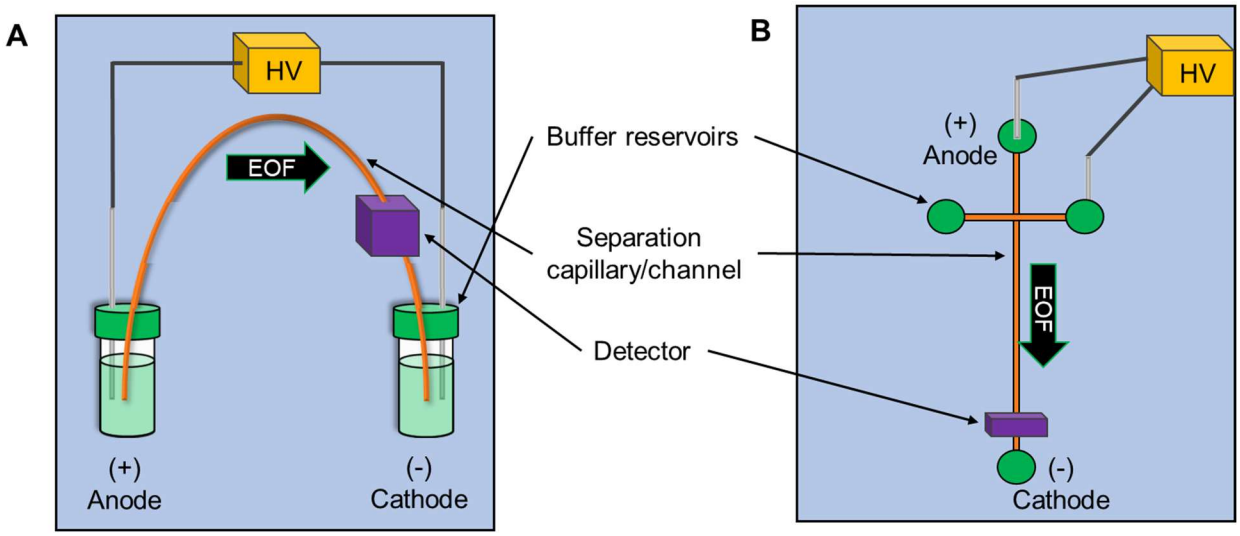

Figure 3.2. Comparison of experimental set-up for (A) capillary and (B) microchip electrophoresis.

3.2.2 Material and fabrication methods

3.2.2.1 Microchip substrates

ME devices have been fabricated from a variety of materials[30], including glass[31], thermoplastics such as polymethylmethacrylate (PMMA) or cyclic olefin copolymer (COC)[32], paper[33], and soft polymers such as polydimethylsiloxane (PDMS)[34]. Hybrid microchips that combine two or more materials into one device have also been employed, providing convenience while resulting in chips that exhibit properties of each substrate[35]. Glass and PDMS chips are typically manufactured using conventional photolithographic techniques with a mask containing the desired microfluidic features used to define the structure. The channel is created using positive photoresist and chemical etching (glass)[36] or negative photoresist to produce a raised structure for imprinting (PDMS) (Figure 3.3A)[37]. The PDMS or glass channel layer can then be either reversibly or irreversibly bonded to a second layer of PDMS or glass containing the electrode (Figure 3.3D). Glass-glass chips are generally produced using high-temperature bonding of the channel and electrode substrate layers[36, 38]. This high-temperature bonding limits the use of some electrode materials for ME-EC, as will be discussed later. Although most glass channels are produced by chemical etching, reactive ion etching has also been used. Reactive ion etching has also been applied to the fabrication of PDMS chips by etching a patterned, photoresist-coated Si wafer or glass substrate to the desired depth, leaving raised features that may be used as a master[36, 38, 39]. Thermoplastics are another popular substrate for microfluidic devices. These can be produced using hot embossing or, in high volumes, using injection molding[40, 41]. Recently, several groups have explored the use of 3D printing technology for fabrication of microfluidic devices; however, more work needs to be done to enable reproducible fabrication of smooth channels on the low-micron scale via commercially available 3D printers[42-49]. This will be discussed in greater detail in a later chapter.

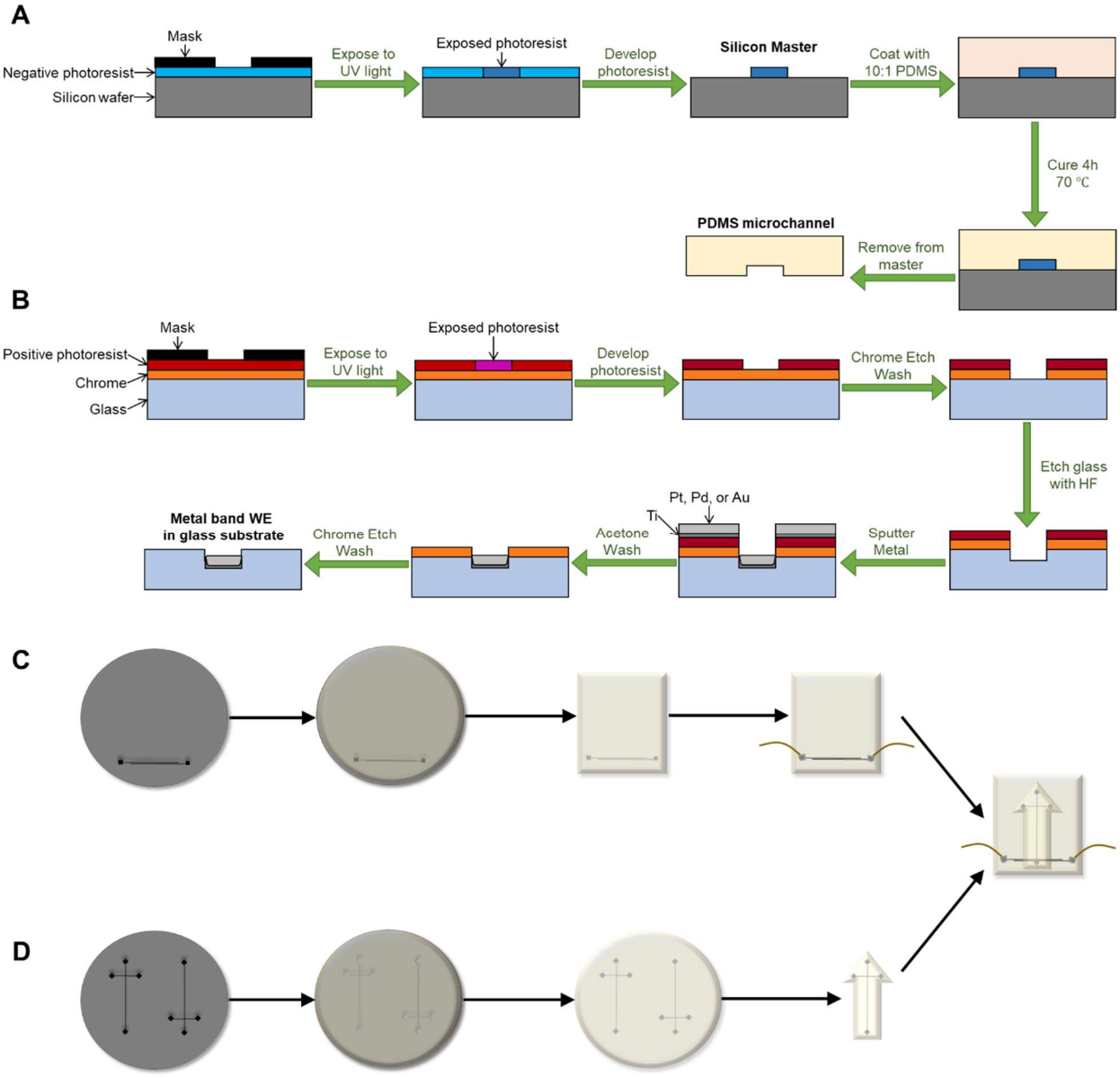

Figure 3.3. Microfabrication methods used in this dissertation (A) Fabrication of a silicon master and PDMS microchip; (B) fabrication of a metal working electrode in a glass substrate; (C) fabrication of a carbon fiber working electrode in a PDMS substrate topped with a PDMS 5-cm simple-T microchip (D).

3.2.2.2 Microelectrode fabrication

In this thesis, microchip electrophoresis with electrochemical detection is used for the determination of RNOS and their reaction products. One of the important parameters in a ME-EC system is the working electrode material and its compatibility with the microchip substrate. Electrode materials used in ME-EC range from metals such as platinum, gold, or palladium to variations of carbon, including carbon fiber, carbon ink, carbon paste, and pyrolyzed photoresist film (PPF). Important considerations are the solvent potential window and the redox properties of the analyte at the electrode surface[50, 51]. Once the optimal electrode material has been identified, an appropriate substrate may then be selected. Metal electrodes are typically fabricated on glass using photolithographic techniques to define the electrode area prior to depositing the metal onto the surface directly (metal film electrodes)[51] or into an etched channel (embedded metal electrodes)[31] (Figure 3.3B). PPF carbon electrodes are also fabricated on glass substrates using similar photolithographic procedures. The electrode is produced by pyrolyzing photoresist in a tube furnace under an inert gas atmosphere. However, PPF electrodes are incompatible with the high temperatures and pressures necessary for glass bonding and, therefore, can be used with hybrid microchips only[52, 53]. Other types of carbon electrodes are more compatible with thermoplastic and polymer substrates.

Many of the earliest applications of carbon working electrodes for ME-EC used carbon fibers with PDMS substrates. The fibers can be placed in a trench created in the bottom layer of a PDMS chip that is perpendicular to the separation channel (Figure 3.3C,D)[54]. Alternatively, the trench can be filled with carbon paste to produce a working electrode[55]. Carbon ink electrodes are popular materials for commercial versions of ME-EC, and may be fabricated in a similar manner or through screen printing on PDMS, glass, or epoxy[50, 51, 56-58]. Another carbon-based electrode material that has been used is boron-doped diamond (BDD). BDD is known for its wide potential

window, low background current, rapid electron transfer kinetics, and low adsorption of organic compounds[59, 60]. To date, BDD working electrodes used with ME-EC have been on the millimeter-width scale[61-63]. As a result, the BDD electrode has to be integrated parallel to the microchannel using a specially designed electrode platform[58].

There have been several studies aimed at improving the mechanical ruggedness and substrate compatibility of carbon electrodes. Regel *et al.* reported the development of graphite/polymethylmethacrylate (PMMA) composite electrodes in PMMA substrates capable of being thermally bonded to another PMMA layer to form a complete ME-EC microchip[64]. More recently, Gouyon *et al.* reported the use of a graphite/PDMS composite material to produce 30 μm wide microband electrodes in a PDMS substrate for amperometric detection in ME[65]. While most of the electrode fabrication processes reported in this section were used to generate band electrodes, another approach recently published describes the fabrication of disk electrodes using metal wires or carbon fibers that are imbedded in a polymer substrate by slow melting of polystyrene (PS) particles around suspended electrodes or by encapsulating the electrodes in an epoxy substrate[66, 67]. A specific advantage of this approach is that, once the substrate has solidified, it can then be polished to reveal the smooth electrode surface, and a PDMS layer containing the separation channels can be aligned on the surface of the substrate.

Several groups have described electrode fabrication methods that do not require the use of a cleanroom or expensive materials to produce low-cost ME-EC devices. These approaches generally produce much larger electrodes than those fabricated by conventional photolithographic methods. One report describes the use of pencil graphite to generate 500 μm-wide electrode channels in PDMS, which are then filled with carbon black paste for amperometric detection[68]. Another simple fabrication approach involves the use of adhesive tape to define the electrode area

(400 μm wide) on an acrylic substrate. Carbon ink was then deposited on the substrate, dried, and polished to generate a microband electrode[69]. Although many of the applications of ME-EC feature PDMS substrates, some groups have investigated other substrate materials, including PMMA[70] and paper[71]. Further details regarding novel electrode materials that have been used for ME-EC can be found in a review by Randviir and Banks[72]. It should also be noted that several companies, including MicruX[73], microLIQUID[74], and microfluidic ChipShop[75], sell microchips with integrated electrodes.

3.2.2.3 Electrode modifications

Modified electrodes can be used to improve the selectivity and sensitivity of ME-EC for specific analytes. In particular, reduced graphene oxide has become a popular material for modified electrodes and electrochemical sensors in the past decade[76-80]. However, only a few examples of the use of graphene oxide modified electrodes for ME-EC have been reported[81-84]. In one application, electrochemically reduced graphene was shown to exhibit better performance for the detection of dopamine and catechol than thermally and chemically reduced graphene[83]. A platinum microband electrode modified with electrochemically reduced graphene oxide for the selective amperometric detection of iodide and ascorbate has also been reported by Lucca *et al.*[84]. Research in our group has focused on using electrochemically reduced graphene oxide to modify gold electrodes for the detection of catecholamines following ME separation. It was found that the graphene-modified electrodes exhibited an initial signal enhancement; however, they tended to show reduced activity over time.[85] Another popular electrode modification is platinization, or the deposition of platinum black nanoparticles on a carbon or platinum working electrode. Platinization increases the surface area of the electrode and improves the electron transfer kinetics for small molecules, such as reactive nitrogen and oxygen species[86-89]. Platinum black electrodes have been used not only with ME-EC but also in miniaturized sensors for monitoring reactive

species from cells such as peroxynitrite, hydrogen peroxide, and nitric oxide[86, 88, 90-93]. More extensive details on the use of carbon and metallic nanomaterials for electrochemical detection in both CE and ME can be found in two recent reviews by the Escarpa group[94, 95].

3.2.3 ME-EC configurations

3.2.3.1 Electrode alignments

The effect of the separation field and current on the electrochemical response is a major consideration in ME. Typical separation fields are in the range of 100–1500 V/cm, while the potential of the working electrode is between –0.5 and 1.0 V versus Ag/AgCl. In addition, separation currents are generally on the μA scale and electrochemical detection occurs at the nA to pA scale[50]. To minimize the interaction of the two fields and protect the potentiostat from the high currents generated by the electrophoretic separation several, electrode configurations have been described. Each of these configurations has its own strengths, weaknesses, and unique characteristics. The three major configurations are end-channel, in-channel, and off-channel electrode alignment (Figure 3.4)[50, 51].

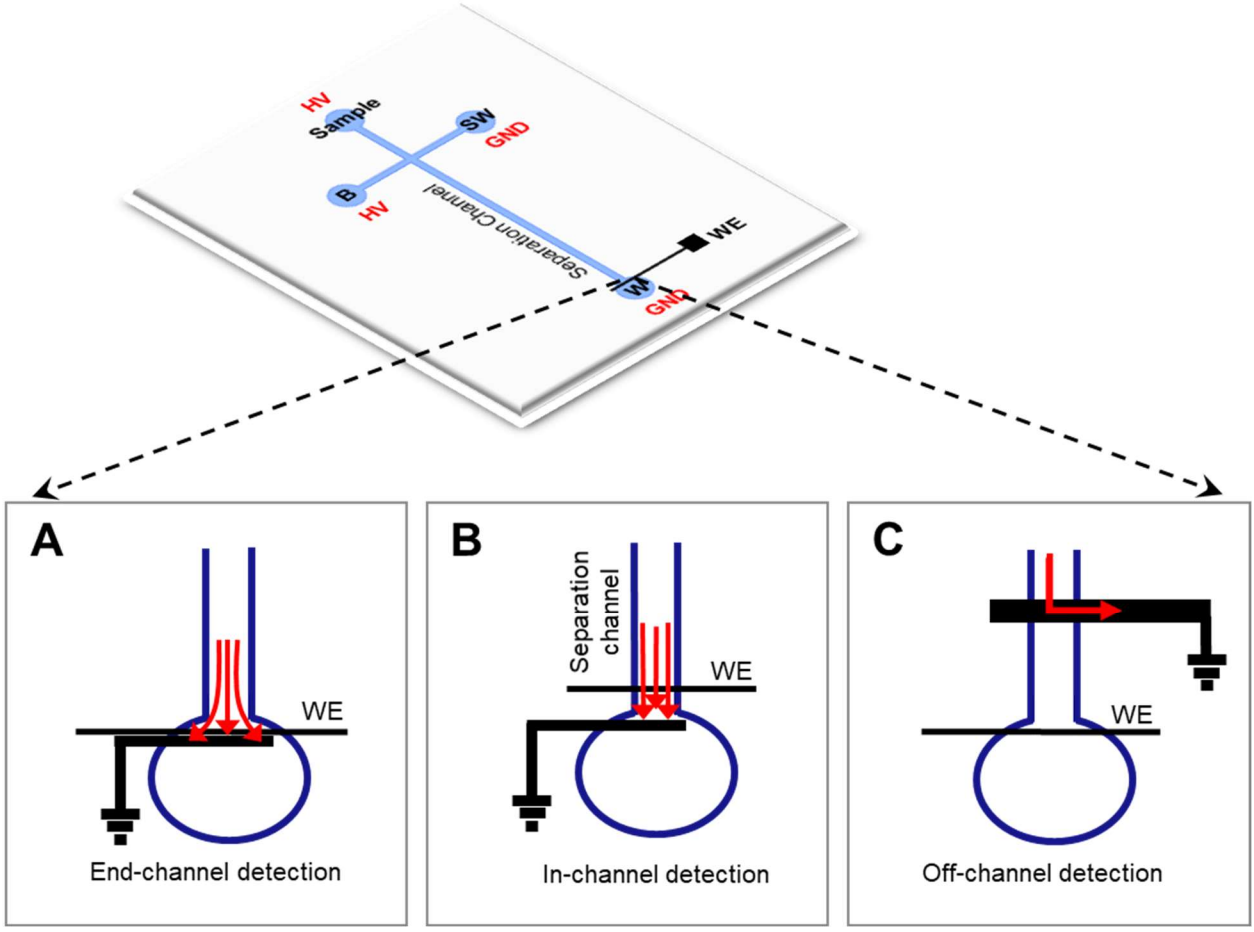

Figure 3.4. Electrode alignments used with ME-EC with a single working electrode; arrows indicate the path of the separation current. (A) End-channel detection (B) In-channel detection (C) Off-channel detection; B: buffer, S: sample waste, W: waste, GND: ground, WE: working electrode, HV: high voltage. Adapted from reference[96].

3.2.3.1.1 End-channel alignment

End-channel alignment was the first and is the most common electrode configuration for ME-EC[97]. In this configuration, the working electrode is aligned within the bottom well of the microchip, 5–20 μm past the channel end (Figure 3.4a). The separation field in ME is dramatically reduced as it moves from the narrow separation channel into the wider ground reservoir. Therefore, if the working electrode is placed in the reservoir outside the channel, the potentiostat is protected from the high voltage, reducing the chance of damaging the electronics. This alignment normally exhibits low background noise at the working electrode due its isolation from the separation field; however, band broadening and asymmetric peak shapes can result due to the diffusion of the analyte once it exits the channel into the bottom well[50, 51].

3.2.3.1.2 In-channel alignment

In-channel alignment utilizes an electrically isolated potentiostat that prevents the separation field from grounding through the potentiostat and damaging it[98]. In this case, the electrode is aligned within the separation channel, minimizing band broadening due to diffusion and resulting in higher separation efficiencies and sharper peaks than the end-channel alignment (Figure 3.4b). However, because the electrode is placed directly in the separation channel, the separation voltage has a direct effect on the potential of the working electrode. The separation voltage causes a shift in the actual potential at the working electrode when compared to the potential applied by the potentiostat. This shift is proportional to the electric field applied across the separation channel and the width of the working electrode. For example, for a normal polarity separation, a 200 V/cm separation field may cause up to a 400 mV potential drop across a 20 μm working electrode, inducing an approximately 200 mV shift toward a more negative potential. Practically, this means the potentiostat must be set to a more positive potential than is expected to

accomplish any given electrochemical reaction. In reverse polarity, where a negative potential is applied, the opposite effect is observed, resulting in a positive potential shift. In addition, the in-channel configuration usually leads to more background noise than that observed for end-channel alignment due to fluctuations in the high voltage power supply. This can affect the limits of detection, even as the separation efficiency is improved[50].

3.2.3.1.3 Off-channel alignment

A third configuration used to isolate the working electrode from the separation voltage is off-channel alignment. In this configuration, a decoupler is placed ahead of the working electrode in the separation channel (Figure 3.4c). The decoupler grounds the separation field before it reaches the working electrode. This leads to low background noise and no shifts in the working electrode potential due to the separation voltage. However, since the decoupler completely isolates the working electrode from the separation field, the residual hydrodynamic flow produced from the EOF is responsible for moving analytes to the working electrode. Therefore, the plug flow profile of the electrophoretic separation is converted to the parabolic flow characteristic of laminar flow. If the EOF is slow or the distance between the decoupler and the working electrode is large, this can lead to significant band-broadening and a loss of resolution[50].

The integration of a decoupler into a ME-EC device can be challenging as the decoupler and working electrode are typically composed of different materials that require different fabrication methods. A major issue is the generation of gas at the decoupler (anode or cathode) due to the reduction of protons or oxidation of water, depending on the polarity of the separation. This can lead to the formation of bubbles in the channel and stop the separation[50]. To get around this problem, platinum and palladium decouplers have been used in the normal polarity mode because they adsorb hydrogen gas[99-101]. However, decouplers for a reverse polarity separation require a material that will adsorb oxygen gas and this type of decoupler has not yet been reported

for ME-EC. A cellulose acetate membrane cast in a series of holes placed above the channel has been used as a decoupler in ME-EC in normal polarity and could theoretically be applied to a reverse polarity separation as well[50, 102].

3.2.3.2 Dual channels and/or electrodes

For most ME-EC applications that use a single working electrode, multiple injections and separations of the same sample at different working electrode potentials must be performed to obtain voltammetric information. This can be problematic if one is sample-limited or trying to detect a labile species. Voltammetric detection is an alternative approach; however, the charging currents generated while the potential is scanned limit its sensitivity. Another approach that maintains the advantage of low background currents characteristic of amperometry is the use of multiple electrode systems. Micro- and nanoarrays and have been used extensively in ME-EC to increase the analytical signal while decreasing the capacitive current and, therefore, noise of the system, leading to lower limits of detection[67, 103-106]. If the multiple electrode approach is used for voltammetric information, at least two working electrodes at different potentials should be used. Such dual electrode systems have been implemented in ME-EC in both the series and parallel electrode configurations.

3.2.3.2.1 Dual-series electrode configuration

In the dual-series configuration, two electrodes are placed in the channel perpendicular to the flow 10–50 μm apart (Figure 3.5a). The sample plug travels over the two electrodes sequentially at different times. This configuration is relatively easy to integrate into a simple-t microchip and can be used for either selective detection of species undergoing chemically reversible redox reactions or voltammetric characterization. In the first mode, termed "generation-collection mode," a stable product, typically an oxidized form of the original analyte (*e.g.,* catechol oxidized to its quinone form), is generated at the first electrode followed by the reduction of that

product at the second electrode, thereby providing a selective detection method for those substances (Figure 3.5b)[107-109]. The collection efficiency, or percent of redox product formed at the first electrode relative to the amount of redox analytes reacted at the second electrode, is one of the most important parameters in generation-collection mode. It is determined by the heterogeneous rate constant of the redox species, the distance between the electrodes, and the flow rate. Therefore, collection efficiencies can be used with migration times to identify analytes that have different electrochemical rate constants. This mode can also be used to detect a stable electrogenerated product at a more desirable potential than that of the initial oxidation/reduction. Examples of this application include the detection of glutathione disulfide and nitrotyrosine. Additionally, this configuration has been used for the selective detection of catecholamines and phenolic acids based on their redox chemistry[110-112].

The dual-series configuration can also be used to determine current ratios for voltammetric identification of electroactive compounds. In this mode, the two working electrodes are biased at two preselected potentials and a current ratio for the analytes of interest is generated. The combination of the migration time and current ratio (voltammetric data) can be used for peak identification. To select electrode potentials for analyte identification, the upper potential and the lower potential should be at the current-limiting plateau potentials of the most easily oxidizable/reducible and the least easily oxidizable/reducible analytes, respectively. Analytes between these two potentials will give an intermediate current ratio between 0 (most difficult to oxidize or reduce) and 1 (easiest to oxidize/reduce)[113]. In the series configuration, electrolysis of the analytes at the first electrode and the relative placement of electrodes must be optimized to obtain good results. We have recently reported the need for two unique correction factors, the oxidation ratio difference and the sensitivity ratio, that should be applied to the current ratios when using this approach[113]. The oxidation ratio difference is a measure of the amount of analyte

depletion at the first electrode, which results in less analyte reaching the second electrode and, therefore, a lower current response. The sensitivity ratio is a correction factor that takes into account the relative alignments of the electrodes with respect to the channel end (*e.g.,* one aligned in-channel and one aligned end-channel). As discussed above, the different positions result in a change in the active surface area of the electrode used in the electrochemical reaction and, therefore, a change in the sensitivity[113]. The dual series electrode configuration has been employed to identify poorly resolved species in microdialysis samples and cell lysates. One example is shown in Figure 3.5c, where this configuration was used selectively to identify homovanillic acid (HVA) that was comigrating with ascorbic acid (AA)[114].

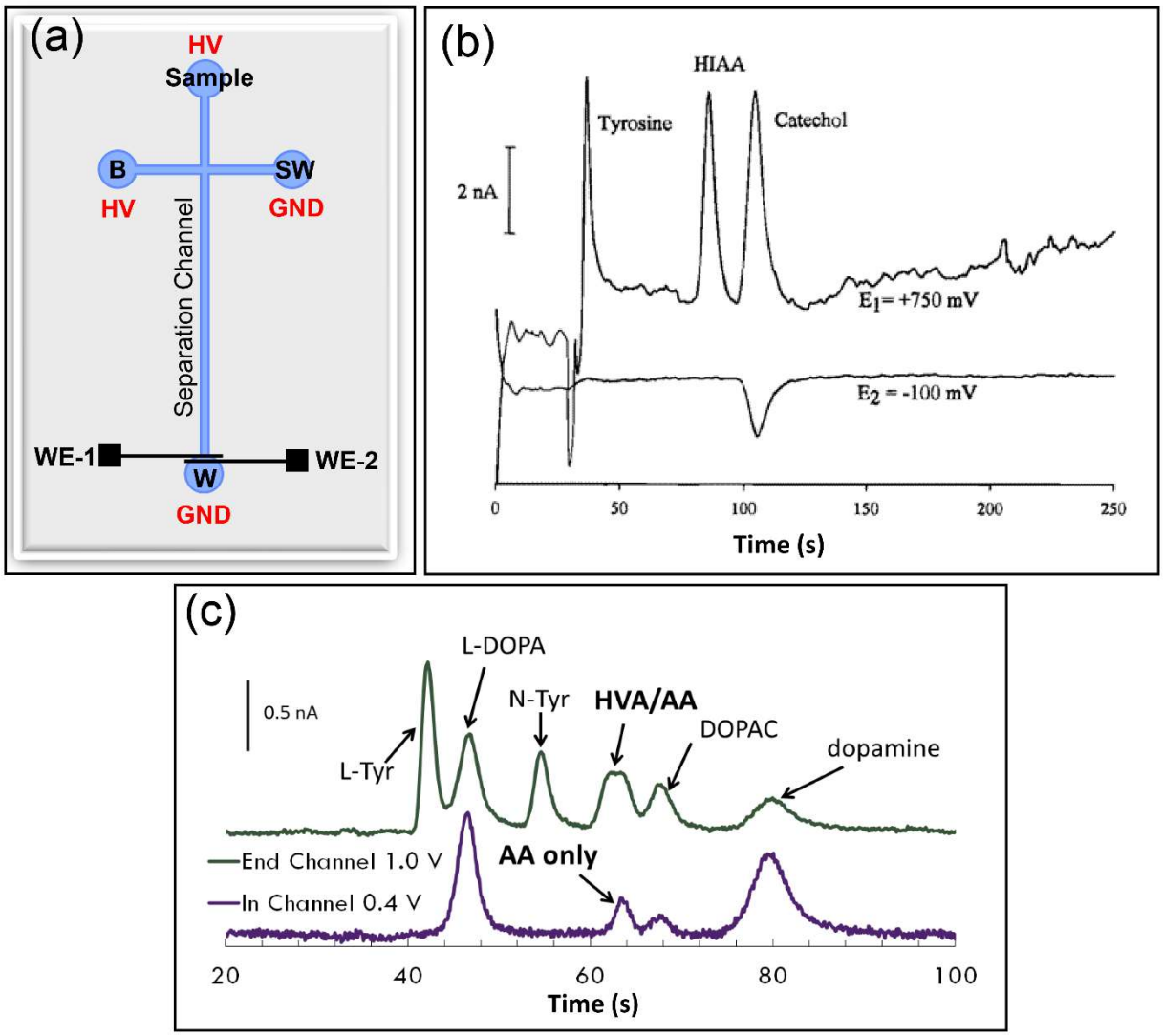

Figure 3.5. (a) Dual-series electrode configuration for ME-EC (b) Dual-electrode detection of tyrosine, 5-hydroxyindoleacetic acid (HIAA), and catechol; E_1 = +750 mV, E_2 = -100 mV. Reprinted with permission from reference[110]. Copyright (2000) American Chemical Society (c) Dual-electrode detection used to identify comigrating ascorbic acid (AA) and homovanillic acid (HVA) peaks with E_1 = +400 mV and E_2 = +1000 mV. Reproduced from reference[114]. B: buffer, S: sample waste, W: waste, GND: ground, WE: working electrode, HV: high voltage.

3.2.3.2.2 Dual-channel, dual-parallel electrode configuration

The development of dual-channel dual-electrode ME was first reported by Chen and Hahn in 2007 (Figure 3.6a)[115]. In that report, sample was injected into one channel (sample channel) and a buffer blank was injected into the other channel (reference channel). Two 50 μm wide gold electrodes were fabricated using standard photolithographic techniques and were aligned in the two channels at a fixed distance from the channel outlet. A three-electrode system was used for the EC detection. The electrode aligned at the reference channel was used as the reference electrode and the electrode aligned at the sample channel served as the working electrode. Under these conditions, both electrodes are exposed to the same separation field, thereby canceling out the fluctuations in the separation voltage and leading to lower noise[115]. The same configuration was later used with a low-cost gold nanoparticle-modified indium tin oxide (ITO)-coated polyethylene terephthalate electrode for the determination of antibiotics in human plasma[116, 117]. This configuration has also been evaluated for reverse polarity separations by Meneses *et al.* using an in-channel alignment and an isolated potentiostat for the determination of nitrite in a microdialysis sample (Figure 3.6a, b)[118].

A dual-channel/dual-parallel electrode microchip configuration for voltammetric identification of redox active species was recently reported by our group[113]. In this unique configuration, seen in Figure 3.6c, sample is injected from a single reservoir into two distinct separation channels in equal portions. The two working electrodes are aligned as closely as possible to the same position relative to the two separate channel ends. Thus, the two electrodes have similar areas exposed to the solution. This eliminates the sensitivity correction factor that is necessary for the dual-series configuration described earlier. Additionally, as both electrodes see identical analyte plugs independently, a correction factor for the oxidation ratio difference is not needed. This electrode configuration was tested using nitrite, azide, tyrosine, and iodide as model

analytes (Figure 3.6d). It was demonstrated that the sample plug injection was reproducible within 6% based on the peak heights obtained for multiple injections (n=3). It was also possible to obtain current ratios that did not need to be corrected for response factor and were closer to theoretical prediction than those obtained with the dual-series configuration. This configuration was demonstrated for the determination of RNOS by ME-EC. Due to their similar electrophoretic mobilities, it can be difficult to separate nitrite, an indicator of cellular nitrosative stress, from azide, a contaminant from the cell filters, in cell lysate samples. Although these species are difficult to resolve electrophoretically, they can be distinguished based on their differences in electrochemistry using current ratios. The dual-channel, dual-parallel electrode ME-EC system described here was used to confirm the presence of nitrite in cell lysate from a single sample injection[113].

(a)

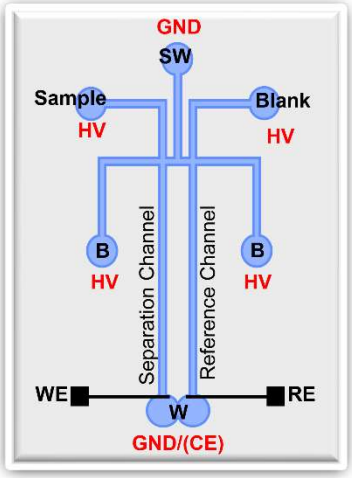

(b)

Parameter	Dual-channel			Single-channel
	15 mm Pt reference	50 mm Pt reference	Ag/AgCl reference	Ag/AgCl reference
Noise (pA)	4	17	27	25
Background current (nA)	2.8	4.7	4.2	~4

(c)

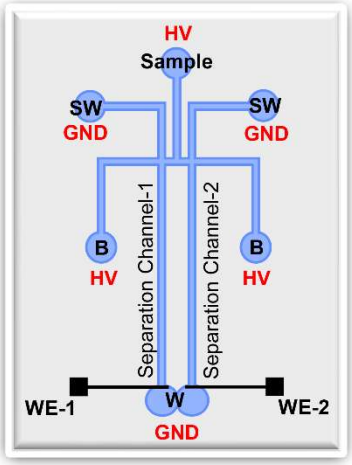

(d)

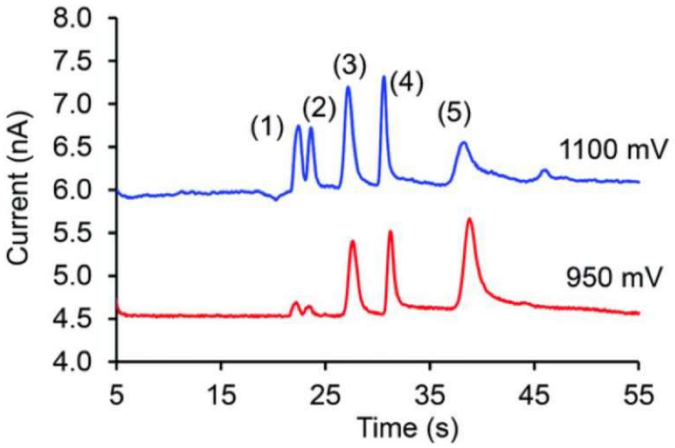

Figure 3.6. Comparison of two dual-channel, dual-parallel electrode configurations (a) Schematic of a dual-channel microchip with one separation channel and one reference channel. Adapted with permission from [115] Copyright (2007) American Chemical Society (b) Comparison of approximate baseline noise and background currents when different reference electrodes were employed in dual- and single-channel microchips operated in reverse polarity. Reproduced from [118] with permission (c) Schematic of a dual-channel microchip with two separation channels. Adapted from [113] with permission from The Royal Society of Chemistry. (d) Electropherogram obtained using the dual-channel, dual-parallel configuration for (1) nitrite, (2) azide, (3) iodide, (4) tyrosine, and (5) hydrogen peroxide standards using reverse polarity. Reproduced from [113] with permission from The Royal Society of Chemistry. B: buffer, S: sample waste, W: waste, GND: ground, WE: working electrode, HV: high voltage.

3.3 Conclusions

Capillary and microchip electrophoresis are powerful tools that allow fast, highly efficient separations of charged analytes. In this thesis, both techniques are used in combination with UV and electrochemical detection to investigate the role of reactive oxygen and nitrogen species (RNOS) in oxidative stress. RNOS as well as their products will be detected and the biochemistry of these reactions that are so important to the redox homeostasis of cells will be explored.

3.4 References

1. Jorgenson, J. W.; Lukacs, K. D., Zone electrophoresis in open-tubular glass capillaries. *Anal. Chem.* **1981,** *53* (8), 1298-1302.
2. Kubáň, P.; Dvořák, M.; Kubáň, P., Capillary electrophoresis of small ions and molecules in less conventional human body fluid samples: A review. *Anal. Chim. Acta* **2019,** *1075* (1-26).
3. Kostal, V.; Katzenmeyer, J.; Arriaga, E. A., Capillary electrophoresis in bioanalysis. *Anal. Chem.* **2008,** *80* (12), 4533-4550.
4. Tamizi, E.; Jouyban, A., The potential of the capillary electrophoresis techniques for quality control of biopharmaceuticals—A review. *Electrophoresis* **2015,** *36* (6), 831-858.
5. Ouimet, C. M.; D'amico, C. I.; Kennedy, R. T., Advances in capillary electrophoresis and the implications for drug discovery. *Expert opinion on drug discovery* **2017,** *12* (2), 213-224.
6. Baciu, T.; Botello, I.; Borrull, F.; Calull, M.; Aguilar, C., Capillary electrophoresis and related techniques in the determination of drugs of abuse and their metabolites. *TrAC, Trends Anal. Chem.* **2015,** *74*, 89-108.
7. Shewale, J. G.; Qi, L.; Calandro, L. M., Principles, practice, and evolution of capillary electrophoresis as a tool for forensic DNA analysis. *Forensic Sci. Rev.* **2012,** *24* (2), 79.
8. Hamdan, I. I., Capillary electrophoresis in the analysis of pharmaceuticals in environmental water: A critical review. *J. Liq. Chromatogr. Rel. Technol.* **2017,** *40* (3), 111-125.
9. Rojano-Delgado, A. M.; Luque de Castro, M. D., Capillary electrophoresis and herbicide analysis: Present and future perspectives. *Electrophoresis* **2014,** *35* (17), 2509-2519.
10. Manz, A.; Harrison, D. J.; Verpoorte, E. M.; Fettinger, J. C.; Paulus, A.; Lüdi, H.; Widmer, H. M., Planar chips technology for miniaturization and integration of separation techniques into monitoring systems: capillary electrophoresis on a chip. *Journal of Chromatography A* **1992,** *593* (1-2), 253-258.
11. Yang, R.; Pagaduan, J. V.; Yu, M.; Woolley, A. T., On chip preconcentration and fluorescence labeling of model proteins by use of monolithic columns: device fabrication, optimization, and automation. *Anal. Bioanal. Chem.* **2015,** *407* (3), 737-747.
12. Patabadige, D. E.; Jia, S.; Sibbitts, J.; Sadeghi, J.; Sellens, K.; Culbertson, C. T., Micro total analysis systems: fundamental advances and applications. *Anal. Chem.* **2015,** *88* (1), 320-338.
13. Landers, J. P., *Handbook of capillary and microchip electrophoresis and associated microtechniques*. CRC press: **2007**.

14. Pagaduan, J. V.; Sahore, V.; Woolley, A. T., Applications of microfluidics and microchip electrophoresis for potential clinical biomarker analysis. *Anal. Bioanal. Chem.* **2015,** *407* (23), 6911-6922.
15. Nuchtavorn, N.; Suntornsuk, W.; Lunte, S. M.; Suntornsuk, L., Recent applications of microchip electrophoresis to biomedical analysis. *J. Pharm. Biomed. Anal.* **2015,** *113*, 72-96.
16. Castro, E. R.; Manz, A., Present state of microchip electrophoresis: state of the art and routine applications. *Journal of Chromatography A* **2015,** *1382*, 66-85.
17. Oborny, N. J.; Costa, E. E. M.; Suntornsuk, L.; Abreu, F. C.; Lunte, S. M., Evaluation of a portable microchip electrophoresis fluorescence detection system for the analysis of amino acid neurotransmitters in brain dialysis samples. *Anal. Sci.* **2016,** *32* (1), 35-40.
18. Sahore, V.; Sonker, M.; Nielsen, A. V.; Knob, R.; Kumar, S.; Woolley, A. T., Automated microfluidic devices integrating solid-phase extraction, fluorescent labeling, and microchip electrophoresis for preterm birth biomarker analysis. *Anal. Bioanal. Chem.* **2018,** *410* (3), 933-941.
19. Fresta, C. G.; Hogard, M. L.; Caruso, G.; Costa, E. E. M.; Lazzarino, G.; Lunte, S. M., Monitoring carnosine uptake by RAW 264.7 macrophage cells using microchip electrophoresis with fluorescence detection. *Analytical Methods* **2017,** *9* (3), 402-408.
20. DeLaney, K.; Sauer, C. S.; Vu, N. Q.; Li, L., Recent Advances and New Perspectives in Capillary Electrophoresis-Mass Spectrometry for Single Cell "Omics". *Molecules* **2019,** *24* (1), 42.
21. Štěpánová, S.; Kašička, V., Recent developments and applications of capillary and microchip electrophoresis in proteomic and peptidomic analyses. *J. Sep. Sci.* **2016,** *39* (1), 198-211.
22. Feng, X.; Liu, B. F.; Li, J.; Liu, X., Advances in coupling microfluidic chips to mass spectrometry. *Mass Spectrom. Rev.* **2015,** *34* (5), 535-557.
23. Oedit, A.; Vulto, P.; Ramautar, R.; Lindenburg, P. W.; Hankemeier, T., Lab-on-a-Chip hyphenation with mass spectrometry: strategies for bioanalytical applications. *Curr. Opin. Biotechnol.* **2015,** *31*, 79-85.
24. Khatri, K.; Klein, J. A.; Haserick, J. R.; Leon, D. R.; Costello, C. E.; McComb, M. E.; Zaia, J., Microfluidic capillary electrophoresis–mass spectrometry for analysis of monosaccharides, oligosaccharides, and glycopeptides. *Anal. Chem.* **2017,** *89* (12), 6645-6655.
25. Tanyanyiwa, J.; Leuthardt, S.; Hauser, P. C., Conductimetric and potentiometric detection in conventional and microchip capillary electrophoresis. *Electrophoresis* **2002,** *23* (21), 3659-3666.
26. Vandaveer IV, W. R.; Pasas, S. A.; Martin, R. S.; Lunte, S. M., Recent developments in amperometric detection for microchip capillary electrophoresis. *Electrophoresis* **2002,** *23* (21), 3667-3677.
27. Vandaveer IV, W. R.; Pasas-Farmer, S. A.; Fischer, D. J.; Frankenfeld, C. N.; Lunte, S. M., Recent developments in electrochemical detection for microchip capillary electrophoresis. *Electrophoresis* **2004,** *25* (21-22), 3528-3549.
28. Coltro, W. K. T., Capacitively coupled contactless conductivity detection (C4D) applied to capillary electrophoresis (CE) and microchip electrophoresis (MCE) *Capillary Electrophoresis and Microchip Capillary Electrophoresis: Principles, Applications, and Limitations* **2013**, 145.
29. Mark, J. J.; Scholz, R.; Matysik, F.-M., Electrochemical methods in conjunction with capillary and microchip electrophoresis. *Journal of Chromatography A* **2012,** *1267*, 45-64.
30. Nge, P. N.; Rogers, C. I.; Woolley, A. T., Advances in microfluidic materials, functions, integration, and applications. *Chem. Rev.* **2013,** *113* (4), 2550-2583.

31. Scott, D. E.; Grigsby, R. J.; Lunte, S. M., Microdialysis Sampling Coupled to Microchip Electrophoresis with Integrated Amperometric Detection on an All-Glass Substrate. *ChemPhysChem* **2013,** *14* (10), 2288-2294.
32. Castaño-Álvarez, M.; Fernández-Abedul, M. T.; Costa-García, A., Poly (methylmethacrylate) and Topas capillary electrophoresis microchip performance with electrochemical detection. *Electrophoresis* **2005,** *26* (16), 3160-3168.
33. Akyazi, T.; Basabe-Desmonts, L.; Benito-Lopez, F., Review on microfluidic paper-based analytical devices towards commercialisation. *Anal. Chim. Acta* **2018,** *1001*, 1-17.
34. Effenhauser, C. S.; Bruin, G. J.; Paulus, A.; Ehrat, M., Integrated capillary electrophoresis on flexible silicone microdevices: analysis of DNA restriction fragments and detection of single DNA molecules on microchips. *Anal. Chem.* **1997,** *69* (17), 3451-3457.
35. Saylor, R. A.; Lunte, S. M., PDMS/glass hybrid device with a reusable carbon electrode for on-line monitoring of catecholamines using microdialysis sampling coupled to microchip electrophoresis with electrochemical detection. *Electrophoresis* **2018,** *39* (3), 462-469.
36. Van Toan, N.; Inomata, N.; Toda, M.; Ono, T., Glass Patterning: Technologies and Applications. *Advances in Glass Science and Technology* **2018**, 151.
37. Fujii, T., PDMS-based microfluidic devices for biomedical applications. *Microelectron. Eng.* **2002,** *61*, 907-914.
38. Iliescu, C.; Taylor, H.; Avram, M.; Miao, J.; Franssila, S., A practical guide for the fabrication of microfluidic devices using glass and silicon. *Biomicrofluidics* **2012,** *6* (1), 016505.
39. Wunderlich, B.; Nettels, D.; Benke, S.; Clark, J.; Weidner, S.; Hofmann, H.; Pfeil, S. H.; Schuler, B., Microfluidic mixer designed for performing single-molecule kinetics with confocal detection on timescales from milliseconds to minutes. *Nature protocols* **2013,** *8* (8), 1459.
40. Lee, U. N.; Su, X.; Guckenberger, D. J.; Dostie, A. M.; Zhang, T.; Berthier, E.; Theberge, A. B., Fundamentals of rapid injection molding for microfluidic cell-based assays. *Lab on a Chip* **2018,** *18* (3), 496-504.
41. Tsao, C.-W.; DeVoe, D. L., Bonding of thermoplastic polymer microfluidics. *Microfluid. Nanofluid.* **2009,** *6* (1), 1-16.
42. Beauchamp, M. J.; Nielsen, A. V.; Gong, H.; Nordin, G. P.; Woolley, A. T., 3D printed microfluidic devices for microchip electrophoresis of pre-term birth biomarkers. *Anal. Chem.* **2019,** *91* (11), 7418-7425.
43. Castiaux, A. D.; Pinger, C.; Hayter, E. A.; Bunn, M. E.; Martin, R. S.; Spence, D. M., PolyJet 3D-Printed Enclosed Microfluidic Channels without Photocurable Supports. *Anal. Chem.* **2019,** *91* (10), 6910-6917.
44. Chen, C.; Mehl, B. T.; Munshi, A. S.; Townsend, A. D.; Spence, D. M.; Martin, R. S., 3D-printed microfluidic devices: fabrication, advantages and limitations—a mini review. *Analytical Methods* **2016,** *8* (31), 6005-6012.
45. Ho, C. M. B.; Ng, S. H.; Li, K. H. H.; Yoon, Y.-J., 3D printed microfluidics for biological applications. *Lab on a Chip* **2015,** *15* (18), 3627-3637.
46. Bhattacharjee, N.; Urrios, A.; Kang, S.; Folch, A., The upcoming 3D-printing revolution in microfluidics. *Lab on a Chip* **2016,** *16* (10), 1720-1742.
47. Waheed, S.; Cabot, J. M.; Macdonald, N. P.; Lewis, T.; Guijt, R. M.; Paull, B.; Breadmore, M. C., 3D printed microfluidic devices: enablers and barriers. *Lab on a Chip* **2016,** *16* (11), 1993-2013.
48. He, Y.; Wu, Y.; Fu, J. Z.; Gao, Q.; Qiu, J. J., Developments of 3D printing microfluidics and applications in chemistry and biology: a review. *Electroanalysis* **2016,** *28* (8), 1658-1678.

49. Amin, R.; Knowlton, S.; Hart, A.; Yenilmez, B.; Ghaderinezhad, F.; Katebifar, S.; Messina, M.; Khademhosseini, A.; Tasoglu, S., 3D-printed microfluidic devices. *Biofabrication* **2016,** *8* (2), 022001.
50. Gunasekara, D. B.; Wijesinghe, M. B.; Saylor, R. A.; Lunte, S. M., Principles and Strategies for Microchip Electrophoresis with Amperometric Detection. In *Electrochemical Strategies in Detection Science*, **2015**; pp 85-124.
51. Fischer, D. J.; Hulvey, M. K.; Regel, A. R.; Lunte, S. M., Amperometric detection in microchip electrophoresis devices: Effect of electrode material and alignment on analytical performance. *Electrophoresis* **2009,** *30* (19), 3324-3333.
52. Ranganathan, S.; Mccreery, R.; Majji, S. M.; Madou, M., Photoresist-derived carbon for microelectromechanical systems and electrochemical applications. *J. Electrochem. Soc.* **2000,** *147* (1), 277.
53. Saylor, R. A.; Reid, E. A.; Lunte, S. M., Microchip electrophoresis with electrochemical detection for the determination of analytes in the dopamine metabolic pathway. *Electrophoresis* **2015,** *36* (16), 1912-1919.
54. Gawron, A. J.; Martin, R. S.; Lunte, S. M., Microchip electrophoretic separation systems for biomedical and pharmaceutical analysis. *Eur. J. Pharm. Sci.* **2001,** *14* (1), 1-12.
55. Martin, R. S.; Gawron, A. J.; Fogarty, B. A.; Regan, F. B.; Dempsey, E.; Lunte, S. M., Carbon paste-based electrochemical detectors for microchip capillary electrophoresis/electrochemistry. *Analyst* **2001,** *126* (3), 277-280.
56. Wang, J.; Pumera, M.; Prakash Chatrathi, M.; Rodriguez, A.; Spillman, S.; Martin, R. S.; Lunte, S. M., Thick-film electrochemical detectors for poly (dimethylsiloxane)-based microchip capillary electrophoresis. *Electroanalysis: An International Journal Devoted to Fundamental and Practical Aspects of Electroanalysis* **2002,** *14* (18), 1251-1255.
57. Kovarik, M. L.; Torrence, N. J.; Spence, D. M.; Martin, R. S., Fabrication of carbon microelectrodes with a micromolding technique and their use in microchip-based flow analyses. *Analyst* **2004,** *129* (5), 400-405.
58. Wang, J.; Tian, B.; Sahlin, E., Micromachined electrophoresis chips with thick-film electrochemical detectors. *Anal. Chem.* **1999,** *71* (23), 5436-5440.
59. Park, J.; Quaiserová-Mocko, V.; Patel, B. A.; Novotný, M.; Liu, A.; Bian, X.; Galligan, J. J.; Swain, G. M., Diamond microelectrodes for in vitro electroanalytical measurements: current status and remaining challenges. *Analyst* **2008,** *133* (1), 17-24.
60. Richter, E.; Freitas, J. M.; de Oliveira, T. C.; Munoz, R. A. A., Boron doped diamond electrodes in flow-based systems. *Frontiers in chemistry* **2019,** *7*, 190.
61. Wang, J.; Chen, G.; Muck Jr, A.; Shin, D.; Fujishima, A., Microchip capillary electrophoresis with a boron-doped diamond electrode for rapid separation and detection of purines. *Journal of Chromatography A* **2004,** *1022* (1-2), 207-212.
62. Wang, J.; Chen, G.; Chatrathi, M. P.; Fujishima, A.; Tryk, D. A.; Shin, D., Microchip capillary electrophoresis coupled with a boron-doped diamond electrode-based electrochemical detector. *Anal. Chem.* **2003,** *75* (4), 935-939.
63. Shin, D.; Tryk, D. A.; Fujishima, A.; Muck Jr, A.; Chen, G.; Wang, J., Microchip capillary electrophoresis with a boron-doped diamond electrochemical detector for analysis of aromatic amines. *Electrophoresis* **2004,** *25* (17), 3017-3023.
64. Regel, A.; Lunte, S., Integration of a graphite/poly (methyl-methacrylate) composite electrode into a poly (methylmethacrylate) substrate for electrochemical detection in microchips. *Electrophoresis* **2013,** *34* (14), 2101-2106.

65. Gouyon, J.; d'Orlyé, F.; Griveau, S.; Bedioui, F.; Varenne, A., Characterization of home-made graphite/PDMS microband electrodes for amperometric detection in an original reusable glass-NOA®-PDMS electrophoretic microdevice. *Electrochim. Acta* **2019**, 135164.
66. Selimovic, A.; Johnson, A. S.; Kiss, I. Z.; Martin, R. S., Use of epoxy-embedded electrodes to integrate electrochemical detection with microchip-based analysis systems. *Electrophoresis* **2011,** *32* (8), 822-831.
67. Johnson, A. S.; Selimovic, A.; Martin, R. S., Integration of microchip electrophoresis with electrochemical detection using an epoxy-based molding method to embed multiple electrode materials. *Electrophoresis* **2011,** *32* (22), 3121-3128.
68. da Silva, E. N. T.; Ferreira, V. S.; Lucca, B. G., Rapid and inexpensive method for the simple fabrication of PDMS-based electrochemical sensors for detection in microfluidic devices. *Electrophoresis* **2019,** *40* (9), 1322-1330.
69. Petroni, J. M.; Lucca, B. G.; Ferreira, V. S., Simple approach for the fabrication of screen-printed carbon-based electrode for amperometric detection on microchip electrophoresis. *Anal. Chim. Acta* **2017,** *954*, 88-96.
70. Gomez, F. J. V.; Martín, A.; Silva, M. F.; Escarpa, A., Microchip electrophoresis-single wall carbon nanotube press-transferred electrodes for fast and reliable electrochemical sensing of melatonin and its precursors. *Electrophoresis* **2015,** *36* (16), 1880-1885.
71. González-López, A.; García-Manrique, P.; Blanco-López, M. d. C.; Fernández-Abedul, M. T., Integrated electrophoresis separation and electrochemical detection in a paper-based device. *Procedia technology* **2017,** *27*, 21-22.
72. Randviir, E. P.; Banks, C. E., Electrode substrate innovation for electrochemical detection in microchip electrophoresis. *Electrophoresis* **2015,** *36* (16), 1845-1853.
73. Technologies, M., Flavones and phenolic acids analysis in MEs-ED. In *MicruX Application Note*, 2014.
74. Microfluidic Custom Design and Mass-Manufacturing. https://www.microliquid.com/microfluidic-custom-design-and-mass-manufacturing-technologies/.
75. Materials in Microfluidics. https://www.microfluidic-chipshop.com/microfluidics/materials-in-microfluidics/.
76. Yang, B.; Wang, H.; Du, J.; Fu, Y.; Yang, P.; Du, Y., Direct electrodeposition of reduced graphene oxide on carbon fiber electrode for simultaneous determination of ascorbic acid, dopamine and uric acid. *Colloids Surf. Physicochem. Eng. Aspects* **2014,** *456*, 146-152.
77. Chen, L.; Tang, Y.; Wang, K.; Liu, C.; Luo, S., Direct electrodeposition of reduced graphene oxide on glassy carbon electrode and its electrochemical application. *Electrochem. Commun.* **2011,** *13* (2), 133-137.
78. Wu, S.; Huang, F.; Lan, X.; Wang, X.; Wang, J.; Meng, C., Electrochemically reduced graphene oxide and Nafion nanocomposite for ultralow potential detection of organophosphate pesticide. *Sensors Actuators B: Chem.* **2013,** *177*, 724-729.
79. Raj, M. A.; John, S. A., Simultaneous determination of uric acid, xanthine, hypoxanthine and caffeine in human blood serum and urine samples using electrochemically reduced graphene oxide modified electrode. *Anal. Chim. Acta* **2013,** *771*, 14-20.
80. Dreyer, D. R.; Park, S.; Bielawski, C. W.; Ruoff, R. S., The chemistry of graphene oxide. *Chem. Soc. Rev.* **2010,** *39* (1), 228-240.
81. Chen, B.; Zhang, L.; Chen, G., Determination of salidroside and tyrosol in Rhodiola by capillary electrophoresis with graphene/poly (urea-formaldehyde) composite modified electrode. *Electrophoresis* **2011,** *32* (8), 870-876.

82. Wang, X.; Li, J.; Qu, W.; Chen, G., Fabrication of graphene/poly (methyl methacrylate) composite electrode for capillary electrophoretic determination of bioactive constituents in Herba Geranii. *Journal of Chromatography A* **2011,** *1218* (32), 5542-5548.
83. Chua, C. K.; Ambrosi, A.; Pumera, M., Graphene based nanomaterials as electrochemical detectors in lab-on-a-chip devices. *Electrochem. Commun.* **2011,** *13* (5), 517-519.
84. Lucca, B. G.; de Lima, F.; Coltro, W. K.; Ferreira, V. S., Electrodeposition of reduced graphene oxide on a Pt electrode and its use as amperometric sensor in microchip electrophoresis. *Electrophoresis* **2015,** *36* (16), 1886-1893.
85. Gunawardhana, S. M. Development of mirochip electrophoresis platforms coupled with electrochemical detection for continuous on-line monitoring of neurochemicals *in vivo* Dissertation University of Kansas, KU Scholarworks, **2019**.
86. Selimovic, A.; Martin, R. S., Encapsulated electrodes for microchip devices: microarrays and platinized electrodes for signal enhancement. *Electrophoresis* **2013,** *34* (14), 2092-2100.
87. Siegel, J. M.; Schilly, K. M.; Wijesinghe, M. B.; Caruso, G.; Fresta, C. G.; Lunte, S. M., Optimization of a microchip electrophoresis method with electrochemical detection for the determination of nitrite in macrophage cells as an indicator of nitric oxide production. *Analytical methods* **2019,** *11* (2), 148-156.
88. Li, Y.; Sella, C.; Lemaitre, F.; Guille-Collignon, M.; Thouin, L.; Amatore, C., Electrochemical Detection of Nitric Oxide and Peroxynitrite Anion in Microchannels at Highly Sensitive Platinum-Black Coated Electrodes. Application to ROS and RNS Mixtures prior to Biological Investigations. *Electrochim. Acta* **2014,** *144*, 111-118.
89. Li, Y.; Sella, C.; Lemaître, F.; Guille Collignon, M.; Thouin, L.; Amatore, C., Highly Sensitive Platinum-Black Coated Platinum Electrodes for Electrochemical Detection of Hydrogen Peroxide and Nitrite in Microchannel. *Electroanalysis* **2013,** *25* (4), 895-902.
90. Shim, J. H.; Lee, Y., Amperometric nitric oxide microsensor based on nanopore-platinized platinum: the application for imaging NO concentrations. *Anal. Chem.* **2009,** *81* (20), 8571-8576.
91. Lee, Y.; Oh, B. K.; Meyerhoff, M. E., Improved planar amperometric nitric oxide sensor based on platinized platinum anode. 1. Experimental results and theory when applied for monitoring NO release from diazeniumdiolate-doped polymeric films. *Anal. Chem.* **2004,** *76* (3), 536-544.
92. Lee, Y.; Yang, J.; Rudich, S. M.; Schreiner, R. J.; Meyerhoff, M. E., Improved planar amperometric nitric oxide sensor based on platinized platinum anode. 2. Direct real-time measurement of NO generated from porcine kidney slices in the presence of L-arginine, L-arginine polymers, and protamine. *Anal. Chem.* **2004,** *76* (3), 545-551.
93. Kicela, A.; Daniele, S., Platinum black coated microdisk electrodes for the determination of high concentrations of hydrogen peroxide in phosphate buffer solutions. *Talanta* **2006,** *68* (5), 1632-1639.
94. García-Carmona, L.; Martín, A.; Sierra, T.; González, M. C.; Escarpa, A., Electrochemical detectors based on carbon and metallic nanostructures in capillary and microchip electrophoresis. *Electrophoresis* **2017,** *38* (1), 80-94.
95. Sierra, T.; Crevillen, A. G.; Escarpa, A., Electrochemical detection based on nanomaterials in CE and microfluidic systems. *Electrophoresis* **2019,** *40* (1), 113-123.
96. Gunawardhana, S. M. Development of microchip electrophoresis platforms coupled with electrochemical detection for continuous on-line monitoring of neurochemicals *in vivo*. Dissertation, University of Kansas, KU ScholarWorks, **2019**.
97. Woolley, A. T.; Lao, K.; Glazer, A. N.; Mathies, R. A., Capillary electrophoresis chips with integrated electrochemical detection. *Anal. Chem.* **1998,** *70* (4), 684-688.

98. Gunasekara, D. B.; Hulvey, M. K.; Lunte, S. M., In-channel amperometric detection for microchip electrophoresis using a wireless isolated potentiostat. *Electrophoresis* **2011,** *32* (8), 832-837.
99. Lacher, N. A.; Lunte, S. M.; Martin, R. S., Development of a microfabricated palladium decoupler/electrochemical detector for microchip capillary electrophoresis using a hybrid glass/poly (dimethylsiloxane) device. *Anal. Chem.* **2004,** *76* (9), 2482-2491.
100. Bowen, A. L.; Scott Martin, R., Integration of serpentine channels for microchip electrophoresis with a palladium decoupler and electrochemical detection. *Electrophoresis* **2009,** *30* (19), 3347-3354.
101. Wu, C.-C.; Wu, R.-G.; Huang, J.-G.; Lin, Y.-C.; Chang, H.-C., Three-electrode electrochemical detector and platinum film decoupler integrated with a capillary electrophoresis microchip for amperometric detection. *Anal. Chem.* **2003,** *75* (4), 947-952.
102. Osbourn, D. M.; Lunte, C. E., On-column electrochemical detection for microchip capillary electrophoresis. *Anal. Chem.* **2003,** *75* (11), 2710-2714.
103. Keynton, R.; Roussel Jr, T.; Crain, M.; Jackson, D.; Franco, D.; Naber, J.; Walsh, K.; Baldwin, R., Design and development of microfabricated capillary electrophoresis devices with electrochemical detection. *Anal. Chim. Acta* **2004,** *507* (1), 95-105.
104. Ordeig, O.; Godino, N.; del Campo, J.; Muñoz, F. X.; Nikolajeff, F.; Nyholm, L., On-chip electric field driven electrochemical detection using a poly (dimethylsiloxane) microchannel with gold microband electrodes. *Anal. Chem.* **2008,** *80* (10), 3622-3632.
105. Holcomb, R. E.; Kraly, J. R.; Henry, C. S., Electrode array detector for microchip capillary electrophoresis. *Analyst* **2009,** *134* (3), 486-492.
106. Mecker, L. C.; Filla, L. A.; Martin, R. S., Use of a Carbon-Ink Microelectrode Array for Signal Enhancement in Microchip Electrophoresis with Electrochemical Detection. *Electroanalysis* **2010,** *22* (19), 2141-2146.
107. Gawron, A. J.; Martin, R. S.; Lunte, S. M., Fabrication and evaluation of a carbon-based dual-electrode detector for poly (dimethylsiloxane) electrophoresis chips. *Electrophoresis* **2001,** *22* (2), 242-248.
108. Zhong, M.; Lunte, S. M., Tubular-wire dual electrode for detection of thiols and disulfides by capillary electrophoresis/electrochemistry. *Anal. Chem.* **1999,** *71* (1), 251-255.
109. Lin, B. L.; Colon, L. A.; Zare, R. N., Dual electrochemical detection of cysteine and cystine in capillary zone electrophoresis. *Journal of Chromatography A* **1994,** *680* (1), 263-270.
110. Martin, R. S.; Gawron, A. J.; Lunte, S. M.; Henry, C. S., Dual-electrode electrochemical detection for poly (dimethylsiloxane)-fabricated capillary electrophoresis microchips. *Anal. Chem.* **2000,** *72* (14), 3196-3202.
111. Mecker, L. C.; Martin, R. S., Use of micromolded carbon dual electrodes with a palladium decoupler for amperometric detection in microchip electrophoresis. *Electrophoresis* **2006,** *27* (24), 5032-5042.
112. Fischer, D. J.; Vandaveer IV, W. R.; Grigsby, R. J.; Lunte, S. M., Pyrolyzed Photoresist Carbon Electrodes for Microchip Electrophoresis with Dual-Electrode Amperometric Detection. *Electroanalysis: An International Journal Devoted to Fundamental and Practical Aspects of Electroanalysis* **2005,** *17* (13), 1153-1159.
113. Gunasekara, D. B.; Wijesinghe, M. B.; Pichetsurnthorn, P.; Lunte, S. M., Evaluation of Dual Electrode Configurations for Microchip Electrophoresis Used for Voltammetric Characterization of Electroactive Species. *Analyst* **2020**, *145* (865-872).

114. Saylor, R. A. Development of a Separation-Based Sensor using Microdialysis Coupled to Microchip Electrophoresis with Electrochemical Detection for Monitoring Catecholamines. Dissertation, University of Kansas, KU ScholarWorks, **2015**.
115. Chen, C.; Hahn, J. H., Dual-channel method for interference-free in-channel amperometric detection in microchip capillary electrophoresis. *Anal. Chem.* **2007,** *79* (18), 7182-7186.
116. Zhu, G.; Song, Q.; Liu, W.; Yan, X.; Xiao, J.; Chen, C., A gold nanoparticle-modified indium tin oxide microelectrode for in-channel amperometric detection in dual-channel microchip electrophoresis. *Analytical Methods* **2017,** *9* (29), 4319-4326.
117. Tan, Y.; Song, Q.; Liu, W.; Li, M.; Xiao, J.; Chen, C., Dual-channel Microchip Electrophoresis with Amperometric Detection System for Rapid Analysis of Cefoperazone and Sulbactam. *Anal. Sci.* **2019**, 19P088.
118. Meneses, D.; Gunasekara, D. B.; Pichetsurnthorn, P.; da Silva, J. A.; de Abreu, F. C.; Lunte, S. M., Evaluation of in-channel amperometric detection using a dual-channel microchip electrophoresis device and a two-electrode potentiostat for reverse polarity separations. *Electrophoresis* **2015,** *36* (3), 441-448.

Chapter 4

Improved detection of intracellular nitrite in macrophage cells

This chapter is reproduced by permission of The Royal Society of Chemistry.

Siegel, J.M., **Schilly, K.M.**, Wijesinghe, M.B., Caruso, G., Fresta, C.G., Lunte, S.M. "Optimization of a microchip electrophoresis method with electrochemical detection for the determination of nitrite in macrophage cells as an indicator of nitric oxide production," *Anal. Methods.* **2019**; 11: 148 – 156.

4 Chapter 4: Improved detection of intracellular nitrite in macrophage cells

4.1 Abstract

Nitric oxide (NO) is involved in many biological functions, including blood pressure regulation, the immune response, and neurotransmission. However, excess production of NO can lead to the generation of reactive nitrogen species and nitrosative stress and has been linked to several neurodegenerative diseases and cardiovascular disorders. Because NO is short-lived and generally difficult to detect, its primary stable degradation product, nitrite, is frequently monitored in its place. In this paper, an improved method using microchip electrophoresis with electrochemical detection (ME-EC) was developed for the separation and detection of nitrite in cell lysates. A separation of nitrite from several electroactive cell constituents and interferences was optimized, and the effect of sample and buffer conductivity on peak efficiency was explored. It was found that the addition of 10 mM NaCl to the run buffer caused stacking of the nitrite peak and improved limits of detection. A platinum black working electrode was also evaluated for the detection of nitrite and other electroactive cellular species after electrophoretic separation. The use of a modified platinum working electrode resulted in 2.5-, 1.7-, and 7.2-fold signal enhancement for nitrite, ascorbic acid, and hydrogen peroxide, respectively, and increased the sensitivity of the method for nitrite 2-fold. The optimized ME-EC method was used to compare nitrite production by native and lipopolysaccharide-stimulated RAW 264.7 macrophage cells.

4.2 Introduction

Nitric oxide (NO) is an important molecule involved in cellular signaling and platelet regulation. It is generated *in vivo* from arginine via the enzyme nitric oxide synthase (NOS).[1] A specific form of NOS, inducible nitric oxide synthase (iNOS), is activated to produce nitric oxide as part of the immune response.[1, 2] The resulting NO is capable of reacting with cellular components and can disrupt biological function.[3] Under conditions of inflammation, NO can also

react with superoxide to form peroxynitrite.[1, 2] Peroxynitrite can then cause nitration of proteins, peroxidation of lipids, and cleavage of the phosphate backbone of DNA.[2-4] These biomolecular modifications have been implicated in the pathology of several neurodegenerative and cardiovascular diseases.[2, 5] It is therefore important to have robust analytical methods that are capable of monitoring reactive nitrogen and oxygen species (RNOS) in biological systems.

Currently, several methods exist to detect NO, including fluorescence, chemiluminescence, electron paramagnetic resonance spectroscopy, amperometry, and voltammetry.[6-18] Fluorescence detection of RNOS in cells requires the use of a derivatization reagent that can enter cells and generate a product that is highly specific for the analyte of interest, as well as being stable and nontoxic to the biological system.[6, 10, 19] Diaminofluorescein (DAF) dyes have been commonly used to monitor NO production in cells.[20-22] However, DAF-FM has been shown to react with dehydroascorbic acid (DHA) and ascorbic acid, producing side products that must be resolved from the product of interest.[19, 20, 23] While some approaches for correcting these issues have been developed, it is still of interest to explore other more direct detection methods for RNOS that do not require derivatization.

Electrochemical detection has been used for the direct detection of nitric oxide.[10, 24] In most cases, the working electrode is modified for the specific detection of NO at the expense of the simultaneous detection of other analytes.[14, 25-27] In addition, the very short half-life of NO *in vivo* (approximately 1 s) makes it impossible to detect in cell samples, tissue homogenates, and microdialysate samples because it is degraded prior to analysis. Therefore, its stable primary degradation product, nitrite, is often used as an indicator of nitric oxide production.[7, 11]

A microchip electrophoresis (ME) method for the separation of nitrosative stress markers in macrophage cells was recently described by our group.[28] While ME systems are more complicated to assemble and operate than capillary electrophoresis (CE) instruments, ME has the advantage of

being well-suited for further adaptation into a single cell analysis device capable of cell lysis and separation and detection of intercellular components on-chip.[20] In these studies, amperometric detection (EC) was used as the detection method for nitrosative stress markers as they are electrochemically active. In addition, PDMS/glass hybrid chips were employed because they enable easier incorporation and alignment of the working electrode compared to all-glass devices.[29, 30] EC typically suffers from lower sensitivity and higher limits of detection (LOD) than laser-induced fluorescence (LIF)-based detection for ME. While the previously developed ME-EC method was capable of detecting nitrite in the bulk cell lysates of macrophage cells, it was not sensitive enough to detect the small changes in RNOS expected in a microchip single cell analysis system.

Platinum (Pt) black electrodes have been extensively employed for the improved detection of NO. Platinization, or Pt black deposition, on a variety of electrode materials, including gold, carbon, and Pt, has been shown to improve electron transfer kinetics as well as increase the active surface area of the electrode.[31] Enhanced signals for NO and related compounds, including nitrite, peroxynitrite, and hydrogen peroxide, have been reported.[25, 26, 31-37] These Pt black-modified electrodes have been used for a variety of applications, including imaging of NO generated on microdisks by scanning electrochemical microscopy,[38] microarrays for the detection of NO released from endothelial cells,[26] amperometric sensors to measure NO generation from kidney slices,[39, 40] 3D printed microfluidic devices for the detection NO solutions,[25] and the detection of RNOS released by single cells.[9] Platinized carbon electrodes have also been inserted through the cell membrane[35, 41] and incorporated into biosensors for pond snail homogenates[33] to monitor RNOS production.

While many groups have employed platinized electrodes to obtain better sensitivity for a particular analyte, only a few have extended this to the simultaneous measurement of multiple

analytes. Most sensors employing Pt black are designed specifically for NO detection and employ selective membranes such as Nafion to exclude nitrite and other electroactive anions.[25, 26] Alternatively, sensors that have been used for the determination of multiple analytes are based on using voltammetry to distinguish between species.[33, 39, 41-44] This requires precise knowledge of the electrochemical behavior of all possible interfering species under the given conditions in order to quantify the analyte of interest.

There are few reports of integrating a Pt black electrode with capillary or microchip electrophoresis. One group has incorporated Pt black into a glucose-selective biosensor as a detector for CE.[45] In a separate report, a platinized decoupler and reference electrodes were used in a ME device.[46] However, to our knowledge, there have been no attempts to integrate a Pt black working electrode with microchip electrophoresis for the separation and detection of multiple RNOS. In this work, microchip electrophoresis with electrochemical detection using a Pt black-modified working electrode is evaluated for the detection of nitrite, a marker of NO production, and hydrogen peroxide, a marker of superoxide. Ascorbic acid (AA) and azide were also included as potential interfering species within the biological system. In addition, the effect of sample conductivity on the separation efficiency and overall limits of detection was investigated. The optimized method was then evaluated for the detection of nitrite in native and lipopolysaccharide (LPS)-stimulated RAW 264.7 macrophage cells.

4.3 Materials and methods

4.3.1 Reagents and materials

The following materials and chemicals were used as received: boric acid, sodium chloride, tetradecyltrimethylammonium chloride (TTAC), sodium nitrite, ascorbic acid, lipopolysaccharide (LPS), lead(II) acetate trihydrate, and hydrogen hexachloroplatinate(IV) solution (Sigma-Aldrich, St. Louis, MO, USA); sodium hydroxide (NaOH), acetone, 2-propanol (IPA), phosphate-buffered

saline (PBS), 30% hydrogen peroxide (H2O2), and ethanol (Fisher Scientific, Pittsburgh, PA, USA); SU-8 photoresist, SU-8 developer, and MIF 300 developer (Micro-Chem, Newton, MA, USA); glass substrates (4″ × 4″ × 0.090″) coated with chrome and AZ1518 photoresist (Nanofilm, Westlake, CA, USA); buffered oxide etchant (JT Baker, Austin, TX, USA); chrome etchant (Cyantek Corp., Freemont, CA, USA); Ti and Pt targets (Kurt J. Lesker Co., Jefferson Hills, PA, USA); polydimethylsiloxane (PDMS) and curing agent (Sylgard 184 elastomer kit, Ellsworth Adhesives, Germantown, WI, USA); 4″ diameter silicon wafers (Silicon, Inc., Boise, ID, USA); epoxy and Cu wire (Westlake Hardware, Lawrence, KS, USA); silver colloidal (Ted Pella, Inc., Redding, CA, USA); RAW 264.7 cells, Delbecco's Modified Eagle's medium (DMEM), fetal bovine serum (FBS), penicillin-streptomycin solution (ATCC, Manassas, VA, USA), 25 mL polystyrene culture flasks (Fisher Scientific, Pittsburgh, PA, USA), C-Chip disposable hemocytometers (Bulldog Bio, Inc., Portsmouth, NH, USA), trypan blue exclusion assay (Fisher Scientific, Pittsburgh, PA, USA), 3 kDa molecular weight cut-off filters (VWR International, West Chester, PA, USA). All water was ultrapure (18.2 MΩ) and generated from a Milli-Q Synthesis A10 system (Millipore, Burlington, MA, USA).

4.3.2 PDMS microchip fabrication

The fabrication of PDMS microchips has been previously described.[47] Briefly, a 4″ diameter silicon wafer was coated with SU-8 10 negative photoresist to a thickness of 15 μm with a Cee 100 spincoater (Brewer Science Inc., Rolla, MO, USA). The wafer then underwent a soft bake at 65 °C for 2 min and then 95 °C for 5 min on a programmable hotplate (Thermo Scientific, Waltham, MA, USA). The designs for the microchip were drawn with AutoCad (Autodesk, San Rafael, CA, USA) and printed onto a transparency (Infinite Graphics, Minneapolis, MN, USA). The coated wafer was then covered with the negative transparency and exposed at 344 mJ cm^{-2} with a UV flood source (ABC Inc., San Jose, CA, USA). Next, the wafer was transferred to a

programmable hotplate again for a postbake at 65 °C for 1 min and then 95 °C for 2 min. After the postbake, the wafer was developed in SU-8 developer, rinsed with IPA, and dried with nitrogen. Lastly, the wafer underwent a hard bake at 200 °C for 2 h. The final silicon master contained 15 μm thick and 40 μm wide microchannels, which were measured with an Alpha Step-200 surface profiler (KLA-Tencor Instruments, Milpitas, CA, USA). The microchip used for these studies consisted of a simple-T design with a 5 cm separation channel and 0.75 cm side arms. A PDMS microchip was made by pouring a degassed 10:1 mixture of PDMS and curing agent, respectively, over the silicon master and curing the mixture overnight at 70 °C. The PDMS microchip was then peeled from the master and reservoirs were punched into the PDMS with a 4 mm biopsy punch (Harris Uni-Core, Ted Pella, Inc., Redding, CA, USA).

4.3.3 Electrode fabrication

The method of fabricating in-house Pt electrodes has been previously described.29 Briefly, electrode designs are drawn with AutoCad and printed onto a transparency with a resolution of 50,000 dpi. A borofloat glass substrate (4″ × 4″ × 0.090″) pre-coated with a layer of chrome and then AZ1518 positive photoresist is covered by the transparency and exposed at 344 mJ cm^{-2} with a UV flood source for 4 s. Then the glass substrate is developed in MIF 300 developer for about 15 s and baked at 100 °C for 10 min on a programmable hotplate. At this point, the electrode pattern is imprinted in the photoresist, thereby exposing the chrome layer below. The exposed chrome is removed with chrome etchant. Trenches in the pattern of the electrodes are then created with the use of buffered oxide etchant to a depth of about 300 nm. After thoroughly washing the substrate with CaCO3 solution and water, the trench depth is measured with an Alpha Step-200 surface profiler. Next, the glass substrate is exposed to an oxygen plasma for 1 min (March Plasmod, Concord, CA, USA) and immediately placed into an AXXIS DC magnetron sputtering system (Kurt J. Lesker Co., Jefferson Hills, PA, USA). After allowing the sputterer chamber to

reach a pressure of 1.0×10^{-6} Torr, Ti is deposited onto the substrate for 40 s at 220 V and 5.0×10^{-3} Torr to produce a 20 nm Ti layer. Then Pt is deposited for 15 min at 200 V and 5.0×10^{-3} Torr. Next, the substrate is washed with acetone and then chrome etchant. The final width and height of the fabricated Pt electrodes are measured with an Alpha Step-200 surface profiler.

4.3.4 Electrophoresis procedure

Microchips were constructed by reversibly bonding a layer of PDMS containing the simple-T design to the glass substrate containing the embedded Pt electrode. The Pt electrode was aligned at the intersection of the separation channel and the waste reservoir. Pt leads were inserted into each reservoir. Two Spellman CZE 1000R high voltage power supplies (Spellman, Hauppauge, NY, USA) controlled with a LabView (National Instruments, Austin, TX, USA) program written in-house were used for all electrophoresis procedures. Samples were injected using a gated injection protocol. A gate was established by applying −2400 V and −2200 V to the buffer and sample reservoirs, respectively, while both the buffer waste and sample waste reservoirs were grounded. Sample injection occurred by floating the voltage in the buffer reservoir for 1 s. The run buffer used in these experiments was 10 mM borate with TTAC and NaCl. TTAC was varied between 3 mM and 9 mM, and NaCl was varied between 0 mM and 15 mM. The pH was adjusted to 10 with NaOH.

4.3.5 Electrochemical detection and data analysis

Electrochemical detection was accomplished with a two-channel wireless isolated potentiostat (Pinnacle Technology, Inc., Lawrence, KS, USA). The potentiostat used had a sampling rate of 6.5 to 13 Hz (gain = 5,000,000 V A^{-1}, resolution = 47 fA). Sirenia software (Pinnacle Technology) was used for all data acquisition. Electrochemical measurements were taken at a working electrode potential of +1.100 V versus Ag/AgCl reference electrode (BASi,

West Layfayette, IN, USA). All data analysis was performed with Origin 8.6 software (OriginLab, Northhampton, MA, USA).

4.3.6 Pt black deposition

A 10 mM lead(II) acetate trihydrate stock solution was prepared. The Pt black deposition solution was then prepared by adding 1 mL of 8% w/v hydrogen hexachloroplatinate solution and 0.42 mL of 10 mM lead(II) acetate trihydrate stock solution to 5.94 mL of PBS. Pt black deposition was achieved by running a cyclic voltammogram on the Pt working electrode in the presence of the deposition solution, from +0.6 V to −0.35 V versus Ag/AgCl reference at a scan rate of 0.02 V s^{-1}. The potential was controlled using a CHI electrochemical analyzer (CH Instruments, Inc., Austin, TX, USA) controlled by CHI software. After deposition, the area around the electrode was thoroughly washed with water to remove salt crystals formed during the deposition. Next, the modified electrode area was activated while in 10 mM borate at pH 10 by applying alternating pulses of +0.2 V and −0.5 V for 1 s each for 30 cycles.

4.3.7 Cell culture and sample preparation

RAW 264.7 cells were cultured, stimulated, and tested for viability as previously reported.[28] Briefly, cells were cultured in DMEM containing 10% (v/v) FBS, L-glutamine (2 mM), penicillin (50 IU mL^{-1}), and streptomycin (50 μg mL^{-1}). Cells were maintained in 25 mL polystyrene culture flasks in a humidified environment at 37 °C and 5% CO2. To prevent overgrowth, cells were passaged every 2–3 days. Cell viability was determined via the trypan blue exclusion assay and a C-Chip disposable hemocytometer. When stimulation of NO production was desired, a flask of healthy macrophage cells was incubated for 24 h with 100 ng mL^{-1} purified LPS from the Escherichia coli line 0111:B4 (Figure 4.1). For such experiments, a control (native) flask of unstimulated RAW 264.7 macrophage cells from the population was incubated under the same conditions.

To prepare the cell lysate samples, cells grown to approximately 80% confluence (around 5 million cells per flask) were counted, harvested with a scraper, and then centrifuged at 3500 rpm for 3 min. The supernatant medium was removed, leaving behind a cell pellet. This pellet was washed once with cold 10 mM PBS and once with sterile water. The cell pellet was then lysed in 150 μL of buffer consisting of 10 mM borate at pH 10 and 5.5 mM TTAC. After lysis, the lysate was centrifuged through a 3 kDa molecular weight cut-off filter for 8 min to remove large compounds, such as membranes and proteins. The filtered lysate was run on the ME-EC device for analysis.

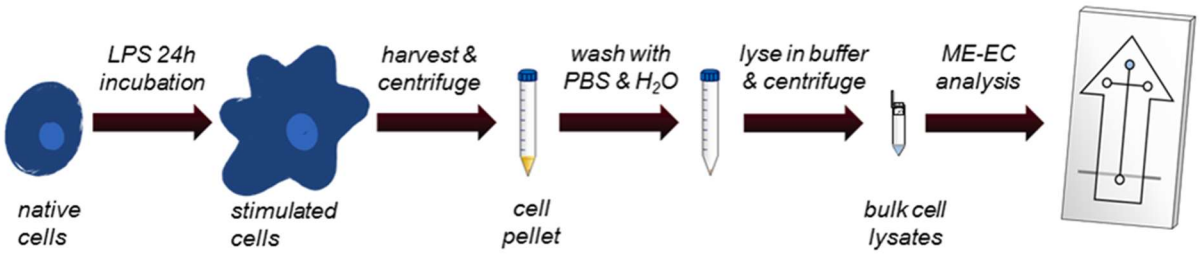

Figure 4.1. Protocol for the analysis of LPS-stimulated macrophage cells. (A) Native cells are incubated with LPS for 24 h to induce stimulation. (B) Cells are harvested and centrifuged to produce a cell pellet. (C) The cell pellet is washed once with PBS to remove excess medium and once with water to remove any remaining salt. (D) The cell pellet is resuspended in borate buffer at pH 10 with 5.5 mM TTAC to lyse the cells, and the lysate is centrifuged through a molecular weight cutoff filter to remove any proteins and large insoluble species. (E) Filtered cell lysate is placed in the sample well of a PDMS/glass microchip for ME-EC analysis.

4.4 Results and discussion

Several strategies were investigated to improve the limits of detection for nitrite in cell lysate samples. A separation was first optimized to resolve nitrite and several other electroactive species in cells. Then, the effect of sample conductivity on the separation efficiency was evaluated. A Pt black-modified working electrode was then employed with the goal of detecting nitrite in macrophage cell lysates.

4.4.1 Separation optimization and stacking of nitrite

For the analysis of cell lysate samples by ME-EC, the initial experiments employed a background electrolyte consisting of 10 mM borate with 2 mM TTAC at pH 10. However, when cell lysate samples were analyzed, it was found that nitrite comigrated with an interferent peak (azide) that was present on the filters used for sample preparation. In an attempt to resolve these two compounds, the concentration of TTAC in the BGE was varied from 2 mM to 9 mM. As shown in Figure 4.2, the optimal TTAC concentration was determined to be 5.5 mM. These separation conditions were also capable of separating two other analytes of interest to the redox balance of the cell: ascorbic acid, an antioxidant, and hydrogen peroxide, a reactive oxygen species and product of superoxide. These four species were baseline resolved in less than 30 s (Figure 4.2).

Our group has previously reported severe destacking of the nitrite peak during the analysis of cell lysate samples due to the high conductivity of the sample matrix. In those studies, cells were washed with PBS, which contains a high amount of NaCl (154 mM), prior to the final lysing with the run buffer. In this previous report, it was found that the addition of 7.5 or 10 mM NaCl to the BGE restored the peak height to that observed for low conductivity standard samples.[28] However, this phenomenon was not optimized or explored further. Figure 4.3 shows the effects of both sample and buffer conductivities on the separation efficiency of the nitrite peak. An

electropherogram (Figure 4.3a) was obtained using standards dissolved in run buffer. If the sample contains 10 mM NaCl and is analyzed using a low conductivity buffer, the peak efficiency for nitrite decreases 6-fold compared to that of a low conductivity sample as can be seen in (Figure 4.3b). This loss in efficiency can be restored by adding 10 mM NaCl to the BGE, which matches the conductivity of the sample as shown in electropherogram (Figure 4.3c). Most importantly, it was found that if the conductivity of the BGE is significantly increased relative to the sample (such that there is 10 mM NaCl in the run buffer and no NaCl in the sample), a nearly 10-fold increase in peak efficiency is observed (Figure 4.3d). This last set of parameters results in a greatly enhanced nitrite peak due to transient isotachophoretic stacking without affecting the peak heights or resolution of the other analytes. In order to ensure low conductivity cell samples, the sample preparation protocol was modified to include a second wash of the cell pellet with water to remove excess saline prior to lysis with run buffer.

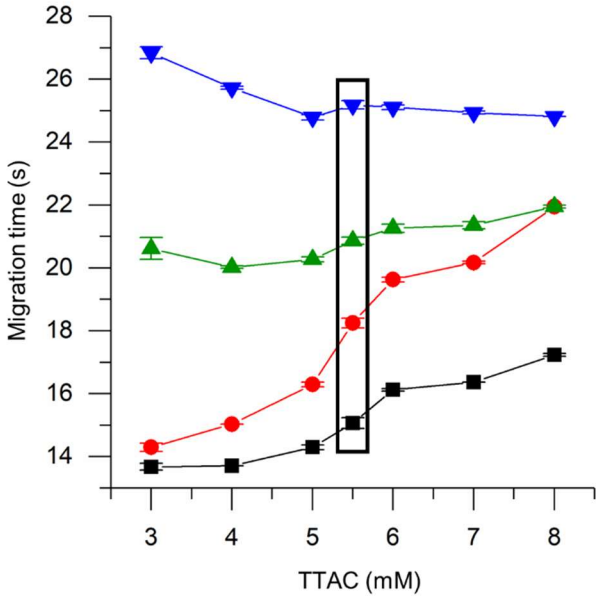

Figure 4.2. Migration times of nitrite (■), azide (●), ascorbic acid (▲), and hydrogen peroxide (▼) by ME-EC with a BGE consisting of 10 mM borate at pH 10 with varying concentration of TTAC.

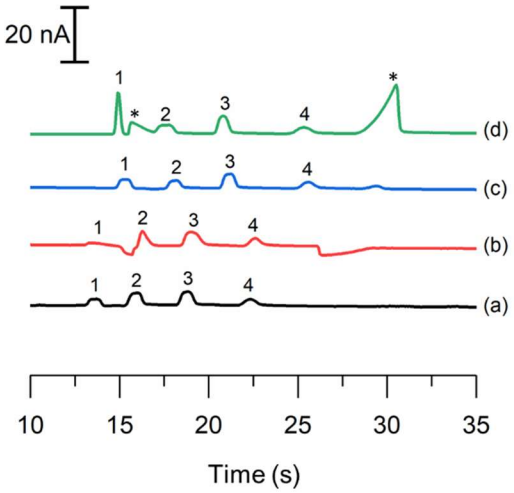

Figure 4.3. Electropherograms illustrating a standard solution of 50 µM nitrite (1), 20 µM azide (2), 40 µM ascorbic acid (3), and 100 µM hydrogen peroxide (4) using (a) a run buffer and sample buffer consisting of 10 mM borate and 5.5 mM TTAC at pH 10, and the effect of adding 10 mM NaCl (b) to the sample buffer, (c) to both the run buffer and sample buffer, and (d) to only the run buffer. System peaks are denoted by *.

It is hypothesized that the increase in peak height and plate numbers for nitrite is due to transient isotachophoresis (tITP) occurring prior to the separation. In tITP, the zone of the analyte of interest is stacked between a leading and a tailing electrolyte that have faster and slower electrophoretic mobilities, respectively, than the analyte of interest. In this system, the leading electrolyte would be the chloride ion because its electrophoretic mobility is slightly higher than that of nitrite under these separation conditions.[48] Chloride ions have been shown to be responsible for stacking effects observed in capillary electrophoresis analysis of biological samples.[49] It is postulated that the borate ion is the tailing electrolyte under these conditions. Additional evidence of this phenomenon is that the concentration of NaCl must be in excess compared to the nitrite sample concentration in order for stacking to occur.[50] Figure 4.4A shows the effect of increasing NaCl concentration in the run buffer on the height of the nitrite peak. As the concentration of NaCl is increased from 2.5 mM to 15 mM, the nitrite peak height increases. This stacking is also reflected in the significant increase in peak efficiency for nitrite compared to those of all other analytes, which remained constant as can be seen in Figure 4.4B. While the addition of 15 mM NaCl also yielded higher peak heights and efficiencies compared to 10 mM NaCl, the higher salt concentration resulted in a greatly increased separation current and generated larger system peaks due to the increased buffer conductivity. Also, when the separation current rises above 40 μA, bubbles can form within the PDMS channel and limit the lifetime of the device, negatively impacting the analysis. Therefore, a concentration of 10 mM NaCl was chosen for this study as it provided greatly improved peak efficiency while minimizing the negative effects of a highly conductive buffer. Using the combination of tITP and a bare Pt electrode, the LOD for nitrite was reduced to 0.50 μM from a value of 2.6 μM that was previously reported by our group.[51]

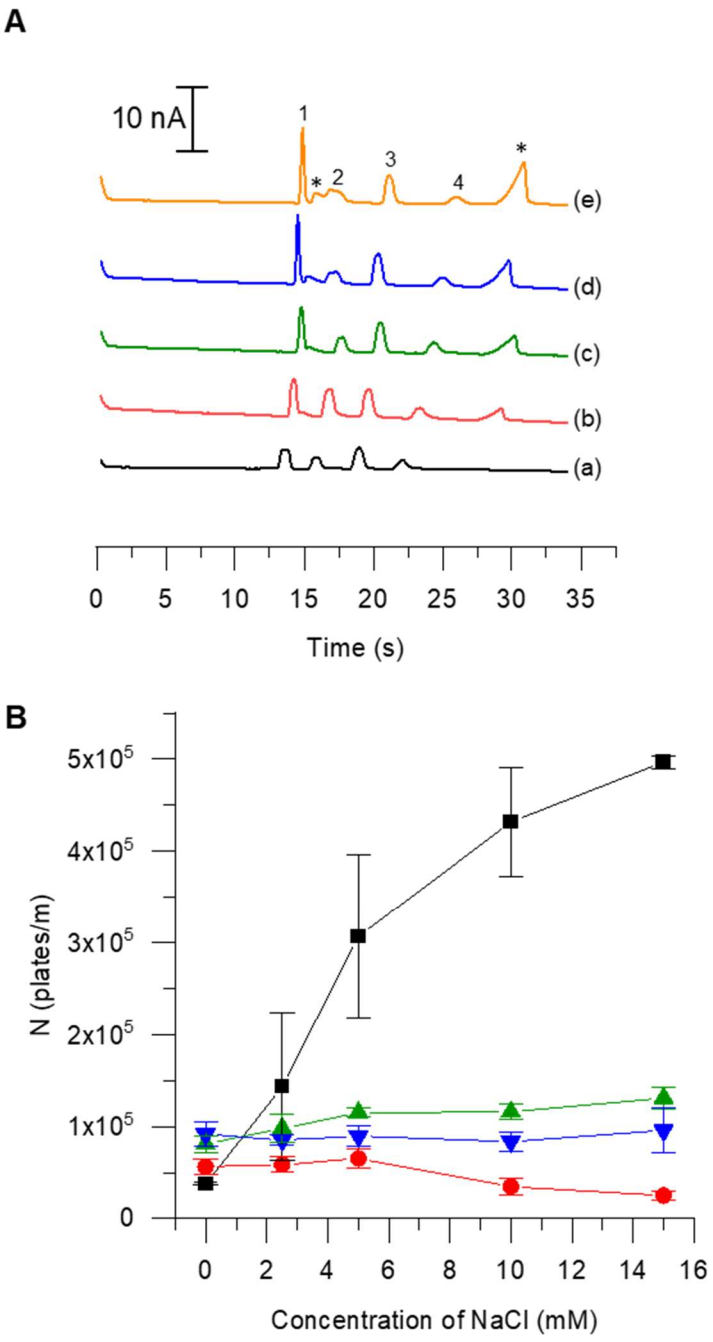

Figure 4.4. (A) Electropherograms depicting the change in nitrite stacking due to transient isotachophoresis as a result of adding NaCl to the run buffer at a concentration of (a) 0 mM, (b) 2.5 mM, (c) 5 mM, (d) 10 mM, and (e) 15 mM. (B) Effect of increasing NaCl concentration on peak efficiency (N) of each analyte (n = 3). Legend: nitrite (1, ■), azide (2, ●), ascorbic acid (3, ▲), hydrogen peroxide (4, ▼). System peaks are denoted by *.

4.4.2 Electrode deposition optimization

A Pt black working electrode was evaluated to see if it would further improve the limits of detection of the device for nitrite. Two different electrochemical deposition methods have been reported, application of a constant current density and cyclic voltammetry (CV). In both methods, the electrochemical program is applied while the electrode to be modified is in contact with a deposition solution consisting of chloroplatinic acid to generate the platinization and lead acetate to control the morphology of the deposition.

In the initial experiments, a 4 mm diameter PDMS well was aligned on top of the glass substrate such that the bare Pt electrode bisected the well. The well was filled with deposition solution, and Pt black was generated on the 4 mm length exposed to the solution using CV. During these experiments, the electrode turned black, indicating that the modification was successful. However, this deposition process prevented subsequent sealing of the PDMS microchip to the glass substrate due to the height of the electrode that was produced. A typical electrode produced by sputtering is less than 200 nm in height, which is low enough that a reversible seal between the PDMS and the glass substrate can be achieved. However, this electrochemical deposition procedure resulted in an electrode with a height greater than 200 nm.

To overcome this problem and make it possible to seal the PDMS separation channel to the electrode containing the glass chip, in situ generation was evaluated. The layer of PDMS containing the separation channel microchip was first aligned with the Pt working electrode on the glass substrate. The two layers were then sealed together prior to the deposition process. Then the deposition solution was added to the bottom waste reservoir and pulled through the separation channel with an aspirator. Therefore, in this configuration, only the 40 μm wide electrode region within the channel was exposed to the solution. Solution flow was stopped during the CV deposition process to allow the deposition to occur directly over the electrode. This resulted in a

well-defined deposition area. It also prevented the deposition from occurring underneath the PDMS substrate and kept the seal intact. A black color was again observed on the working electrode. ME-EC experiments could immediately be performed with this device without removing the PDMS channel layer. As shown in the scanning electron micrograph in Figure 4.5A, this deposition procedure resulted in a greatly increased electrode surface area.

Unfortunately, it was found that depositing the Pt black onto the surface of the working electrode using only CV resulted in an unstable modification. When a voltage was applied to the separation channel, a large drop in the background current at the working electrode was observed, which implied that the Pt black was detaching from the working electrode. Therefore, a combination of CV and differential pulse voltammetry (DPV) was evaluated. DPV has been reported by others to increase the stability of the Pt black modification.[43] SEM images of activated and non-activated modified electrodes show a drastic difference in the physical properties of the two electrodes due to the activation procedure (Figure 4.5A and B).

The deposition process resulted in the formation of salt crystals in both the buffer waste reservoir and the separation channel, so the chip had to be washed with water after this process and inspected to ensure that no crystals were present. The presence of crystals can lead to irreproducible signal measurements due to irregular flows throughout the microchip channels.

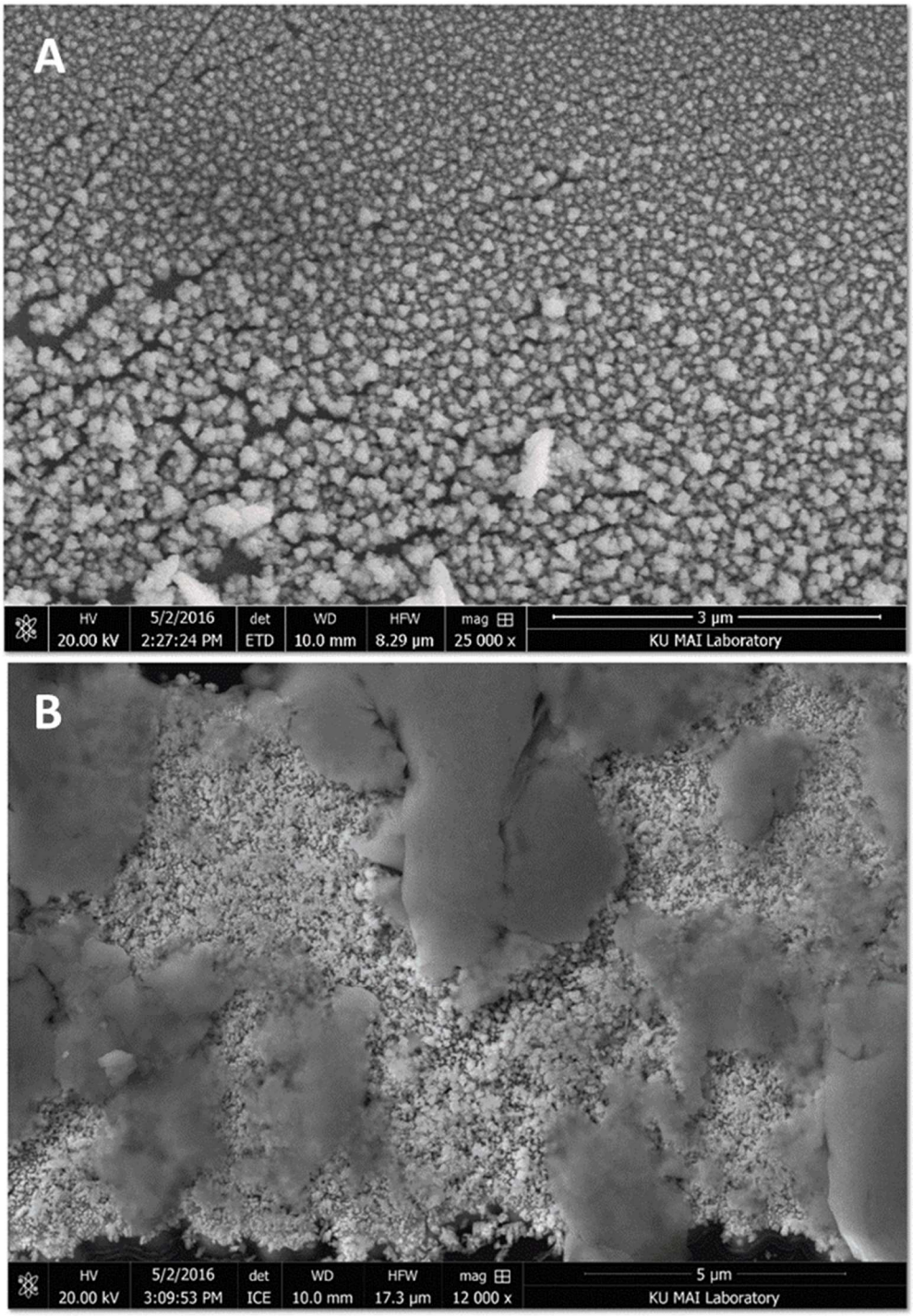

Figure 4.5. SEM images of a (A) non-activated and (B) activated Pt black-modified working electrode.

4.4.3 Signal enhancement

Once the electrode modification procedure was optimized, the response of the Pt black electrode was compared to that obtained by a bare Pt electrode. Peak heights for nitrite, AA, and hydrogen peroxide were measured before and after the deposition with the same microchip and electrode alignment. This was important because variations in electrode alignment can cause changes in the amplitude of both the noise and the signal. While using the same microchip for these enhancement measurements, the channels of the microchip were thoroughly washed with water to ensure that no run buffer remained in the channel during deposition. Figure 4.6A shows electropherograms of a mixture of nitrite, AA, and hydrogen peroxide standards before and after modification of a Pt working electrode using the optimized tITP separation conditions. The modified electrode generated a significant increase in signal, but also exhibited a higher background current. This increase in background current was expected since the geometric area of the electrode was increased. Average signal enhancements of 2.5 ± 0.2, 1.7 ± 0.2, and 7.2 ± 0.2 were observed for nitrite, AA, and hydrogen peroxide, respectively with the Pt black-modified electrode compared to a bare Pt electrode.

An external calibration curve was generated to determine the effect of the Pt black deposition and activation on the sensitivity for nitrite (Figure 4.7). The sensitivities for the detection of nitrite with a bare Pt and Pt black-modified working electrode were 0.245 ± 0.001 and 0.580 ± 0.008 nA μM^{-1}, respectively. The modification of the working electrode resulted in a 2.36 ± 0.03-fold enhancement in the sensitivity toward nitrite. These results are comparable with those reported by Shim *et al.*, where a 3-fold sensitivity enhancement for NO was observed when a Pt working electrode underwent platinization. This increase was believed to be due to the increase in the active surface area of the electrode.[38] Unfortunately, this increase in the geometric area of the electrode also resulted in an increase in noise (Figure 4.6B), leading to an unchanged S/N ratio

and, therefore, the LOD of the system did not change. Amatore's group has reported LOD for nitrite approximately 10-fold lower when using a Pt black electrode embedded in a microchannel with hydrodynamic flow. The differences in LODs of our work and these values can be attributed to both the presence of high voltage separation field and the difficulty of controlling the geometric area of the Pt black modification within the separation channel.

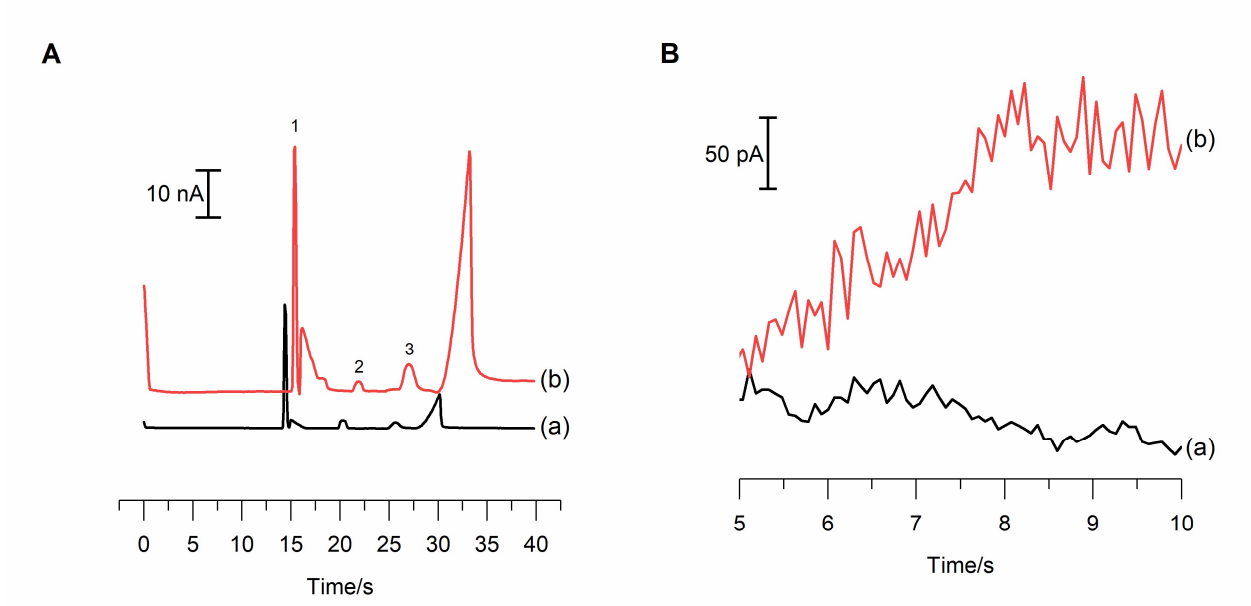

Figure 4.6. (A) Electropherograms of 100 µM nitrite (1), 40 µM AA (2), and 100 µM hydrogen peroxide (3) standards (a) before and (b) after Pt black modification. (B) Comparison of the noise at (a) a bare Pt electrode versus (b) a Pt black electrode during a ME separation.

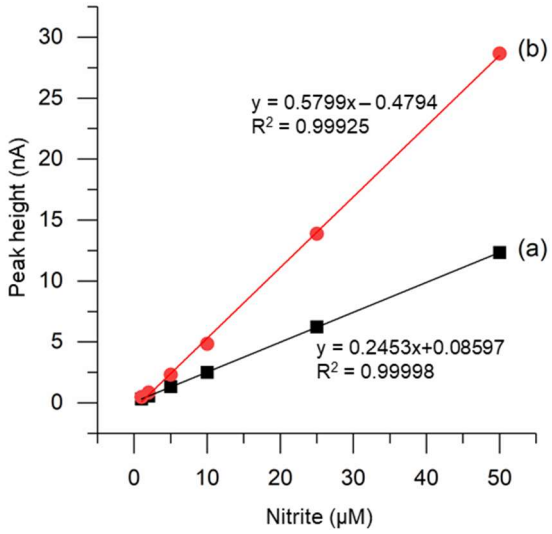

Figure 4.7. Calibration curves generated for nitrite using (a) bare Pt and (b) Pt black as the working electrode.

4.4.4 Nitrite in biological samples

Cell lysate samples with high conductivities have been shown to suppress the nitrite peak due to destacking effects.[28] Previously, our group has remedied this destacking effect by increasing the conductivity of the buffer to match that of the sample matrix. However, we observed that the nitrite peak efficiency could be greatly improved by using a buffer with a higher conductivity than the sample. Therefore, in the present study great care was taken to minimize the conductivity of the cell samples. The cell pellet was washed first with PBS, as previously reported, and then with water to eliminate the high salt content of the cell sample prior to lysing with run buffer. The addition of the water wash step in the cell preparation resulted in samples that had much lower conductivities (similar to normal standard solutions in run buffer). The lower conductivity cell lysates allowed stacking of the nitrite peak with the tITP system, which provided additional signal enhancement and peak consistency when compared to the previously published method.

It is well established that LPS-stimulated RAW 264.7 macrophages produce high amounts of NO.[52] LPS is an endotoxin found on the outer membrane of gram-negative bacteria that causes the activation of iNOS in macrophages and overproduction of NO. In this study, cells were stimulated with LPS to generate higher NO production and, therefore, an increased nitrite signal. The effect of the new separation conditions and signal enhancement obtained with the Pt black modified electrodes on the determination of intracellular nitrite was investigated in both native and LPS-stimulated bulk cell lysate samples. Figure 4.8 shows electropherograms obtained for a LPS-stimulated cell lysate sample with the same electrode and microchip before and after the working electrode had been modified with Pt black. The identity of the nitrite peak was confirmed through spiking. The electrode modification resulted in an average 4.31 ± 0.33-fold enhancement in the nitrite signal, which was averaged over both native and stimulated (n = 3 for both sets) cell lysates. Due to the differing number of cells in each sample, the results were corrected based on

their respective cell counts. When considered in combination with the tITP separation conditions facilitated by the improved washing procedure, this modification results in an increase between 10- and 20-fold in nitrite peak height in cell lysates. This improvement could prove useful in future studies to quantify nitrite electrochemically in single macrophage cells, where a significantly lower LOD may be necessary.

This increase in nitrite due to the presence of LPS was also calculated to ensure that the same result was achieved with both an unmodified and a modified working electrode. Upon stimulation, a 3.9 ± 0.9 times increase in nitrite was observed with the bare Pt working electrode and a 4.0 ± 0.6 times increase with the Pt black working electrode. A t-test was performed to compare these data, and it was determined that at 95% confidence there is no statistically significant difference between the two sets of data. This increase in nitrite production after exposure to LPS agrees with previous results reported by Gunasekara *et al.*[28] Therefore, it confirms that the Pt black modification does not impact the use of the method for monitoring changes in nitrite concentration with varying cell conditions. Furthermore, these results are comparable with measurements of nitric oxide in Jurkat cells taken using laser-induced fluorescence detection, in which the indirect NO probe DAF-FM was used to observe a 2-fold increase in NO upon LPS stimulation.[20] This suggests that electrochemical detection of nitrite is capable of providing results similar to those of indirect fluorescence detection of nitric oxide when studying cellular nitrosative stress.

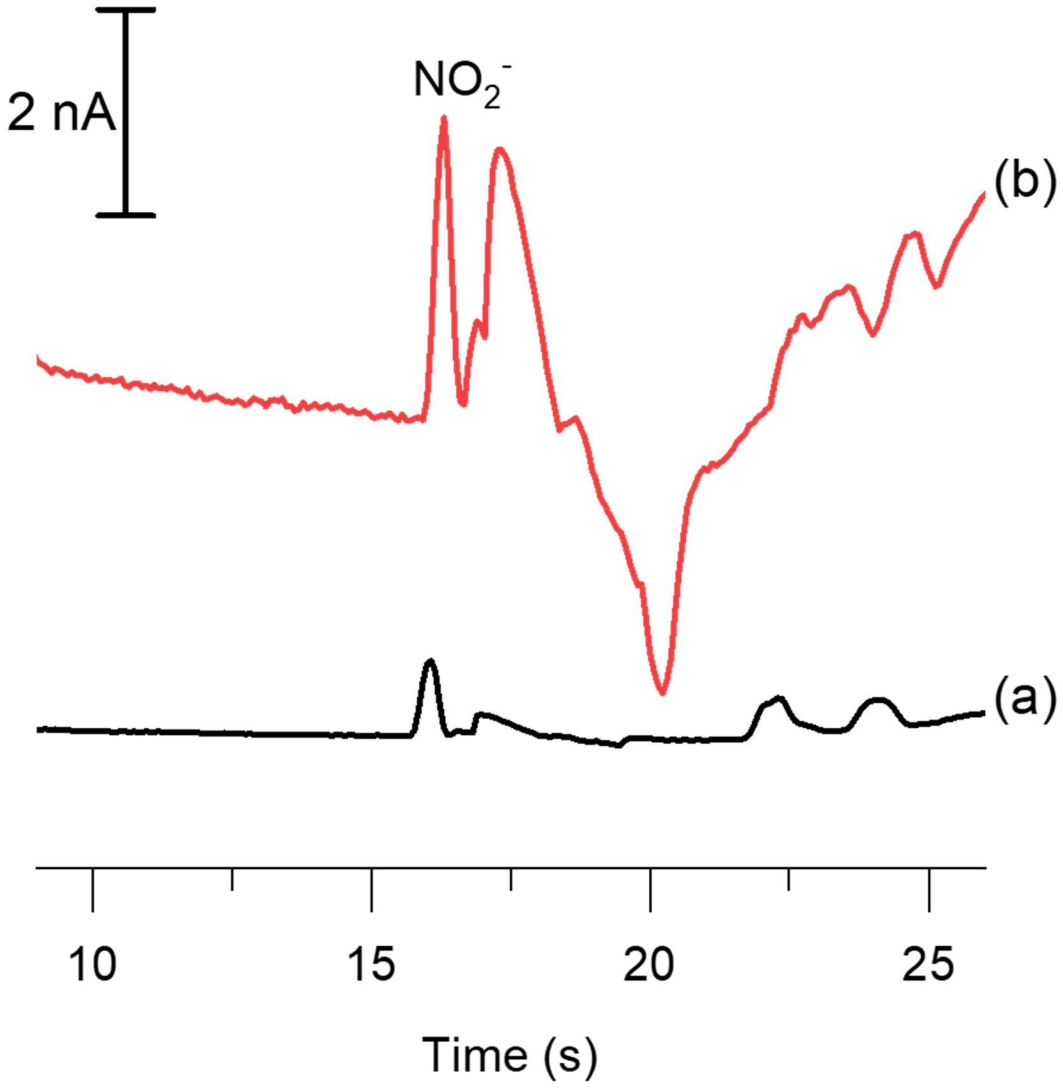

Figure 4.8. Electropherograms of an LPS-stimulated RAW 264.7 macrophage cell lysate sample obtained using (a) bare Pt and (b) Pt black.

4.5 Conclusions

A ME-EC method that uses transient isotachophoresis and a Pt black-modified working electrode to enhance the signal and detect nitrite as well as other electrochemically active species was reported. First, a stacking method to enhance the signal of nitrite through the addition of NaCl to the run buffer was developed that provided a 5.2-fold decrease in the LOD for nitrite. Then, a procedure to modify a Pt working electrode with Pt black for the detection of nitrite was optimized. This electrode modification was then coupled with a ME-EC method, and a signal enhancement for nitrite, hydrogen peroxide, and ascorbic acid was obtained. The use of a Pt black-modified working electrode resulted in an increased sensitivity for nitrite. This method was then used to detect nitrite as an indicator of NO production in a bulk cell lysate sample. The incorporation of the tITP system and Pt black-modified working electrode improved the method previously reported by our group by increasing the sensitivity and decreasing the LOD. In the future, this method will be used to study the production of nitric oxide in microglia and other immune cells. The incorporation of this method into a single cell analysis device will make it possible to monitor short-lived species, such as NO and peroxynitrite, directly in order to investigate the conditions which lead to neurodegeneration.

4.6 Acknowledgements

This research was funded by the National Science Foundation (CHE-1411993) and National Institutes of Health (COBRE P20GM103638). J. M. S. thanks the Madison and Lila Self Graduate Fellowship for support. K. M. S. would like to acknowledge the NIH Graduate Training Program in Dynamic Aspects of Chemical Biology Grant (T32GM008545) from the National Institutes of General Medicinal Sciences for support. G. C. acknowledges the support of an American Heart Association-Midwest Affiliate Postdoctoral Research Fellowship (NFP0075515). The authors would like to thank Nancy Harmony for editorial support, Scott Martin for assistance

with the Pt black deposition procedure, Heather Shinogle and the Microscopy and Analytical Imaging Laboratory at the University of Kansas for help with obtaining SEM images, and Pinnacle Technologies, Inc. (Lawrence, KS) for loaning the lab isolated potentiostats as well as assisting in potentiostat troubleshooting.

4.7 References

1. MacMicking, J.; Xie, Q.-w.; Nathan, C., Nitric oxide and macrophage function. *Annu. Rev. Immunol.* **1997,** *15* (1), 323-350.
2. Pacher, P.; Beckman, J. S.; Liaudet, L., Nitric oxide and peroxynitrite in health and disease. *Physiol. Rev.* **2007,** *87* (1), 315-424.
3. Kröncke, K.-D.; Fehsel, K.; Kolb-Bachofen, V., Nitric oxide: cytotoxicity versus cytoprotection—how, why, when, and where? *Nitric oxide* **1997,** *1* (2), 107-120.
4. Calabrese, V.; Cornelius, C.; Rizzarelli, E.; Owen, J. B.; Dinkova-Kostova, A. T.; Butterfield, D. A., Nitric oxide in cell survival: a janus molecule. *Antioxidants & redox signaling* **2009,** *11* (11), 2717-2739.
5. Minghetti, L.; Levi, G., Microglia as effector cells in brain damage and repair: focus on prostanoids and nitric oxide. *Prog. Neurobiol.* **1998,** *54* (1), 99-125.
6. Gomes, A.; Fernandes, E.; Lima, J. L., Use of fluorescence probes for detection of reactive nitrogen species: a review. *Journal of fluorescence* **2006,** *16* (1), 119-139.
7. Tsikas, D., Analysis of nitrite and nitrate in biological fluids by assays based on the Griess reaction: appraisal of the Griess reaction in the L-arginine/nitric oxide area of research. *J. Chromatogr. B* **2007,** *851* (1), 51-70.
8. Tsikas, D., A critical review and discussion of analytical methods in the L-arginine/nitric oxide area of basic and clinical research. *Anal. Biochem.* **2008,** *379* (2), 139-163.
9. Amatore, C.; Arbault, S. p.; Koh, A. C., Simultaneous detection of reactive oxygen and nitrogen species released by a single macrophage by triple potential-step chronoamperometry. *Anal. Chem.* **2010,** *82* (4), 1411-1419.
10. Bedioui, F.; Griveau, S., Electrochemical detection of nitric oxide: assessement of twenty years of strategies. *Electroanalysis* **2013,** *25* (3), 587-600.
11. Hetrick, E. M.; Schoenfisch, M. H., Analytical chemistry of nitric oxide. *Annual review of analytical chemistry (Palo Alto, Calif.)* **2009,** *2*, 409.
12. Trouillon, R., Biological applications of the electrochemical sensing of nitric oxide: fundamentals and recent developments. *Biol. Chem.* **2013,** *394* (1), 17-33.
13. Ye, X.; Rubakhin, S. S.; Sweedler, J. V., Detection of nitric oxide in single cells. *Analyst* **2008,** *133* (4), 423-433.
14. Hunter, R. A.; Privett, B. J.; Henley, W. H.; Breed, E. R.; Liang, Z.; Mittal, R.; Yoseph, B. P.; McDunn, J. E.; Burd, E. M.; Coopersmith, C. M., Microfluidic amperometric sensor for analysis of nitric oxide in whole blood. *Anal. Chem.* **2013,** *85* (12), 6066-6072.
15. Gunasekara, D. B.; Hulvey, M. K.; Lunte, S. M.; da Silva, J. A. F., Microchip electrophoresis with amperometric detection for the study of the generation of nitric oxide by NONOate salts. *Anal. Bioanal. Chem.* **2012,** *403* (8), 2377-2384.
16. Bryan, N. S.; Grisham, M. B., Methods to detect nitric oxide and its metabolites in biological samples. *Free Radical Biol. Med.* **2007,** *43* (5), 645-657.

17. Csonka, C.; Páli, T.; Bencsik, P.; Görbe, A.; Ferdinandy, P.; Csont, T., Measurement of NO in biological samples. *Br. J. Pharmacol.* **2015,** *172* (6), 1620-1632.
18. Zhang, H.-X.; Chen, J.-B.; Guo, X.-F.; Wang, H.; Zhang, H.-S., Highly sensitive low-background fluorescent probes for imaging of nitric oxide in cells and tissues. *Anal. Chem.* **2014,** *86* (6), 3115-3123.
19. Zhang, X.; Kim, W.-S.; Hatcher, N.; Potgieter, K.; Moroz, L. L.; Gillette, R.; Sweedler, J. V., Interfering with nitric oxide measurements 4, 5-diaminofluorescein reacts with dehydroascorbic acid and ascorbic acid. *J. Biol. Chem.* **2002,** *277* (50), 48472-48478.
20. Metto, E. C.; Evans, K.; Barney, P.; Culbertson, A. H.; Gunasekara, D. B.; Caruso, G.; Hulvey, M. K.; Fracassi da Silva, J. A.; Lunte, S. M.; Culbertson, C. T., An integrated microfluidic device for monitoring changes in nitric oxide production in single T-lymphocyte (Jurkat) cells. *Anal. Chem.* **2013,** *85* (21), 10188-10195.
21. Vogel, P. A.; Halpin, S. T.; Martin, R. S.; Spence, D. M., Microfluidic transendothelial electrical resistance measurement device that enables blood flow and postgrowth experiments. *Anal. Chem.* **2011,** *83* (11), 4296-4301.
22. Letourneau, S.; Hernandez, L.; Faris, A. N.; Spence, D. M., Evaluating the effects of estradiol on endothelial nitric oxide stimulated by erythrocyte-derived ATP using a microfluidic approach. *Anal. Bioanal. Chem.* **2010,** *397* (8), 3369-3375.
23. Kim, W.-S.; Ye, X.; Rubakhin, S. S.; Sweedler, J. V., Measuring nitric oxide in single neurons by capillary electrophoresis with laser-induced fluorescence: use of ascorbate oxidase in diaminofluorescein measurements. *Anal. Chem.* **2006,** *78* (6), 1859-1865.
24. Amatore, C.; Arbault, S.; Guille, M.; Lemaitre, F., Electrochemical monitoring of single cell secretion: vesicular exocytosis and oxidative stress. *Chem. Rev.* **2008,** *108* (7), 2585-2621.
25. Erkal, J. L.; Selimovic, A.; Gross, B. C.; Lockwood, S. Y.; Walton, E. L.; McNamara, S.; Martin, R. S.; Spence, D. M., 3D printed microfluidic devices with integrated versatile and reusable electrodes. *Lab on a Chip* **2014,** *14* (12), 2023-2032.
26. Selimovic, A.; Martin, R. S., Encapsulated electrodes for microchip devices: Microarrays and platinized electrodes for signal enhancement. *Electrophoresis* **2013,** *34* (14), 2092-2100.
27. Griveau, S.; Bedioui, F., Overview of significant examples of electrochemical sensor arrays designed for detection of nitric oxide and relevant species in a biological environment. *Anal. Bioanal. Chem.* **2013,** *405* (11), 3475-3488.
28. Gunasekara, D. B.; Siegel, J. M.; Caruso, G.; Hulvey, M. K.; Lunte, S. M., Microchip electrophoresis with amperometric detection method for profiling cellular nitrosative stress markers. *Analyst* **2014,** *139* (13), 3265-3273.
29. Scott, D. E.; Grigsby, R. J.; Lunte, S. M., Microdialysis Sampling Coupled to Microchip Electrophoresis with Integrated Amperometric Detection on an All-Glass Substrate. *ChemPhysChem* **2013,** *14* (10), 2288-2294.
30. Saylor, R. A.; Reid, E. A.; Lunte, S. M., Microchip electrophoresis with electrochemical detection for the determination of analytes in the dopamine metabolic pathway. *Electrophoresis* **2015,** *36* (16), 1912-1919.
31. Zhou, L.; Cheng, Y.; Amrein, M., Fabrication by electrolytic deposition of platinum black electrocatalyst for oxidation of ammonia in alkaline solution. *J. Power Sources* **2008,** *177* (1), 50-55.
32. Li, Y.; Meunier, A.; Fulcrand, R.; Sella, C.; Amatore, C.; Thouin, L.; Lemaître, F.; Guille-Collignon, M., Multi-chambers Microsystem for Simultaneous and Direct Electrochemical Detection of Reactive Oxygen and Nitrogen Species Released by Cell Populations. *Electroanalysis* **2016,** *28* (8), 1865-1872.

33. Fagan-Murphy, A.; Hachoumi, L.; Yeoman, M.; Patel, B., Electrochemical sensor for the detection of multiple reactive oxygen and nitrogen species from ageing central nervous system homogenates. *Mechanisms of Ageing and Development* **2016,** *160*, 28-31.
34. Li, Y.; Sella, C.; Lemaître, F.; Guille-Collignon, M.; Thouin, L.; Amatore, C., Electrochemical Detection of Nitric Oxide and Peroxynitrite Anion in Microchannels at Highly Sensitive Platinum-Black Coated Electrodes. Application to ROS and RNS Mixtures prior to Biological Investigations. *Electrochim. Acta* **2014,** *144*, 111-118.
35. Zhang, X. W.; Qiu, Q. F.; Jiang, H.; Zhang, F. L.; Liu, Y. L.; Amatore, C.; Huang, W. H., Real-Time Intracellular Measurements of ROS and RNS in Living Cells with Single Core–Shell Nanowire Electrodes. *Angew. Chem.* **2017,** *129* (42), 13177-13180.
36. Lee, Y.; Oh, B. K.; Meyerhoff, M. E., Improved planar amperometric nitric oxide sensor based on platinized platinum anode. 1. Experimental results and theory when applied for monitoring NO release from diazeniumdiolate-doped polymeric films. *Anal. Chem.* **2004,** *76* (3), 536-544.
37. Casella, I. G.; Salvi, A. M., Voltammetric behavior and ion chromatographic detection of nitrite at a dispersed platinum glassy carbon electrode. *Electroanalysis* **1997,** *9* (8), 596-601.
38. Shim, J. H.; Lee, Y., Amperometric nitric oxide microsensor based on nanopore-platinized platinum: the application for imaging NO concentrations. *Anal. Chem.* **2009,** *81* (20), 8571-8576.
39. Lee, Y.; Kim, J., Simultaneous electrochemical detection of nitric oxide and carbon monoxide generated from mouse kidney organ tissues. *Anal. Chem.* **2007,** *79* (20), 7669-7675.
40. Lee, Y.; Yang, J.; Rudich, S. M.; Schreiner, R. J.; Meyerhoff, M. E., Improved planar amperometric nitric oxide sensor based on platinized platinum anode. 2. Direct real-time measurement of NO generated from porcine kidney slices in the presence of L-arginine, L-arginine polymers, and protamine. *Anal. Chem.* **2004,** *76* (3), 545-551.
41. Li, Y.; Hu, K.; Yu, Y.; Rotenberg, S. A.; Amatore, C.; Mirkin, M. V., Direct electrochemical measurements of reactive oxygen and nitrogen species in nontransformed and metastatic human breast cells. *Journal of the American Chemical Society* **2017,** *139* (37), 13055-13062.
42. Stamler, J. S., Redox signaling: nitrosylation and related target interactions of nitric oxide. *Cell* **1994,** *78* (6), 931-936.
43. Li, Y.; Sella, C.; Lemaitre, F.; Guille-Collignon, M.; Thouin, L.; Amatore, C., Electrochemical Detection of Nitric Oxide and Peroxynitrite Anion in Microchannels at Highly Sensitive Platinum-Black Coated Electrodes. Application to ROS and RNS Mixtures prior to Biological Investigations. *Electrochim. Acta* **2014,** *144*, 111-118.
44. Park, S. S.; Tatum, C. E.; Lee, Y., Dual electrochemical microsensor for simultaneous measurements of nitric oxide and oxygen: Fabrication and characterization. *Electrochem. Commun.* **2009,** *11* (10), 2040-2043.
45. Wang, X.; Zhang, Y.; Cheng, C.; Dong, R.; Hao, J., Glucose in human serum determined by capillary electrophoresis with glucose micro-biosensor. *Analyst* **2011,** *136* (8), 1753-1759.
46. Wu, C.-C.; Wu, R.-G.; Huang, J.-G.; Lin, Y.-C.; Chang, H.-C., Three-electrode electrochemical detector and platinum film decoupler integrated with a capillary electrophoresis microchip for amperometric detection. *Anal. Chem.* **2003,** *75* (4), 947-952.
47. Daiber, A.; Herold, S.; Schöneich, C.; Namgaladze, D.; Peterson, J. A.; Ullrich, V., Nitration and inactivation of cytochrome P450BM-3 by peroxynitrite. *Eur. J. Biochem.* **2000,** *267* (23), 6729-6739.

48. Timerbaev, A. R.; Hirokawa, T., Recent advances of transient isotachophoresis-capillary electrophoresis in the analysis of small ions from high-conductivity matrices. *Electrophoresis* **2006,** *27* (1), 323-340.
49. Křivánková, L.; Pantůčková, P.; Gebauer, P.; Boček, P.; Caslavska, J.; Thormann, W., Chloride present in biological samples as a tool for enhancement of sensitivity in capillary zone electrophoretic analysis of anionic trace analytes. *Electrophoresis* **2003,** *24* (3), 505-517.
50. Szökő, É.; Tábi, T.; Halász, A. S.; Pálfi, M.; Magyar, K., High sensitivity analysis of nitrite and nitrate in biological samples by capillary zone electrophoresis with transient isotachophoretic sample stacking. *Journal of Chromatography A* **2004,** *1051* (1-2), 177-183.
51. Gunasekara, D. B.; Hulvey, M. K.; Lunte, S. M., In-channel amperometric detection for microchip electrophoresis using a wireless isolated potentiostat. *Electrophoresis* **2011,** *32* (8), 832-837.
52. Lorsbach, R. B.; Murphy, W. J.; Lowenstein, C. J.; Snyder, S. H.; Russell, S. W., Expression of the nitric oxide synthase gene in mouse macrophages activated for tumor cell killing. Molecular basis for the synergy between interferon-gamma and lipopolysaccharide. *J. Biol. Chem.* **1993,** *268* (3), 1908-1913.

Chapter 5

Capillary electrophoresis with diode array detection as a tool for the study of oxidative modifications of tyrosine-containing species

5 Chapter 5: Capillary electrophoresis with diode array detection as a tool for the study of oxidative modifications of tyrosine-containing species

5.1 Abstract

Oxidative modifications of tyrosine residues are often used as biomarkers of conditions of oxidative and nitrosative stress that are prevalent in a variety of disease states. In this work, a capillary electrophoresis (CE) separation of several modified tyrosine residues and short, tyrosine-containing peptides was optimized. Then, peroxynitrite was synthesized from nitrite and acidified hydrogen peroxide and the tyrosine-containing species were exposed to this reaction mixture under a variety of conditions. The resulting products were separated and detected using the optimized CE method with diode array detection (DAD). DAD enabled the monitoring of the electropherogram at several different wavelengths that corresponded to different functional groups present in these species (*e.g.* phenol, nitro groups). By observing the ratio of peak heights at different wavelengths, product peaks could be identified as either known species (by comparison to a standard) or proposed structures based on these spectra. Nitration of both free and peptide-bound tyrosine was observed via this reaction with peroxynitrite along with other further oxidation and substitution reaction products. Possible structures of these by-products are presented. Ultimately, this work provides a framework for analysis of low volumes of highly conductive reaction products using CE that could be used to explore other more physiologically relevant oxidative conditions to gain a greater understanding of the factors that influence these reactions.

5.2 Introduction

Nitrosative and oxidative stress has been implicated in a wide variety of disease states, including cardiovascular disease, stroke, and neurodegenerative diseases such as Alzheimer's disease. Under conditions of nitrosative and oxidative stress, reactive nitrogen and oxygen species (RNOS) begin to proliferate and react with biomolecules, resulting in structural modifications that

can impact their function and ultimately result in cell damage or death.[1] One of the most commonly observed oxidative modifications is the nitration of tyrosine to form 3-nitrotyrosine (3-NT), which has been found in increased quantities in the tissues affected by these conditions.[2] However, efforts to understand the exact mechanisms of tyrosine nitration and other oxidative modifications, as well as to identify the sites that are preferentially modified, are still ongoing. Therefore, it is of great interest to develop methods for the quantification of biological tyrosine nitration. Additionally, much attention has been paid to the study of artifactual NT formation during sample preparation and storage.[3-5] The design of experiments to screen these conditions for their effects on artifactual NT formation is beneficial to the continued progress of quantification and identification of biological NT.

Liquid chromatography with electrochemical, UV, fluorescence, or mass spectrometric detection are the methods of choice for most previous studies.[3, 6] While these methods are capable of quantification of biological 3-NT, they typically require relatively large amounts of sample for compound identification. In this work, we describe a capillary electrophoresis method with diode array detection for profiling the oxidative modifications of tyrosine and short, tyrosine-containing peptides under a variety of oxidative conditions relevant both to protein sample preparation and physiological conditions. This method features lower sample requirements than LC-MS and enables rapid analysis of reaction mixtures. In addition, the diode array detector can be used to elucidate rough structural information about unknown byproducts of these reactions through comparison of peaks at several wavelengths corresponding to key functional groups. In this work, tyrosine-containing species dissolved in water are exposed to a highly oxidative environment containing peroxynitrite at a very low pH and the resulting products, including 3-NT and other modified tyrosine species, are tentatively identified without the use of costly structural characterization techniques that require large quantities of purified product.

5.3 Materials and methods

5.3.1 Reagents and materials

Sodium phosphate monobasic, sodium phosphate dibasic, sodium phosphate tribasic, boric acid, sodium hydroxide, phosphoric acid, sodium acetate, glacial acetic acid, sodium dodecyl sulfate (SDS), tetradecyltrimethylammonium chloride (TTAC), sodium nitrite, sodium nitrate, manganese dioxide, hydrogen peroxide (30%), hydrochloric acid, L-tyrosine, 3-L-nitrotyrosine, 3-chlorotyrosine, 3-aminotyrosine were obtained from Fisher. Peptides AY, A(3-NO_2Y), AYL, A(3-NO_2Y)L, FSAYLER, and FSA(3-NO_2Y)LER as well as dityrosine were obtained from the KU Synthetic Chemical Biology Core.

5.3.2 Electrophoresis procedure

An Agilent 7100 capillary electrophoresis system with DAD was used for all experiments. A 63.5 cm capillary (55 cm to detector) with 50 μm I.D., 360 μm O.D. capillary (Polymicro, Molex) was used. The capillary was conditioned prior to initial use with water, HCl, water, NaOH, water, and then BGE. Between runs, the capillary was flushed with background electrolyte (BGE) for 3 min. Hydrodynamic injection at 30 mbar for 15 s was used to inject sample into the capillary and the separation potential was 30 kV for the normal polarity separations and -19.7 kV for the reverse polarity separations. Standard stock solutions (approximately 2 mM) were prepared monthly in 18.2 MΩ water and diluted into BGE at an appropriate concentration (typically 50-100 μM) prior to analysis. For reverse polarity separations of nitrite, nitrate, and peroxynitrite, a BGE of 25 mM phosphate at pH 12.0 with 2 mM TTAC was used. The optimization of the normal polarity separation of analytes of interest will be discussed below, but, unless otherwise specified, the BGE contained 2 mM SDS.

5.3.3 Peroxynitrite synthesis

Peroxynitrite was synthesized according to the protocol of Robinson *et al.*[7] Stock solutions of (1) 0.6 M $NaNO_2$, (2) 0.6 M H_2O_2 with 0.7 M HCl, and (3) 3 M NaOH were prepared and chilled on ice prior to reaction. $NaNO_2$ (200 µL) was added first to a 2-mL Eppendorf tube. The acidified H_2O_2 solution (150 µL) and NaOH solution (200 µL) were then added in quick succession to the tube to first synthesize the peroxynitrite by the addition of the acidified H_2O_2 followed by the stabilization of peroxynitrite in its anionic form through the addition of the base (Figure 5.1A,B). This reaction protocol resulted in an average peroxynitrite concentration of approximately 100 mM. If desired, the resulting solution was purified through addition of manganese dioxide to react with any residual H_2O_2 followed by filtration through a 0.22 µm syringe filter to obtain a hydrogen peroxide-free peroxynitrite solution. To evaluate the reactions of these products with the tyrosine residue, free tyrosine or a tyrosine-containing peptide dissolved in water was added in lieu of the NaOH to react with the acidic reaction mixture (Figure 5.1C).

5.3.4 Data analysis

Data was obtained on the CE instrument using ChemStation. Electropherograms and UV spectra for peaks of interest were exported to .csv files from this software and Origin software (OriginLabs) was used for all subsequent data analysis, including plotting, baseline correction, and peak integration.

5.3.5 LC-MS protocol

Electrospray ionization spectra in positive mode were acquired on a LCT Premier (Waters Corp.) time-of-flight mass spectrometer (TOF-MS) linked to a Waters Acquity UPLC system consisting a photodiode array detector. The analyzer was operated in W mode with extended dynamic range. The cone voltages (CV) for sample scans and reference scans were maintained at 50 V and 35 V, respectively. The analysis was carried out by scanning from 70 m/z to 2100 m/z

with a capillary set to 2,800 V at a scan rate of two scans per second. The temperatures for desolvation gas and source were set to 350 ℃ and 120 ℃, respectively. The lock mass and attenuated lock mass features in MassLynx V4.1 SCN639 were implemented to perform mass correction for exact mass determination where leucine enkephalin acetate salt hydrate was used as the reference for high resolution mass calibration.

Waters Acquity ultraperformance liquid chromatography (UPLC) linked to the LCT Premier was fitted with a reverse phase ACQUITY UPLC HSS T3, 1.8 μm, 2.1 x 50 mm column and the separations were conducted using the solvent gradient shown in Table 5.1. Absorbance was recorded at a wavelength of 214 nm using the photodiode array detector. Washes of 500 μL acetonitrile and 800 μL of water/methanol (1:1) between each injection were carried out to minimize contamination.

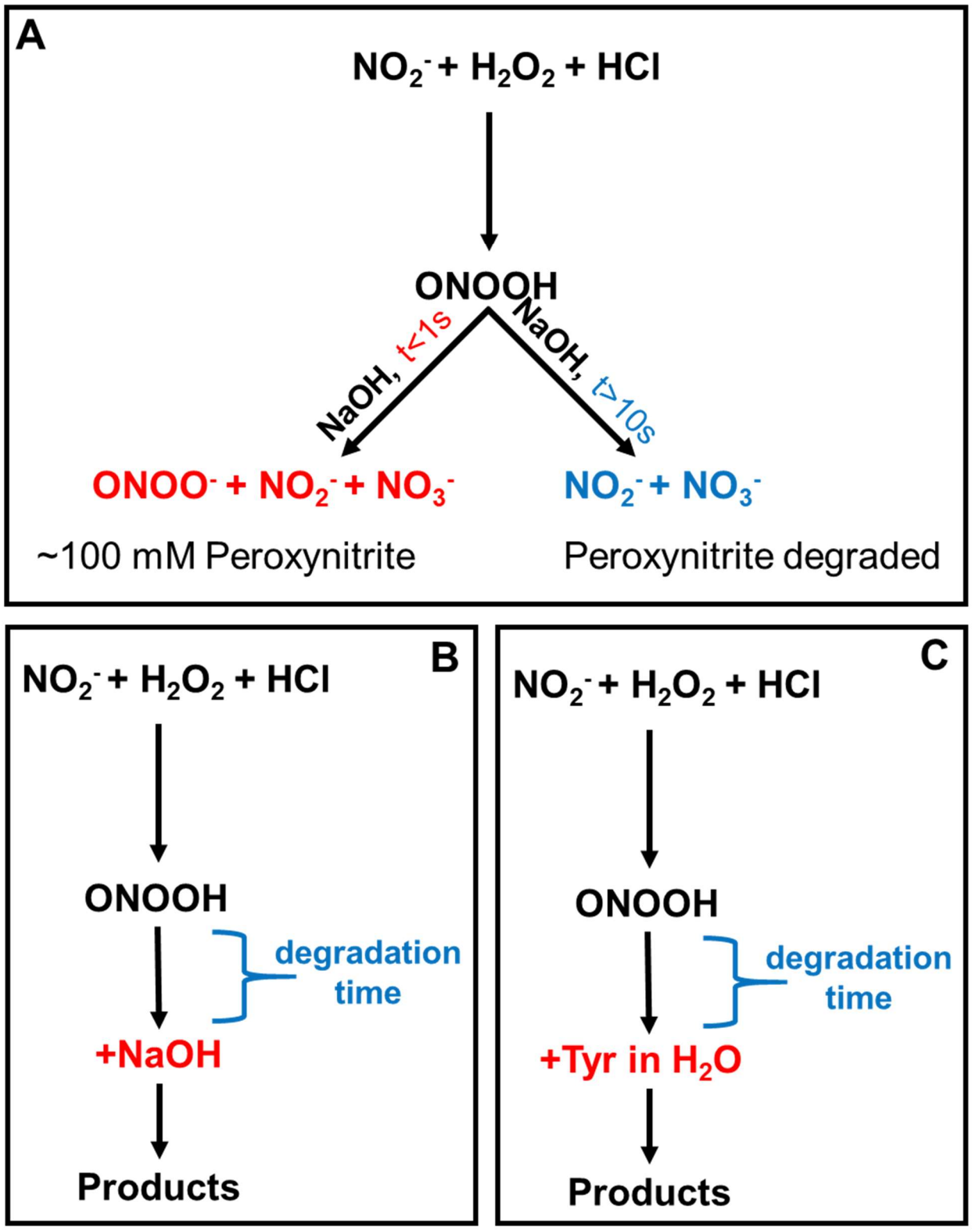

Figure 5.1. Protocol for synthesis of peroxynitrite and subsequent (A,B) stabilization with NaOH or (C) reaction with tyrosine.

Table 5.1. LC gradient. Solvent A: water with 0.05% difluoroacetic acid (DFA). Solvent B: acetonitrile.

Time (min)	Flow (mL/min)	%A	%B
0.0	0.600	95.0	5.0
2.70	0.600	0.1	99.9
3.10	0.600	0.1	99.9
3.11	0.600	95.0	5.0

5.4 Results and discussion

5.4.1 Separation optimization

5.4.1.1 Analyte selection

A series of tyrosine-containing analytes was selected for separation using CE based on their relevance to future experiments of interest. 3-nitrotyrosine (3-NT, 3-NO_2Y), 3-chlorotyrosine (3-CT, 3-ClY), L-DOPA, and dityrosine (DiY) are common oxidative modifications of tyrosine observed *in vivo* under conditions of stress. Additionally, 3-aminotyrosine (3-AT, 3-NH_2Y) was added to the separation due to its relevance in certain analytical methods in which 3-NT is reduced first to 3-AT and then 3-AT is selectively detected. This has been reported with selective derivatization of 3-AT *via* a fluorescent probe or other derivatization agents to make the species GC-MS-compatible, as well as with electrochemical detection in which the reduced species is then oxidized at a potential low enough to eliminate potential oxidizable interferences.[3, 8, 9] For these applications, evaluating the extent of reduction of 3-NT to 3-AT after this step could prove beneficial. Finally, three tyrosine-containing peptides of varying length were selected. FSAYLER is a peptide from the protein phosphorylase B which has been used for studies of the site specificity of tyrosine nitration in the past by our collaborators.[10, 11] The peptides AYL and AY were also selected as shorter versions of this peptides so the ability of the optimized experimental workflow to produce and then identify nitrated peptides of varying lengths could be established. Additionally, the nitrated forms of each of these three peptides (A(NO_2Y), A(NO_2Y)L, FSA(NO_2Y)LER) were also obtained for incorporation into the separation.

5.4.1.2 Effect of BGE pH on separation

As the pI of most tyrosine-containing analytes is below 6, efforts to resolve these species electrophoretically were focused above pH 6. A series of BGEs was prepared spanning the pH range of 6 to 10, including pH 6.4 and 7.8 phosphate and pH 8.2, 9.2, and 10.2 borate. It was

observed that below pH 8.2, the resolution between the analytes was poor. This pH range corresponds to the region where all the amino acids' carboxylic acid groups are deprotonated and the amine groups are protonated, resulting in the analytes having similar charge/size ratios. As the pH of the BGE was raised into the pK_a range of these amines, however, the species began to be better resolved, with optimal resolution occurring in the pH 8.2 – 9.2 range (Figure 5.2).

5.4.1.3 Effect of BGE concentration on separation

Once the optimal BGE pH range was selected, the ionic strength of the BGE was changed by varying the concentration of the borate ion from 5 mM to 20 mM at both pH 8.2 and pH 9.2. Optimal resolution was observed at 20 mM borate at pH 8.2 and 10 mM borate at pH 9.2 (Figure 5.3). Because a low pH was desirable for future applications of this work to microchip electrophoresis with electrochemical detection, the pH 8.2 system was selected for further optimization.

5.4.1.4 Effect of surfactant concentration on separation

The concentration of surfactant, SDS, in the BGE was then varied from 0 to 20 mM (Figure 5.4). It was observed that increasing the SDS content past its critical micelle concentration of 8 mM did not dramatically affect the migration times of most analytes of interest, although it did result in reduced resolution of several closely migrating peaks. However, a significant shift in the migration times of the FSAYLER peptide and its nitrated form occurred with increasing SDS concentration above 7 mM. It is postulated that this shift is due to increased interaction between these longer peptides and the SDS micelles that are forming beyond this point, resulting in their delayed migration times. Optimal resolution of all analytes was observed at 5 mM SDS; however, two analyte groups still were not resolved using these conditions: Y comigrated with NH_2Y and ClY comigrates with both DiY and AY.

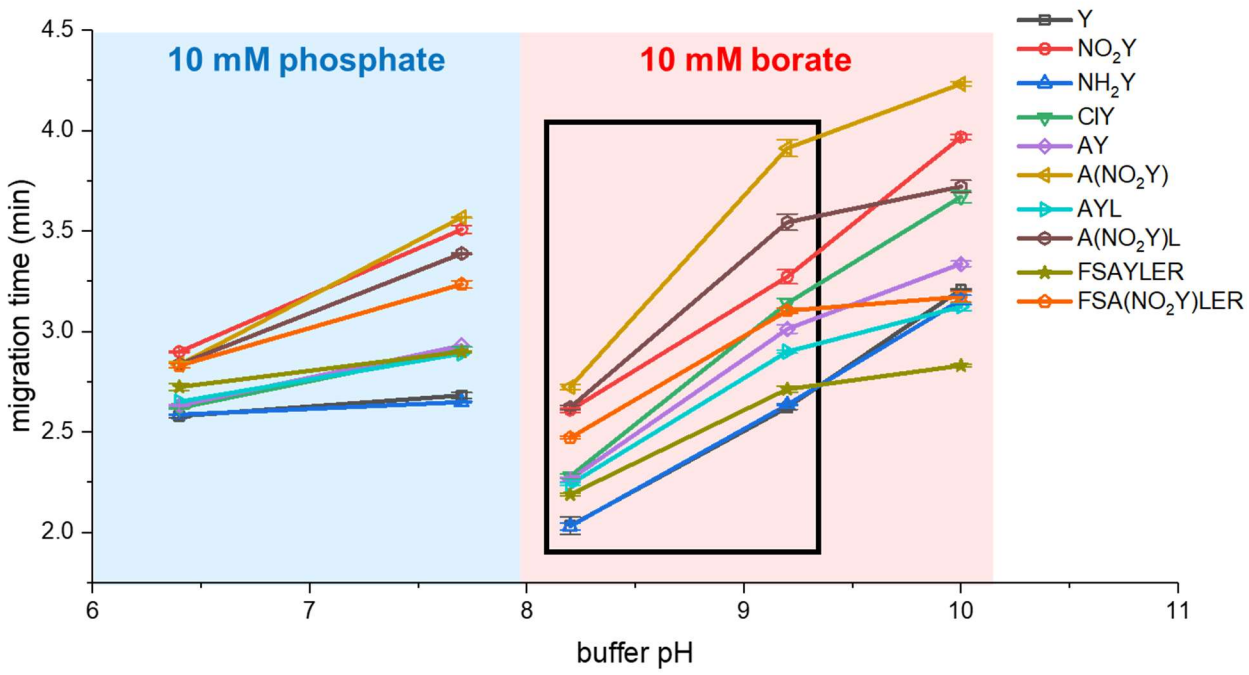

Figure 5.2. Effect of buffer pH on separation of analytes of interest (n = 3).

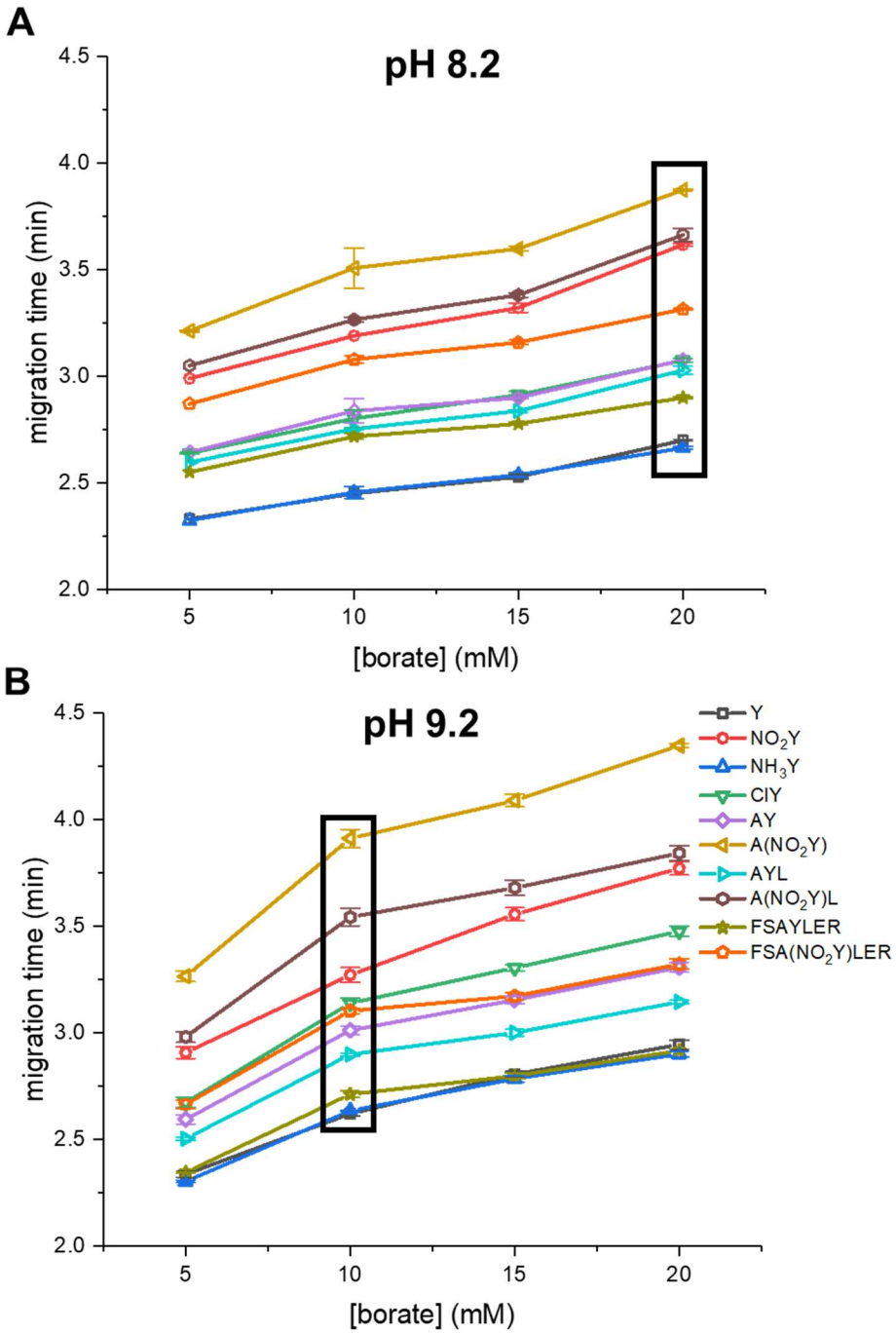

Figure 5.3. Effect of buffer concentration on separation of analytes at (A) pH 8.2 borate and (B) pH 9.2 borate (n = 3)

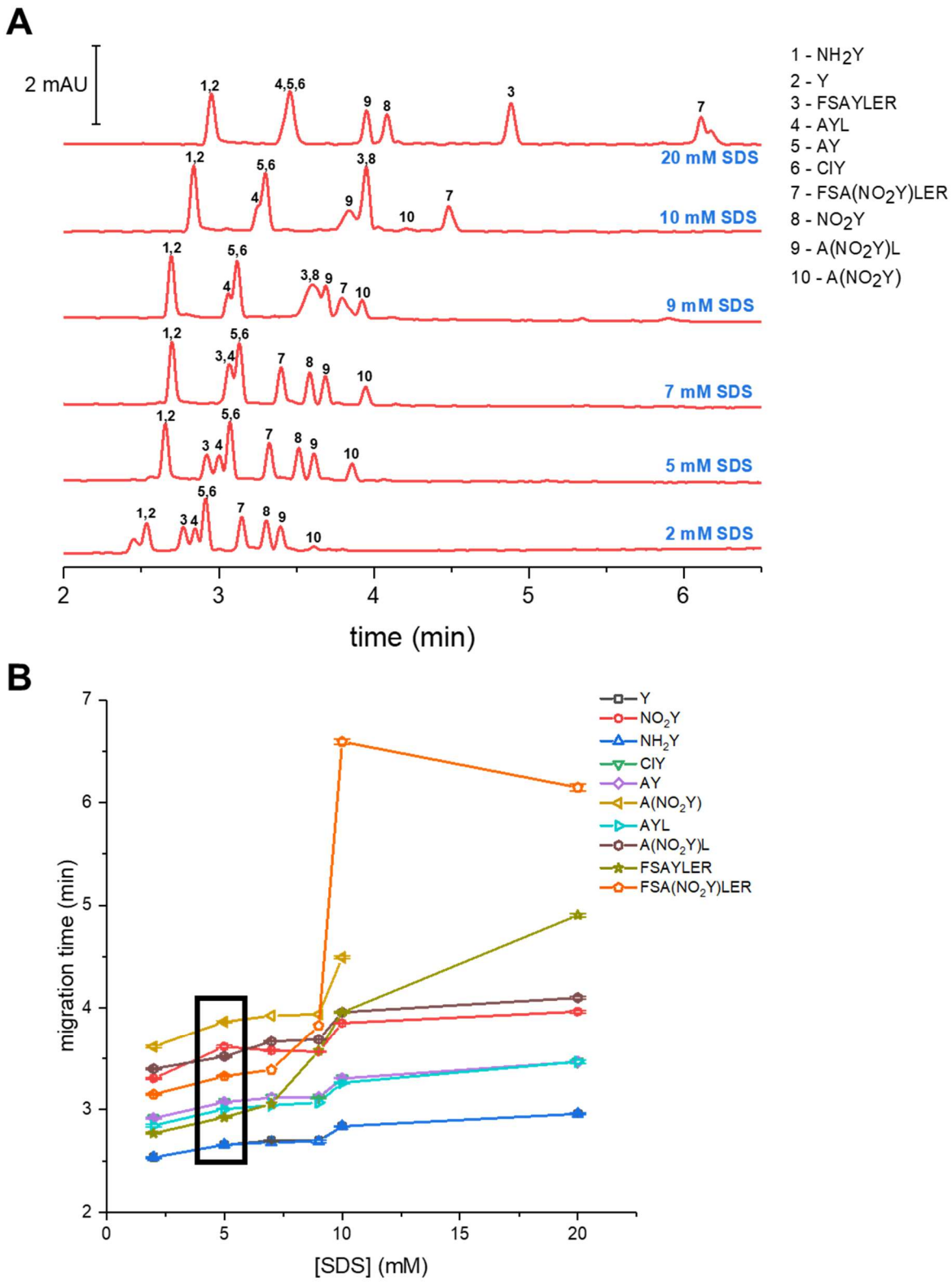

Figure 5.4. Effect of SDS concentration on separation of analytes, visualized with (A) electropherograms and (B) plot of migration times with varied concentration (n = 3).

5.4.1.5 Addition of cyclodextrins to improve separation

In an effort to resolve these comigrating peaks, a variety of β-cyclodextrins were selected to screen for their effects on the separation. β-cyclodextrins were selected based on their cavity size, which is in good agreement with the approximate size of the analytes of interest. Among all the different cyclodextrins tested, sulfobutylether-β-cyclodextrin (Captisol) exhibited the most promising results (Figure 5.5A,B). This cyclodextrin was therefore selected for further optimization, in which the concentration was varied until optimal separation was observed. With 20 mM SBE-β-CD, Y and NH_2Y were fully resolved; however, AY, ClY, and DiY continued to comigrate with one another (Figure 5.5C). No efforts to further increase the CD concentration beyond this point were successful, as increasing the concentration of SBE-β-CD in the BGE tended to lead to a decreased number of successful injections before to needing to recondition the capillary and replenish all solutions.

5.4.1.6 Optimal CE separations of analytes of interest

Ultimately, two separation conditions were produced using the same capillary and the same separation field strength. With 20 mM borate at pH 8.2 and 5 mM SDS and 20 mM SBE-β-CD, 9 analytes (Y, NH_2Y, FSAYLER, AYL, AY or ClY or DiY, NO_2Y, A(NO_2Y)L, FSA(NO_2Y)LER, and A(NO_2Y)) were able to be fully resolved from one another within 10 minutes (Figure 5.6B). By eliminating the CD from the BGE, the separation time was decreased to 5 minutes, but at the expense of resolving Y and NH_2Y at all and a loss in resolution of FSAYLER, AYL, and AY/ClY; however, diY was resolved from AY and ClY under these conditions (Figure 5.6A). Therefore, the buffer selected for a given experiment was dependent on which analytes needed to be resolved to obtain desirable results.

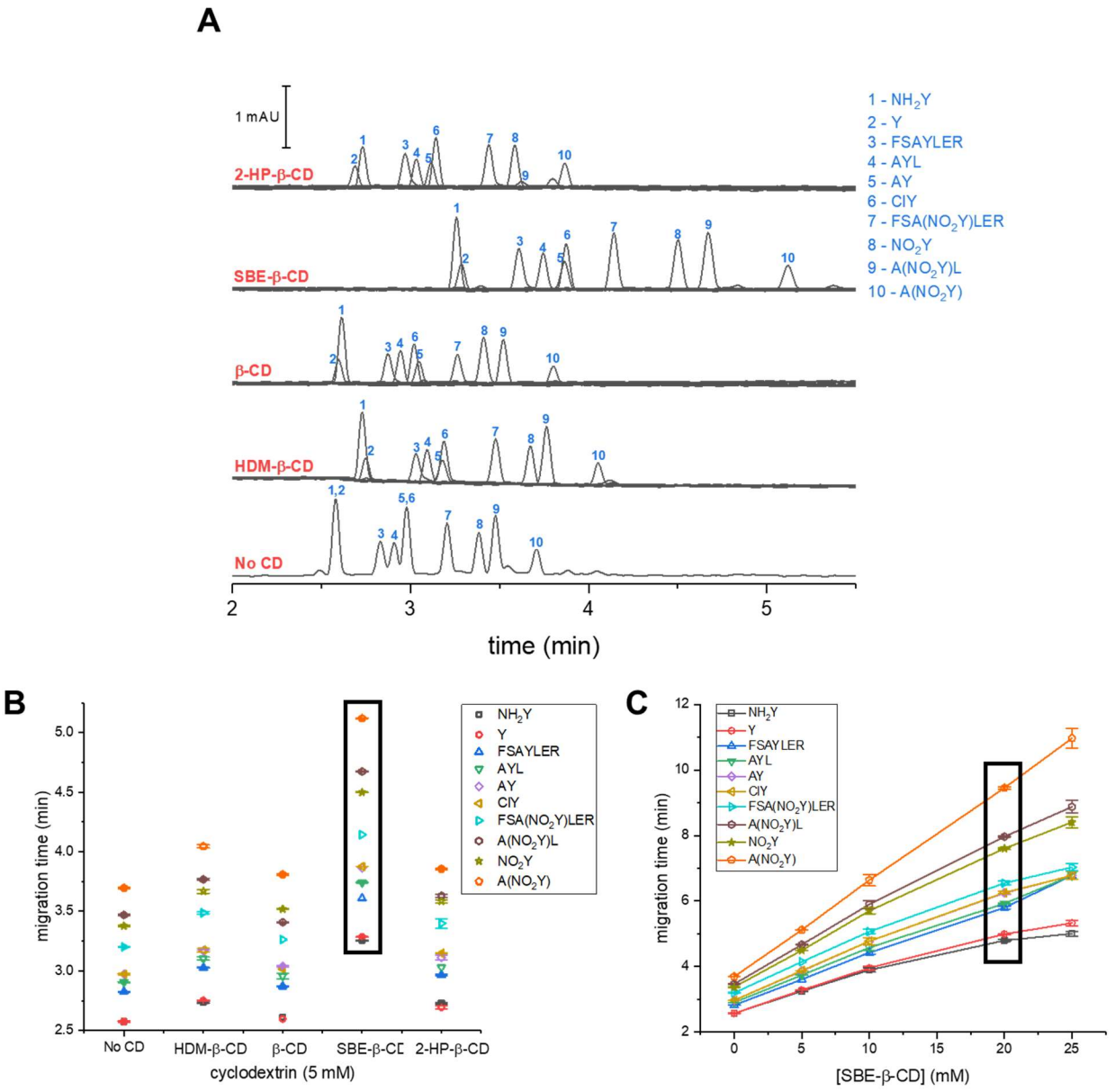

Figure 5.5. Effect of cyclodextrins on analyte separation (A) electropherograms demonstrating effects of different cyclodextrins, (B) migration times of analytes with different cyclodextrins at the same concentration (n = 3), (C) effect of varied SBE-β-CD concentration on separation (n = 3). *Abbreviations: HDM-β-CD = Heptakis(2,6-di-o-methyl)-β-CD; SBE-β-CD = sulfobutylether-β-CD; 2-HP-β-CD = 2-hydroxypropyl-β-CD.*

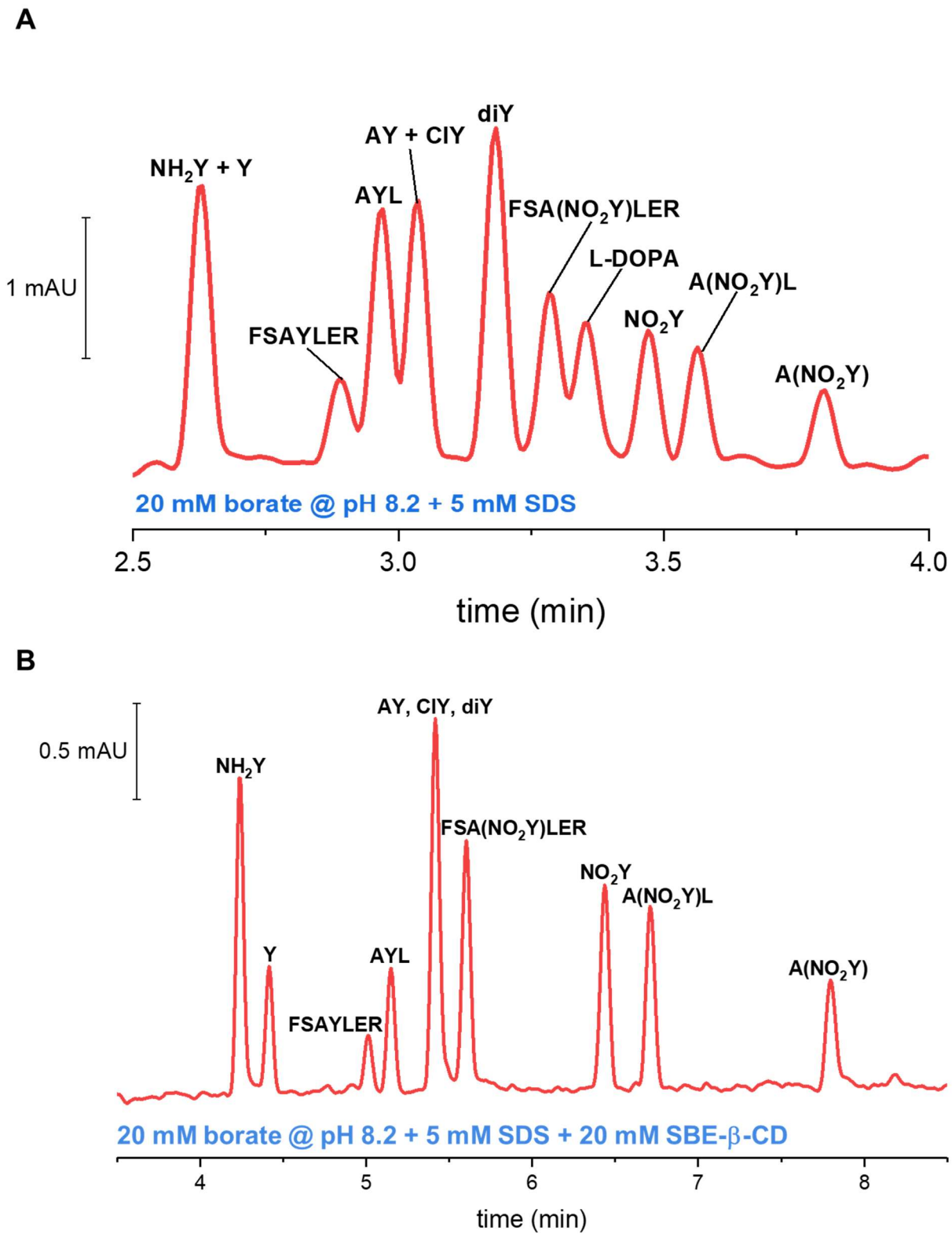

Figure 5.6. Optimal separations obtained (A) without and (B) with addition of cyclodextrin.

5.4.2 Oxidation and nitration of tyrosine-containing species

5.4.2.1 Generation of a highly reactive, oxidizing environment

Once the separation was optimized, it was then necessary to generate an oxidizing environment to induce formation of oxidative tyrosine products. To accomplish this, peroxynitrite was synthesized from reaction of nitrite and acidified hydrogen peroxide as shown in Figure 5.1A. By varying the degradation time (t_{deg}) between the addition of the acidified hydrogen peroxide to initiate the reaction and the addition of the NaOH to quench the reaction and stabilize the peroxynitrite in its anionic form, a picture of the degradation kinetics of peroxynitrite in acidic solution could be obtained. The final reaction mixture was diluted 10-fold in the background electrolyte used for reverse polarity separation of nitrite, nitrate, and peroxynitrite (25 mM phosphate @ pH 12.0 with 2 mM TTAC) and analyzed using the reverse polarity CE-UV method. The peroxynitrite peak was identified based on its selective absorbance at 302 nm and the remaining peaks were identified based on spiking with standards and comparison of the UV spectra (210-400 nm) of the reaction mixture peaks to those of standards.

When peroxynitrite was allowed to degrade in acidic solution (approximately 0.2 M HCl) for t_{deg} seconds before the addition of NaOH to stabilize it, the amount of peroxynitrite remaining in solution decreased steadily with increasing degradation time. As shown in Figure 5.7A, a large peroxynitrite peak was observed when peroxynitrite was only allowed to degrade for 1 s, while minimal peroxynitrite was left in the system by t_{deg} = 7 s and all detectable peroxynitrite had degraded completely by 15 s after the initiation of the reaction (t_{deg} = 15 s). By conducting this experiment, the reactive time window for exposure of tyrosine-containing species dissolved in water to peroxynitrite under acidic conditions was determined. As shown in Figure 5.7B, a difference in degradation time of 1 s results in a substantial change in the amount of peroxynitrite left in the system. This change is particularly marked in the first 4 seconds after the reaction is

initiated, as may be understood by the relatively large error bars in Figure 5.7B for these t_{deg} timepoints. In future experiments, unless the peroxynitrite is stabilized with the addition of NaOH, any other reagents must be added at a controlled time after the synthesis (ideally within 1 s of synthesis) in order to obtain reproducible reaction products.

5.4.2.2 Exposure of tyrosine to the peroxynitrite reaction mixture

Once the window for exposure of tyrosine to peroxynitrite under acidic conditions was determined, an experiment was then conducted to determine the products formed under these conditions. It was hypothesized that the primary product would be 3-NT, as is observed under physiological conditions. First, peroxynitrite was synthesized and allowed to degrade for a designated time (t_{deg}). At this point, tyrosine dissolved in water was added to the system as shown in Figure 5.1C. The resulting reaction mixture was then diluted 10-fold in the optimal background electrolyte (20 mM borate at pH 8.2 with 5 mM SDS) and immediately analyzed using the optimized normal polarity CE-UV method. The pH of this buffer was determined to be sufficiently basic to prevent any further reaction of the tyrosine with any sample components on the timescale of these experiments.

When tyrosine dissolved in water was added in place of the NaOH after t_{deg} = 1 s, two primary products and one minor product were observed (Figure 5.8A). The first of these peaks was identified as 3-NT based on the results of spiking the sample with pure 3-NT as well as comparison of the UV spectra. This identification, as well as tentative identification of the other two product peaks, will be discussed further in 5.4.2.3. By t_{deg} = 7 s, Products A and B were no longer produced to much extent, while 3-nitrotyrosine was still prominent in addition to a large peak representing unreacted tyrosine, and by t_{deg} = 15 s only unreacted tyrosine was observed in the system (Figure 5.8A). When the average peak height of each of these species (tyrosine, 3-nitrotyrosine, Product A, and Product B) at 230 nm is plotted versus degradation time (Figure

5.8B) and compared to the degradation kinetics of peroxynitrite (Figure 5.7B), it can be observed that both peroxynitrite and Products A and B decrease rather steadily throughout, while 3-nitrotyrosine production increases to a maximum at approximately 3-4 seconds degradation time before beginning to decrease. At that time, unreacted tyrosine remaining in the solution increases steadily as degradation time increases. This data gives us a picture of the kinetics of peroxynitrite degradation under these acidic synthesis conditions as well as the products being produced at different stages of peroxynitrite production and degradation.

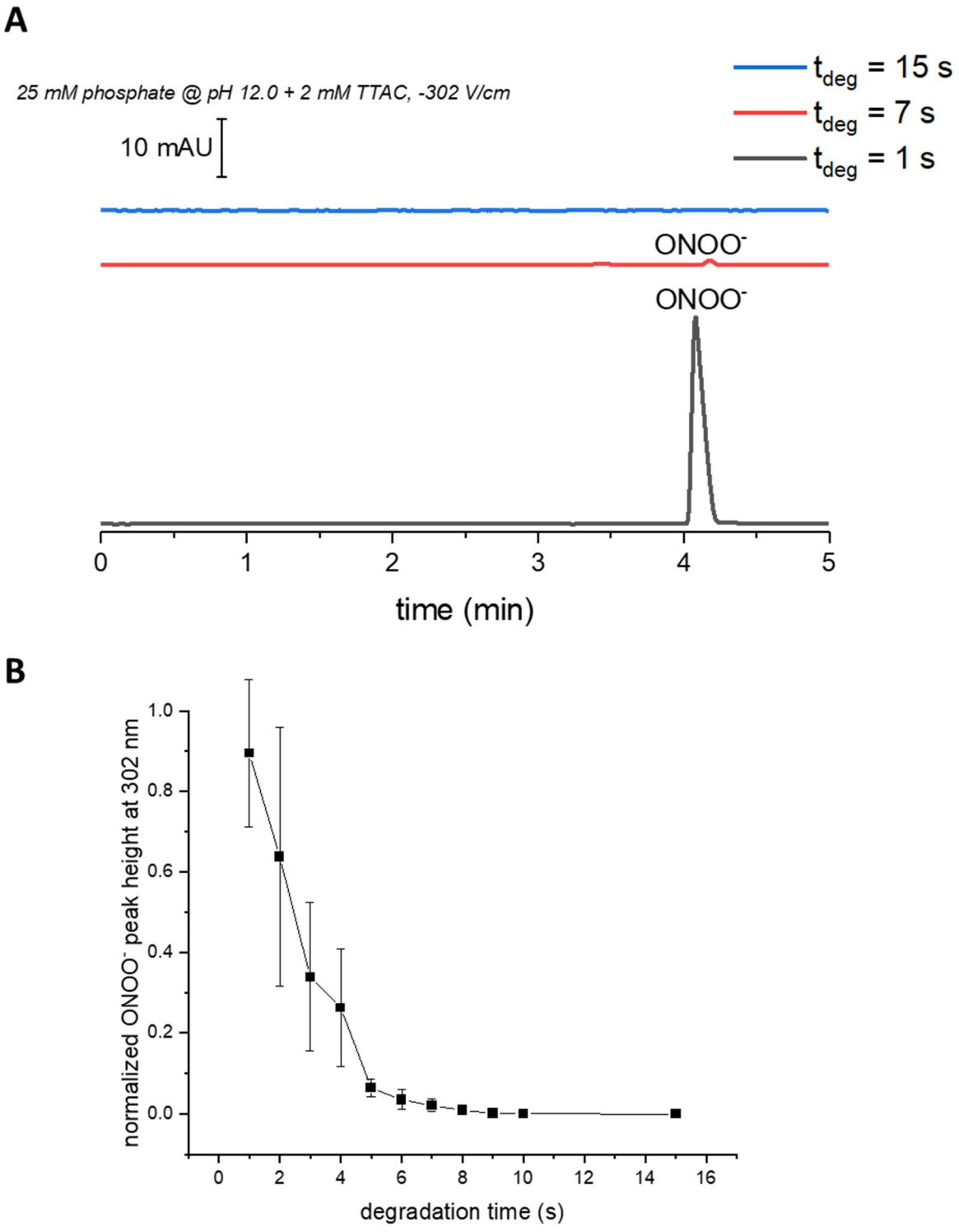

Figure 5.7. (A) Electropherogram of the products of peroxynitrite synthesis reaction at 302 nm after 1, 7, or 15 s degradation time between synthesis and stabilization with NaOH. (B) Average normalized peak height of peroxynitrite at 302 nm with varied degradation time (n = 3).

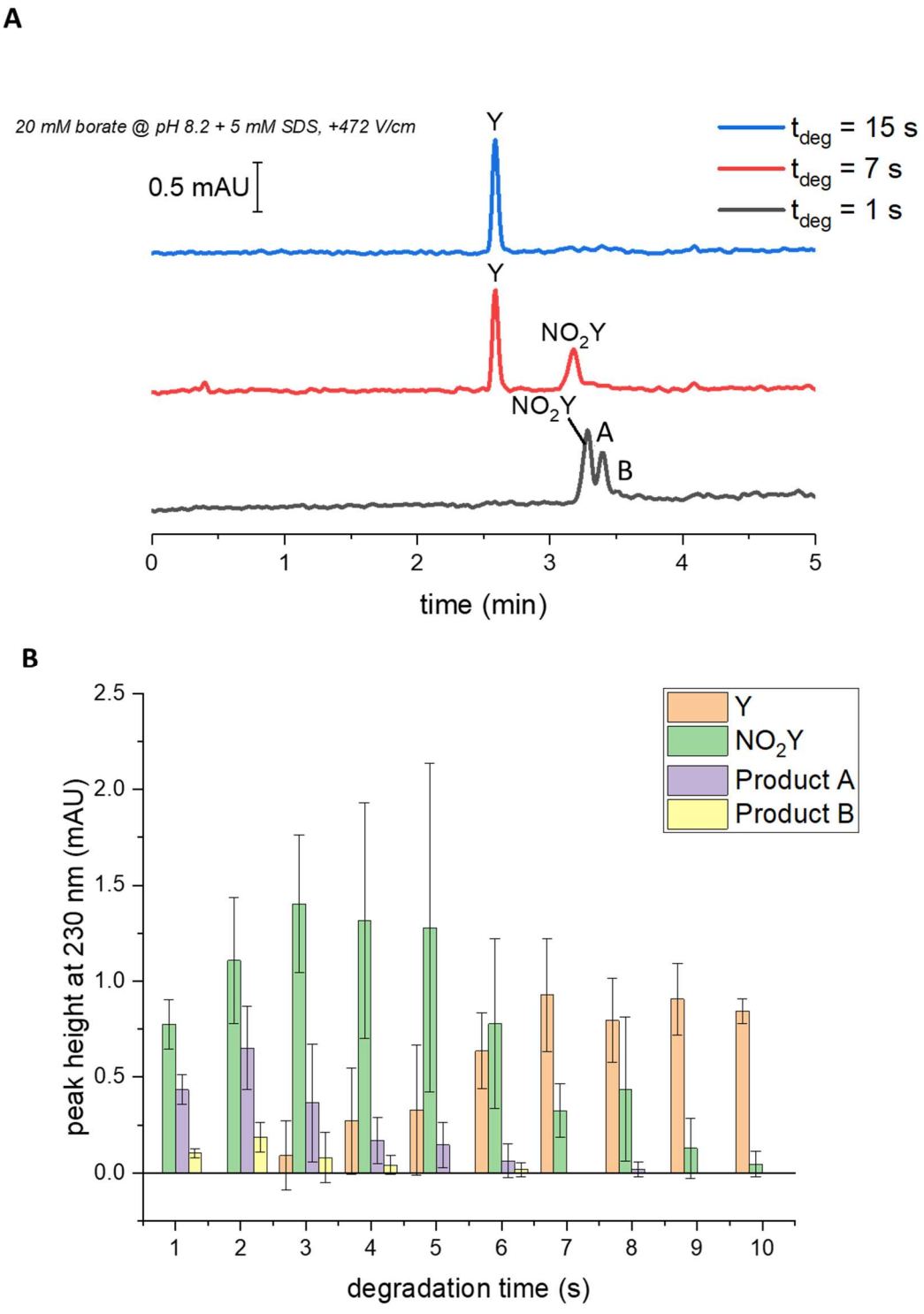

Figure 5.8. (A) Electropherograms of the peroxynitrite/tyrosine reaction product mixture at 1, 7, and 15 s degradation times; (B) the average peak height of each of the products and of unreacted tyrosine at varied degradation time under these reaction conditions (n = 4).

5.4.2.3 Identification of reaction products using CE-DAD

As CE-DAD is not able to provide the same structural information that can be achieved from techniques such as mass spectrometry or NMR, several strategies were explored in an attempt to identify reaction products without isolation, large amounts of product, and turning to these conventional structural elucidation techniques. The simplest methods for peak identity confirmation involve comparison of the migration time of the product peak with standards or spiking the sample with a standard solution of the analyte of interest and observing whether the product peak height increases. While these methods were sufficient for tentative identification of the 3-NT peak in Figure 5.8A, they rely on having a standard on hand. The migration times of unidentified products A and B were compared to the migration times of each of the possible oxidative modifications of tyrosine separated in the optimal separation, particularly 3-chlorotyrosine, L-DOPA, and dityrosine, and none of the product peaks matched any of the standards. Furthermore, because products A and B migrate after 3-NT in the normal polarity separation, it could be concluded that these products must have a more negative electrophoretic mobility than 3-NT, which has a net charge of -1 at pH 8.2.

Because these products were stable over time at both the low pH synthesis conditions and the pH 8.2 separation conditions and did not comigrate with any of the common oxidative products of tyrosine modification, it was presumed that there was a secondary reaction occurring in the system that could be independent of peroxynitrite itself. In order to learn more about the structure of products A and B, electropherograms were captured at a variety of wavelengths corresponding to key functional groups. These were 254 nm for aromatic conjugation, 280 nm for a phenol group, and 400 nm for a nitro group. The peak heights at each of these wavelengths were normalized to the height at the wavelength of maximum absorbance (Figure 5.9B) and these ratios were compared to standards (Figure 5.9A). While these ratios make it evident that the first peak

observed in the 1 s degradation time reactions is in fact 3-NT, as previously determined, they also indicate that the products A and B do contain phenol rings, so they do appear to be further modifications of tyrosine.

The next question was whether the by-products are further modifications of 3-NT or separate modifications of Tyr. To test this concept, 3-NT was reacted under the same conditions as tyrosine. The same peak profile was observed for the 3-NT reaction as was observed in the reaction with tyrosine, which indicates that 3-NT is a precursor to products A and B (Figure 5.10). This can help explain the pattern observed in Figure 5.8B that Products A and B are formed in the largest quantities at a degradation time of 1-2 seconds, while 3-nitrotyrosine reaches its maximum at a degradation time of 3-4 seconds. This could indicate that peaks A and B are products of the reaction of 3-nitrotyrosine with a species that is only present in the first several seconds of peroxynitrite's production and degradation, and that while this species is present the reaction is favored similarly to the terminal production of 3-NT. Therefore, the question now is what species in the system is reacting with the nitrotyrosine to form A and B.

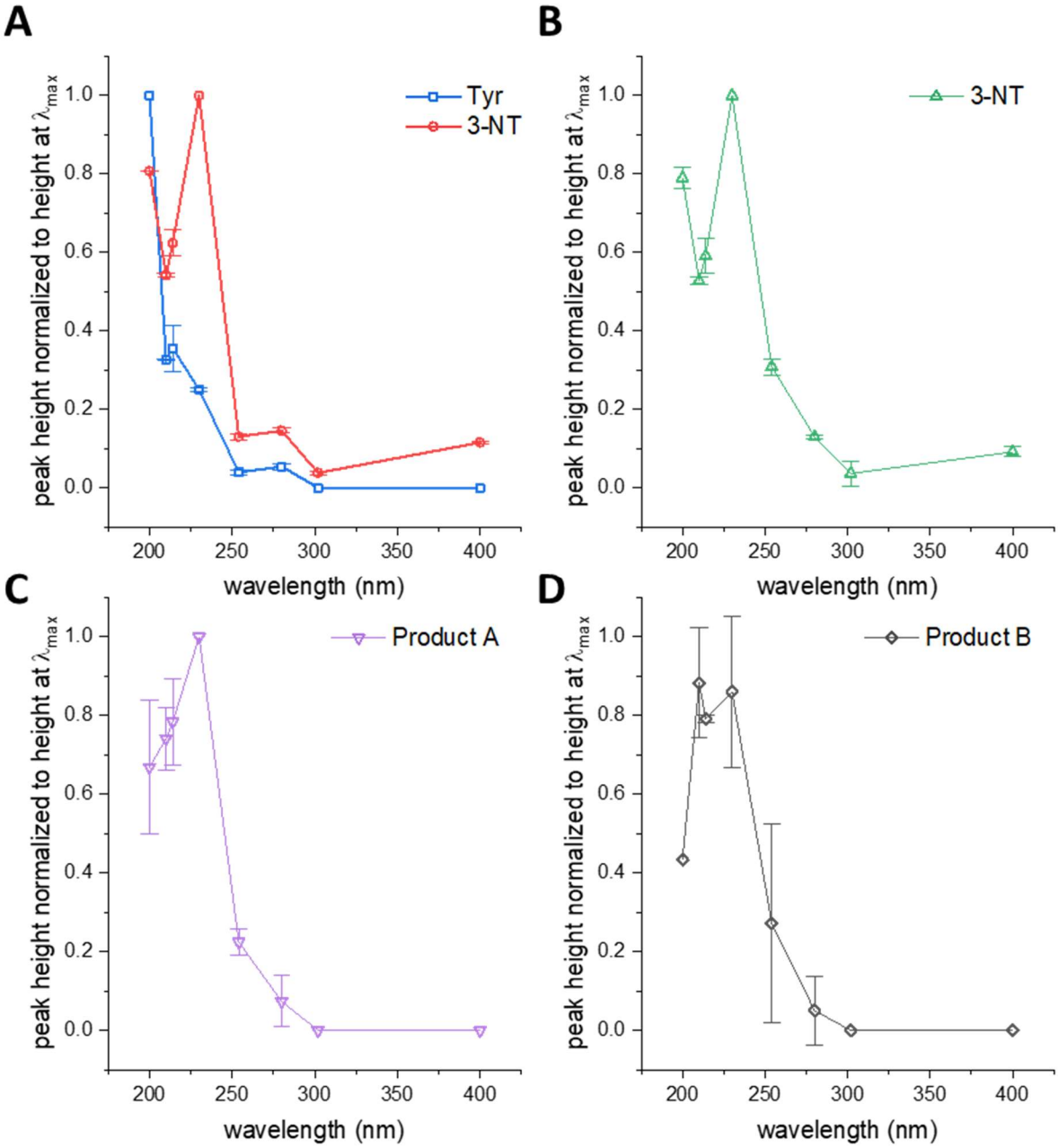

Figure 5.9. Ratio of peak heights at varied wavelengths for (A) tyrosine and 3-NT standards, (B) the product peak identified as 3-NT, (C) Product A, and (D) Product B. (n = 3)

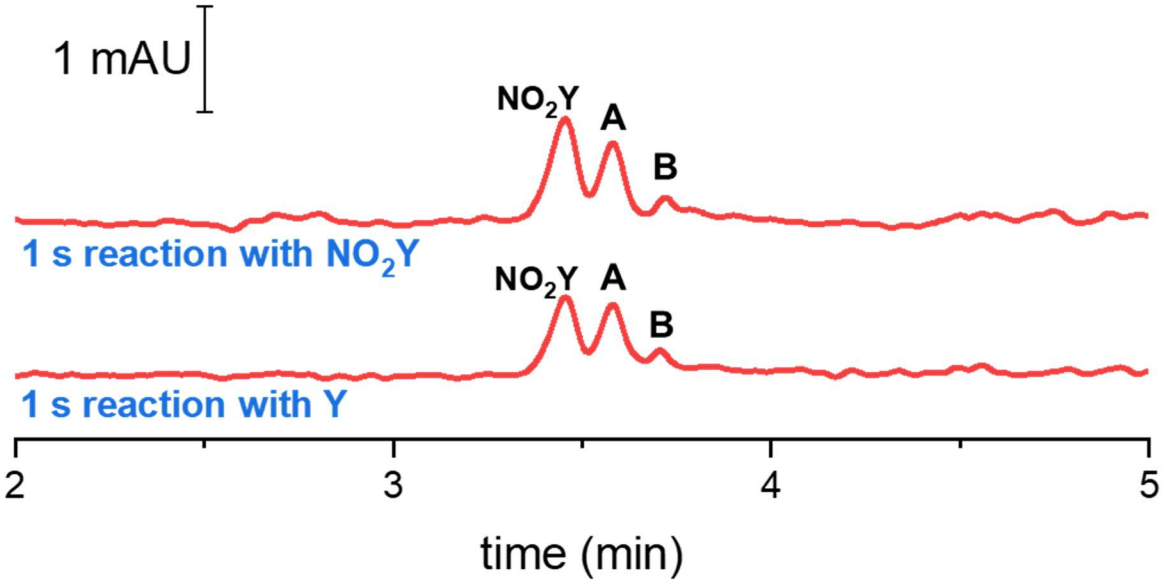

Figure 5.10. Result of reacting peroxynitrite (tdeg = 1s) with tyrosine (bottom) vs reacting it with 3-nitrotyrosine (top).

To elucidate the mechanism and identity of these products, we designed experiments to vary the reaction mixture composition in order to determine which species could be responsible for the formation of A and B. The reaction scheme for the synthesis of peroxynitrite is reproduced from Robinson and Beckman in Figure 5.11.[7] The ratio of reactants (nitrite to hydrogen peroxide) was varied as well as the concentration of HCl in the system for reactions with a 1 s peroxynitrite degradation time. As shown in Table 5.2, when hydrogen peroxide was the limiting reactant, as in the optimal reaction conditions used for the synthesis of peroxynitrite, the production of nitrotyrosine exceeded the production of the by-product peaks A and B. However, when nitrite was the limiting reactant, more A and B than nitrotyrosine was observed. In the intermediate case of stoichiometric amounts of each of these reactants, the preferred product is dependent on the concentration of acid in the system, with a higher HCl concentration resulting in an excess of A and B and a lower HCl concentration resulting in an excess of nitrotyrosine.

Based on the observations shown in Table 5.2, it may be inferred that the formation of products A and B involves a reaction with acidified hydrogen peroxide. When hydrogen peroxide is the limiting reactant, it is completely consumed within around 5-7 s of its addition to the nitrite, resulting in a loss of products A and B after this time and preservation of 3-nitrotyrosine. However, when hydrogen peroxide is not the limiting reagent, the 3-nitrotyrosine produced can continue to be converted into A or B until little nitrotyrosine remains. At this point, it was hypothesized that protonated hydrogen peroxide was undergoing aromatic attack at the 5 position of the benzene ring to produce a dihydroxylated, nitrated ring.

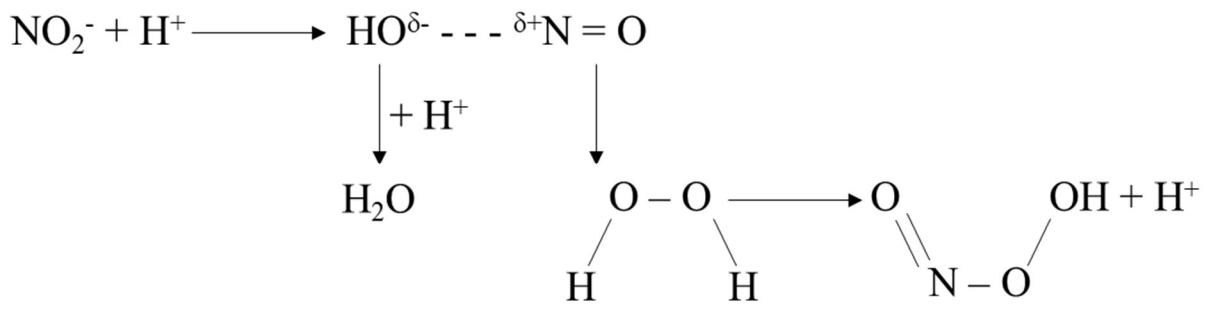

Figure 5.11. Reaction scheme of the synthesis of peroxynitrite.[7]

Table 5.2. Effect of varying the ratio of reactants and acidity on the observed reaction products A and B (n = 2).

NO_2^-	H_2O_2	HCl	Result
Excess	Limiting	Lower	NO_2Y > A/B
Excess	Limiting	Higher	NO_2Y > A/B
Stoichiometric	Stoichiometric	Lower	NO_2Y > A/B
Stoichiometric	Stoichiometric	Higher	A/B > NO_2Y
Limiting	Excess	Lower	A/B > NO_2Y
Limiting	Excess	Higher	A/B > NO_2Y

To test this hypothesis, tyrosine and nitrotyrosine were each exposed to acidified hydrogen peroxide over time. As shown in Figure 5.12A, no peaks were observed in the region of products A or B when water or tyrosine were exposed to acidified hydrogen peroxide, while a tail was observed on the nitrotyrosine peak during its exposure. This tail was more pronounced on some subsequent runs over a period of 4 h, although it never was resolved from a second peak (Figure 5.12B). This leaves two possibilities: either the nitrotyrosine underwent complete conversion to A under these conditions and there was no residual nitrotyrosine present to be resolved from A, or the two peaks were comigrating and the tail was representative of the production of A. Further experiments are needed to know definitively, as the UV spectra of these peaks are inconclusive (Figure 5.12C).

Based on the data gathered thus far, the proposed reaction scheme may be found in Figure 5.13, which shows H_2O_2 reacting under acidic conditions to impart additional hydroxyl groups on the 3-NT that is being produced through reaction with peroxynitrite. Once all the H_2O_2 has been consumed in the synthesis of peroxynitrite, no further hydroxylation would be observed and any 3-NT produced at this point would remain unmodified, thus explaining the maximum 3-NT production at later degradation times.

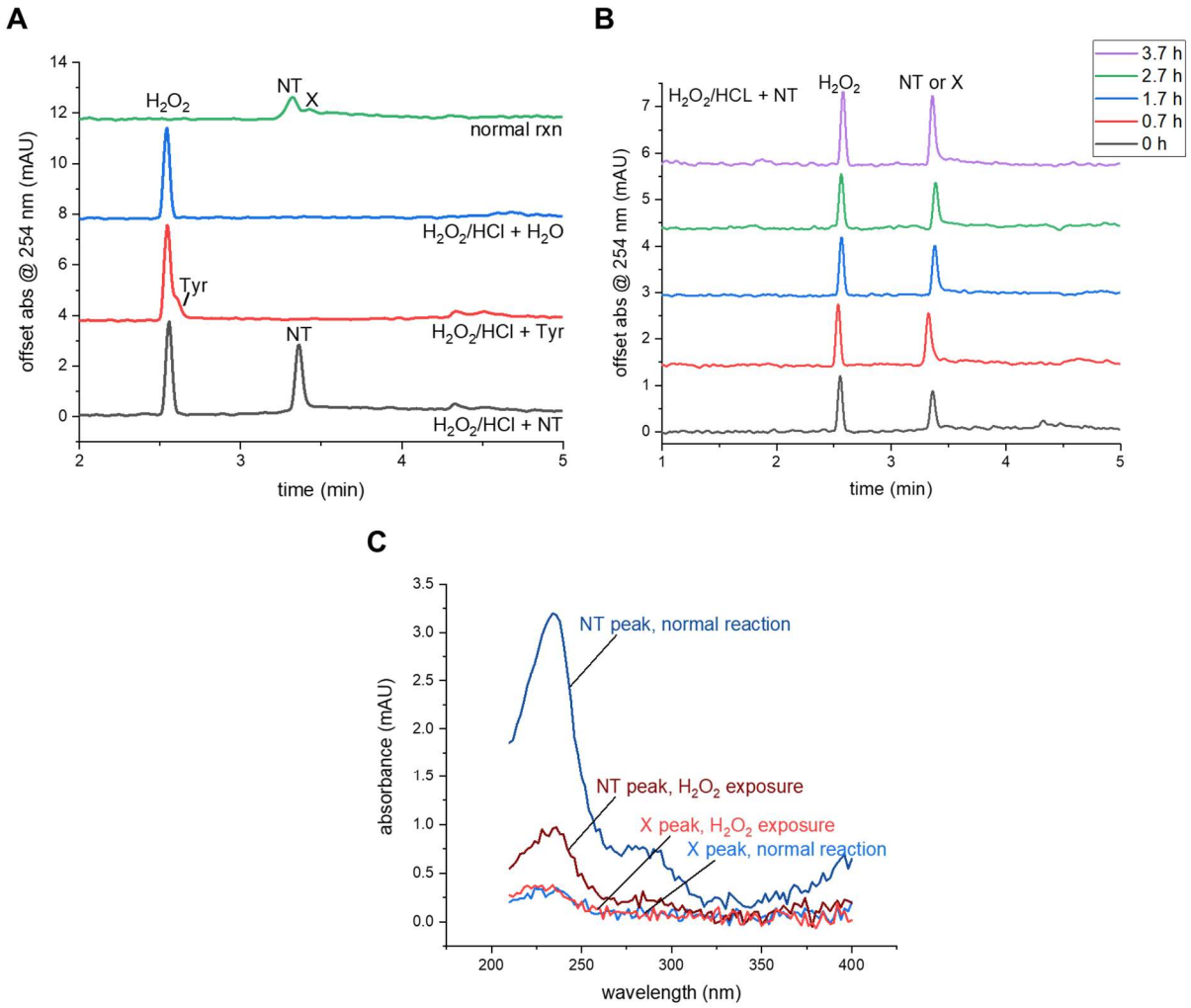

Figure 5.12. (A) comparison of a typical reaction (green) with exposure of (blue) water, (red) tyrosine, and (black) nitrotyrosine to acidified hydrogen peroxide. (B) results of nitrotyrosine exposure to acidified hydrogen peroxide over 4 h, (C) spectra of reaction peaks (blue) and exposure peaks (red). "X" denotes peaks A/B. (n = 1)

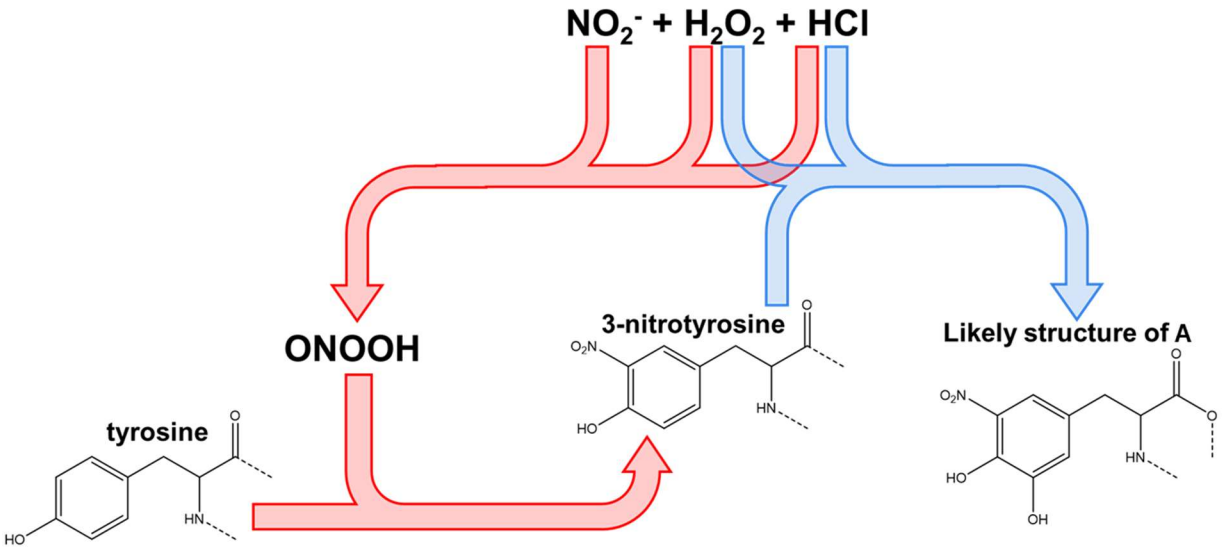

Figure 5.13. Proposed reaction scheme for the production of 3-nitrotyrosine and Product A.

5.4.2.4 Reactions of peroxynitrite with other tyrosine-containing analytes

From our initial studies, it was evident that, while peroxynitrite was acting to nitrate the free tyrosine residues, there were other factors at play resulting in the formation of additional products. We then wondered whether other tyrosine-containing species would undergo similar reactions. Therefore, we reacted a variety of modified tyrosine residues and tyrosine-containing peptides under the same conditions as used previously (1 s degradation time) and detected the products using the optimal CE separation conditions (Figure 5.14). For any reaction that induced a peak shift, the reaction was repeated in the absence of nitrite in order to determine whether the product was a result of peroxynitrite formation or the H_2O_2/HCl mixture. From these experiments, it was evident that AY and A(NO_2Y) react in a nearly identical manner to free Y and NO_2Y, while AYL and A(NO_2Y)L likely do as well (although under these separation conditions the resulting products are largely comigrating) (Figure 5.14A-C).

The reaction with the FSAYLER peptide resulted in the production not only of nitration peaks but also of another product that migrates between the nitrated and non-nitrated peptide (Figure 5.14D). When different aliquots of this peptide were exposed to the H_2O_2/HCl mixture or to each reagent individually, the CE results showed that the unknown product is dependent on the presence of HCl in the system. We hypothesize this product is therefore due to acid hydrolysis of the peptide, although we can rule out AY and AYL as possible products based on the migration time and absorbance data. This product did not appear in every reaction mixture, however, and must be further studied. Similarly, reaction of the peroxynitrite reaction mixture with FSA(NO_2Y)LER produced a similar array of comigrating nitration peaks to those observed in FSAYLER, although in the trials run thus far the additional acid hydrolysis product has not been observed.

The reactions of dityrosine, 3-chlorotyrosine, and L-DOPA in this peroxynitrite-generating system also each resulted in the formation of new products. The reaction of dityrosine results in two new prominent peaks with negative electrophoretic mobilities, indicating that these products likely contain one or more nitro-groups (Figure 5.14F). The reaction of 3-chlorotyrosine in this environment resulted in a single peak shifted to a more negative electrophoretic mobility (Figure 5.14E). Interestingly, the reaction of L-DOPA resulted in a loss of any peak that absorbs between 200 and 400 nm and migrates within the 5-minute separation window (not pictured). One possible explanation for this would be the oxidation and then polymerization of L-DOPA under the highly oxidizing conditions, which could result in a loss of the peak. The only analyte that did not show any significant shift in migration time was 3-aminotyrosine; however, when the peak height ratio relative to the height at the wavelength of maximum absorbance of the reaction mixture peak is compared to that of 3-aminotyrosine, several key differences are noted that could be indicative of a change in its structure or the production of a comigrating product (Figure 5.14E).

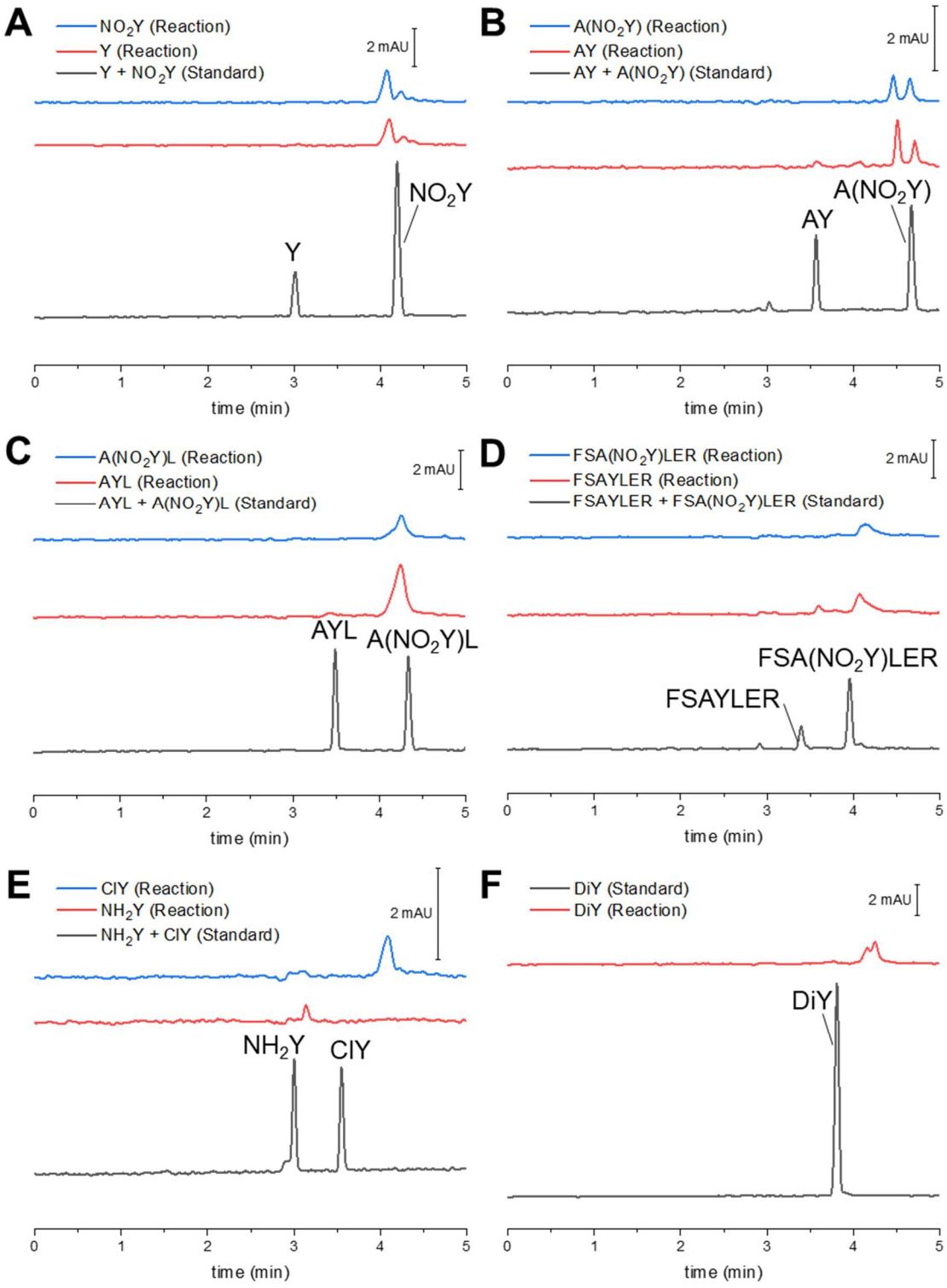

Figure 5.14. Comparison of products of the reaction of various tyrosine-containing species with peroxynitrite reaction mixture with standard solutions of (A) Y and 3-NO_2Y, (B) AY and A(NO_2Y), (C) AYL and A(NO_2Y)L, (D) FSAYLER and FSA(NO_2Y)LER, (E) NH_2Y and ClY,, and (F) DiY. Reaction with L-DOPA is unpictured but results in a loss of the L-DOPA peak.

5.4.3 Additional uses of the optimized CE-DAD method

5.4.3.1 Evaluation of the formation of artifactual 3-nitrotyrosine during sample storage

In the literature, much of the controversy surrounding quantification of biological 3-nitrotyrosine is based on the production of artifactual 3-nitrotyrosine during sample preparation and analysis. Therefore, it is important to develop an understanding of the conditions under which artifactual 3-nitrotyrosine may form in order to develop strategies to address its formation. These strategies could include avoiding nitrating conditions during sample preparation, accounting for the artifactual formation through use of internal standards, or additional steps to ensure all detected NT was present in the original biological system of interest. Therefore, this CE method was also used to evaluate one of the most common sources of artifactual 3-nitrotyrosine formation, acidified nitrite. Peroxynitrite was produced as shown in Figure 5.15A and tyrosine was added with a degradation time of 15 s which had previously proved sufficient to result in no detectable 3-nitrotyrosine formation. Then, this mixture of tyrosine with "degraded peroxynitrite" and a high concentration of HCl was left to incubate at room temperature for 10 h and the conversion of tyrosine to nitrotyrosine was observed at multiple time points. As shown in Figure 5.15B, by the 10 h point around half the tyrosine had been converted into 3-nitrotyrosine due to this exposure to acidified nitrite.

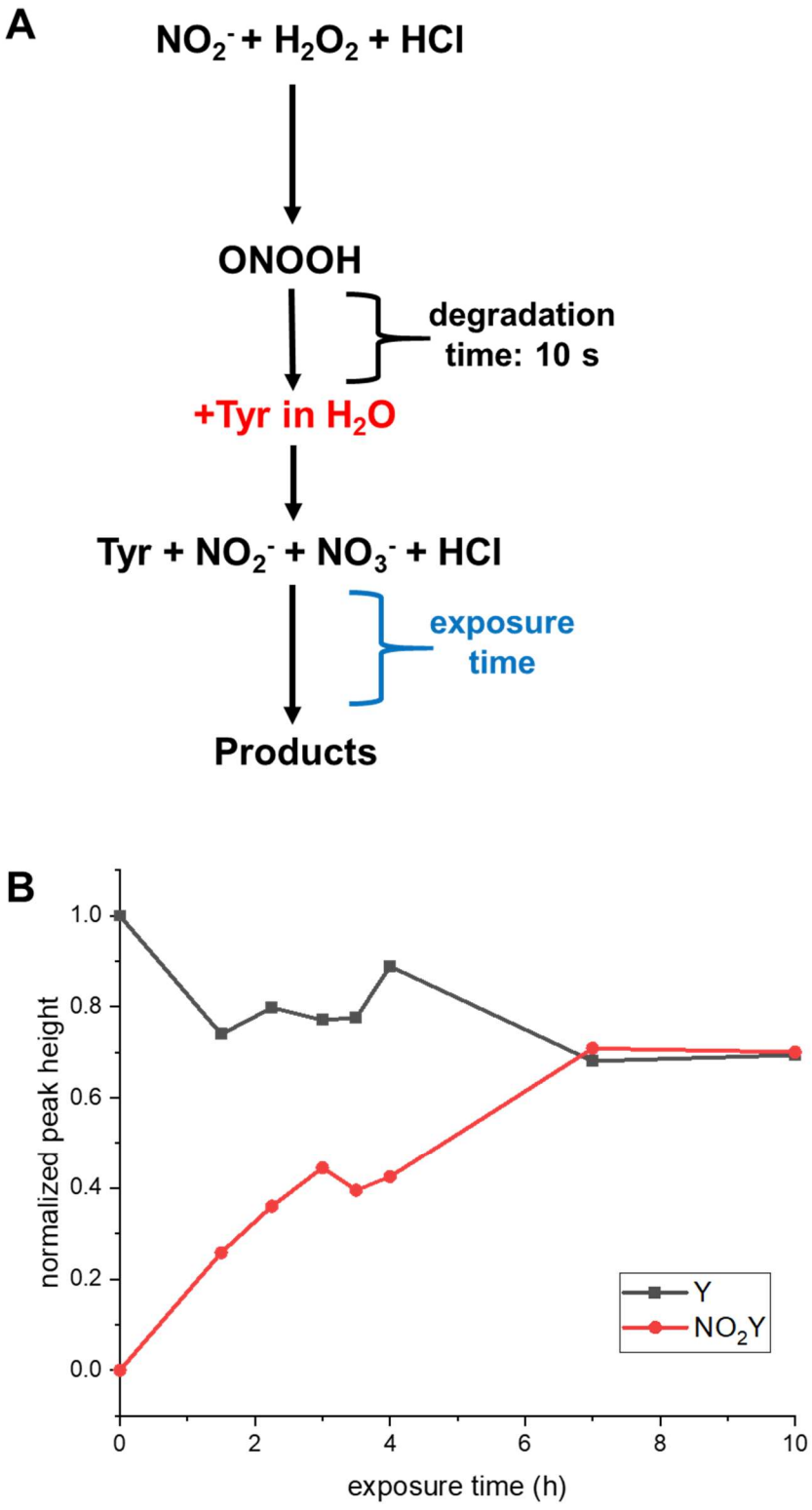

Figure 5.15. (A) Scheme for exposure of tyrosine to acidified nitrite, (B) Conversion of tyrosine to nitrotyrosine upon exposure to acidified nitrite (n = 1).

In a separate experiment, samples were left in different conditions for a period of one week and again the conversion of tyrosine into nitrotyrosine was observed over time. In the sample left at -80 ℃, no nitration was observed, while in the sample left at room temperature, the tyrosine was almost entirely converted into 3-nitrotyrosine over the course of one week, and the samples left at 4 ℃ and -20 ℃ exhibited intermediate conversion to 3-nitrotyrosine (Figure 5.16). Of the four storage temperatures, the -20 ℃ storage condition resulted in the greatest degree of variability in the extent of nitration among the three samples. This resulted in nearly complete overlap of the -20 ℃ and 4 ℃ nitration vs exposure time curves when standard deviation is considered, indicating that there is still significant nitration possible even when samples are stored in a typical freezer. Other works have discussed the artifactual nitration of tyrosine during freezing and freeze-thaw cycles and have reported on conditions prone to increased artifactual NT formation.[5] Ultimately, this data demonstrates the importance of careful control of nitrite content and storage conditions for biological samples if one wishes to avoid the artifactual nitration of tyrosine post-sampling and pre-analysis. While this is an extreme example, this CE-DAD method could theoretically be used to rapidly evaluate more subtle changes in the storage and sample preparation conditions in order to confirm that no detectable 3-NT is produced during those processes. Additionally, in each situation, no additional byproducts were observed, supporting the hypothesis that nitrite does not play a role in the generation of products A and B once nitrotyrosine is produced and that hydrogen peroxide is essential for the formation of these byproducts.

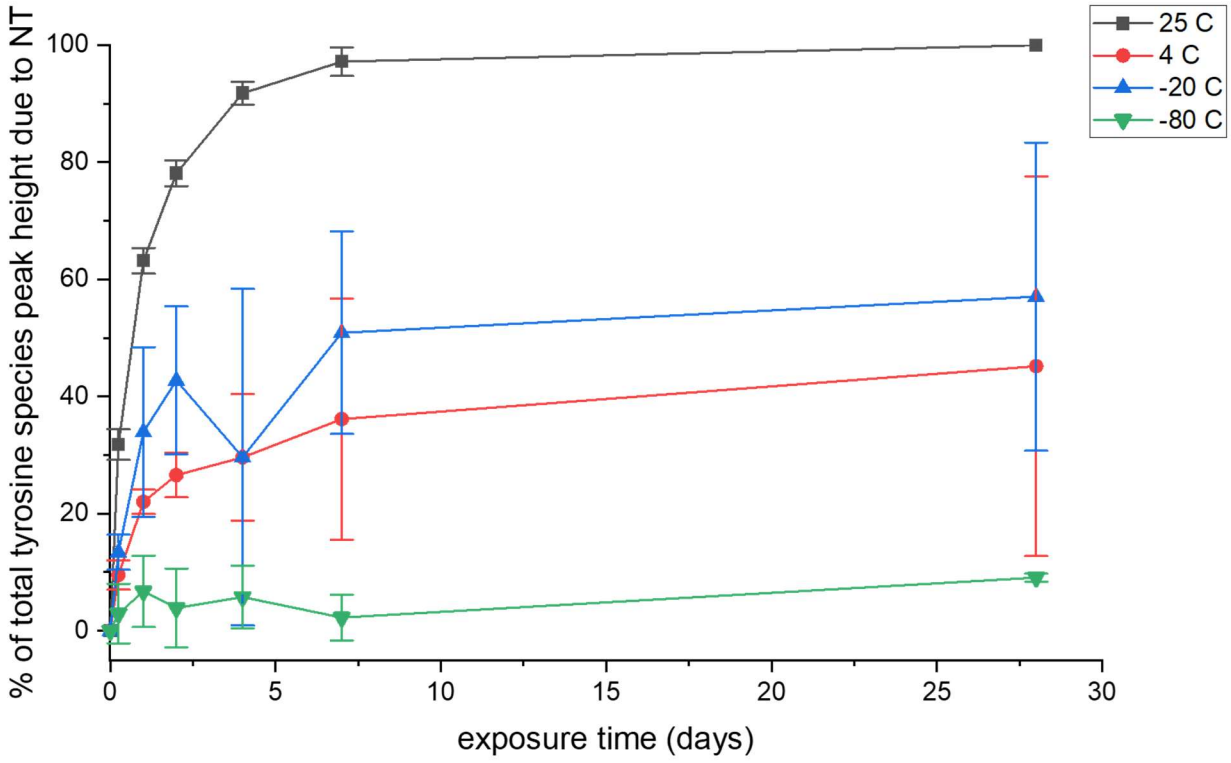

Figure 5.16. Conversion of tyrosine to 3-nitrotyrosine upon exposure to nitrite under acidic conditions at a variety of temperature (n=3).

5.4.3.2 Detection of tyrosine reaction products in the presence of SIN-1

While the nitrite/acidic hydrogen peroxide synthesis of peroxynitrite is useful for producing a wide variety of products to validate the CE-DAD system's ability to detect oxidative tyrosine products, these conditions are not comparable to the manner in which peroxynitrite is produced and exposed to proteins in the cell. Similarly to physiological conditions, in the presence of oxygen, SIN-1 produces superoxide and nitric oxide, which in turn react to produce peroxynitrite. SIN-1 was exposed to oxygen upon addition of tyrosine or water and the products were tracked at 10 timepoints, each approximately 20 min after the last, for a total exposure time of around 2.5 h. The same prominent peaks from the SIN-1 system were observed in each electropherogram at around 2.0 (Peak 1) and 2.6 min (Peak 2), while a large unreacted tyrosine peak at around 2.5 min (Peak 3) was also observed in the tyrosine system (Figure 5.17). At $t > 20$ min, a few other small peaks unique to the tyrosine system were also observed migrating between 3.0 and 4.0 min (Peaks 4, 6, 7), while both systems exhibited Peak 5 growing in over time. While it is possible that these peaks could be dityrosine, L-DOPA, or 3-nitrotyrosine, the peaks were not intense enough to attain a UV spectrum capable of definitive identification. Further experiments must be done to improve the peroxynitrite production kinetics and result in an observable decrease of the tyrosine peak over time.

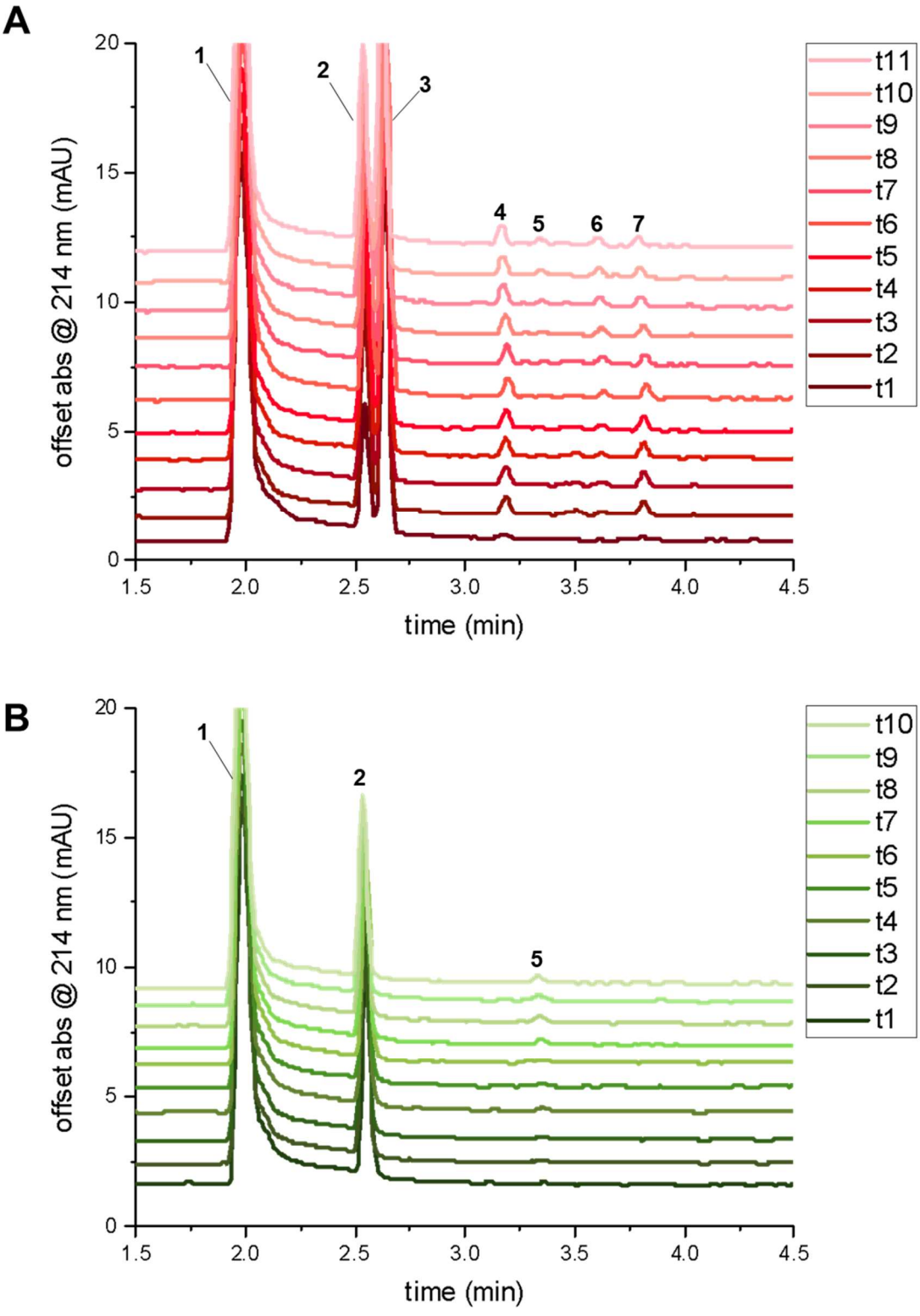

Figure 5.17. SIN-1 with (A) tyrosine or (B) water at 10 timepoints (t1 → t10). Peak 3 can be identified as tyrosine, and peaks 4, 6, and 7 could be oxidative modifications of tyrosine. (n = 1)

5.4.3.3 Observation of the reduction of 3-nitrotyrosine *via* sodium dithionite

Sodium dithionite is often used to reduce nitro groups to amino groups for selective detection of 3-nitrotyrosine in the presence of artifactual 3-nitrotyrosine formation. Therefore, we attempted to reduce 3-NT to 3-AT in an effort to confirm that the reduction was proceeding to completion under these conditions and to observe which product peaks contained reducible nitro groups. Initially, a standard of approximately 60 μM 3-NT diluted in 1.5 mL run buffer was analyzed using the CE method. Then, approximately 3 mg sodium dithionite was added to the vial and the sample was analyzed a second time to determine the extent of reduction. Under these conditions, the nitrotyrosine was completely converted to 3-aminotyrosine, as evidenced by its comparison to a sample of 3-aminotyrosine of similar concentration (Figure 5.18A). Then, the reaction of peroxynitrite with tyrosine with 1 s degradation time was run and the 1.5 mL product mixture in BGE was incubated briefly with 3.0 mg sodium dithionite before reinjection into the CE. As shown in Figure 5.18B, this resulted in a loss of the primary 3-NT peak and the growth of a peak at approximately 2.9 min, comigrating with the 3-AT peak observed in Figure 5.18A. When the peak height of this 2.9 min peak at various key wavelengths both before and after the sodium dithionite exposure is compared to the 3-aminotyrosine peak, it may be concluded that the absorbance of the post-reduction peak follows a similar pattern to 3-aminotyrosine. This indicates that the 3-nitrotyrosine produced in the reaction has been completely converted to 3-aminotyrosine. Therefore, this CE-UV method has been demonstrated to be capable of evaluating reduction conditions for sample preparation in other more selective analytical methods.

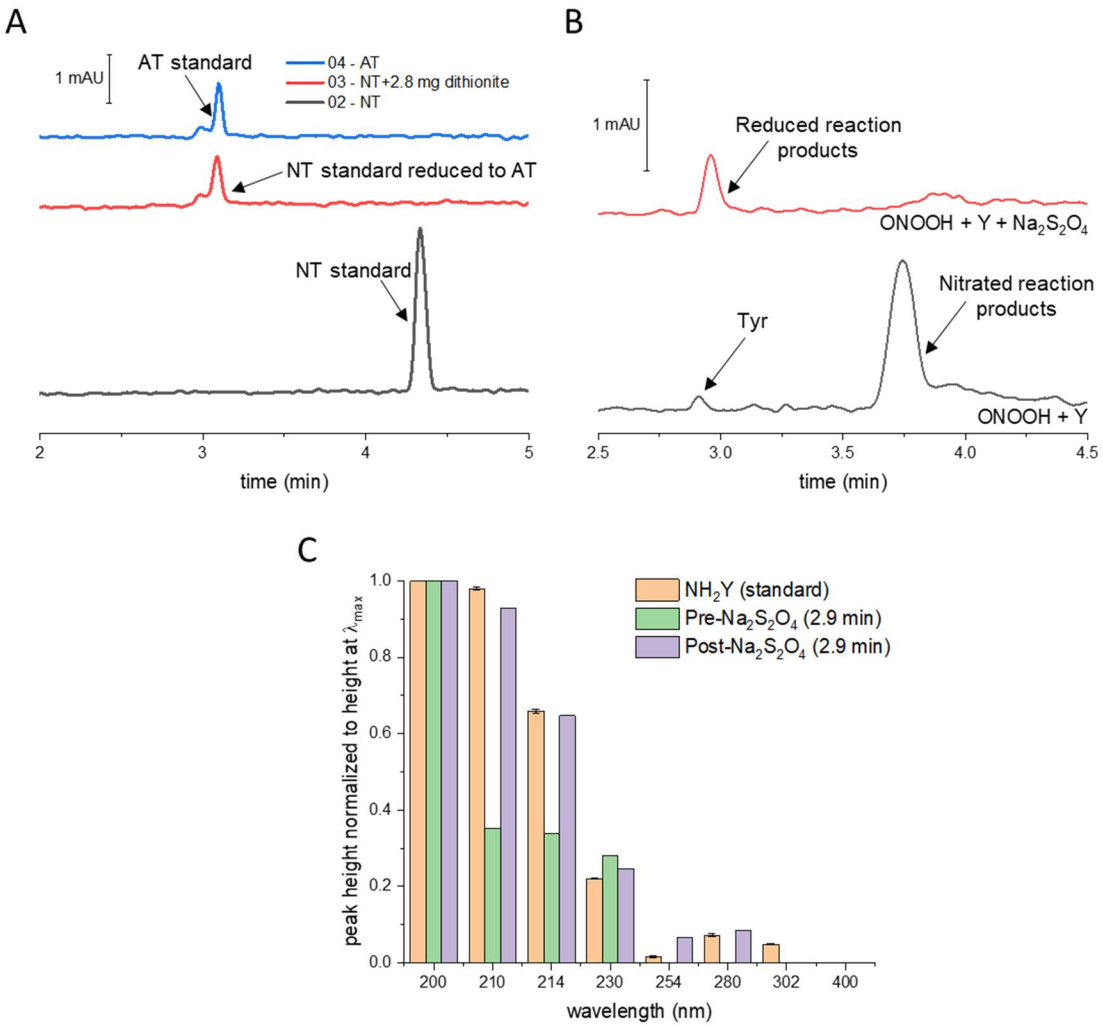

Figure 5.18. Use of sodium dithionite to reduce (A) 3-NT standard solution and (B) tyrosine/peroxynitrite reaction mixture (t_{deg} = 1 s); (C) comparison of DAD data of the peak at approximately 2.9 min before and after the sodium dithionite reduction with DAD data.

5.4.3.4 Evaluation of extraction conditions for further analysis of complex samples

An extraction step post-reaction could enable the elimination of salt content for MS confirmation of peak identities as well as the elimination of sodium dithionite post-reduction in order to clear the electropherogram of excess noise and unwanted background peaks. Therefore, peroxynitrite and tyrosine were reacted under the conditions described above and the pH of the resulting mixture was adjusted via addition of a sodium bicarbonate solution to obtain various pH values ranging from 2 – 7. Next, an equivalent volume of ethyl acetate was added to the sample and the sample vial was sealed and inverted several times to mix. The organic fraction containing the organic molecules of interest was then obtained and the solvent was evaporated in a stream of nitrogen gas. To assess the success of the extraction, this dried sample was then resuspended in a volume of water equivalent to the initial volume of the reaction and this "undiluted" sample was then injected into the CE. As expected, as the pH of the aqueous phase of the extraction nears the pK_a of the hydroxyl group of 3-nitrotyrosine (approximately 6.7), the extraction efficiency decreases as the nitrated species of interest become charged and have greater affinity for the aqueous phase (Figure 5.19A). A pH of 3.0 was selected for future experiments based on the peak intensities obtained at each pH. However, it was observed that while some extractions at this pH resulted in the peak pattern observed in Figure 5.19A, others resulted in a different peak intensity pattern, as shown in Figure 5.19B and compared to a 10-times diluted typical unextracted reaction mixture. This seems to indicate that while pH 3.0 is appropriate for extraction of multiple products in detectable quantities, small variations in the pH may be resulting in inconsistent extractions. This could be because the pH is close to the pK_a of the carboxylic acid and the products must be neutral with a deprotonated carboxylic acid in order to be efficiently extracted into the ethyl acetate. Ultimately, the CE-DAD method has enabled the rapid evaluation and initial optimization of an extraction protocol for further analysis.

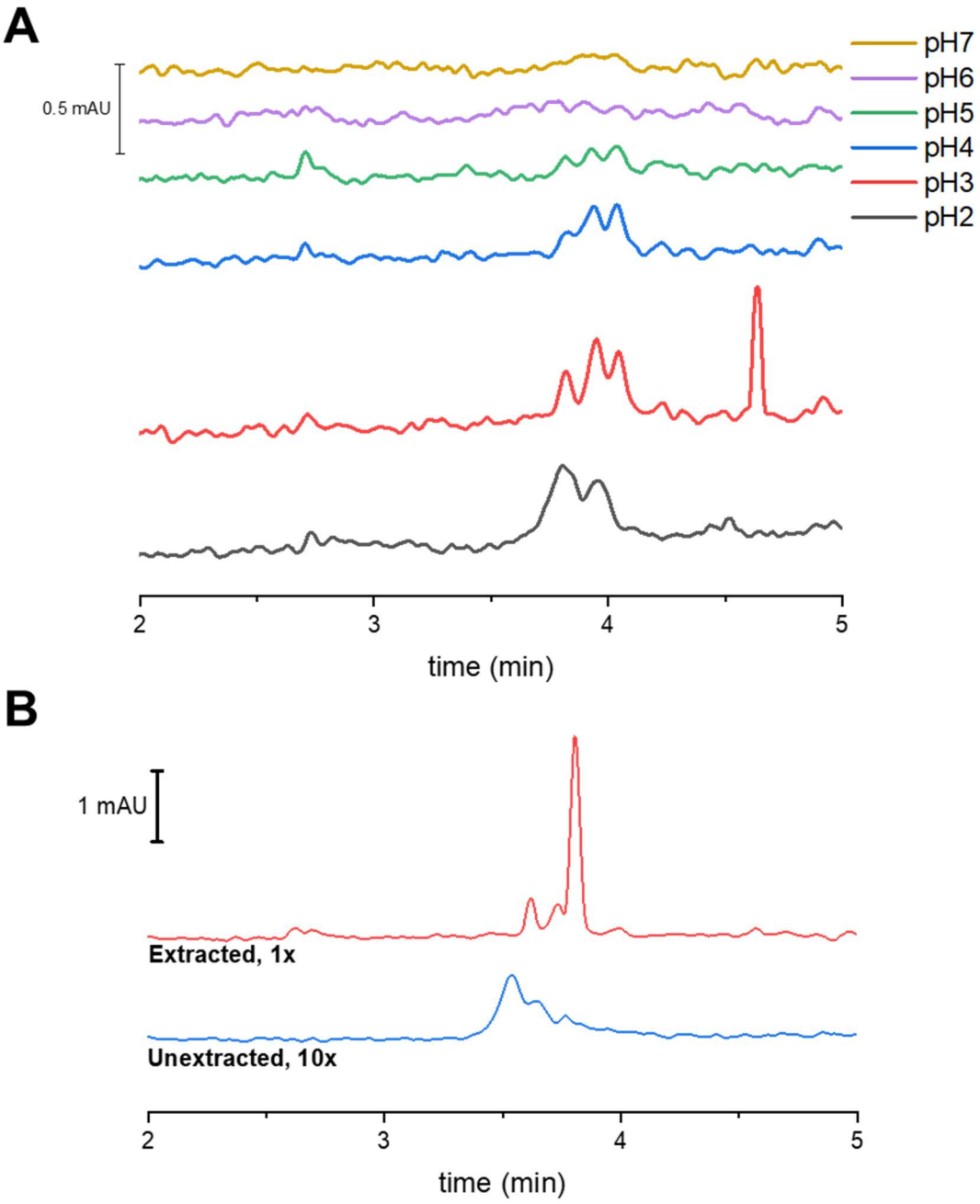

Figure 5.19. (A) Effect of varying pH on the extraction efficiency of reaction product peaks and (B) Result of extraction step on reaction samples.

5.4.4 Confirmation of peak identities using mass spectrometry

In this work, we have demonstrated the wide range of information that can be gained using only a capillary electrophoresis instrument with diode array detector. However, it was of interest to use another method to attempt to confirm the peak identities that were proposed earlier in this work. Reaction samples were analyzed using a LC-MS method and the presence of 3-nitrotyrosine in both the extracted sample and the filtered crude reaction mixture was confirmed. Additionally, low signals were observed for 3-NT with one or three additional hydroxyl groups on it (two or four total), although at the quantity analyzed it was not possible to definitively confirm the presence of these species. In order to determine whether these species are present in the reaction mixture, this experiment will be repeated in the future with a more high-resolution instrument. The comparison of our approach to liquid chromatography-mass spectrometry highlights the benefits of low sample requirements and analysis of samples with complex biological matrices that are highlights of CE and demonstrates that, although CE-DAD is not a structural characterization method, significant structural information may be gained through careful design of experiments.

5.5 Concluding remarks

Peroxynitrite has been synthesized and samples characterized via CE-UV. A separation of several tyrosine-containing analytes has been optimized using CE-UV and the products of the exposure of tyrosine and nitrotyrosine with peroxynitrite, acidified nitrite, acidified hydrogen peroxide, and sodium dithionite have been observed using this separation. Several reaction products have been tentatively identified using this CE-DAD method, highlighting the broad applications of this technique for low volume analysis of complex, highly conductive reaction mixtures. In the future, this method will be applied to less extreme reaction conditions in order to profile more physiologically relevant conditions of nitrosative and oxidative stress and the conditions that impact free and peptide-bound tyrosine nitration and oxidation.

5.6 References

1. Cheignon, C.; Tomas, M.; Bonnefont-Rousselot, D.; Faller, P.; Hureau, C.; Collin, F., Oxidative stress and the amyloid beta peptide in Alzheimer's disease. *Redox Biology* **2018,** *14*, 450-464.
2. Bartesaghi, S.; Radi, R., Fundamentals on the biochemistry of peroxynitrite and protein tyrosine nitration. *Redox Biology* **2018,** *14*, 618-625.
3. Teixeira, D.; Fernandes, R.; Prudencio, C.; Vieira, M., 3-Nitrotyrosine quantification methods: Current concepts and future challenges. *Biochimie* **2016,** *125*, 1-11.
4. Tsikas, D., What we—authors, reviewers and editors of scientific work—can learn from the analytical history of biological 3-nitrotyrosine. *J. Chromatogr. B* **2017,** *1058*, 68-72.
5. Daiber, A.; Bachschmid, M.; Kavaklí, C.; Frein, D.; Wendt, M.; Ullrich, V.; Munzel, T., A new pitfall in detecting biological end products of nitric oxide—nitration, nitros (yl) ation and nitrite/nitrate artefacts during freezing. *Nitric Oxide* **2003,** *9* (1), 44-52.
6. Herce-Pagliai, C.; Kotecha, S.; Shuker, D. E., Analytical methods for 3-nitrotyrosine as a marker of exposure to reactive nitrogen species: a review. *Nitric Oxide* **1998,** *2* (5), 324-336.
7. Robinson, K. M.; Beckman, J. S., Synthesis of peroxynitrite from nitrite and hydrogen peroxide. *Methods Enzymol.* **2005,** *396*, 207-214.
8. Dremina, E. S.; Li, X.; Galeva, N. A.; Sharov, V. S.; Stobaugh, J. F.; Schöneich, C., A methodology for simultaneous fluorogenic derivatization and boronate affinity enrichment of 3-nitrotyrosine-containing peptides. *Anal. Biochem.* **2011,** *418* (2), 184-196.
9. Ryberg, H.; Caidahl, K., Chromatographic and mass spectrometric methods for quantitative determination of 3-nitrotyrosine in biological samples and their application to human samples. *J. Chromatogr. B* **2007,** *851* (1-2), 160-171.
10. Sharov, V. S.; Galeva, N. A.; Kanski, J.; Williams, T. D.; Schöneich, C., Age-associated tyrosine nitration of rat skeletal muscle glycogen phosphorylase b: characterization by HPLC–nanoelectrospray–Tandem mass spectrometry. *Experimental gerontology* **2006,** *41* (4), 407-416.
11. Sharov, V.; Pal, R.; Dremina, E.; Michaelis, E.; Schöneich, C., Fluorogenic tagging of protein 3-nitrotyrosine with 4-(aminomethyl) benzene sulfonate in tissues: a useful alternative to immunohistochemistry for fluorescence microscopy imaging of protein nitration. *Free Radical Biol. Med.* **2012,** *53* (10), 1877-1885.

Chapter 6

Microchip electrophoresis with dual electrode amperometric detection for the selective study of tyrosine nitration

6 Chapter 6: Microchip electrophoresis with dual electrode amperometric detection for the selective study of tyrosine nitration

6.1 Introduction

During conditions of nitrosative and oxidative stress biomolecules, such as proteins, are often subjected to posttranslational modifications that result in the introduction functional groups such as nitro-, hydroxy-, or chloro- onto specific amino acids. Tyrosine is one of the most commonly modified residues, due to its ease of being oxidized to the tyrosyl radical, which in turn may react with a variety of endogenous free radicals to form modified tyrosine residues such as 3-nitrotyrosine (3-NT), 3-chlorotyrosine, dityrosine, and 3,4-dihydroxytyrosine (L-DOPA).[1, 2] While these modifications are a hallmark of nitrosative and oxidative stress that are often quantified in place of the far more difficult to detect transient reactive species themselves, such as peroxynitrite, unmodified tyrosine will still always appear in significant excess compared to the modified residues, with some estimates stating that nitrotyrosine residues will be 1 in every 10,000 unmodified tyrosine residues under conditions of oxidative stress.[2] Therefore, it is of interest to develop methods capable of selective detection of nitrotyrosine in the presence of an excess of tyrosine.

A variety of methods have been used to detect nitrotyrosine, including liquid or gas chromatography with mass spectrometry, fluorescence, or electrochemical detection and immunoassays.[3-8] While LC-MS remains the gold standard for detection of posttranslational modifications in proteins, quantification can be difficult, it is expensive, and it generates a large amount of data. [9,44] Electrochemical detection, conversely, is a lower cost approach that is still sensitive. Several groups have used LC-EC in generation-collection mode to selectively detect nitrotyrosine by first reducing the nitro group to a hydroxylamine or amine followed by detection at a lower oxidation potential than that required for tyrosine.[9-12] Using these dual electrode

detection methods, increased amounts of 3-NT have been detected in a variety of biological samples, including the cerebrospinal fluid of Alzheimer's disease patients.[13, 14]

This chapter describes efforts towards adapting this dual electrode detection method for 3-NT so it is compatible with microchip electrophoresis (ME) enabling lower sample volumes and faster analysis than LC. While dual electrode electrochemical detection of 3-NT has not been reported on a microchip, dual electrode ME-EC of other species has been achieved in two configurations: dual-series and dual-parallel.[15, 16] The dual-parallel configuration may be used with dual-channel ME-EC either to background correct through using one channel/electrode pair as a reference channel and the other as the sampling channel or to obtain voltammetric information by monitoring the same sample at two separate potentials. [17-19] In the dual-series configuration, the same sample plug passes over two working electrodes held at different potentials. This can produce voltammetric information, as in dual-parallel detection; however, correction factors may be necessary to account for analyte depletion at the first working electrode and the difference in alignment of each working electrode relative to the separation field.[19] Dual series electrode ME-EC has also been used in generation-collection mode, as in the LC-EC experiments described above, for the selective detection of catecholamines and phenolic acids[20-22] and a peptide-copper complex[23] based on their electrochemistry. This generation-collection mode imparts selectivity by selecting the potentials based on the specific redox properties of the analyte of interest and its most prominent interfering species.

In this work, we describe progress towards the development of a dual electrode ME-EC method for the selective detection of nitrotyrosine in the presence of a significant excess of tyrosine. A single electrode ME-EC method was used first to detect the peroxynitrite-mediated nitration of tyrosine. Then, the method is transferred to a dual-electrode format. Factors affecting the reproducibility and ruggedness of the method are discussed. Additionally, hydrodynamic

voltammograms and calibration curves are used to tentatively identify system peaks and analyte peaks in the reduction and oxidation electropherograms of the dual electrode ME-EC system.

6.2 Material and methods

6.2.1 Reagents and materials

Sodium phosphate monobasic, sodium phosphate dibasic, phosphoric acid, isopropyl alcohol, sodium acetate, acetic acid, boric acid, sodium hydroxide, sodium dodecyl sulfate (SDS), tetradecyltrimethylammonium chloride (TTAC), sodium nitrite, hydrogen peroxide (30%), hydrochloric acid, L-tyrosine, 3-L-nitrotyrosine, 3-chlorotyrosine, 3-aminotyrosine, dopamine, and resazurin were obtained from Fisher. Peptides A(3-NO_2Y)L and AYL were obtained from the CMADP KU Synthetic Chemical Biology Core.

6.2.2 Microchip fabrication

5 cm simple-T PDMS microchips were fabricated as previously described.[24] Briefly, a silicon master was produced with the desired channel pattern and a 10:1 mixture of PDMS elastomer to curing agent was poured onto the master and cured at 70 ℃ for at least 3 hours. The cured microchip was then removed from the master and aligned on an electrode substrate. Chips containing carbon fiber (CF) working electrodes were fabricated in the same manner, except the silicon master contained a single channel in it for insertion of a 33 μm diameter carbon fiber and the PDMS chip was sealed against a piece of glass after removal from the master to add rigidity.[25] An electrical connection was then made between the fiber and a copper wire using silver colloidal and the copper wire was fixed to the substrate using epoxy. Pt band electrodes were fabricated on borofloat glass substrates as previously described using conventional photolithographic techniques.[24] A channel for the electrode (10 or 15 μm wide) was defined in AZ1518 photoresist using a UV exposure mask and then it was etched to the desired depth (~300 nm) using hydrofluoric acid. An adhesive titanium layer was first sputtered onto the substrate followed by

the Pt electrode layer, and excess metal, photoresist, and chrome was removed from the plate prior to connection to a copper lead.

6.2.3 ME-EC procedure

For each set of experiments, a fresh PDMS microchip was aligned on a working electrode substrate with the desired alignment. The separation channel was then flushed with IPA, 0.1 M NaOH, and then background electrolyte (BGE) consisting of a buffer and surfactant. Pt leads connected to high voltage power supplies were placed in the sample and buffer reservoirs and 1600 V and 1900 V were applied to them, respectively, to induce the separation field via a homebuilt LabVIEW program. A ground electrode, counter electrode, and reference electrode were place in the waste reservoir and the WE, CE, and RE were connected to a potentiostat. Electrochemical detection was accomplished using a Dropsens MicroSTAT 300 or 400 potentiostat with Dropview software. Data was then exported as .csv files for analysis in Origin (OriginLabs).

6.2.4 Cyclic voltammetry procedure

Approximately 5 mL of sample was prepared in a beaker containing the working electrode (WE, glassy carbon or gold, 2 mm diameter, obtained from CHI), reference electrode (RE, Ag/AgCl), counter electrode (CE, Pt wire), and an electrolyte solution. A CHI potentiostat was used to apply the CV potential program. Whenever the potential was to be scanned past -0.5 V, the sample was purged for 15-20 min with N_2 prior to taking the CV in order to eliminate the O_2 reduction peak. Data was then exported as .csv files for analysis in Origin (OriginLabs).

6.2.5 Peroxynitrite synthesis

Peroxynitrite was synthesized according to the protocol of Robinson, *et al.*[26] Stock solutions of (1) 0.6 M $NaNO_2$, (2) 0.6 M H_2O_2 with 0.7 M HCl, and (3) 3 M NaOH were prepared and chilled on ice prior to reaction. $NaNO_2$ (200 μL) was added first to a 2-mL Eppendorf tube. The acidified H_2O_2 solution (150 μL) and NaOH solution (200 μL) were then added in quick

succession to the tube to first synthesize the peroxynitrous acid with the addition of the acidified H_2O_2 followed by its stabilization in its anionic form (peroxynitrite) with the addition of the base. This reaction protocol resulted in an average peroxynitrite concentration of around 100 mM based on the absorbance of these solutions at 302 nm.

6.3 Results and discussion

6.3.1 Single electrode detection of tyrosine and nitrotyrosine

First, single electrode ME-EC was used to detect peroxynitrite-mediated tyrosine nitration. A single carbon fiber working electrode was aligned at the end of the separation channel (~0 μm in-channel) of a 5-cm PDMS microchip. Tyrosine and 3-NT were separated using a background electrolyte (BGE) of 10 mM sodium phosphate at pH 6.4 with 2 mM SDS and separation potentials of 1900 V buffer well/1600 V sample well (Figure 6.1A). Next, peroxynitrite was synthesized from the reaction of nitrite with hydrogen peroxide in the presence of hydrochloric acid and a solution of tyrosine in NaOH was added to the reaction mixture immediately after synthesis (<1 s). This sample was then diluted in BGE and injected into the microchip. As shown in Figure 6.1A, this reaction resulted in two peaks in the electropherogram. These peaks, 1 and 2, matched the migration times of tyrosine and 3-NT, respectively, and the relative signals at 0.8 V and 1.0 V matched the general trend of the standards. This indicates that peak 1 is likely unreacted tyrosine and peak 2 is likely a nitrated product. A comparable reaction was then run with the only difference being that the tyrosine was added approximately 5 s after the synthesis of the peroxynitrite, so that most of the peroxynitrite had already degraded to nitrite and nitrate by that point and was no longer reactive. In this electropherogram, only peak 1 was observed, indicating that no detectable levels of product 2 were produced under these reaction conditions.

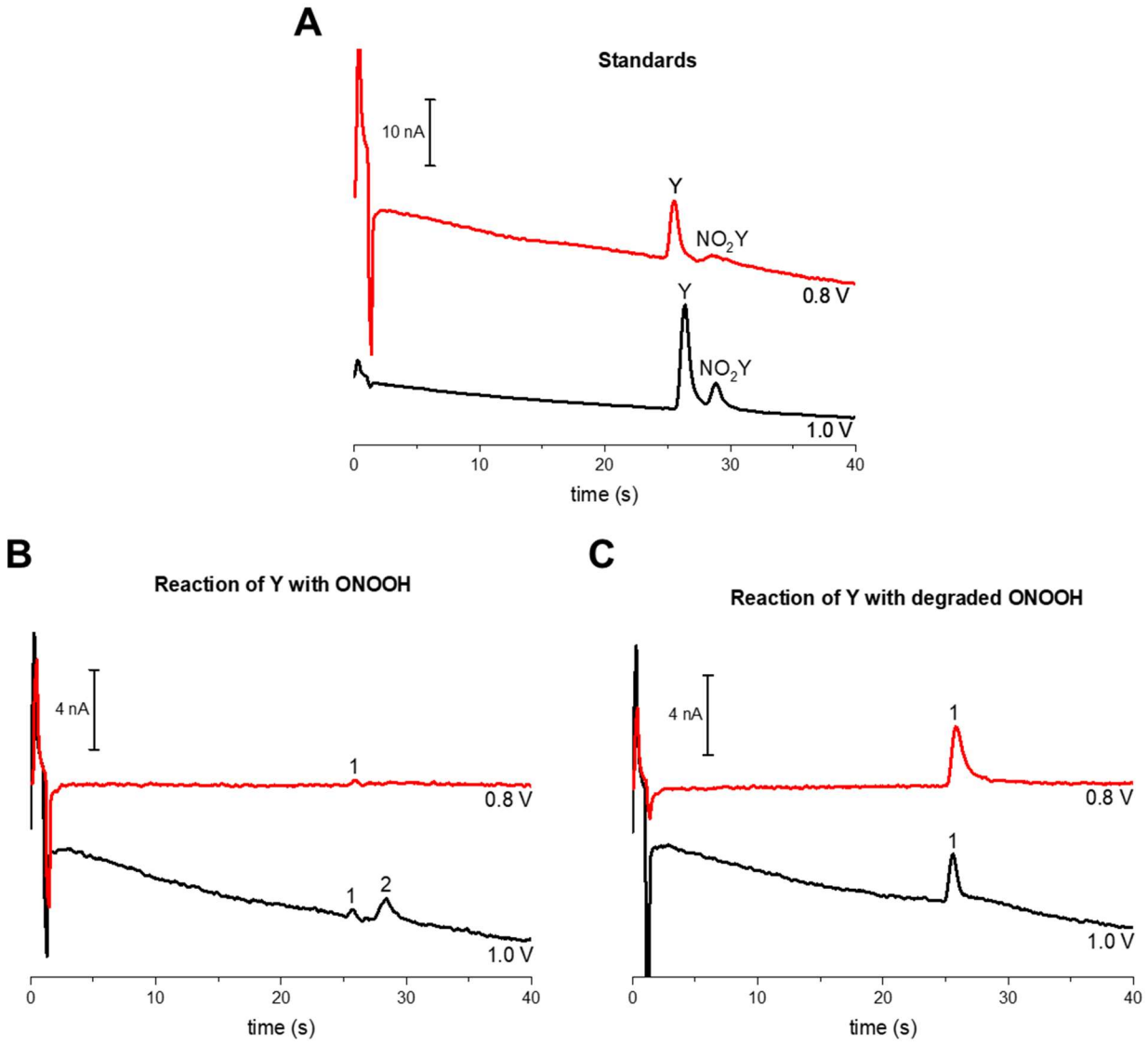

Figure 6.1. ME-EC with a single CF WE aligned pseudo-in-channel of tyrosine (Y) and 3-NT (NO_2Y) at two WE potentials, 0.8 V and 1.0 V *vs*. Ag/AgCl RE. BGE: 10 mM sodium phosphate at pH 6.5, 2 mM SDS. (A) standards (B) products of the reaction of tyrosine and peroxynitrous acid at low pH, (C) products of the reaction of tyrosine with largely degraded peroxynitrous acid (HCl, NO_2^-, NO_3^-). Peak 1 corresponds to unreacted tyrosine and Peak 2 likely corresponds to nitrated tyrosine.

6.3.2 Premise for dual electrode electrochemical detection of 3-NT

Although the single electrode ME-EC method was capable of detecting nitration under these *in vitro* conditions, this method would not be sufficiently sensitive and selective to detect the small amounts of nitrated tyrosine in the presence of large amounts of tyrosine as would be expected in a biological sample. In liquid chromatography methods with electrochemical detection for the analysis of biological 3-NT, the selectivity for 3-NT is often improved through the use of dual electrodes. When dual electrodes in series are used in generator-collector mode, the analyte of interest is first electrochemically converted to a different species at the "generator" working electrode and then this species is detected at a more selective potential at the second "collector" working electrode. This method both enables elimination of interfering peaks through careful selection of potentials and aids in peak identification through collection of voltammetric information.

Cyclic voltammetry is a useful tool for the identification of approximate potentials that can be applied to a dual electrode system. Once these ballpark potentials have been identified, they must then be further evaluated on the microchip system to determine the effect of the electrode alignment and the separation field on the optimal detection potential. Figure 6.2A shows cyclic voltammograms (CVs) of tyrosine, 3-NT, and 3-aminotyrosine (3-AT). When the CVs of tyrosine and 3-NT are compared, it can be observed that tyrosine is more readily oxidizable than 3-NT, so no selectivity for 3-NT can be obtained on that basis; however, only 3-NT exhibits a reduction peak. While reduction of 3-NT would theoretically be a valid means to electrochemically distinguish between itself and tyrosine, the reduction of 3-NT occurs near the reduction potential of O_2. At pH 6.4, for example, the O_2 reduction peak is observed around -0.7 V *vs.* Ag/AgCl while the 3-NT reduction peak is observed around -0.65 V *vs.* Ag/AgCl. Therefore, one can expect significant interference from the reduction of O_2 as well as a greatly increased background current

when detecting the reduction of 3-NT. However, when the potential is scanned back in the positive direction after the production of that 3-NT reduction peak, a second oxidation peak is observed that does not appear in the positive CV scan of 3-NT. This oxidation peak coincides with the oxidation peak of 3-AT, indicating that the complete reduction of 3-NT produces 3-AT which can then be oxidized at a lower potential than either tyrosine or 3-NT.

Because the dual electrochemical detection will be coupled to a microchip electrophoresis separation, it is important to discuss the implications of buffer pH on electrochemistry. The linear relationship between buffer pH and the peak potential (E_p) of oxidation (Figure 6.2B), reduction (Figure 6.2C), and reoxidation (Figure 6.2B) of 3-NT from its cyclic voltammogram in phosphate buffer at each designated pH. As would be expected for a proton-dependent reduction, the reduction of 3-NT becomes more difficult as the pH is increased, while the oxidation of 3-NT and its re-oxidation after reduction (*i.e.* the oxidation of 3-AT or the corresponding hydroxylamine) become easier to accomplish. Therefore, when deciding buffer conditions for a dual ME-EC system, it is important to consider not only the optimal buffer for separation but also whether the pH will be adequate for the desired reduction and oxidation reactions to occur.

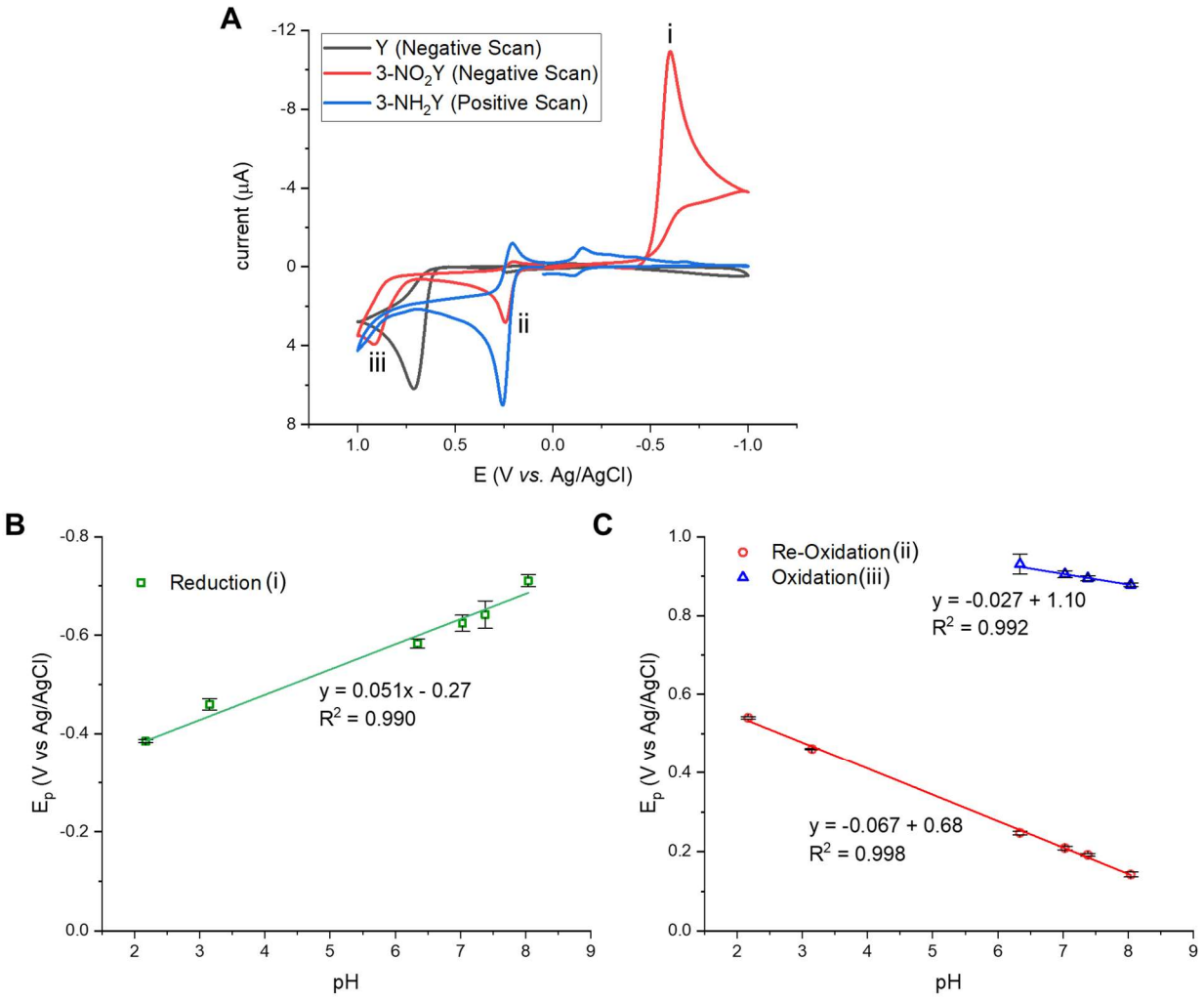

Figure 6.2. (A) Cyclic voltammograms of tyrosine, 3-NT, and 3-AT at pH 6.4; (B) Effect of increasing pH on increasing the absolute potential necessary to reduce 3-NT (i). (C) Effect of increasing pH on decreasing potential necessary to re-oxidize the reduced 3-NT (ii) and to oxidize non-reduced 3-NT (iii). GC WE, Ag/AgCl RE, Pt wire CE, 50 mV/s, 50 mM phosphate buffer at varied pH.

6.3.3 Conditions attempted for dual electrode ME-EC of 3-NT

6.3.3.1 Buffer composition

Once the approximate detection potentials and buffer pH were determined using CV, we could begin optimizing the dual electrode ME-EC method. Initially, a BGE of 15 mM phosphate at pH 7.4 with 15 mM SDS and 2 mM boric acid was used for these experiments. A pH 7.4 buffer was selected based on Figure 6.2B-C, which indicates that at this pH 3-NT should be reduced at approximately -0.6 V *vs.* Ag/AgCl and the reduced product should be oxidized at approximately +0.2 V *vs.* Ag/AgCl. In initial experiments with a Pt dual electrode, it was observed that the baseline stability suffers greatly more negative than -0.6 V and so it was desirable to stay more positive than that potential for this method. Figure 6.3A shows a promising pair of electropherograms achieved early in this project in which a large reduction peak was observed comigrating with the 3-NT oxidation peak ("day A"). However, when this experiment was repeated on another day ("day B") with the same conditions and a sample containing both tyrosine and 3-NT was analyzed, three prominent peaks were observed in the reductive electropherogram, two of which corresponded to the migration times of tyrosine and 3-NT (Figure 6.3B). This seemed to indicate that for some reason, tyrosine was producing a reductive peak despite not being electrochemically active at that potential. Additionally, when the potential at WE1 was varied ("day B"), the height of the peak that comigrates with 3-NT did not change as one would expect (*i.e.* increasing with more negative applied potential) (Figure 6.3C). The third peak observed in Figure 6.3B-C is likely attributed to dissolved oxygen, as purging the BGE and sample solutions with N_2 immediately prior to the run resulted in minimization of that peak in a separate experiment.

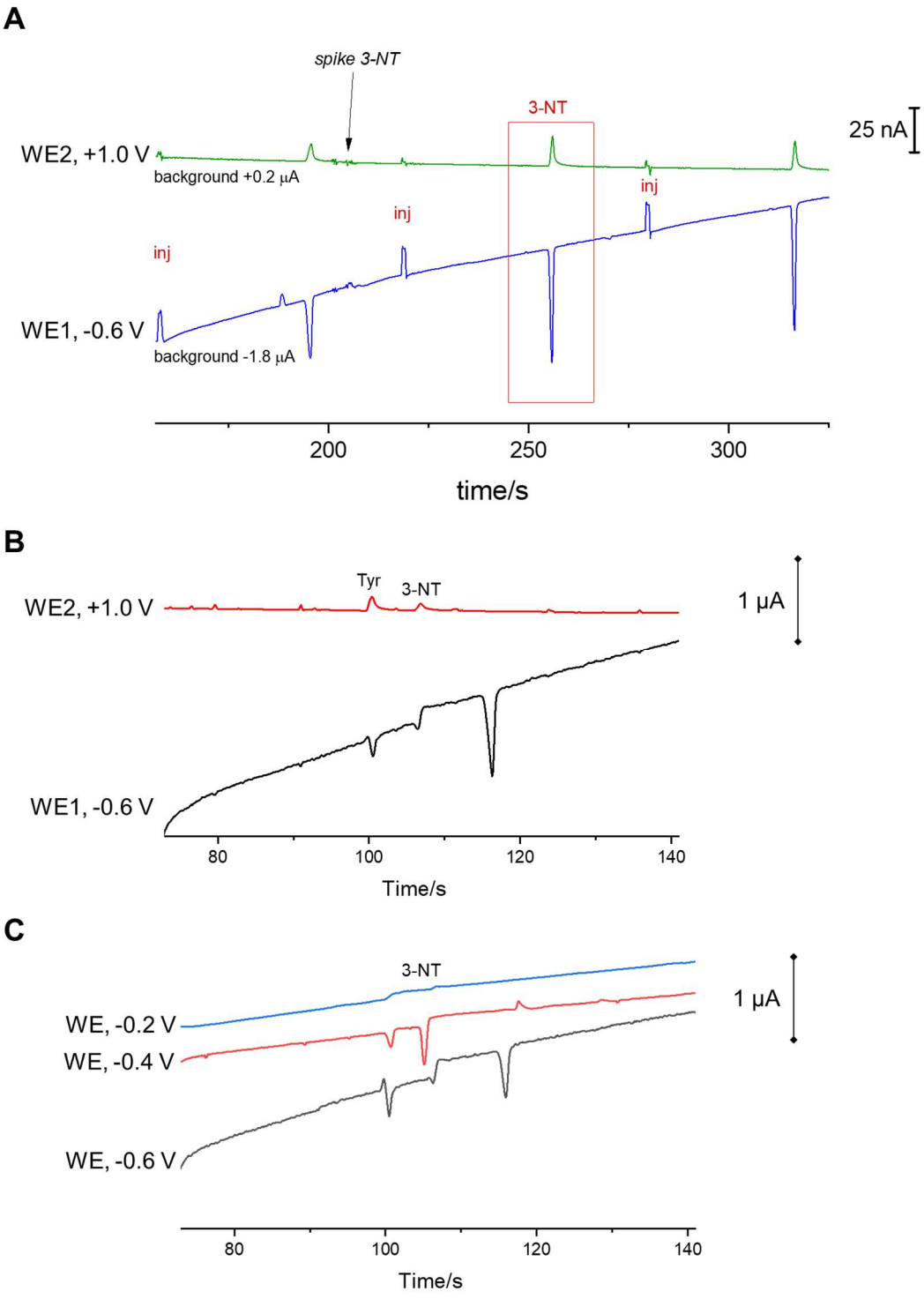

Figure 6.3. Dual electrode ME-EC at dual 15 µm wide Pt working electrodes with a 10 µm gap. WE1 was aligned 0 µm in-channel and the BGE was 15 mM phosphate at pH 7.4 with 15 mM SDS and 2.5 mM boric acid. (A) sample: 3-NT, day A; (B) sample: tyrosine and 3-NT, day B; (C) effect of WE1 potential on reduction peaks (no potential applied to WE2), sample: tyrosine and 3-NT, day B.

It quickly became apparent that the same experimental conditions could result in drastically different electropherograms during different experiments, with some microchips resulting in clear reduction and oxidation peaks that adhered to the expectations of 3-NT's electrochemical behavior, while others exhibited peaks that partially adhered, and some microchips resulted in no peaks whatsoever. In an attempt to determine the cause of this inconsistency, several buffer systems were evaluated, including varying the SDS and boric acid concentration in the phosphate buffer and attempting a separation using borate buffer at pH 9.2 with SDS or TTAC. The only buffer systems that produced nice peaks were acetate buffer at pH 4.7 with 2 mM SDS (Figure 6.4A) and phosphate buffer at pH 6.4 with 2 mM SDS (Figure 6.4B). While the lower pH acetate buffer should theoretically enable a less negative reduction potential, at this pH tyrosine and 3-NT comigrate. Because at pH 6.4 the tyrosine peak was observed to comigrate with the primary system peak, it is likely that there is a system peak comigrating with both tyrosine and 3-NT at pH 4.7 as well.

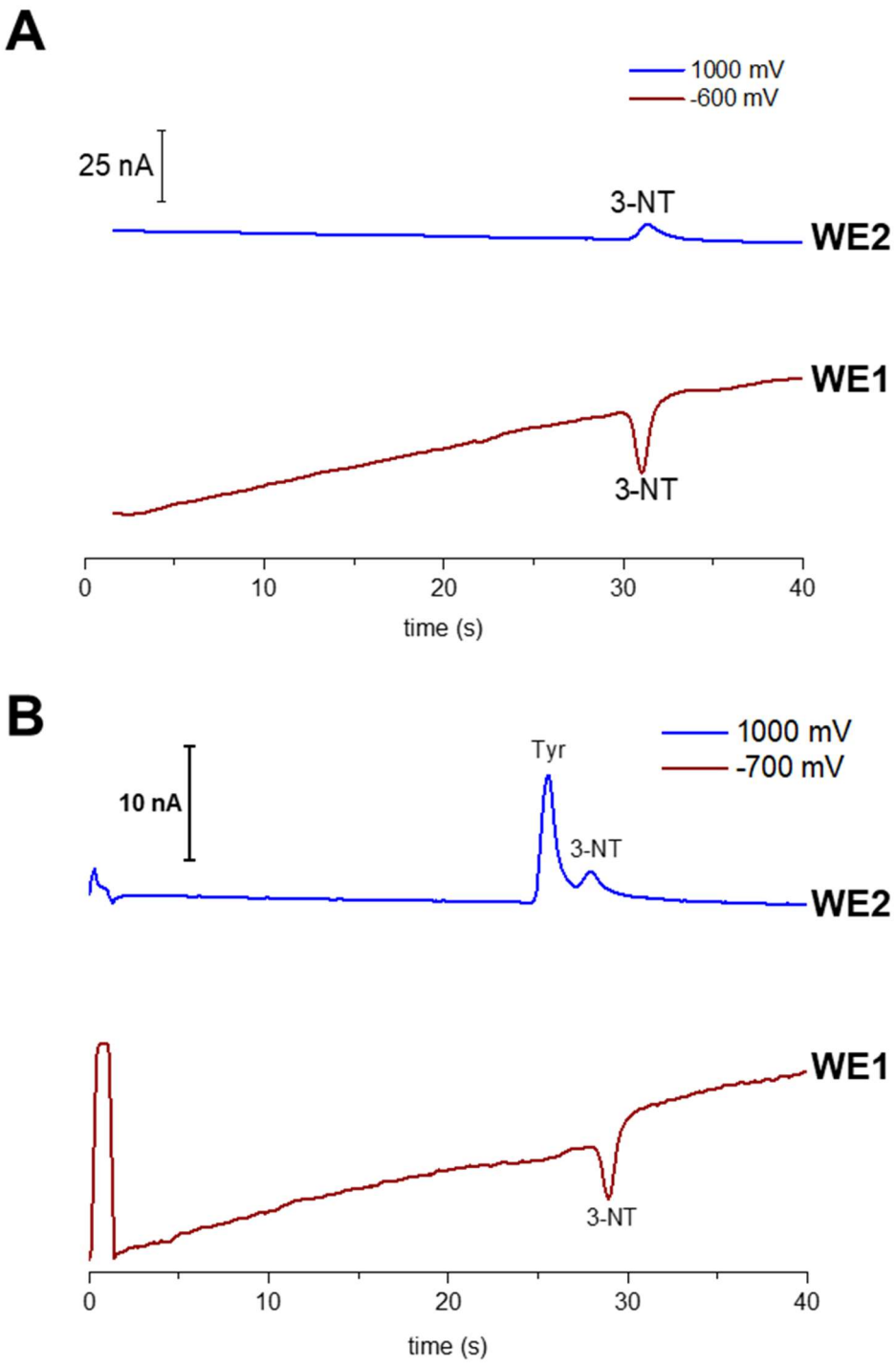

Figure 6.4. Dual electrode ME-EC of (A) 3-NT in 10 mM acetate buffer at pH 4.64 with 2 mM SDS, 10 µm Pt, WE1 0 µm in-channel, WE2 ~20 µm end-channel (B) Tyr and 3-NT in 10 mM phosphate buffer at pH 6.4 with 2 mM SDS, 33 µm CF, WE1 0 µm in-channel, WE2 ~63 µm end-channel.

6.3.3.2 Electrode characteristics

At this point, it also became apparent that Pt was not the ideal electrode material for this application. While metal electrodes used for reduction more often than carbon electrodes, the poor electrochemical background stability at the reductive electropherogram as well as the low oxidation signal at the second working electrode brought us to evaluate a carbon dual electrode substrate. When blanks were run over a range of potentials at a 15 µm Pt WE compared to a 33 µm carbon fiber (CF) working electrode, the CF electrode's background current remained stable over a wider potential range than the Pt WE. Even though the CF electrode ultimately reached a more negative background current with a large magnitude in the µA range, it maintained its stability in the general region of interest for these studies. This is as would be expected, as it is established that the potential window for carbon is greater than that of Pt, particularly when it comes to large negative potentials.[16]

Various electrode alignments were also evaluated for their effect on the quality of the electropherograms obtained. It was theorized that by moving the working electrodes further in-channel, the electroactive area would be more defined and the background current would become more stable. Additionally, the effect of the separation field would be felt more fully by the working electrode, resulting in a shift of the actual potential at the working electrode such that a more positive potential would be necessary to accomplish the same electrochemistry (*i.e.*, application of a less negative potential for the reduction of 3-NT and a more positive potential for the reoxidation of the reduced product). Figure 6.5 shows electropherograms obtained of a mixture of 3-AT and 3-NT at varied electrode alignment and WE1 potential. As WE1 potential is made more negative, the background current stability worsens and the intensity of system peaks in the reductive electropherogram increases. Additionally, moving the WE1 further in-channel

sometimes magnified this effect, as shown in Figure 6.5, likely due to the more negative effective potential at the WE when it was placed within the separation field.

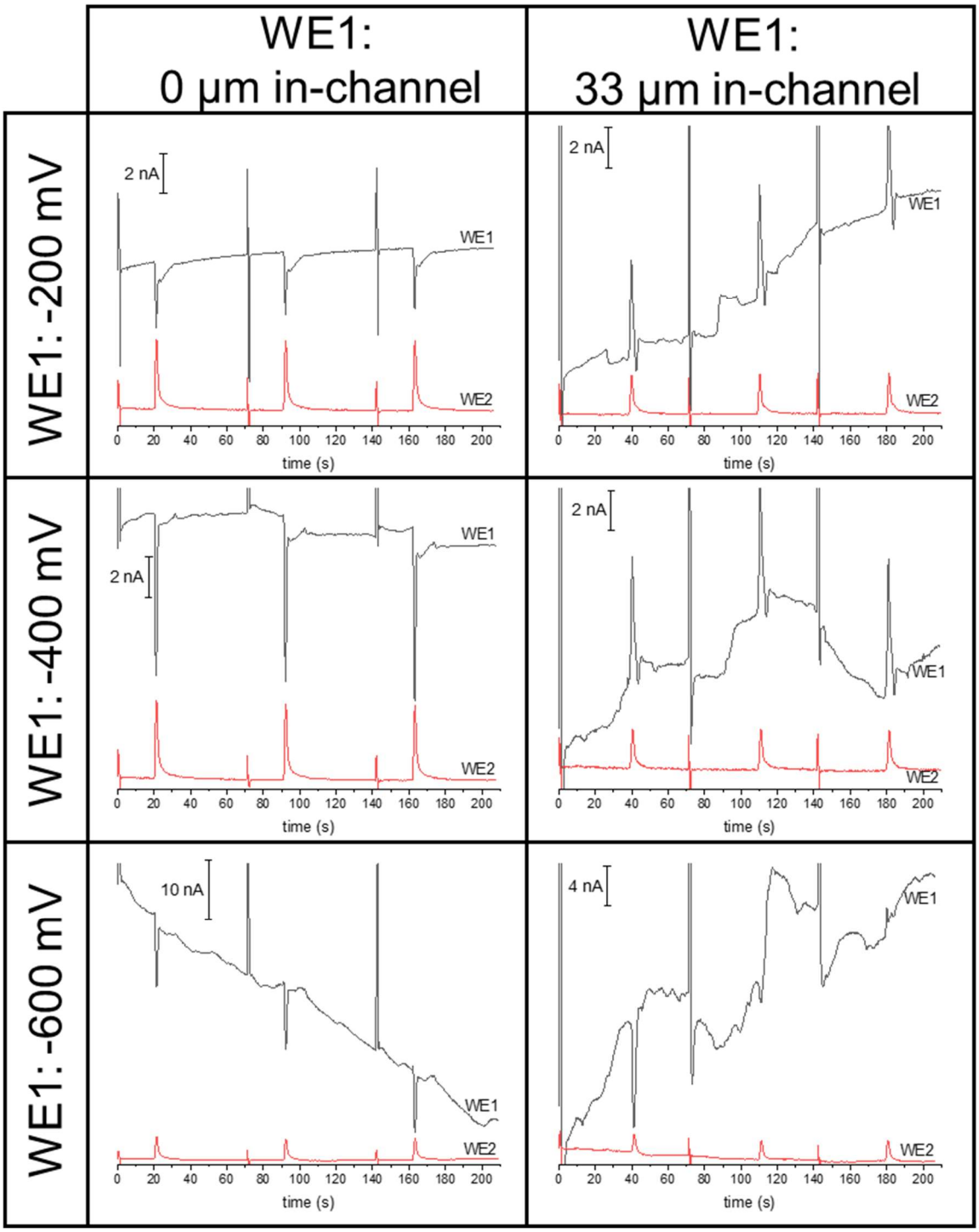

Figure 6.5. Effect of electrode alignment and WE1 potential on background current stability and system peak intensity for a sample of 3-NT and 3-AT injected 3 times (70 s run time), BGE 10 mM phosphate at pH 6.4, 2 mM SDS. Dual 33 µm CF WE, 33 µm gap with indicated WE1 potential and alignment and WE2 +400 mV *vs*. Ag/AgCl, aligned ~63 µm end-channel relative to WE1.

6.3.3.3 Consistency of electrode configuration

Ultimately, through varying the buffer pH and composition, the electrode material and size, and the electrode alignment relative to the separation field, no set of conditions were found that produced consistent, reliable results. It is hypothesized that this is largely due to the challenge of consistently positioning the electrodes relative to one another. At the outlet of the microchip, the working electrodes, separation field ground electrode, reference electrode, and counter electrode must all be positioned carefully relative to the end of the separation channel and one another in order to achieve optimal signal. Through these experiments, it has become evident that the further a working electrode is aligned in-channel, or the more negative the potential applied to a working electrode, the greater impact any slight variation in configuration on the data (Figure 6.5). Two drastically different electrode configurations are shown in Figure 6.6A and Figure 6.6B that would certainly produce different results; however, it appears that even minor shifts in the position of the counter, ground, and reference during the experiment can cause electropherograms obtained before and after that shift to have dramatically different peak heights (both for system peaks and analyte peaks) and noise levels. This can make comparisons between subsequent runs challenging, as it is important (1) to not jostle any of the electrodes in any way during the experiment in order to maintain a constant environment and (2) to carefully empty and replenish the buffer in the bottom waste reservoir that contains these electrodes regularly throughout the experiment in order to maintain a constant chemical environment in which the electrochemistry can occur.

In an attempt to remedy these conflicting requirements, an electrode holder was designed that contained one large hole for the reference electrode that would hold it tightly at a constant position in the well along with two smaller holes for the counter and ground electrodes. Several variations in the positioning of these holes were designed and fabricated using a FormLabs Form2 stereolithographic 3D printer (Figure 6.6C-D). The resulting electrode holders were evaluated,

with the ground and counter electrodes being secured in the holes using hot glue in order to ensure they would not move during the experiment. It was found that the electrode holders that kept the electrodes farthest apart (similar configuration to Figure 6.6A) resulted in the least consistent data, while a configuration closest to Figure 6.6B was ideal; however, the present electrode holder design was not able to keep the counter and ground electrodes close enough together, largely because of how far above the well the base of the holder sits (~0.5 cm). The "tabletop" design was selected to enable easy access of the waste reservoir for cleaning; however, cleaning was still a challenge using this configuration and the electrodes could only be held in a stable position in specific configurations. Ideally, a theoretical model would be built to determine the optimal positioning of these electrodes in order to guide the prototyping process.

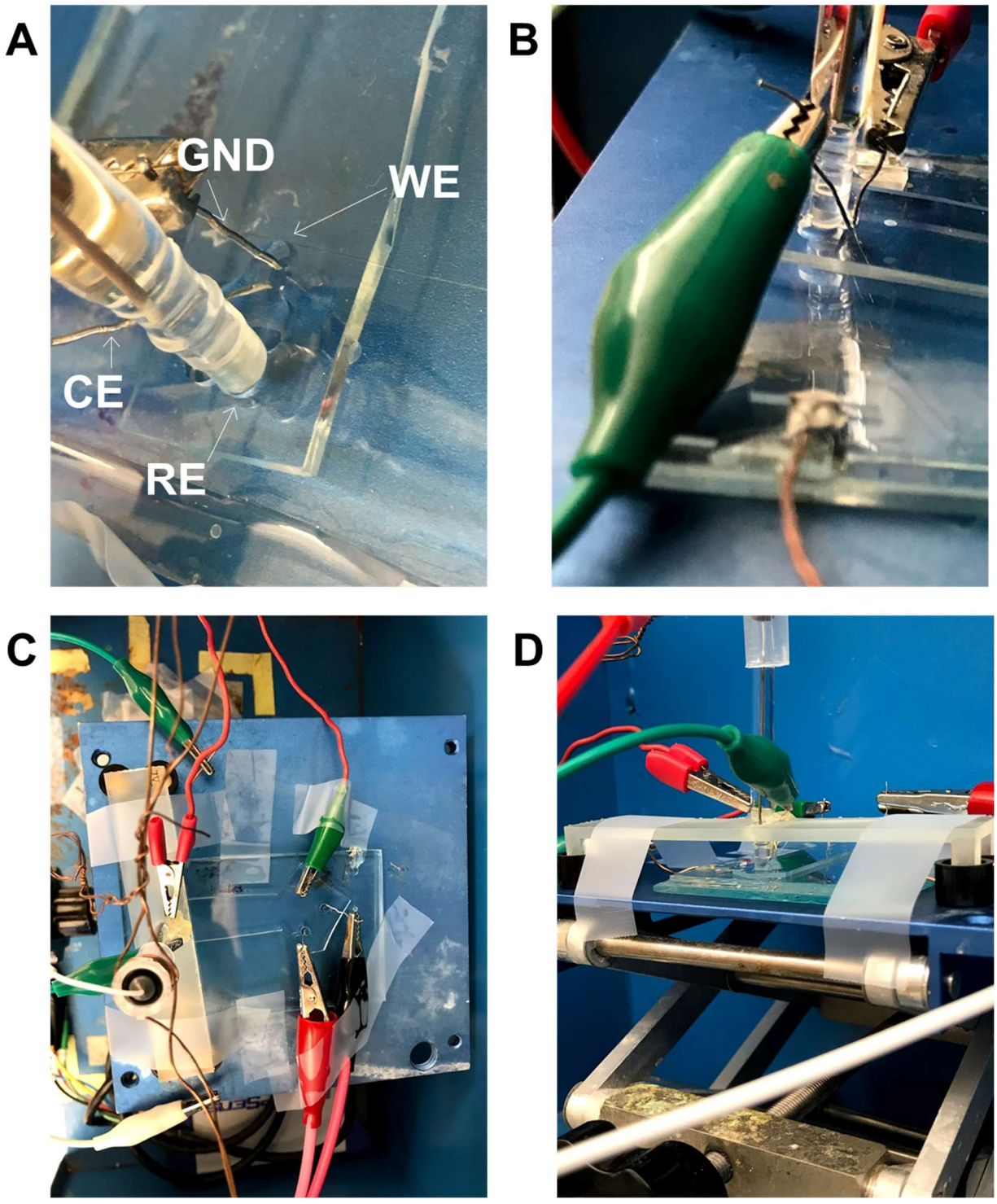

Figure 6.6. A and B depict two different configurations of the ground, counter, and reference electrodes relative to the end of the separation channel and the working electrodes. C and D depict top and side views, respectively, of a 3D-printed electrode holder.

6.3.4 Peak identification

Although there are major reproducibility issues with this method, significant effort has gone into attempting to determine whether the peaks, when they are observed, are in fact the reduction and re-oxidation of 3-NT. The key factors to consider are (1) whether they can be reproduced in a sample blank, (2) whether they exhibit the expected electrochemistry of the species, and (3) whether their peak height is dependent on the concentration of the species.

6.3.4.1 Sample blanks and comparison to other nitrated species

Although peaks had been observed in previous experiments that could be presumed to be 3-NT's reduction to 3-AT or a hydroxylamine followed by oxidation of that species, it was important to identify any system peaks. Previously, our group has observed that differences between the sample matrix and the BGE can result in system peaks in ME-EC.[24, 27] To investigate this phenomenon, a series of samples was prepared with differing composition. The typical 3-NT stock is prepared in water and then diluted in BGE just prior to the experiment, resulting in a decreased buffer concentration in the sample *vs.* the BGE, *e.g.*, 9.5 mM *vs.* 10 mM phosphate. At pH 6.4, two reduction peaks (WE1 Peaks 1 and 2) and one reoxidation peak (WE2 Peak 2) are observed (Figure 6.7A). When a blank solution is prepared that contains the same amount of water as the diluted 3-NT standard from Figure 6.7A and this solution ("diluted BGE") is used for both sample and BGE, such that the matrices of the sample and BGE are matched, WE1 Peak 1 is still observed but at a decreased signal intensity *vs.* when the matrices are mismatched (Figure 6.7B). Because Peak 1 at WE1 can be reproduced with a blank sample and its height is dependent on the conductivity offset between the sample and the BGE, it may be concluded that this peak is a system peak. Additionally, it is evident that efforts to match the conductivities could minimize or even eliminate the system peak at WE1. With this in mind, "diluted BGE" was then used as the BGE for a typical 3-NT sample, and only Peak 2 was observed at both WE1 and WE2 for the first

injections (Figure 6.7C). After this point, Peak 1 proceeded to grow in over time (Figure 6.8). This behavior is consistent with what one would expect from a system peak, as they typically show more variation in peak intensity (especially over subsequent injections) than analyte peaks. The second reduction peak, however, did not exhibit any change in intensity over the course of these injections, as one would expect from a peak that is dependent on an electrochemical reaction of a set concentration of analyte. This data indicates that, while WE1 Peak 1 is a system peak, WE1 Peak 2 is dependent on the reduction of 3-NT and WE2 Peak 2 is dependent on the reoxidation of that reduced species.

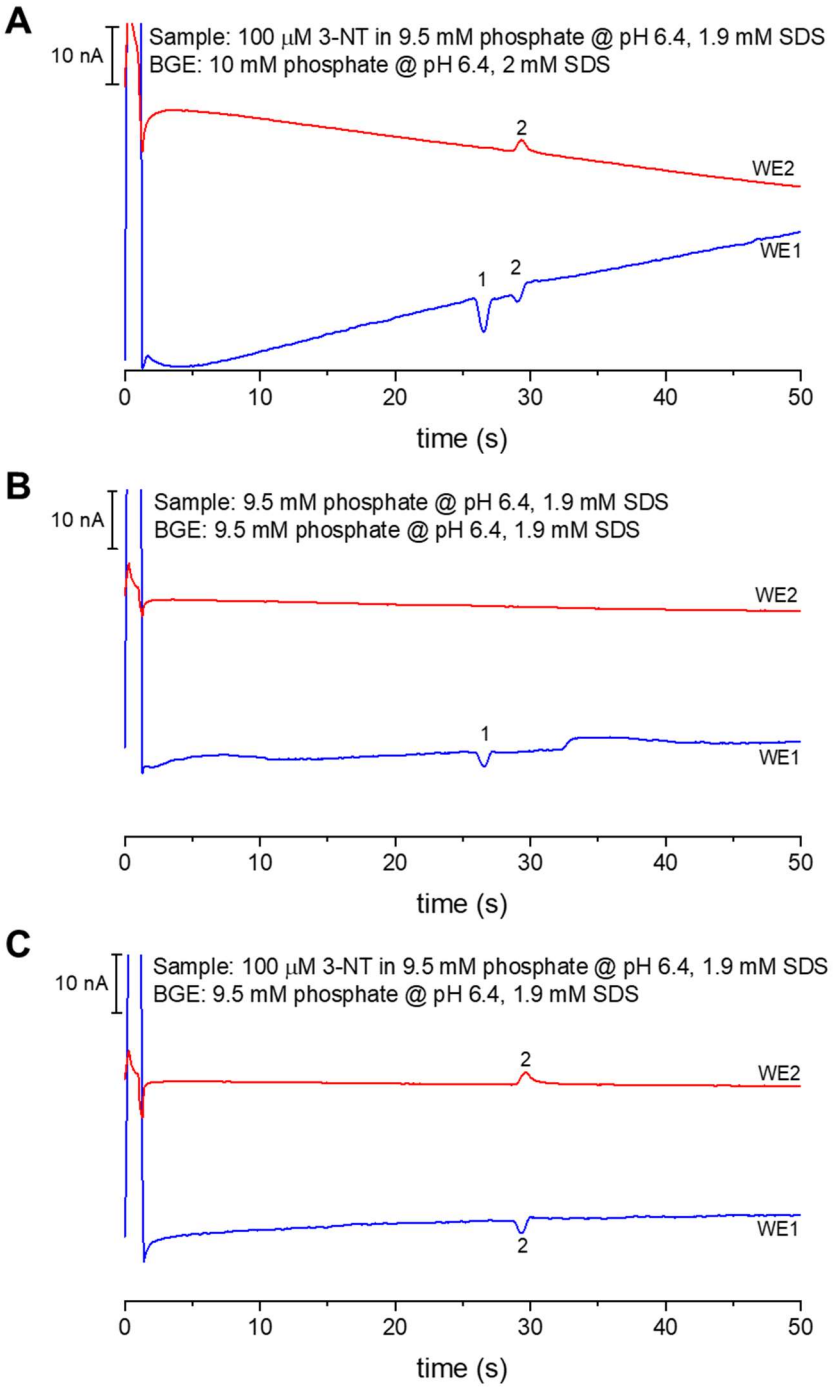

Figure 6.7. Effect of sample matrix on system peaks with a dual 33 µm CF WE, 30 µm gap; WE1 ~63 µm in-channel, -400 mV *vs.* Ag/AgCl; WE2: ~0 µm in-channel, +900 mV *vs.* Ag/AgCl; (A) 3-NT diluted into 10 mM phosphate buffer – conductivity of sample lower than that of BGE; (B) water diluted into 10 mM phosphate to match conductivity of 3-NT sample from A is both sample and BGE – conductivity of sample matches that of BGE; (C) 3-NT diluted into 10 mM phosphate buffer and BGE consists of water diluted into 10 mM phosphate – conductivity of sample matches that of BGE.

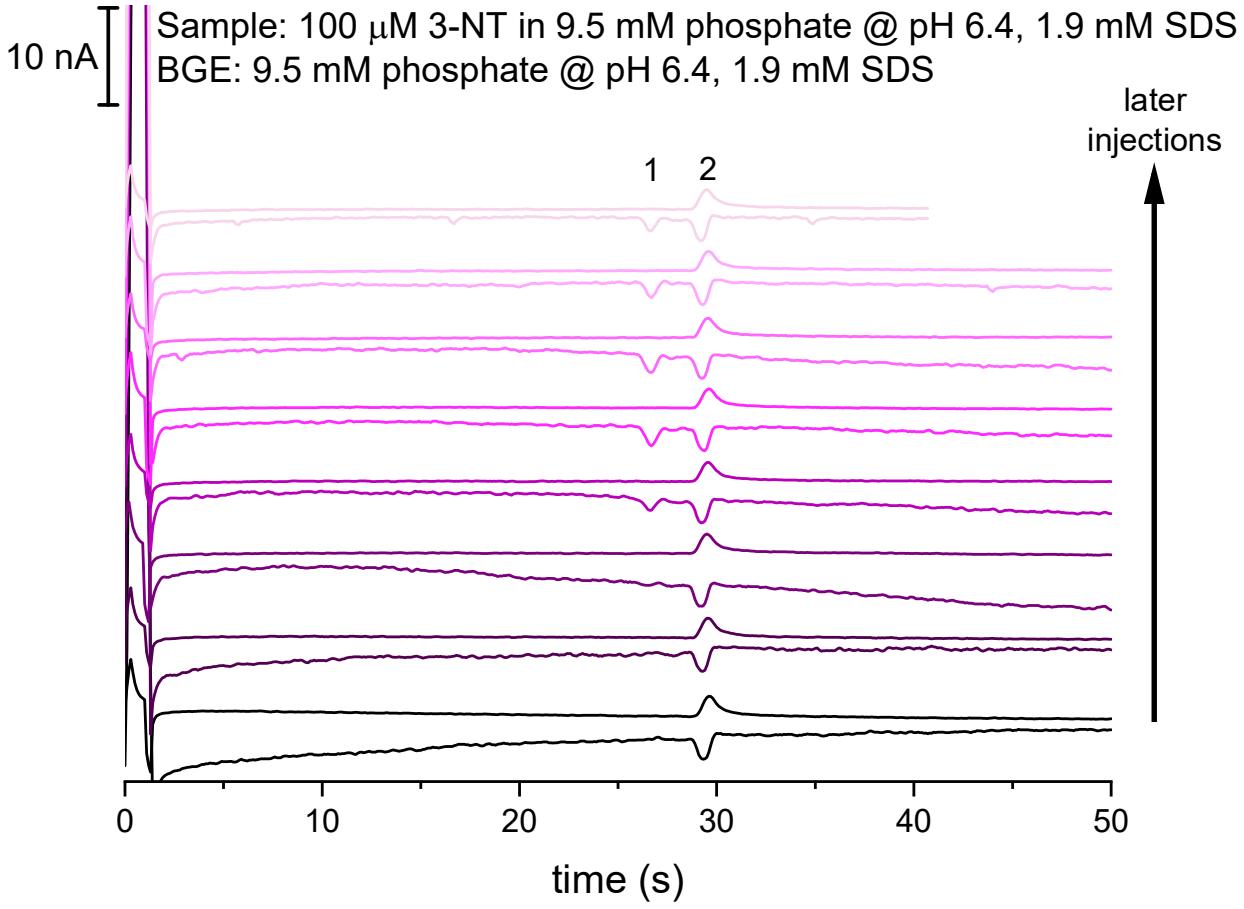

Figure 6.8. Growth of a system peak over time when BGE is matched to the sample matrix. Each subsequent pair of electropherograms depicts an injection immediately following the previous pair. Dual 33 μm CF WE, 30 μm gap; WE1 ~63 μm in-channel, -400 mV *vs.* Ag/AgCl; WE2: ~0 μm in-channel, +900 mV *vs.* Ag/AgCl.

Once it was confirmed that the second reduction peak could not be reproduced *via* a sample blank and was likely dependent on the reduction of 3-NT, the electropherograms were compared to other tyrosine-containing analytes. By applying -200 mV *vs.* Ag/AgCl to WE1 and +600 mV *vs.* Ag/AgCl to WE2, any Tyr-containing species should not show any electrochemical signal at either WE, while any 3-NT-containing species should show a reduction peak at WE1 and a reoxidation peak at WE2. As shown in Figure 6.9, both the Tyr sample and the NaOH blank exhibited an inverted Peak 1 at WE1 and no peaks at WE2, and both the non-nitrated AYL peptide sample and the water blank exhibited a typical Peak 1 at WE1 and no peaks at WE2. This is as expected for samples that do not contain any 3-NT. Both the 3-NT sample and the nitrated AYL peptide (A(NO_2Y)L), however, exhibited two peaks at WE1 and one peak at WE2, indicating that the presence of Peak 2 (both at WE1 and at WE2) is in fact dependent on the presence of nitrated tyrosine in the sample. This further supports the conclusion that the second reduction peak is indicative (at least in some way) of 3-NT reduction and that this reductive product is able to be oxidized at 600 mV, below the oxidation potential of Tyr or 3-NT.

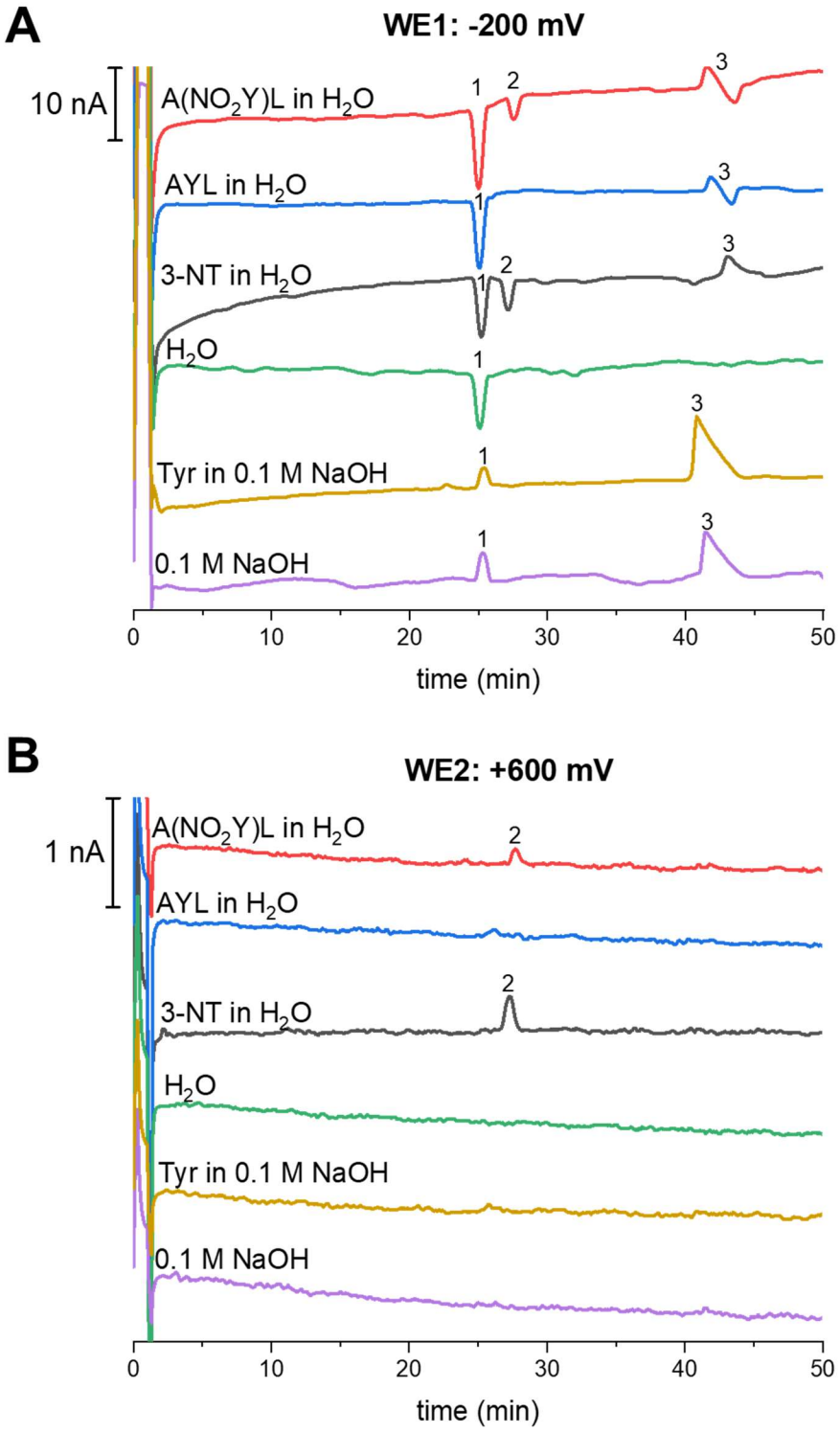

Figure 6.9. Dual electrode ME-EC at 33 µm CF WE, 30 µm gap; BGE: 10 mM phosphate at pH 6.4, 2 mM SDS; Samples: indicated solution diluted into BGE; detection at (A) WE1: -200 mV *vs.* Ag/AgCl, 63 µm in-channel, (B) WE2: +600 mV *vs.* Ag/AgCl/0 µm in-channel. Peaks 1 and 3 are system peaks, Peak 2 is dependent on nitration.

6.3.4.2 Electrochemistry of peaks

In order to determine whether Peak 2 that is observed in the dual electrode ME-EC electropherograms shown in Figure 6.9 is 3-NT at WE1 and 3-AT or the hydroxylamine at WE2, hydrodynamic voltammograms (HDVs) were produced for each peak as well as for standard solutions of Tyr, 3-NT, and 3-AT. The HDVs of Peak 1 and Peak 2 at WE1 (Figure 6.10A) seem to indicate that the two peaks are almost identically dependent on the potential of the working electrode. This likely indicates that, although the peak height for the reduction of Peak 2 does increase with more negative potential over a similar range to what would be expected for 3-NT based on its CV, there is likely a conductivity component to this peak that is magnifying the signal and distorting the HDV, particularly at more negative reduction potentials. The reoxidation peak does exhibit strong similarity to the onset potential of 3-AT; however, they are not identical (Figure 6.10B). One factor that complicates the comparison of the oxidation peak HDV and the electrochemical behavior expected of 3-AT or the hydroxylamine is the occasional presence of a system peak in the dual electrode ME-EC system that comigrates with Peak 2 at WE2. This system peak only becomes visible at low oxidation potentials when the oxidation peak for the reduced product is much smaller and they can be resolved from one another, whereas they merge when the oxidation peak is larger. Because the magnitude of this system peak at higher oxidation potentials is unknown, it is not possible to come to any definitive conclusions from these HDVs. However, if the oxidative HDV of Peak 2 at WE2 is compared to data reported by another group using a dual electrode LC-EC system, the HDVs of the two reduction products show strong similarities to one another. Because Kissinger *et al.* identified their reduction product as the hydroxylamine[12], it seems likely our reduction product is also the hydroxylamine, and 3-NT is not fully reduced to 3-AT under these conditions. (Figure 6.10C). With a more reproducible system, it could ultimately be possible to better characterize electrochemistry of these peaks on this ME-EC system.

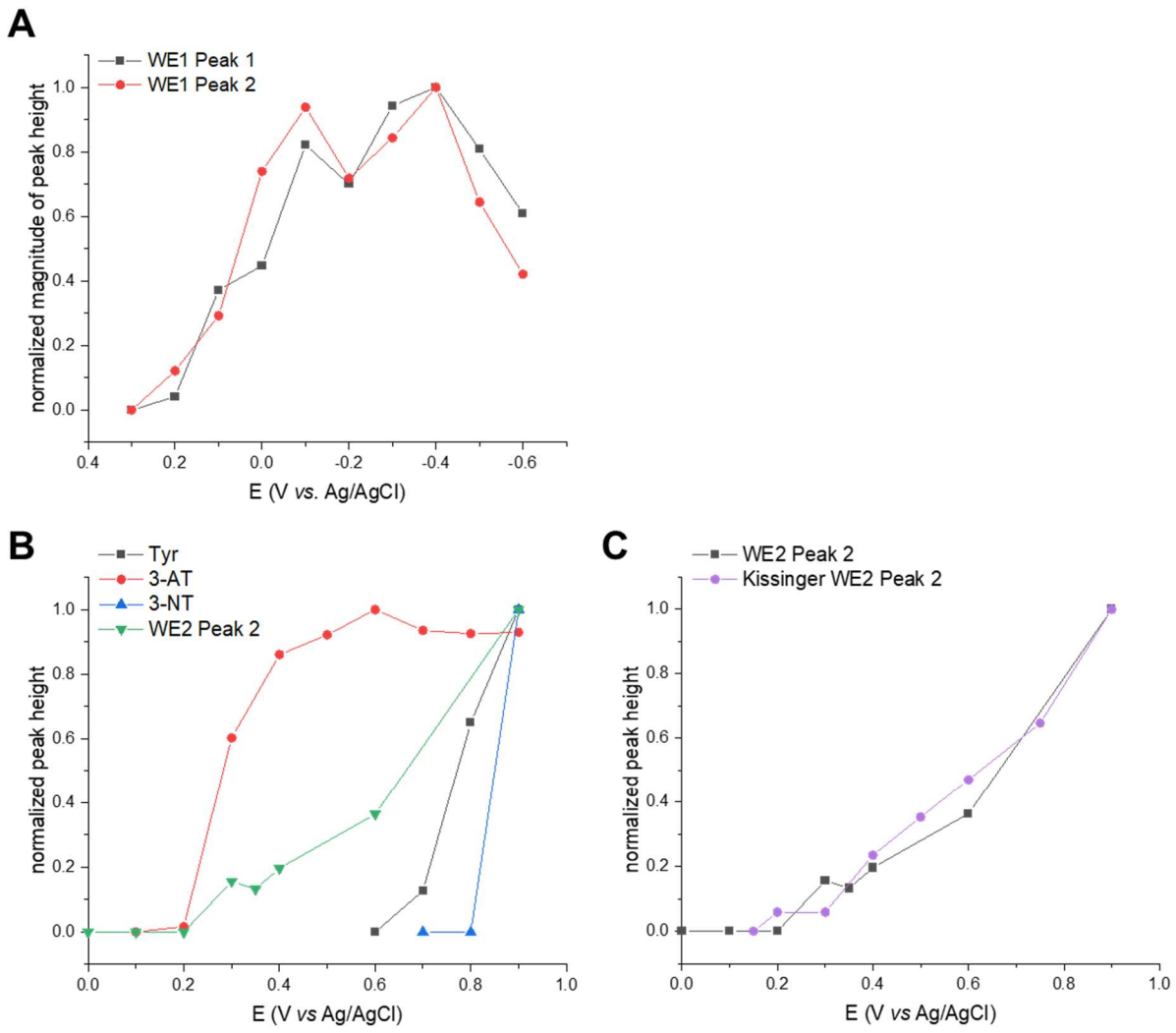

Figure 6.10. (A) Reductive HDVs of the system peak (peak 1) and the peak that comigrates with 3-NT (peak 2) at WE1 aligned 33 µm in-channel; (B) oxidative HDVs of Tyr, 3-NT, 3-AT, and the oxidation peak 2 observed in the dual system at WE2 aligned 0 µm in-channel; (C) oxidative HDVs of the oxidation peak 2 observed in this dual system (WE2 Peak 2) and in the LC-EC system reported by Kissinger, *et al.* (Kissinger WE2 Peak 2) at 3 mm glassy carbon electrodes, WE1 -750 mV *vs*. Ag/AgCl, WE2 varied, and a LC mobile phase of 90 mM sodium acetate – 35 mM citric acid buffer (pH 4.4), 3 mM SOS, 1.0 mM EDTA, 3% (v/v) MeOH.[12] Additional ME-EC parameters: Dual 33 µm CF WE, 30 µm gap, BGE: 10 mM phosphate at pH 6.4, 2 mM SDS.

6.3.4.3 Calibration curves

As shown in Figure 6.11A, the re-oxidation peak at WE2 (peak 2) increases linearly with increasing 3-NT concentration, while no additional system peak (Peak 1) is observed at any of these concentrations. As shown in Figure 6.11B, the first peak in the reduction electropherogram does not show any dependence on 3-NT concentration, while the second peak in the reduction electropherogram is dependent on 3-NT concentration but it is not as linear as the oxidation calibration curve. Based on this data, it is likely that peak 2 in both the reduction and oxidation electropherograms is dependent on 3-NT; however, it is possible there is an additional component to the reduction peak such as a comigrating system peak or some other factor that is altering the linearity of the calibration curve. This supports the conclusions drawn in the previous section that, while 3-NT is being reduced at this working electrode, there is an additional factor that contributes to its inconsistency in peak height and poor adherence to the electrochemical behavior of 3-NT.

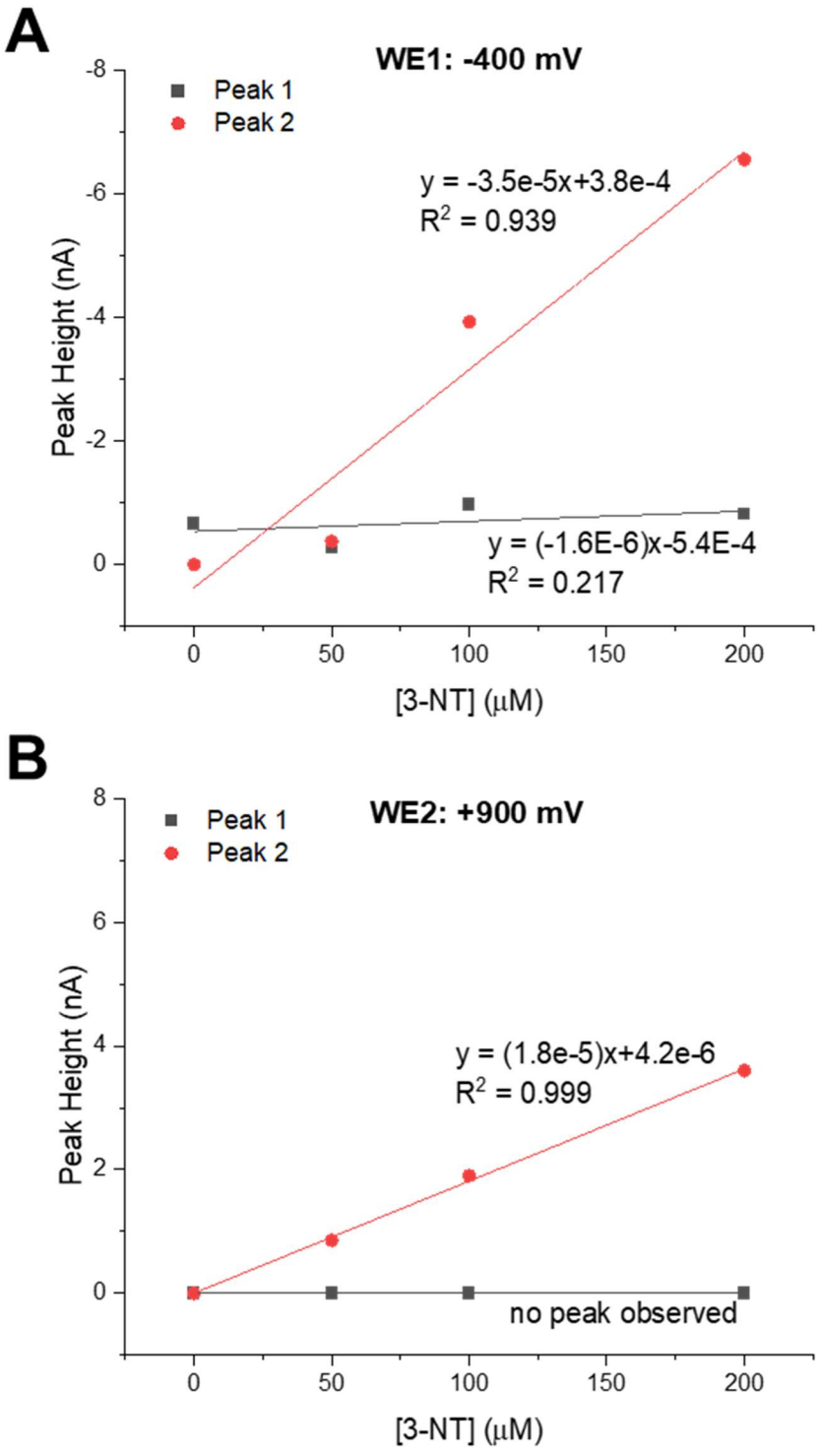

Figure 6.11. Calibration curves for (A) reduction peaks 1 (system peak) and 2 (3-NT-dependent peak) at WE1: -400 mV *vs*. Ag/AgCl, 63 µm in-channel and (B) oxidation peaks 1 (system peak, not observed) and 2 (3-NT) at WE2: +900 mV *vs*. Ag/AgCl, 0 µm in-channel. BGE: 10 mM phosphate at pH 6.4, 2 mM SDS.

6.3.5 Evaluation of dual electrode detection system performance using model analytes

Because the large negative working electrode potential necessary to reduce 3-NT seems to affect the reproducibility of the dual electrode ME-EC system, two other model analytes, dopamine and resazurin, were used to evaluate the system's performance for oxidizable and reducible species, respectively. Dopamine was demonstrated to be oxidizable at WE1 followed by reduction at WE2 at low potentials with high background current stability (Figure 6.12C). Resazurin exhibited stable background current for the reduction at WE1 and reoxidation at WE2 up to -0.6 V *vs.* Ag/AgCl at WE1, although it did become more unstable at more negative reduction potentials (*e.g.*, -0.8 V *vs.* Ag/AgCl). Resazurin also exhibited the same system peak observed in the 3-NT reduction electropherogram that, depending on the potential and alignment, could interfere with the resazurin reduction peak (Figure 6.12B). Compared to 3-NT, which does not always show significant peaks at the potentials at which the background current is stable (Figure 6.12A), each of these analytes is a more promising candidate for dual electrochemical detection.

However, when the peak heights at the first and second working electrodes are compared, it is clear that the collection efficiency must be very low using this system. High concentrations of analyte (*e.g.* 1 mM dopamine) were necessary in order to observe even small peaks at WE2, even as the WE1 peaks were very large. This poor collection efficiency is likely due to two primary factors: (1) the end-channel alignment at WE2 results in poorer peak efficiency and (2) the CF electrodes are 30 μm apart, which may limit the species produced at WE1 that reach WE2 to be oxidized. Efforts to improve this could involve moving the two electrodes closer together, altering the EOF, or increasing the size of the generator working electrode and transitioning to a more ideal material for reduction, such as mercury amalgam. However, bringing the electrodes closer together can result in other complications for the electrochemistry and fabricating a substrate with both

mercury amalgam reduction electrode and a carbon oxidation electrode will be challenging using our current fabrication techniques.

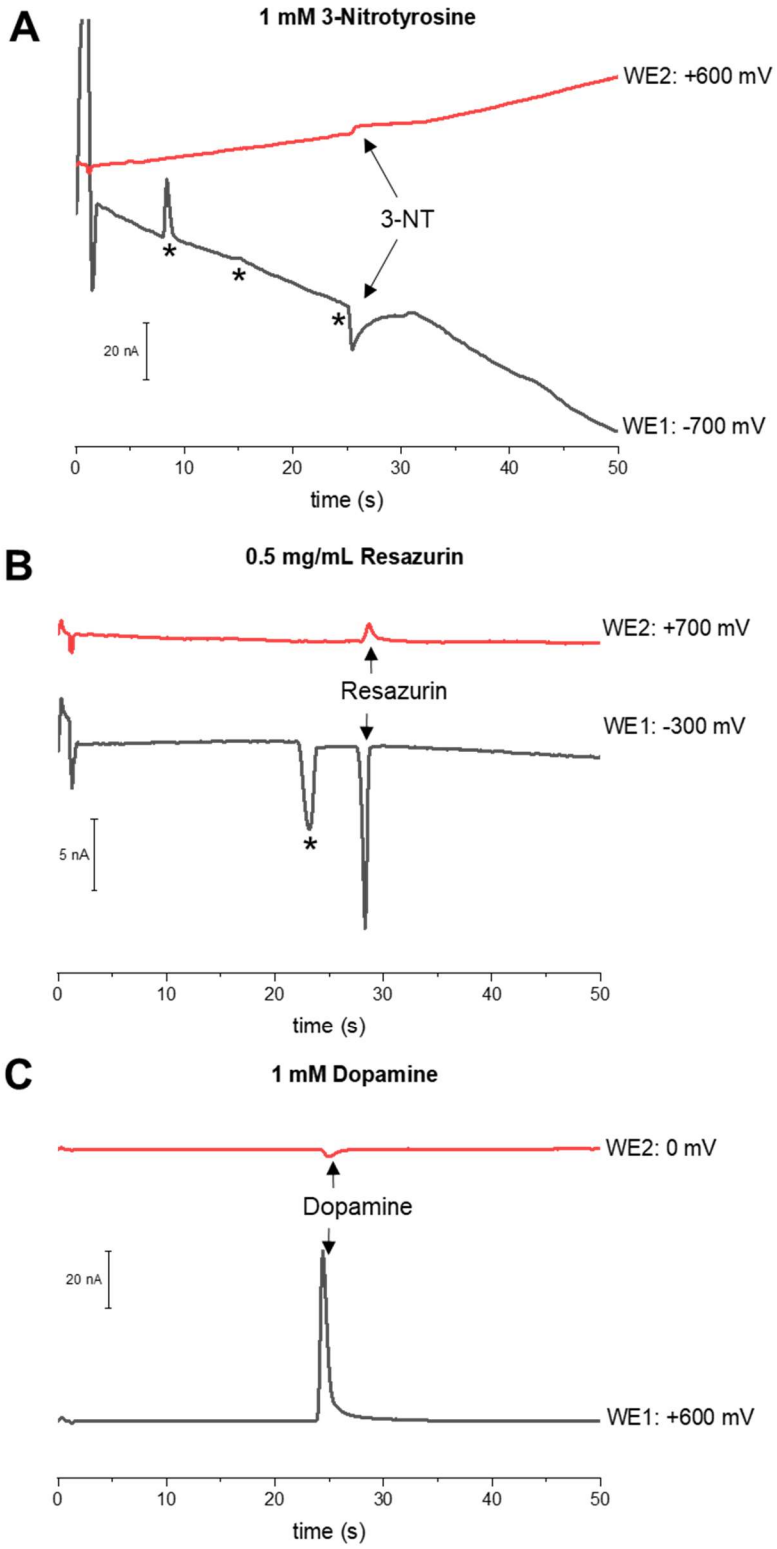

Figure 6.12. Dual electrode ME-EC at 33 µm dual CF WE (30 µm gap, WE1: 0 µm in-channel, WE2: 63 µm end-channel), BGE: 20 mM borate at pH 8.2 with 5 mM SDS of (A) 3-NT, (B) resazurin, and (C) dopamine. * denotes likely system peaks.

Because dopamine exhibited the most consistent signal, it was selected for further studies into the effect of electrode alignment on the HDVs for the oxidation of dopamine into the orthoquinone at WE1 and the reduction of the orthoquinone at WE2.

The WE2 HDVs for dopamine look as expected, with similar plateau potentials for the reduction of the orthoquinone of around 0 mV observed at each alignment. Because they are all end-channel-aligned, however, the peak heights increase as the alignment nears the end separation channel since less diffusion is occurring in the bottom well (Figure 6.13B). However, the WE1 HDVs do not exactly follow the expected pattern of a shift to more difficult oxidation as the electrode is moved into the positive separation field. While the 63 μm in-channel HDV does appear to be shifted to more positive oxidation potentials, the presence of a comigrating system peak conflicted the integration of these peaks (Figure 6.13A), particularly at higher potentials when no system peak was observable. However, since the peak appeared at low potentials it was possibly present at the higher potentials as well, thereby shifting the peak heights unnaturally. The HDVs for the 33 um and 63 um in-channel match closely what was obtained using a single WE (Figure 6.13C). Overall, this data demonstrates that, if the separation conditions are altered to better resolve dopamine and the system peak, it should be possible to carefully evaluate the effect of the separation field, the electrode alignment, and the electrode configuration using dopamine as a model analyte. Although the interference of oxygen reduction further complicates the dual electrode detection of more difficult-to-reduce analytes such as 3-NT, knowledge gained from studying the dopamine system may aid in determining the ideal electrode configurations for obtaining the most reproducible results.

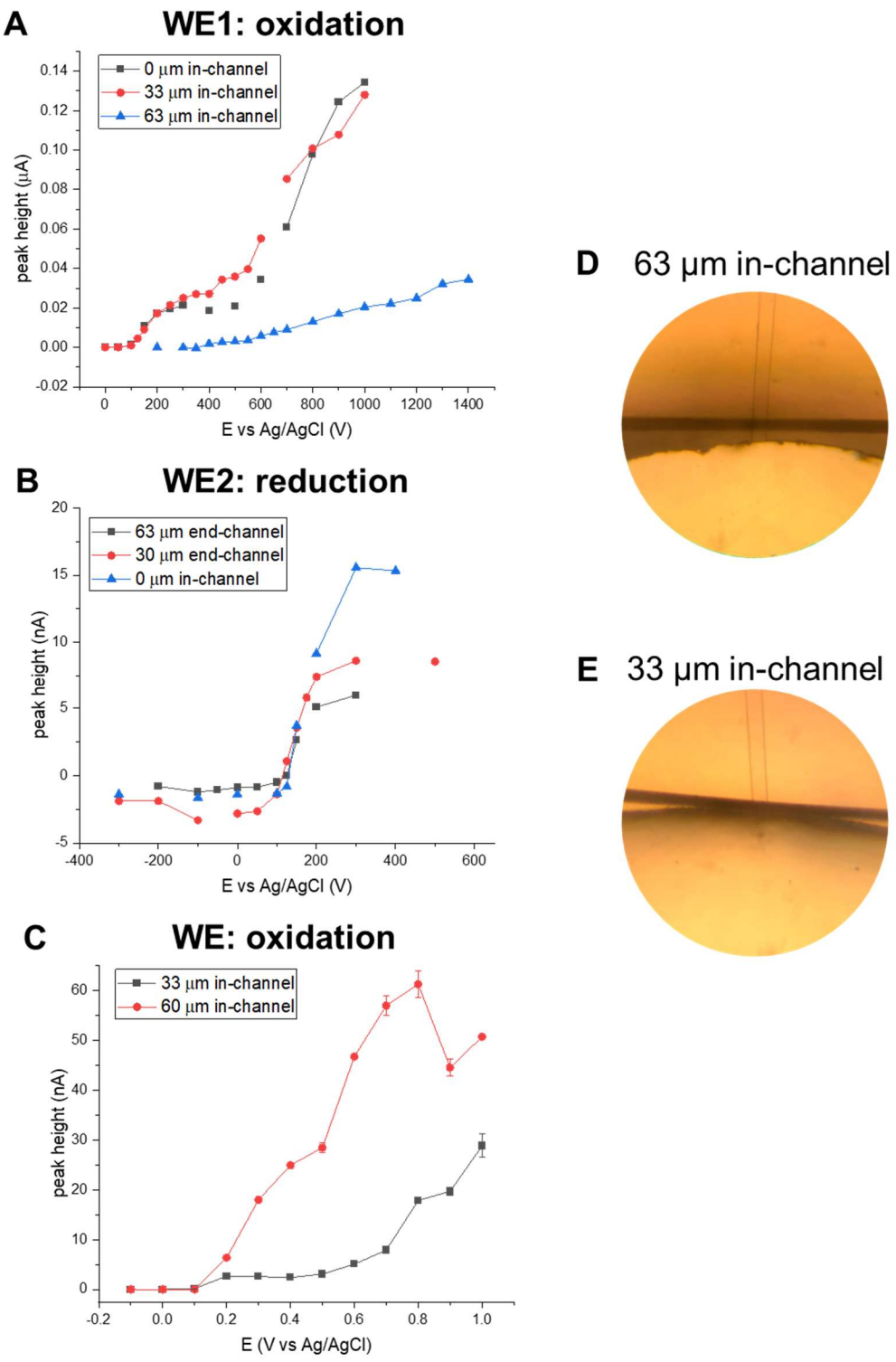

Figure 6.13. HDV of dopamine at different electrode alignments (A) for oxidation to the orthoquinone at WE1, (B) for reduction of the orthoquinone WE2, and (C) for oxidation of dopamine at a single WE. (D) Single WE aligned 63 µm in-channel, (E) Single WE aligned 33 µm in-channel.

6.4 Conclusions

In this chapter, efforts towards the optimization of a dual electrode ME-EC method for selective detection of 3-NT are presented. The product of the nitration of tyrosine by peroxynitrite was detected using single electrode ME-EC. A dual electrode ME-EC method for detection of 3-NT was presented and the irreproducibility of the dual electrode system was discussed. The key factors impacting detection were the reduction of oxygen, the configuration of electrodes, and the differences between the sample matrix and the BGE. Approaches to mitigating these factors are discussed, including the development of a 3D printed electrode holder for reproducible electrode placement. Additionally, data to support the identity of the dual electrode ME-EC peaks as 3-NT reduction and 3-AT oxidation are presented, including hydrodynamic voltammograms, calibration curves, sample blanks, and electropherograms of another nitrated species, the peptide A(NO_2Y)L. Finally, preliminary results using dopamine as a model analyte indicate that there is much to learn about how electrode configuration affects a dual electrode ME-EC system before difficult to reduce analytes such as 3-NT can be consistently detected.

6.5 References

1. Souza, J. M.; Peluffo, G.; Radi, R., Protein tyrosine nitration—functional alteration or just a biomarker? *Free Radical Biol. Med.* **2008,** *45* (4), 357-366.
2. Bartesaghi, S.; Radi, R., Fundamentals on the biochemistry of peroxynitrite and protein tyrosine nitration. *Redox Biology* **2018,** *14*, 618-625.
3. Herce-Pagliai, C.; Kotecha, S.; Shuker, D. E., Analytical methods for 3-nitrotyrosine as a marker of exposure to reactive nitrogen species: a review. *Nitric Oxide* **1998,** *2* (5), 324-336.
4. Teixeira, D.; Fernandes, R.; Prudencio, C.; Vieira, M., 3-Nitrotyrosine quantification methods: Current concepts and future challenges. *Biochimie* **2016,** *125*, 1-11.
5. Frijhoff, J.; Winyard, P. G.; Zarkovic, N.; Davies, S. S.; Stocker, R.; Cheng, D.; Knight, A. R.; Taylor, E. L.; Oettrich, J.; Ruskovska, T., Clinical relevance of biomarkers of oxidative stress. *Antioxidants & redox signaling* **2015,** *23* (14), 1144-1170.
6. Knight, A. R.; Taylor, E. L.; Lukaszewski, R.; Jensen, K. T.; Jones, H. E.; Carré, J. E.; Isupov, M. N.; Littlechild, J. A.; Bailey, S. J.; Brewer, E., A high-sensitivity electrochemiluminescence-based ELISA for the measurement of the oxidative stress biomarker, 3-nitrotyrosine, in human blood serum and cells. *Free Radical Biol. Med.* **2018,** *120*, 246-254.

7. Dremina, E. S.; Li, X.; Galeva, N. A.; Sharov, V. S.; Stobaugh, J. F.; Schöneich, C., A methodology for simultaneous fluorogenic derivatization and boronate affinity enrichment of 3-nitrotyrosine-containing peptides. *Anal. Biochem.* **2011,** *418* (2), 184-196.
8. Batthyány, C.; Bartesaghi, S.; Mastrogiovanni, M.; Lima, A.; Demicheli, V.; Radi, R., Tyrosine-nitrated proteins: Proteomic and bioanalytical aspects. *Antioxidants & Redox Signaling* **2017,** *26* (7), 313-328.
9. Honeychurch, K. C.; Hart, J. P., Voltammetric Behavior of p-Nitrophenol and Its Trace Determination in Human Urine by Liquid Chromatography with a Dual Reductive Mode Electrochemical Detection System. *Electroanalysis: An International Journal Devoted to Fundamental and Practical Aspects of Electroanalysis* **2007,** *19* (21), 2176-2184.
10. Sugiura, H.; Ichinose, M.; Tomaki, M.; Ogawa, H.; Koarai, A.; Kitamuro, T.; Komaki, Y.; Akita, T.; Nishino, H.; Okamoto, S., Quantitative assessment of protein-bound tyrosine nitration in airway secretions from patients with inflammatory airway disease. *Free Radical Res.* **2004,** *38* (1), 49-57.
11. Ryberg, H.; Caidahl, K., Chromatographic and mass spectrometric methods for quantitative determination of 3-nitrotyrosine in biological samples and their application to human samples. *J. Chromatogr. B* **2007,** *851* (1-2), 160-171.
12. Liu, H.; Huang, T.; Kissinger, C. B.; Kissinger, P. T., Comparison of detection methods for liquid chromatographic determination of 3-nitro-L-tyrosine. *Journal of Chromatography B: Biomedical Sciences and Applications* **1998,** *713* (2), 289-295.
13. Tohgi, H.; Abe, T.; Yamazaki, K.; Murata, T.; Ishizaki, E.; Isobe, C., Alterations of 3-nitrotyrosine concentration in the cerebrospinal fluid during aging and in patients with Alzheimer's disease. *Neurosci. Lett.* **1999,** *269* (1), 52-54.
14. Murata, T. A., Takashi; Sato, Chigumi, The concentrations of 3-nitrotyrosine in the cerebrospinal fluid in patients with dementia of Alzheimer's type and vascular dementia. *Iwate Igaku Zasshi* **2001,** *53* (1), 11-18.
15. Schilly, K. M.; Gunawardhana, S. M.; Wijesinghe, M. B.; Lunte, S. M., Biological applications of microchip electrophoresis with amperometric detection: in vivo monitoring and cell analysis. *Anal. Bioanal. Chem.* **2020**.
16. Gunasekara, D. B.; Wijesinghe, M. B.; Saylor, R. A.; Lunte, S. M., Principles and Strategies for Microchip Electrophoresis with Amperometric Detection. In *Electrochemical Strategies in Detection Science*, 2015; pp 85-124.
17. Chen, C.; Hahn, J. H., Dual-channel method for interference-free in-channel amperometric detection in microchip capillary electrophoresis. *Anal. Chem.* **2007,** *79* (18), 7182-7186.
18. Meneses, D.; Gunasekara, D. B.; Pichetsurnthorn, P.; da Silva, J. A.; de Abreu, F. C.; Lunte, S. M., Evaluation of in-channel amperometric detection using a dual-channel microchip electrophoresis device and a two-electrode potentiostat for reverse polarity separations. *Electrophoresis* **2015,** *36* (3), 441-448.
19. Gunasekara, D. B.; Wijesinghe, M. B.; Pichetsurnthorn, P.; Lunte, S. M., Evaluation of Dual Electrode Configurations for Microchip Electrophoresis Used for Voltammetric Characterization of Electroactive Species. *Analyst* **2019**.
20. Martin, R. S.; Gawron, A. J.; Lunte, S. M.; Henry, C. S., Dual-electrode electrochemical detection for poly (dimethylsiloxane)-fabricated capillary electrophoresis microchips. *Anal. Chem.* **2000,** *72* (14), 3196-3202.
21. Mecker, L. C.; Martin, R. S., Use of micromolded carbon dual electrodes with a palladium decoupler for amperometric detection in microchip electrophoresis. *Electrophoresis* **2006,** *27* (24), 5032-5042.

22. Fischer, D. J.; Vandaveer IV, W. R.; Grigsby, R. J.; Lunte, S. M., Pyrolyzed Photoresist Carbon Electrodes for Microchip Electrophoresis with Dual-Electrode Amperometric Detection. *Electroanalysis: An International Journal Devoted to Fundamental and Practical Aspects of Electroanalysis* **2005,** *17* (13), 1153-1159.
23. Gawron, A. J.; Martin, R. S.; Lunte, S. M., Fabrication and evaluation of a carbon-based dual-electrode detector for poly (dimethylsiloxane) electrophoresis chips. *Electrophoresis* **2001,** *22* (2), 242-248.
24. Siegel, J. M.; Schilly, K. M.; Wijesinghe, M. B.; Caruso, G.; Fresta, C. G.; Lunte, S. M., Optimization of a microchip electrophoresis method with electrochemical detection for the determination of nitrite in macrophage cells as an indicator of nitric oxide production. *Analytical methods* **2019,** *11* (2), 148-156.
25. Fischer, D. J.; Hulvey, M. K.; Regel, A. R.; Lunte, S. M., Amperometric detection in microchip electrophoresis devices: Effect of electrode material and alignment on analytical performance. *Electrophoresis* **2009,** *30* (19), 3324-3333.
26. Robinson, K. M.; Beckman, J. S., Synthesis of peroxynitrite from nitrite and hydrogen peroxide. *Methods Enzymol.* **2005,** *396*, 207-214.
27. Gunasekara, D. B.; Siegel, J. M.; Caruso, G.; Hulvey, M. K.; Lunte, S. M., Microchip electrophoresis with amperometric detection method for profiling cellular nitrosative stress markers. *Analyst* **2014,** *139* (13), 3265-3273.

Chapter 7

Development of a 3D printed scaffold for boronate affinity enrichment of cis-diol-containing species

7 Chapter 7: Development of a 3D printed scaffold for boronate affinity enrichment of cis-diol-containing species

7.1 Introduction

While 3D printing has been around for nearly 40 years, recent technological advancements have opened up a wide new array of applications. What began as a crude prototyping technology is rapidly transforming into a valuable fabrication method for analytical applications in environmental analysis, disease diagnosis, cell analysis, and separation science.[1] Traditional microfabrication techniques such as photolithography and reactive ion etching are limited in their material compatibility, require a great deal of technical skill, and can be time-consuming to go from design to final product. In contrast, 3D printing is well-suited for rapid prototyping and is more cost effective and attainable for smaller research groups looking to optimize a plastic device compared to large-scale manufacturing techniques such as injection molding.[1]

There are several different types of 3D printers that can be used to generate patterns in nearly every material imaginable, from the traditional plastics to metal, ceramic, and even paper. The most notable technologies for 3D printing of plastics include fused deposition modeling (FDM), stereolithography (SLA), and PolyJet. In FDM, a filament is extruded through a nozzle that effectively "draws" each layer. As the melted filament cools, it forms the 3D printed piece. In SLA, a laser or LED is used to cure a photocurable resin into the desired design. In PolyJet, a photocurable resin is printed directly onto a platform and then each layer is exposed to UV light to cure the polymer into the desired piece. Each technology has its place in fabrication, depending on the desired material and resolution and the cost limitations.

In the field of analytical chemistry, the number of applications of 3D printing has been increasing and includes a wide variety of devices and analyses.[2-4] One example is its use for separations, including preparation of stationary phases and columns for liquid chromatography

and channels for electrophoresis. Gupta *et al.* 3D printed LC columns in titanium with various geometries including 2D serpentine, 3D spiral, and 3D serpentine that were then filled with stationary phase via in column thermal polymerization of a monolith for improved peak efficiencies.[5, 6] The Woolley group has developed 3D printed devices for microchip electrophoresis,[7] solid phase extraction,[8] and fluorescent labeling[9] utilizing a customized SLA printing system. The Martin group has also explored the application of 3D printing to capillary electrophoresis and has adapted PolyJet 3D printing technology to produce devices with integrated capillaries and integrated electrodes for amperometric detection[10] as well as microfluidic devices with improved support material process.[11] Other groups have utilized 3D printing to produce devices to supplement conventional analytical techniques, such as cartridges for interfacing capillary electrophoresis[12] or paper spray ionization[13] with mass spectrometry. Another interesting application is the development of a miniaturized fluorescence detector that can be integrated into a conventional capillary electrophoresis instrument to enable dual-point detection for Taylor dispersion analysis.[14] Overall, although there is a need for further improvement of 3D printing technology to make printers capable of achieving microfluidic resolution commercially available, the field of microfluidics seems to be trending towards 3D printing fabrication.

In this chapter, efforts to use 3D printing to miniaturize a conventional analytical workflow are described. The Schoeneich, Michaelis, and Swerdlow groups at the University of Kansas Department of Pharmaceutical Chemistry and the University of Kansas Alzheimer's Disease Research Center have been working in collaboration to quantify protein tyrosine nitration in the blood of Alzheimer's disease (AD) patients in order to determine if there are specific protein markers that could be used as a diagnostic of the disease. In their method, shown in Figure 7.1A, white blood cell mitochondria are isolated from a large volume of whole blood (up to 50 mL) in a series of differential centrifugation steps. The mitochondrial proteins are then isolated using

additional centrifugation steps, the proteins are digested, and the 3-nitrotyrosine residues are reduced to 3-aminotyrosine *via* sodium dithionite. The resulting peptides are then labeled with a fluorogenic, cis-diol-containing reagent selective for the 3-aminotyrosine (Figure 7.1B). The final step is to use boronate affinity chromatography to enrich the labeled peptides followed by fluorescence or mass spectrometric detection (Figure 7.1C).[15]

In this procedure, as well as other approaches for studying the blood of AD patients, the key drawbacks are many opportunities for sample loss during the process, human error, and the necessity of a large volume of whole blood to be drawn in order to be able to isolate and detect the trace proteins. To minimize the amount of blood needed for these assays and improve the sample throughput and reproducibility, we have been working with them to develop an automated, miniaturized microfluidic system capable of accomplishing these and similar studies (Figure 7.2). The first step toward the development of this integrated system was the fabrication of an on-line boronate affinity enrichment step. Toward that end, this chapter describes progress towards the development of a 3D printed scaffold for a miniaturized boronate affinity column. In boronate affinity chromatography, a reversible complex is formed between the boronic acid solid phase and the cis diol-containing analyte when the pH is above the pKa of the boronic acid (~pH 8). This selective interaction is reversed when the pH is lowered to far below the pKa (~pH 2). Because the derivatizing agent used in Schoeneich's method contains a cis-diol group, the derivatized, nitrated peptides will be able to be captured on this column and then released in an enriched fraction.

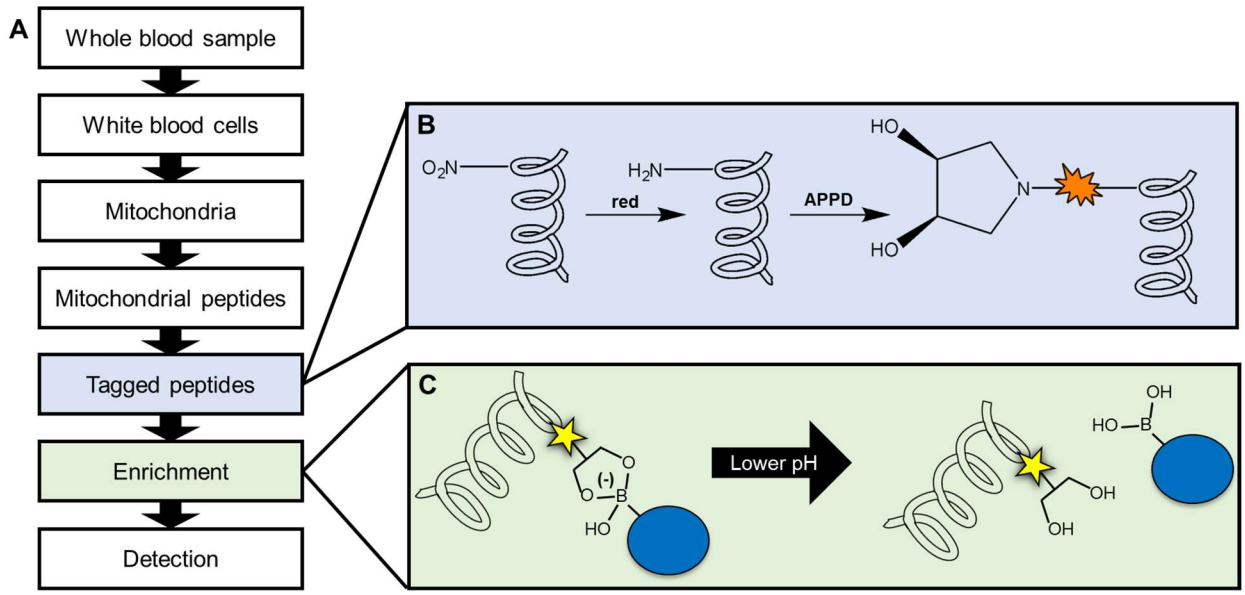

Figure 7.1. (A) Conventional workflow for analysis of nitrated peptides; (B) Tagging of nitrated peptides via sodium dithionite reduction followed by selective derivatization with (3R, 4S)-1-(4-(aminomethyl)phenylsulfonyl)pyrrolidine-3,4-diol (APPD); (C) Trapping of tagged peptides via boronate affinity chromatography at high pH followed by elution in an enriched, purified fraction at low pH.

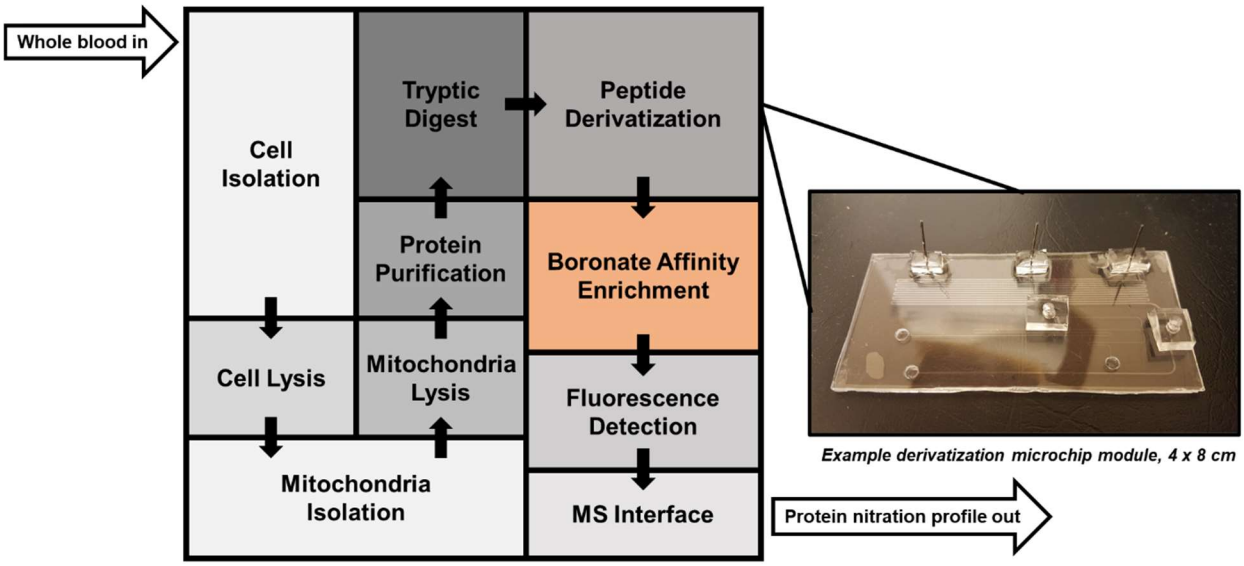

Figure 7.2. Possible layout of an integrated microfluidic device for profiling mitochondrial protein nitration from whole blood

Initial experiments conducted at KU attempting to integrate a boronate affinity monolith directly into a planar glass microchip (Figure 7.3) were based on the work of Cakal *et al*.[16] However, several issues arose that made further development of this device difficult. From a fabrication standpoint, bonding all-glass microchips has a rather low success rate, especially when the channel design increases in complexity and surface area. In addition, adopting any design modifications is a lengthy and labor-intensive process, involving the production of a new UV exposure mask, etching with hydrofluoric acid, and an overnight glass bonding procedure in a high temperature oven. From a user-friendly perspective, integrating a glass microchip with any other module, as will be necessary to include all the elements shown in Figure 7.2, proves difficult. Based on these drawbacks of the conventional microfabricated device, we turned to 3D printing.

3D printing has several potential advantages for this project because it affords the ability to conduct rapid prototyping of the scaffold design as well as the ability to easily integrate the column with other modules. Its key disadvantage lies in its resolution. While traditional photolithographic techniques enable the fabrication of glass or polydimethylsiloxane channels in the low micron range, a typical stereolithographic (SLA) 3D printer is only capable of producing channels in the hundreds of microns range. While this does preclude our ability to directly transfer our previous microchip designs directly to the 3D printed format, these dimensions are compatible with the boronate affinity module, as more surface area for interaction is beneficial. It should be noted that the shift from microfabrication to 3D printing techniques occurred during a collaboration with the University of Groningen and so throughout this chapter there will be mentions of different materials and instrumentation used for the same purpose based on availability at the two universities.

In this chapter, an SLA 3D printer was used to develop a scaffold for a boronate affinity monolith. The polymerization procedure was first optimized for each iteration of the scaffold and

then a model analyte, Alizarin Red S, was used to optimize a loading and elution protocol. Various offline and online detection techniques were investigated for their suitability for monitoring the column's capture efficacy. Preliminary efforts to miniaturize the cell lysis and mitochondria isolation steps in the overall experimental workflow are discussed in the next chapter.

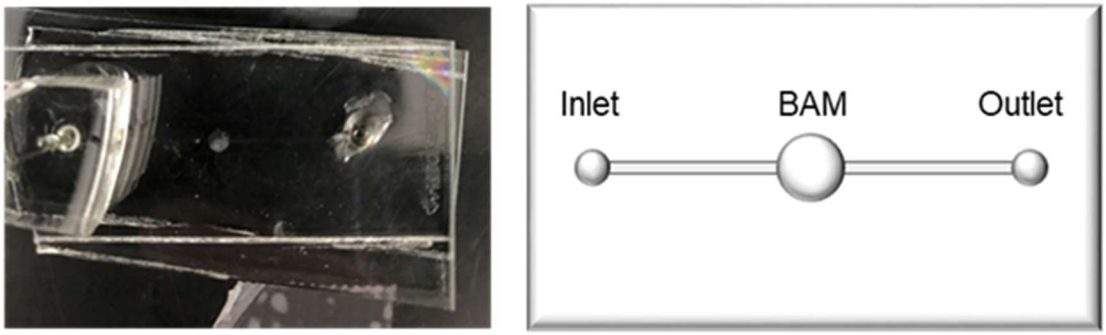

Figure 7.3. All-glass microchip containing a boronate affinity monolith (BAM) with a steel pin secured at the inlet via a piece of PDMS.

7.2 Materials and methods

7.2.1 Reagents and materials

The following materials and chemicals were used as received: isopropanol (IPA), N-propanol, 1,4-butanediol, ethylene glycol dimethacrylate (EGDMA), 4-vinylphenylboronic acid (VPBA), Alizarin Red S (ARS), 2,2'-azobisisobutyronitrile (AIBN), polydimethylsiloxane (PDMS) elastomer and curing agent, sodium phosphate dibasic, sodium phosphate monobasic, phosphoric acid, phosphate buffered saline tablets, acetonitrile, acetone, methanol, isopropanol, dopamine, formic acid, and ammonium bicarbonate. Additional 2,2'-azobisisobutyronitrile (AIBN) was obtained from another group and purified in methanol before use. All chemicals were obtained from Sigma-Aldrich or Fisher Scientific (The Netherlands/USA).

7.2.2 3D printing procedures

Devices were designed in the CAD software Solidworks 2016-2017 Education Edition (Waltham, Ma, USA) and converted to STL files for printing. These files were then uploaded to a FormLabs Form 2 SLA printer (Formlabs, Somerville, MA) using Preform 2.16.0 software. When preparing the files for printing, a resolution of 0.050 or 0.025 mm was used with a support size of 0.60-0.70 mm, support density of 1.25-1.30, and base 2 mm thick with the structure 5 mm high above the base. Supports were placed initially using the auto function and then the positions were fine-tuned manually to ensure optimal feature integrity. Most pieces were printed using Formlabs Clear Resin V4, although some o-rings were printed using the Flexible resin. Finished prints were rinsed in one IPA bath for 15 min followed by a second rinse in a cleaner IPA bath for 10 more min, dried completely, and cured for 30 min at 60 °C in a FormCure curing station (Formlabs). Devices that featured screws were screwed together and separated prior to curing in order to ensure a tight fit.

7.2.3 Monolith polymerization procedure

The composition of the polymerization solution was selected based on the work of Cakal *et al* (Table 7.1).[16] The solution was prepared, mixed well, and then sonicated for 10 minutes prior to being placed in the scaffold of choice and exposed to UV light using either a Dymax BlueWave LED Flood System/RediCure Model with ECE Light Shield or a UV spot source. Optimization of polymerization conditions is described in 7.3.2. Columns were then dried overnight at room temperature or 60 ℃ to eliminate excess solvent.

7.2.4 Offline and online detection procedures

For offline detection of column eluent, fractions from loading, rinsing, or elution steps were collected in plastic sample tubes and then diluted into the corresponding buffer (high pH for loading and rinsing, low pH for elution) to reach the necessary volume for analysis. Either a Unicam UV 500 (UVS 005) UV-Vis spectrophotometer or a plate reader was used for offline absorbance measurements. For online MS detection, a PE Sciex API 3000 LC/MS/MS System with a Turbo Ionspray source and Analyst software was used. Dried columns were loaded with ARS or dopamine in loading buffer and then rinsed with loading buffer. Columns were then connected to the MS for direct infusion of eluent into the ESI ionization source. Scans were performed from 100 Da to 1300 Da with a step size of 0.10 Da and a time of 2.00 s, in positive ion mode for dopamine and negative ion mode for ARS. The nebulizer gas was set to 10.00 psi, the curtain gas to 10.00 psi, the ion spray voltage to 3000.00 V, declustering potential to 5.00 V, focusing potential to 200.00 V, and entrance potential to 10.00 V. The temperature was set to 500.0 °C for ARS and 0.0 °C for dopamine. The low temperature and declustering potential were set to prevent fragmentation of dopamine within the source. For online UV detection, a LC UV flow cell was used set to 254 nm.

Table 7.1. Polymerization solution composition.

Solvents	1-propanol	435 µL
	1,4-butanediol	175 µL
Cross-linker	Ethylene glycol dimethyacrylate (EGDMA)	95.2 µL
Boronate monomer	4-vinylphenylboronic acid (VPBA)	10 mg
Free radical initiator	2,2'-azobisisobutyronitrole (AIBN)	1.1 mg

7.3 Results and discussion

7.3.1 Development of a 3D printed scaffold for boronate enrichment of cis-diol-containing analytes

In order to accomplish *in situ* polymerization of the boronate affinity monolith within the scaffold, there must be a mechanism for temporarily sealing the scaffold at one end to contain the polymerization solution during the UV exposure. The scaffold must then be able to be readily unsealed from this base afterwards without damaging the stationary phase. The process of polymerizing a monolith in a simple cylindrical scaffold is shown in Figure 7.4. The ultimate 3D printed scaffold for the boronate affinity column would then be able to be connected to a syringe pump for perfusion of solution and be able to be integrated with other devices or modules on each end while holding the polymer securely in place during perfusion.

In the process of optimizing the scaffold design, polymerization protocol, and elution protocol, several different iterations of the scaffold and base were explored (Figure 7.5). For the initial optimization of the polymerization conditions, a PDMS scaffold containing a single well reversibly bonded to a PDMS base was used (Figure 7.5A). While this design was effective at enabling rapid screening of polymerization conditions, it was not capable of being connected to any perfusion system or other modules. Another issue is that the monolith would not always remain in the PDMS scaffold when it was removed from the PDMS base.

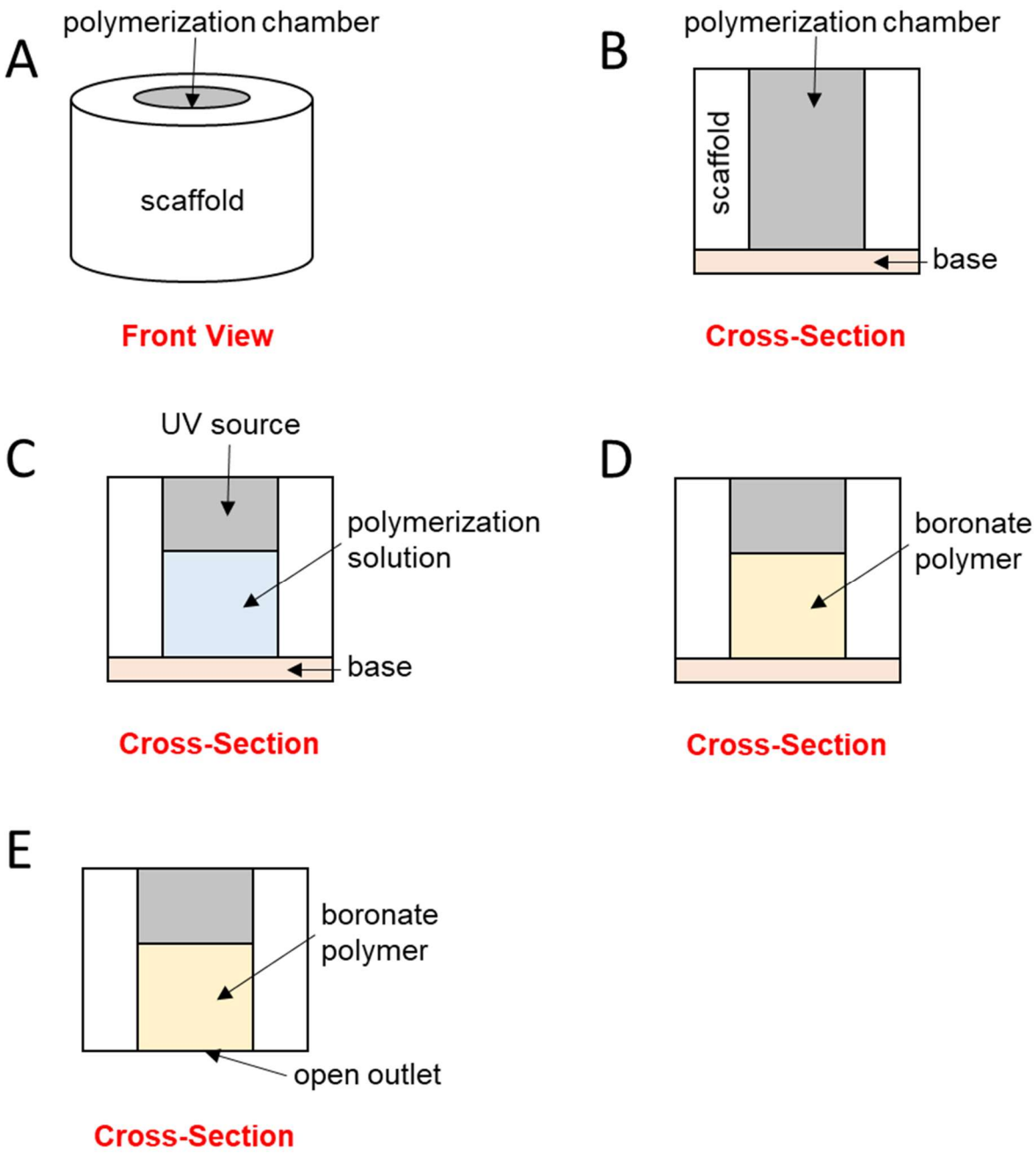

Figure 7.4. (A) Generic scaffold for monolith polymerization containing a central polymerization chamber; (B) Cross-section of the scaffold sealed against a base to form a sealed well; (C) Sealed scaffold containing polymerization solution being exposed to UV light for polymerization; (D) Sealed scaffold containing boronate polymer; (E) Scaffold containing boronate polymer removed from its base so the outlet is open for flow of solution.

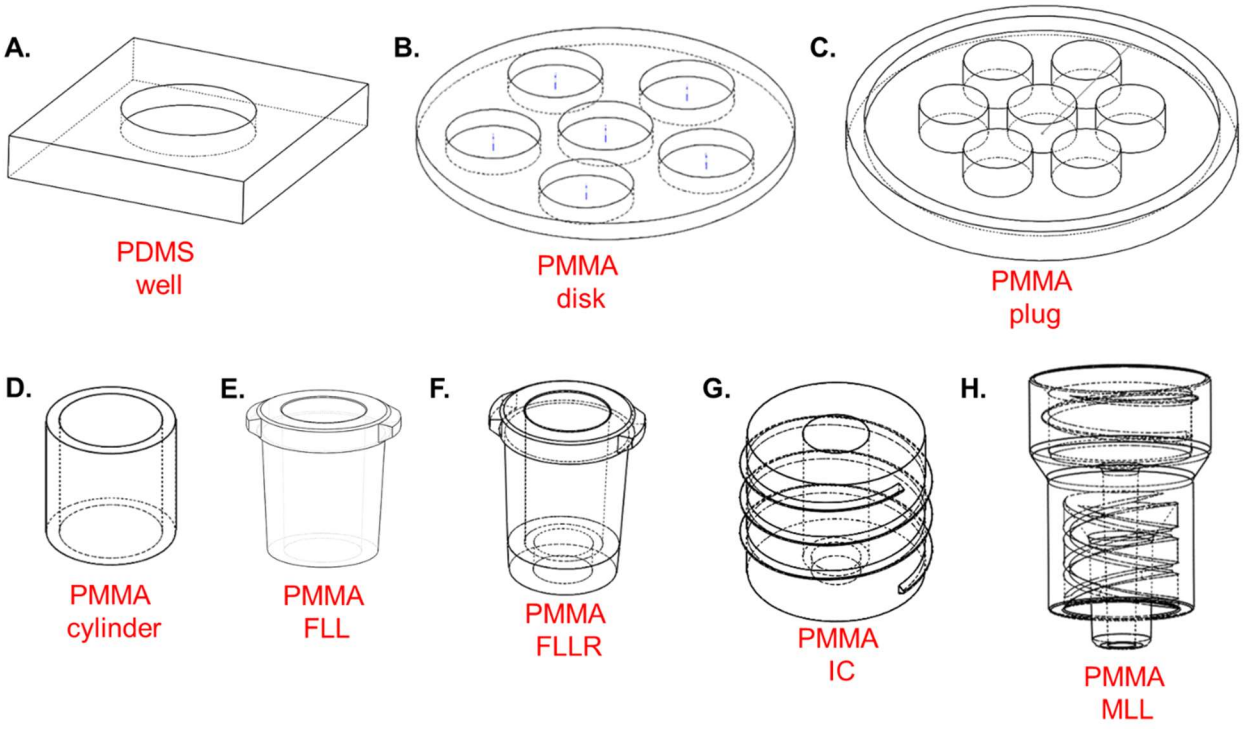

Figure 7.5. Scaffold designs explored during device optimization. (A) PDMS well; (B) 3D-printed disk scaffold; (C) 3D-printed plug for 3D-printed disk scaffold; (D) 3D printed cylinder; (E) 3D printed female portion of a luer-lock (FLL); (D) 3D printed female portion of a luer-lock with a rim around the outlet (FLLR); (E) 3D printed cylinder that can be screwed into connectors (integratable cylinder, IC); (F) 3D printed male luer-lock (MLL) connection cap for the IC scaffold.

The use of 3D-printing to produce a scaffold in a poly(methyl methacrylate) (PMMA)-containing resin was then evaluated (Figure 7.5B, D-G). A disk scaffold containing several PMMA wells was created (Figure 7.5B) and attempts were made seal the entire disk against a PDMS base, as was effective for the all-PDMS scaffold (Figure 7.5). However, it was found that the 3D printed material was not able to form a leak-proof seal against PDMS nor against a 3D-printed plug designed as an alternative to the PDMS base (Figure 7.5C). Therefore, for the remaining PMMA scaffolds shown in Figure 7.5D-G, a thin layer of PDMS was poured onto a substrate and the PDMS cured slightly in a 70 ℃ oven for 5-10 minutes. The PMMA scaffold was then pressed lightly into the still-tacky, partially cured PDMS and the entire substrate was then placed back in the oven for another 10 minutes to allow the PDMS to completely cure. Once the PDMS was cured, the scaffold was filled with solution and polymerized *via* UV exposure (Figure 7.6A). After polymerization, the scaffold could be carefully removed from the PDMS substrate, resulting in a boronate monolith that is open on both ends (Figure 7.6B).

Plain PMMA cylinders of varied diameter were first used for further polymerization optimization, but it was difficult to keep the boronate polymer adhered within the cylinder after polymerization and it was not possible to connect these scaffolds to a syringe in order to perfuse solution through the polymer stationary phase (Figure 7.5D). For elution optimization, the ability to control the flow of solution through the column is essential. Therefore, the cylinder was modified to emulate the structure of a needle's barrel that could fit into a luer-lock syringe, *i.e.* the female portion of a luer lock (FLL) (Figure 7.5E). While this design was perfusable, the polymer was often dislodged during removal from the PDMS base. Therefore, the design was modified to contain a rim on the bottom edge which would enable insertion of a filter paper disk into the bottom of the scaffold to provide extra mechanical stability to the monolith. This secured it within the

scaffold during removal from the PDMS and during perfusion (Figure 7.5F). This rimmed design, known as FLLR, was used for most elution optimization experiments.

Although the FLLR design is effective, in order to position the column vertically for more even flow and in order to connect the column to other modules on either end, a final design that featured the same rimmed well as FLLR was produced (Figure 7.5G). This new design was also able to be screwed into caps containing male luer lock (MLL) or female luer lock connections (Figure 7.5H). This made it possible to connect the needles and tubing required to integrate it with other devices. This design, known as the "integratable" cylinder (IC), was used for proof-of-concept experiments involving direct integration with a detector. The key characteristics of each of these designs may be found in Table 7.2.

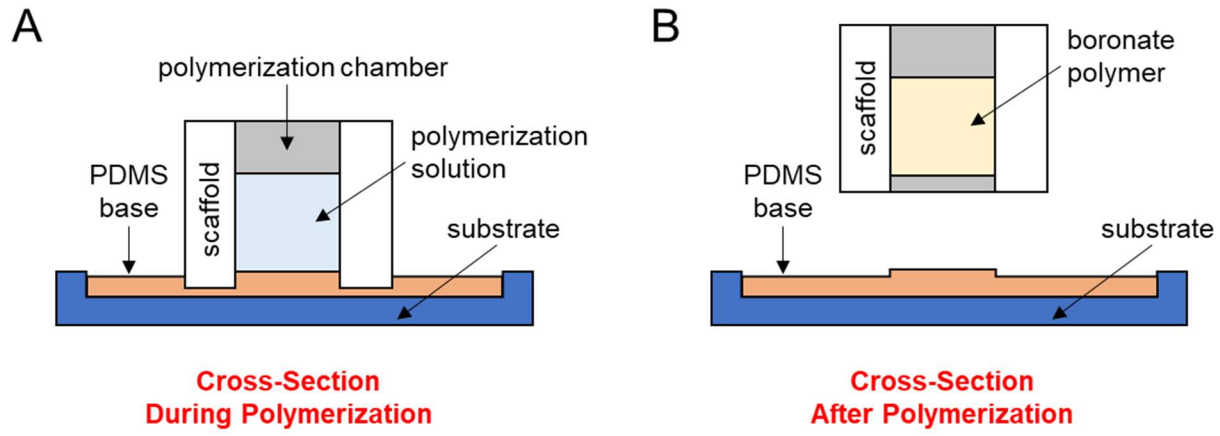

Figure 7.6. Schematic of how uncured PDMS can be used as a base during polymerization. (A) To polymerize a monolith within the scaffold, the scaffold is placed into uncured PDMS such that it sinks slightly into the PDMS layer, forming a seal so the well can be filled with polymerization solution; (B) After polymerization, the scaffold is peeled off the PDMS base, resulting in a scaffold that contains a boronate monolith open on both ends.

Table 7.2. Summary of characteristics of scaffold designs that were explored during device optimization

	Scaffold Design						
Parameter	**A. Well**	**B. Disk**	**B/C. Disk with Plug**	**D. Cylinder**	**E. FLL**	**F. FLLR**	**G. IC**
Well material	PDMS	PMMA	PMMA	PMMA	PMMA	PMMA	PMMA
Base material	Cured PDMS	Cured PDMS	PMMA	Uncured PDMS	Uncured PDMS	Uncured PDMS	Uncured PDMS
Well/base seal	Reversible	Reversible	Reversible	Irreversible	Irreversible	Irreversible	Irreversible
Leak-proof	Yes	No	Aqueous only	Yes	Yes	Yes	Yes
Perfusable	No	No	No	No	Yes	Yes	Yes
Secure polymer	No	No	No	No	No	Yes	Yes
Integratable	No	No	No	No	No	No	Yes

7.3.2 Polymerization conditions optimization

The polymerization solution composition remained constant for all polymerization optimization experiments; however, several other parameters were optimized as shown in Figure 7.7. Initially, PDMS wells (Figure 7.5A) were used to evaluate the effect of exposure time and distance from the UV source on polymerization of a boronate monolith. For the purposes of these experiments, complete polymerization was determined by the presence of a matte white polymer within the well. Using a UV spot source and 20 μL of polymerization solution in each 4 mm diameter PDMS well, the extent of polymerization was determined to level off after around 30 minutes exposure at a distance of 4 mm from the source (Figure 7.7A). When the distance between the polymerization solution and the UV spot source was increased, the extent of polymerization in the same time was observed to rapidly decrease (Figure 7.7B), and optimal polymerization with a completely full well was observed at 2 mm from the UV spot source after 30 min. At shorter polymerization times and further distances, solid polymer was still formed; however, it did not reach the walls of the scaffold, which would result in poor mechanical stability of the monolith and result in perfusion solution flowing around the monolith instead of through it, so it was essential that the polymerization proceed until the polymer reached the walls.

Similar experiments to those shown in Figure 7.7 were also conducted using a more powerful UV LED chamber and the same general dependence on distance was observed (not pictured); however, in the chamber the scaffolds only needed to be positioned within 7 cm of the upper LED sources in order to achieve maximal polymerization. Using each source, the amount of polymerization observed was not improved after 30-45 minutes of exposure (depending on the volume of solution being polymerized), although polymer appeared more matte after exposure in the LED chamber than after exposure with the spot source. It was found that if the polymer was

left to dry at 60 °C overnight, the spot source-polymerized monoliths would achieve the same level of matteness as the chamber-polymerized monoliths.

Once it was determined that polymer could be formed in PDMS wells under these conditions, the experiment was repeated using the FLLR (Figure 7.5F) and the IC scaffolds (Figure 7.5G). The scaffolds were filled with polymerization solution and exposed using the UV spot source or UV LED chamber until the polymer matched the characteristics observed in the optimization using the PDMS wells. Ultimately, it was determined that 45 µL solution could be polymerized successfully in the FLLR scaffold in 30 minutes when positioned 2 mm from the UV spot source (Figure 7.7D(i)). This volume of polymerization solution resulted in maximum monolith volume while reserving enough space for the scaffold to connect to a syringe without disturbing the monolith. In these experiments, the addition of the paper disk to the bottom of the well resulted in a lower chance of damaging the polymer during its removal from the PDMS base after polymerization. Additionally, no polymer was observed forming on the other side of the piece of paper, so the filter paper was shown to prevent polymer from dislodging into the eluent while not hindering fluid flow through the column. The same polymerization conditions were found to be effective at polymerizing 45 µL solution in the IC scaffold (Figure 7.7D(ii)); however, 45 µL is insufficient to completely fill this well. Therefore, the volume of polymerization solution was doubled and attempts were made to polymerize 90 µL solution both at once for 45 min and in two 45-µL increments, with the first exposed for 15 min and the second exposed for 45 min. Each resulted in a similarly sized monolith (Figure 7.7D(iii,iv)), although the polymerization seemed more slightly complete (more matte) when accomplished in layers as in Figure 7.7D(iv). The UV spot source is shown positioned on a PDMS scaffold in Figure 7.7C.

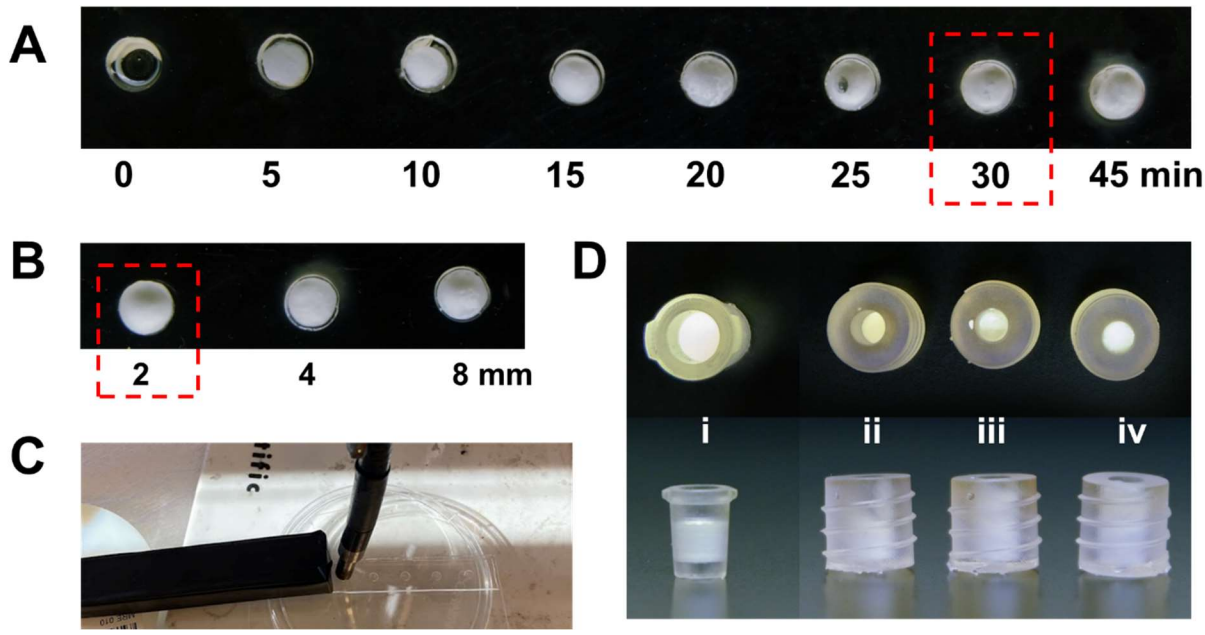

Figure 7.7. Polymerization optimization. (A) Effect of increasing UV exposure time on extent of polymerization; (B) Effect of increasing distance from the UV source on extent of polymerization; (C) Polymerization set-up with UV spot source and PDMS well scaffold; (D) Comparison of i. FLLR scaffold (45 µL polymerization solution (P.S.), 30 min), ii. IC scaffold (45 µL P.S., 30 min), iii. IC scaffold (90 µL P.S., 45 min), iv. IC scaffold (45 µL P.S., 15 min + 45 µL P.S., 45 min)

7.3.3 Column use optimization

7.3.3.1 Model analyte

The FLLR scaffold polymerized according to the optimal protocol (as shown in Figure 7.7D(i)) was used for the optimization of the column loading and elution protocol. The key components to be considered were the experimental set-up, column loading, column dimensions, rinsing and elution steps, and integration with detectors. These are shown in Figure 7.8. For initial experiments, a cis-diol-containing dye, Alizarin Red S (ARS) was used as the model analyte (Figure 7.8A). ARS is well-suited to rapid qualitative optimization of loading and elution conditions. It is a pH indicator and also exhibits an absorbance spectrum shift upon binding to a boronate column (Figure 7.8B,C). In order to confirm that ARS was binding to the boronate polymer, both non-boronated and boronated polymer were exposed to ARS in a typical boronate affinity chromatography loading buffer (PBS at pH 7.4). The color shift of the ARS in contact with the polymer from pale pink (non-boronated column/unbound ARS) to yellow (boronated column/bound ARS) in solution was then observed (Figure 7.8D). As we were able to observe this phenomenon in solution, it followed that this color shift could provide a good indication of whether the loading or elution buffers are functioning as expected.

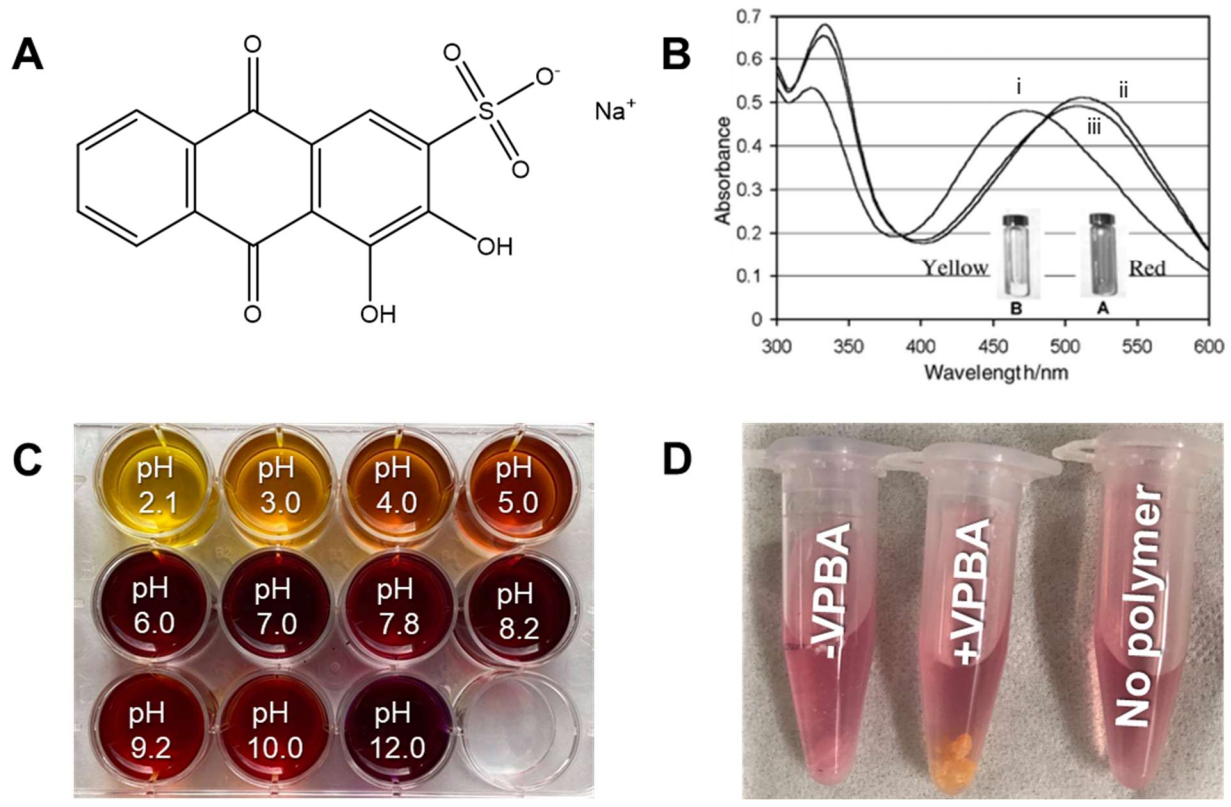

Figure 7.8. (A) Model analyte Alizarin Red S (ARS); (B) Absorbance spectrum of 10^{-4} M ARS in 0.1 M phosphate buffer at pH 7.4 (i) unbound, (ii) after addition of 10^{-3} M phenylboronic acid (PBA) to bind the ARS, and (iii) after addition of 10^{-1} M fructose to preferentially bind to the PBA and displace the bound ARS, reproduced from Ref.[17] with permission from The Royal Society of Chemistry; (C) 1 mg/4 mL ARS at varied pH; (D) Color shift of 100 µM ARS upon exposure to non-boronated (-VPBA) or boronated (+VPBA) polymer.

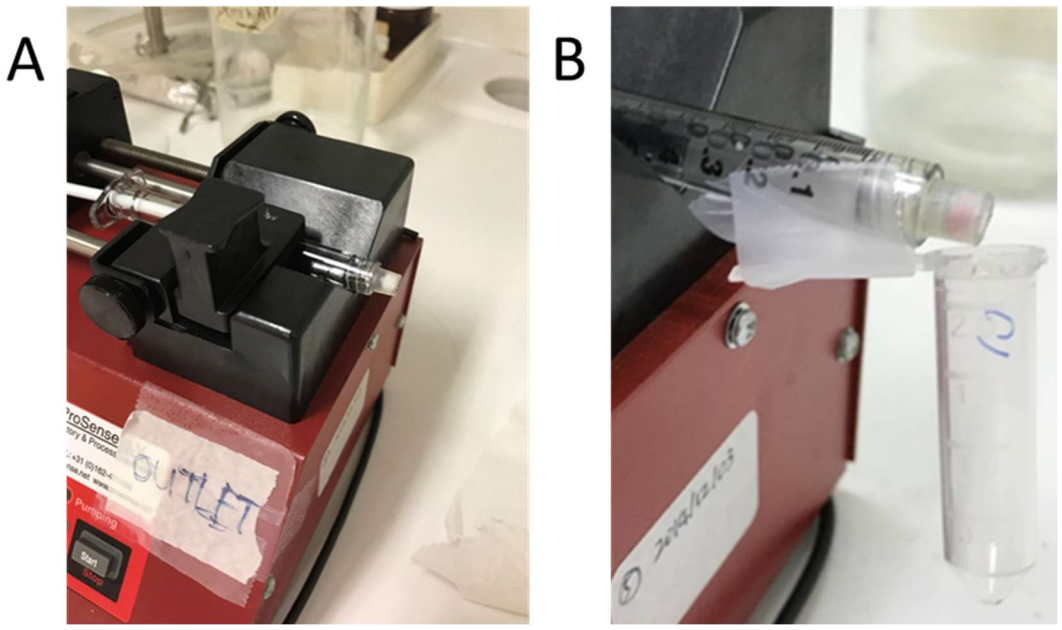

Figure 7.9. (A) Integration of scaffold F with a syringe and syringe pump; (B) Addition of a tube for collection of eluent.

7.3.3.2 Experimental set-up

In order to perfuse solution through the scaffold and collect the eluent for subsequent evaluation, the FLLR scaffold was screwed onto a conventional 1-mL luer-lock syringe which was filled with the desired rinsing, loading, or elution buffer and then placed in a syringe pump (Figure 7.9A). A 2-mL plastic tube was then secured at the end of the scaffold to collect any eluent (Figure 7.9B). Immediately after polymerization, each column was perfused first with at least 200 µL MeOH at 50 µL/min to eliminate any residual solvent or unreacted monomer and then allowed to dry completely in fume hood or 60 ℃ oven overnight to evaporate the excess MeOH.

7.3.3.3 Sample introduction

A few different methods were explored for introducing ARS into columns in Scaffold F. Pipetting a known amount of ARS directly on top of the column would make it possible to know the exact amount of analyte introduced to the column; however, the ARS solution remained in a droplet on top of the column and did not seep evenly into the column. This is likely due to a difference in hydrophobicity between the column and the aqueous ARS solution. Next, a known amount of ARS was pipetted onto a filter paper disk and allowed to dry. This disk was then placed on top of the column before the scaffold was screwed onto a syringe containing pH 7.56 phosphate (loading buffer) and a syringe pump was used to flow the loading solution through the column. However, little to no loading of the ARS from the filter paper disk onto the column was observed. It appeared that the ARS solution was much more attracted to itself or to the filter paper disk than to the column, limiting its loading.

Therefore, it was determined that the best method for loading a column in a FLLR scaffold with ARS was direct perfusion from a syringe in a syringe pump. A known volume of ARS in loading buffer was pumped through the column and then the scaffold was placed on a different syringe containing only loading buffer to rinse the column and remove any nonspecifically bound

analyte. However, this method makes it difficult to quantify exactly the amount of ARS loaded onto the column. Although the syringe was filled completely with ARS prior to connection to the FLLR scaffold, due to the surface tension of the droplet at the outlet of the syringe there was some variation in the starting position of the ARS plug versus the scaffold at the nozzle of the syringe. This variation could result in inconsistent loading even if the same volume was pumped using the syringe pump. Despite these limitations, this method was used for all further optimization of this scaffold. In order to account for differences in loading, each column was photographed after loading in order to compare spot sizes and permeation into the columns. A series of spots of increasing volume are shown in Figure 7.10 to demonstrate the level of consistency that can be achieved with this method. In this example, while the 10 and 30 μL spots are relatively consistent and would be able be compared against one another in later steps of the experiment after differing treatments, the 20 μL spots are not consistent and would not be able to be used to study a different variable.

For later experiments using the IC scaffold, a more quantitative method for introduction of ARS was possible. In this method, a piece of tubing was connected via a needle to a syringe containing a solution of ARS and loaded with a known volume of solution (Figure 7.11). This tubing was then carefully removed from the needle and connected to a different needle attached to a syringe containing the high pH loading buffer, while the other end of the tubing was connected to a needle screwed onto one side of the MLL cap for the IC scaffold (Figure 7.11B). As the loading buffer was pumped into the tubing, it forced the ARS solution plug through the tubing and into the column, at which point the loading buffer functioned as a rinsing buffer to eliminate any unbound analyte from the column (Figure 7.11C). Finally, elution buffer could be pumped through the column to elute the analyte (Figure 7.11D). This method enabled exact loading of known quantities of ARS; however, there were bubbles introduced on either side of the sample plug which

could be an issue if this loading is occurring on a column that is already integrated directly with a detection system. This issue could likely be remedied through the use of a Uniswitch device, as is being used in online detection with a UV detector. It should also be noted that in some later experiments the column was equilibrated with loading buffer prior to introduction of the ARS solution; however, this did not result in a visibly different loading.

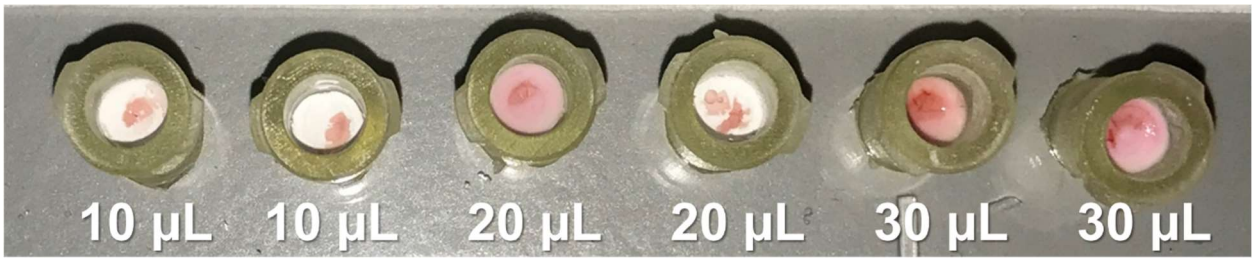

Figure 7.10. Sample reproducibility of spotting varied volumes of 1 mM ARS on Scaffold F columns using a syringe.

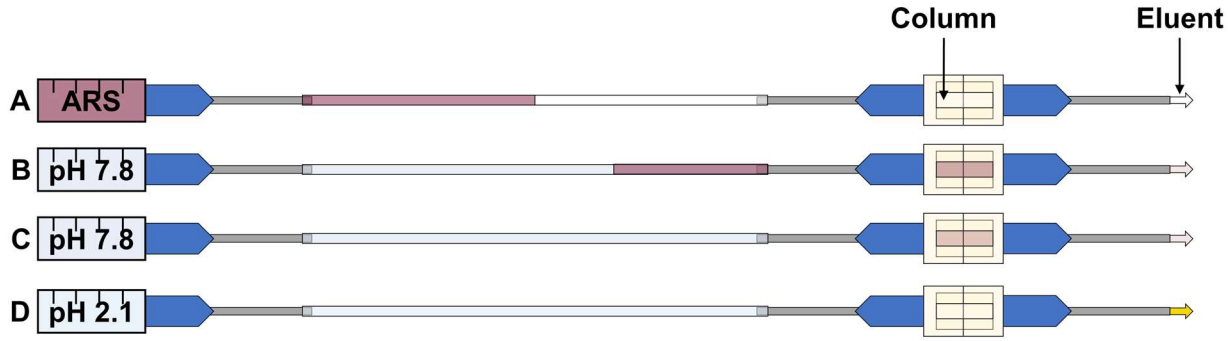

Figure 7.11. Column use protocol for loading of exact volumes of sample. (A) A piece of tubing is loaded with a known volume of analyte; (B) Once the analyte is in the tubing, loading buffer is pumped into the syringe to push the analyte into the column to bind; (C) Once the analyte has passed through the column, loading buffer continues to rinse the column to remove any nonspecifically bound analyte; (D) When elution buffer is pumped through the column, the analyte is released from the column and collected in the eluent.

7.3.3.4 Analyte loading

Once the sample was introduced to the device it was necessary to load the analyte onto the column using a binding buffer. In boronate affinity chromatography, cis-diol-containing analytes are trapped on a column at a high pH above the pKa of the boronate group and then eluted at a low pH. Typically, this is accomplished using phosphate buffer at pH 7.5-7.8 to load and phosphate buffer at pH 2.0 to elute. Therefore, buffers consisting of 50 mM sodium phosphate or PBS between pH 7.5-7.8 were evaluated first for their efficacy as loading buffers.

In order to determine whether these buffers enabled efficient binding of ARS to the column, EGDMA monoliths were prepared both with and without vinylphenylboronic acid (±VPBA) in FLLR scaffolds from 45 µL polymerization solution. For the -VPBA monoliths, the mass of VPBA was replaced with additional mass of EGDMA in the polymerization solution. In these experiments, a 100 µL solution of 250 µM ARS in 50 mM phosphate at pH 7.74 was introduced to the column at 10 µL/min. In Figure 7.12A, the difference in eluent color intensity at the outlet of the scaffolds may be observed as the +VPBA column traps the ARS from the solution as it passes through the column while the -VPBA column does not. Additionally, the difference in color of the ARS bound to the +VPBA column (orange) compared to the ARS nonspecifically interacting with the -VPBA column (pink) may also be observed (Figure 7.12C). After the ARS was introduced to the columns, the columns were each rinsed with 150 µL 50 mM phosphate at pH 7.74 at 25 µL/min. When the buffer passed through the -VPBA column, any residual ARS was immediately flushed out of the column. In contrast, ARS remained bound to the +VPBA column (Figure 7.12B). After the 150 µL rinse, no residual ARS was observed on the -VPBA column, indicating that this rinse was sufficient to remove any nonspecifically bound analyte (Figure 7.12D). The color intensity of the +VPBA column before (Figure 7.12C) and after (Figure 7.12D) the pH 7.74 rinse demonstrates that no observable loss of bound ARS occurred during this rinse.

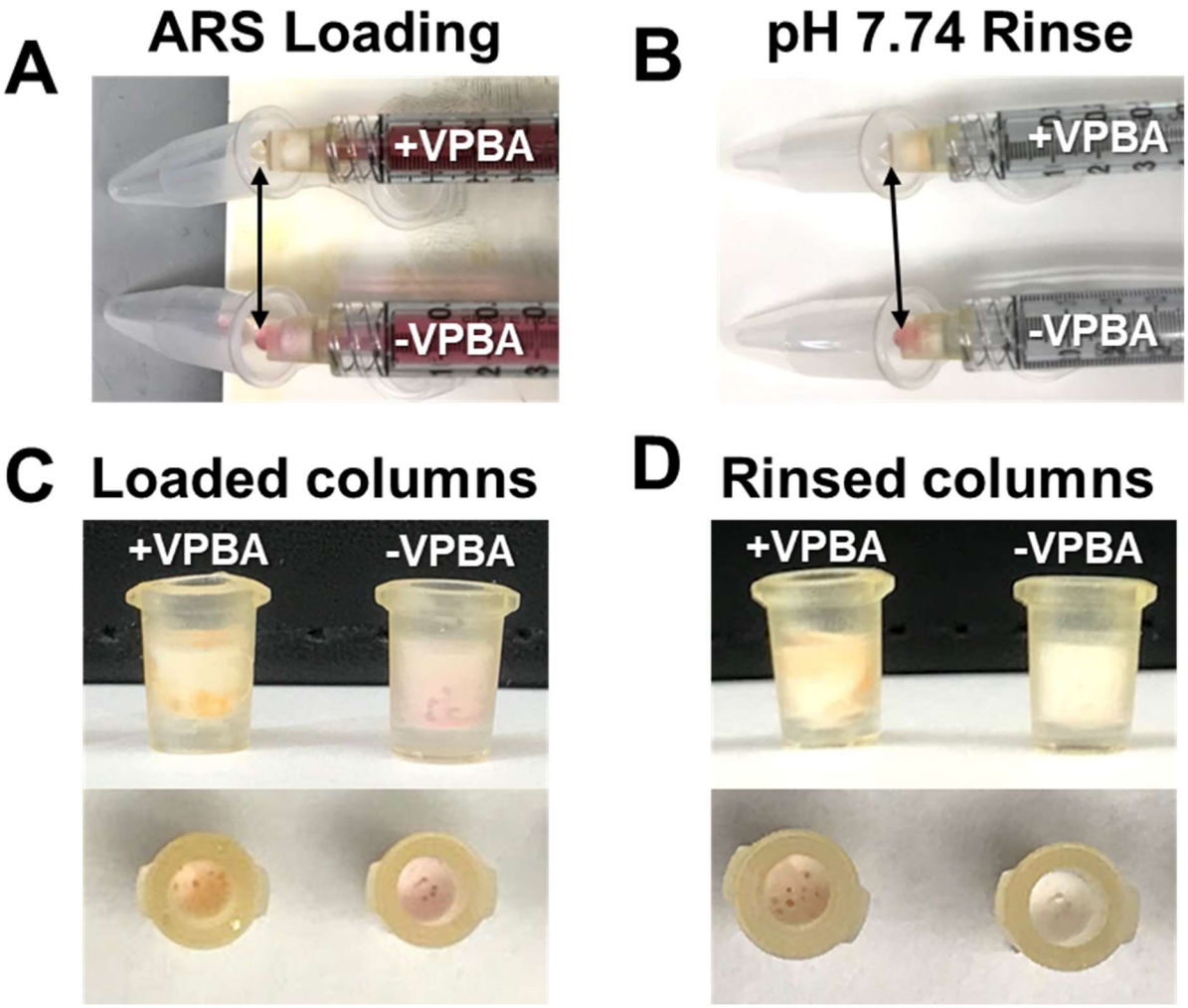

Figure 7.12. Demonstration of efficacy of 50 mM phosphate at pH 7.74 as a loading buffer. (A) The eluent from the +VPBA column is largely colorless, while the eluent from the -VPBA column is the same color as the ARS solution being perfused, demonstrating the ARS being bound to the +VPBA column. (B) No ARS is observed eluting from the +VPBA column, while the ARS is being observed flushing out of the -VPBA column; (C) After loading with ARS, the color difference between ARS bound to the +VPBA column versus unbound to the -VPBA column is observed; (D) After rinsing with pH 7.74, the +VPBA column has retained the ARS, while the -VPBA column has not.

7.3.3.5 Analyte elution

Once it was determined that pH 7.74 phosphate was an adequate loading buffer, it was necessary to identify an elution buffer to release bound ARS from the boronated column. The same columns prepared as in Figure 7.12 (shown again in Figure 7.13A(i,ii) for comparison) were then rinsed with a typical elution buffer for boronate affinity chromatography, 50 mM phosphate at pH 2.1. The result of a 150 µL rinse at 25 µL/min is shown in Figure 7.13A(iii). The -VPBA column had no residual ARS even before the pH 2.1 rinse, as demonstrated by the colorless -VPBA columns (ii) and (iii). Conversely, the +VPBA column had significant ARS both before and after the pH 2.1 rinse, observable as the orange color on column (ii) (high pH, bound ARS) and the yellow color on column (iii) (low pH ARS), and experienced only minimal elution of ARS under these conditions. The eluent from each of these steps is shown in Figure 7.13B, in which the difference in color intensity between the +VPBA and -VPBA columns in the rinse fractions confirms that more ARS is being retained on the +VPBA column. However, the lack of color intensity in the eluted fractions indicates the elution buffer was not functioning as expected.

Because the elution conditions used in the experiment shown in Figure 7.13 were insufficient to release bound ARS from the column, several other variants were tried in an attempt to improve the elution. No improvement of ARS elution was observed with dramatically increased elution volume (up to 1.2 mL) nor with much faster (up 100 µL/min) or slower (down to 2 µL/min) flow rates. It was hypothesized that the retained ARS could be residing in parts of the column that were not receiving adequate flow of the low pH buffer; however, rotating the column on the syringe midway through the elution to vary the flow profile did not result in improved elution of ARS. Incubating the column in elution buffer prior to pumping solution through the column also did not facilitate elution. Additionally, the pH of the eluent was measured during the switch from pH 7.5 to pH 2.0 and it was determined that the first 25 µL of eluent after the switch are still pH

7.5 but by 50 µL the eluent was consistently pH 2.0. This indicates that some factor other than a poor pH equilibration time must be playing a role in the poor elution.

As a result of these observations, as well as the earlier difficulty in wetting the column with a solution of ARS unless pressure is applied via a syringe pump to force the solution through, the use of organic containing buffers was evaluated. Methanol and isopropyl alcohol were screened, but the most promising solvent for analyte elution was acetone. Therefore, the percent of acetone in the elution buffer was varied to determine its effect on ARS elution. Five FLLR scaffolds were loaded with 100 µL 250 µM ARS in pH 7.74 phosphate at 10 µL/min and then rinsed with 150 µL pH 7.74 phosphate at 25 µL/min, as determined in the previous section. Then, each was rinsed with 150 µL pH 2.1 phosphate with varied percent acetone (v/v) at 25 µL/min. During the elution, it was observed that increasing elution of ARS occurred when 0, 10, and 25% acetone was used. From 25% to 50% acetone, little improvement in ARS elution was observed and incomplete ARS elution was observed with 100% acetone (Figure 7.14). This indicates that while the acetone enables the complete elution of the bound ARS, the pH change was also necessary for the reversal of the boronate complex, confirming that while there was a secondary interaction preventing complete elution, the primary binding mechanism was pH dependent. An elution buffer of 50 mM phosphate at pH 2.1 with 50% acetone was selected for future experiments.

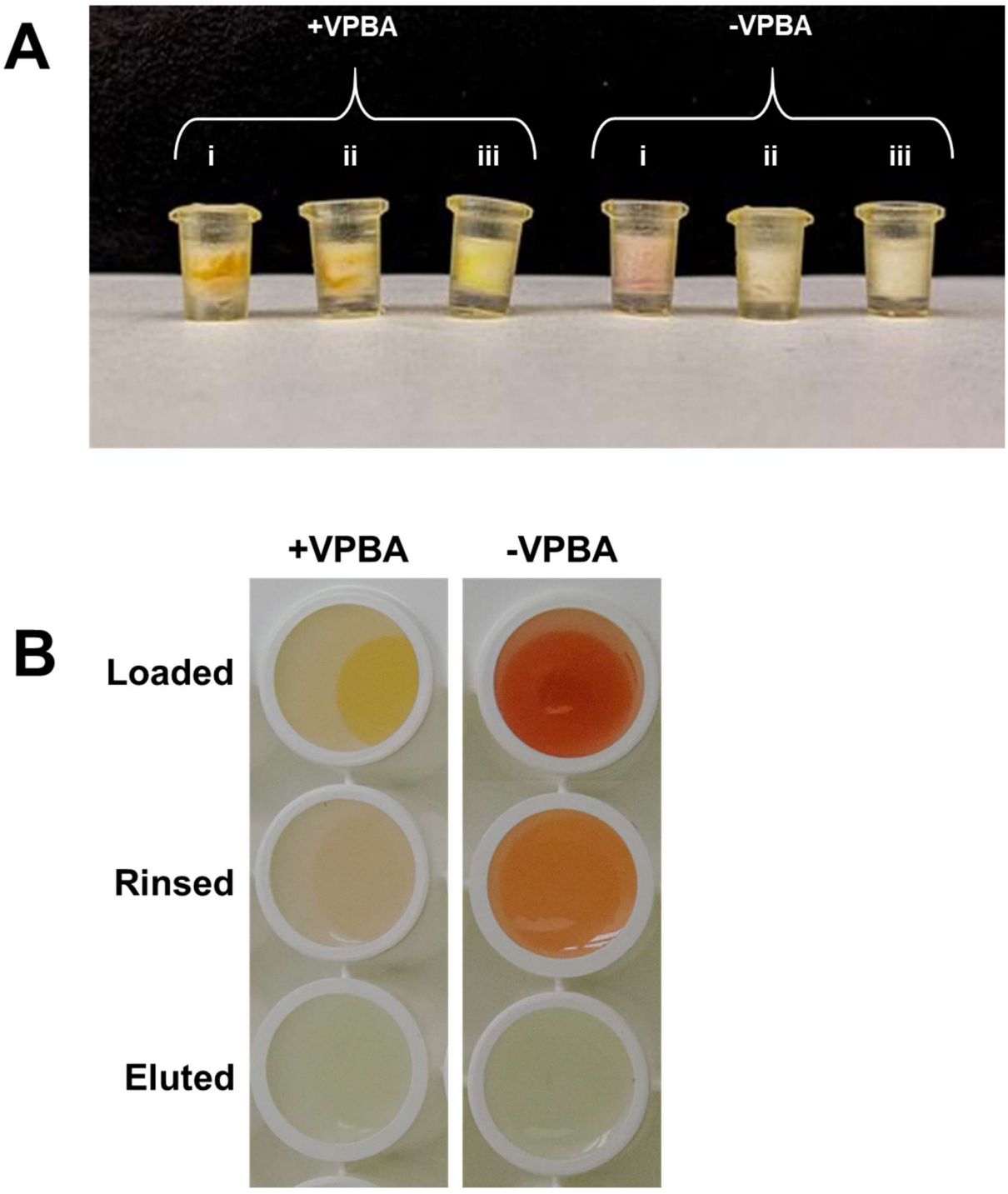

Figure 7.13. (A) Comparison of boronated (+VPBA) and nonboronated (-VPBA) columns (i) loaded with ARS, (ii) rinsed with pH 7.74 phosphate, and (iii) rinsed with pH 2.1 phosphate. (B) Comparison of eluent from each of those steps demonstrating the change in color and color intensity with each condition.

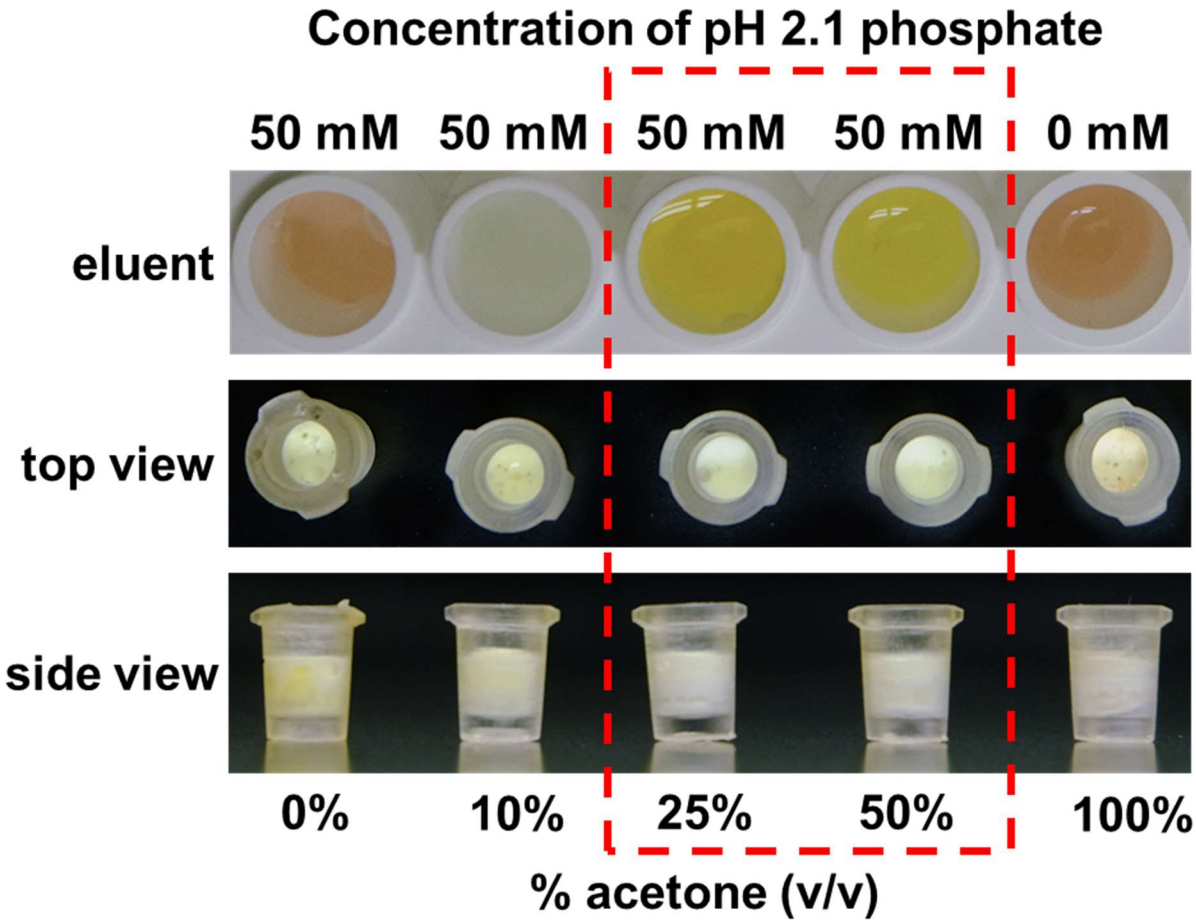

Figure 7.14. Effect of increasing percent acetone (v/v) with pH 2.1 phosphate as elution buffer.

7.3.4 Exploration of possible techniques for eluent detection

7.3.4.1 Off-line detection

Although it is convenient that ARS provides a colorimetric indication of the amount of analyte bound to a column, in order to gain quantitative information about the extent of the binding and elution or to make any conclusions about colorless analytes, a detection method must be integrated with the system. Initially, 100 µL elution fractions were collected as shown in Figure 7.9B and approximately 75 µL of each fraction was diluted into 1 mL in buffer in a cuvette and the absorbance was measured using a conventional spectrophotometer. The absorbance of "loading" and "rinsing" fractions was measured at the λ_{max} of ARS at pH 7.5, 520 nm, and the absorbance of "elution" fractions was measured at the λ_{max} of ARS at pH 2.0, 424 nm (Figure 7.15A). Calibration curves of ARS at each pH using the spectrophotometer are shown in Figure 7.15B. The LOD of this method was approximately 15-30 µM for the samples in the cuvettes, so it was only possible to detect concentrations of 150-300 µM in the undiluted fractions. Although when excess ARS was loaded onto the columns it was sometimes possible to detect unbound ARS being rinsed off in the "rinsing" fractions, this method was not sensitive enough to observe the amount of ARS that was bound to the column. The binding capacity of the columns was so low that even if all bound ARS was present in the pH 2.0 eluent during the elution step, the concentration was below the LOD and no ARS would be detected.

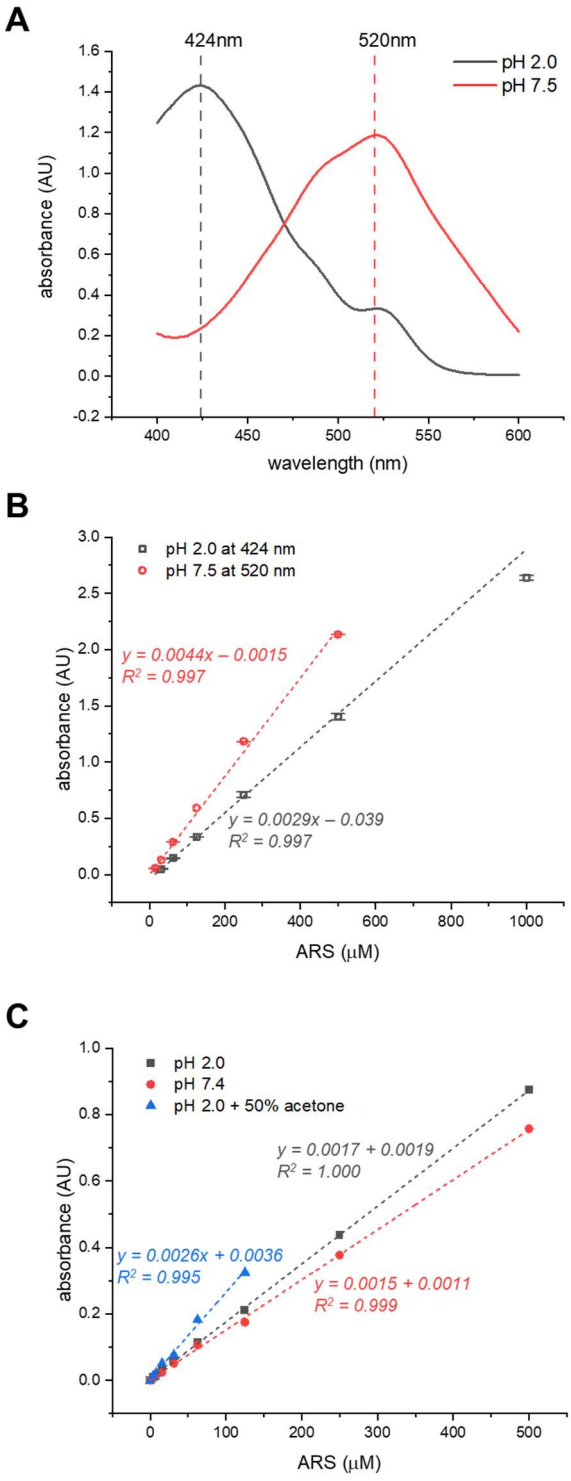

Figure 7.15. (A) Absorbance spectra of ARS at pH 2.0 and pH 7.5 (spectrophotometer); (B) calibration curves of ARS at the λ_{max} for pH 2.0 and 7.5 (spectrophotometer); (C) calibration curves of ARS at the λ_{max} for pH 2.0 and 7.5 and the effect of the addition of acetone on the pH 2.0 calibration curve (plate reader).

In an effort to minimize post-collection dilution, attempts were then made to quantify the amount of ARS in the eluent using a plate reader instead of a spectrophotometer. Although the limits of detection obtained for ARS with the plate reader are only slightly lower than that of the spectrophotometer (approximately 8-25 μM), the key improvement was the decrease in dilution (Figure 7.15C). For these experiments, 180-200 μL fractions were collected and 150 μL of each fraction was measured directly using the plate reader. This method got closer than the spectrophotometer method to providing a quantitative picture of what is happening during each phase of the column use. However, as can be seen in Figure 7.16, the quality of this data was highly variable. In Figure 7.16A, four columns (two boronated, two non-boronated) were loaded with 747 mL 7.81 μM ARS in 50 mM phosphate at pH 7.4, rinsed with 540 μL 50 mM phosphate at pH 7.4, and then rinsed with 360 μL 50 mM phosphate at pH 2.0 with 50% acetone (v/v) at either 50 or 10 μL/min. The absorbance of each 180 μL fraction collected was measured using the plate reader at the same time as calibration solutions and blanks were measured. The amount of ARS in each fraction was calculated from that day's calibration curve and compared to that day's LOD, as some shifts in the background absorbance were observed on different days. While in the experiment shown in Figure 7.16A there is a trend that non-boronated columns had higher ARS concentration in the loading fractions and boronated columns had a higher ARS concentration in the elution fractions, a similar experiment shown in Figure 7.16B detected no elution of ARS from the column. Additionally, the LOD (expressed in nmol ARS/fraction) differed between the two days. These experiments demonstrate that, although the plate reader is superior to the spectrophotometer and is possibly able to differentiate between great differences in column capture efficiency, it is unable to distinguish the smaller changes important for protocol optimization and is not suitable for quantification.

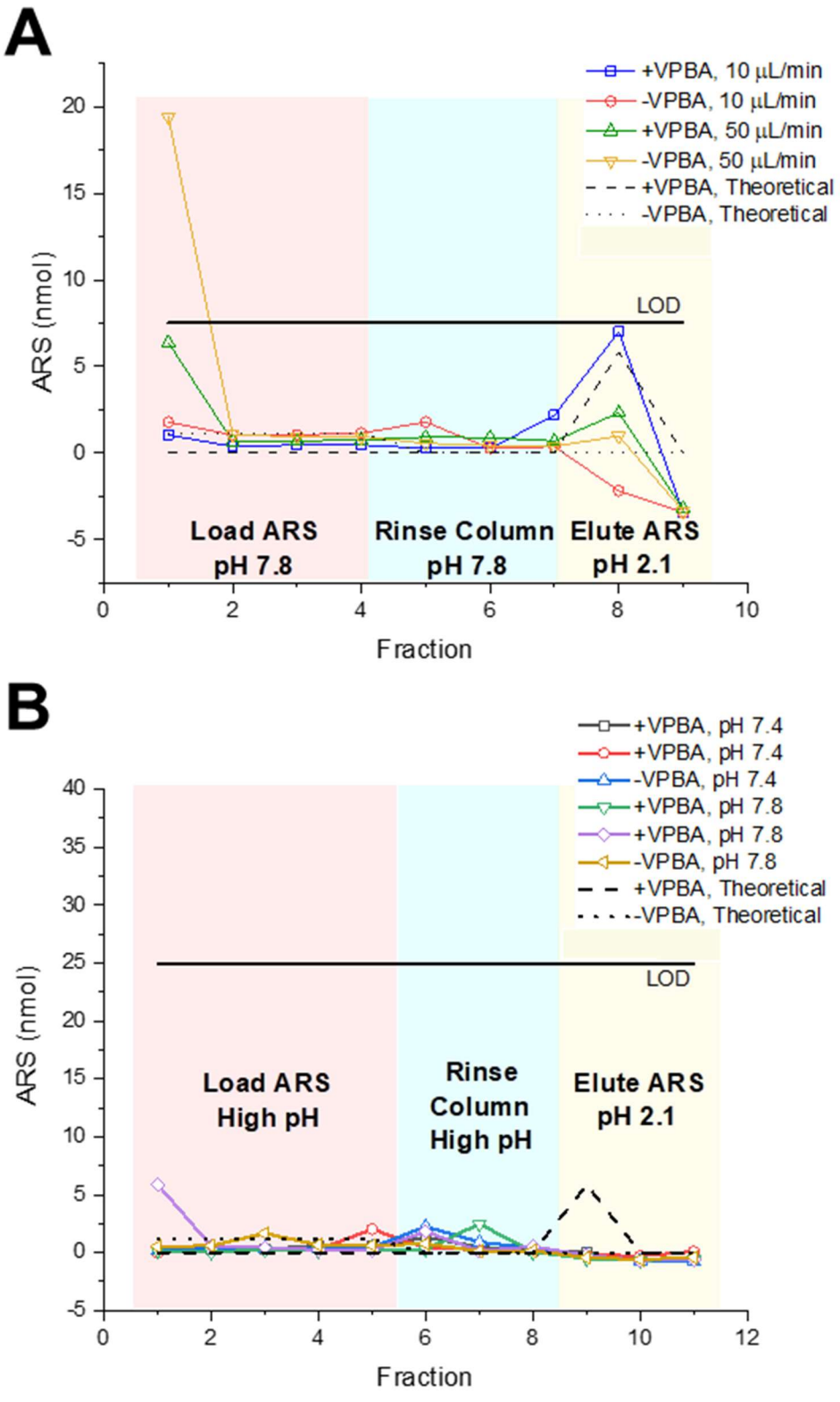

Figure 7.16. Approximate nmol ARS detected in each eluent fraction from boronated and nonboronated columns with (A) varied flow rate and (B) varied loading pH. These plots demonstrate the irreproducibility of this method.

7.3.4.2 On-line detection

In the experiments described above, it was clear that a plate reader or even under some conditions a spectrophotometer could provide some indicator of whether there was a significant amount of ARS in the eluent. However, the necessity of diluting the eluent or gathering a large enough fraction to fill the cuvettes/wells as well as the high LOD of the systems makes these detection systems inadequate for discernment of small variations in efficacy of columns and buffer systems. Therefore, it was desirable to integrate the column directly with a sensitive detector such as a mass spectrometer. In order to accomplish this, it is necessary not only to use the IC scaffold in order to enable direct integration but also to adapt the loading and elution buffers to be MS-compatible. Since it is not ideal to inject salty phosphate buffers into a mass spectrometer, it was necessary to identify volatile buffers that would accomplish similar loading and elution to that observed with the optimal buffers, phosphate at pH 7.74 and phosphate at pH 2.0 with 50% acetone. First, 20 mM ammonium bicarbonate at pH 7.5 was evaluated as a loading/rinsing buffer. ARS was loaded onto two columns with PBS at pH 7.5 and then 20 mM ammonium bicarbonate was used to rinse the columns. After these rinses, ARS was still bound on the column. Because the ammonium bicarbonate did not cause any displacement of the bound ARS, this indicated that ammonium bicarbonate should be able to be used as the rinsing buffer and likely as the loading buffer as well. Then, 0.1% formic acid and 100% acetonitrile, typical MS solvents that possess similar properties to the previously optimized elution buffer, were each evaluated. A combination of 0.1% formic acid with 50% acetonitrile was then used for the elution buffer and under these conditions and using this solution resulted in complete elution of the bound ARS (Figure 7.17). The effect of each of these solvents alone was also evaluated to ensure that the combination was necessary.

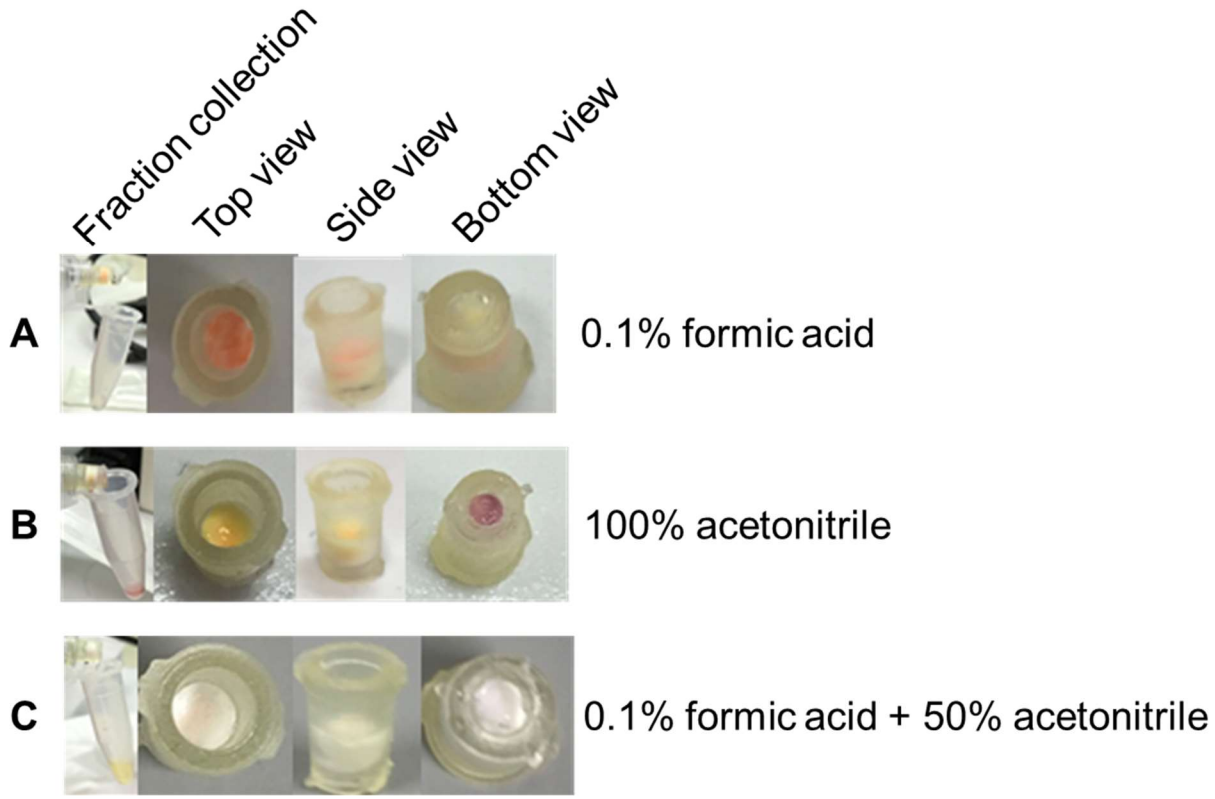

Figure 7.17. Result of using three different MS-compatible solvents as elution "buffer." Images depict the amount of ARS eluted in the first elution fraction *vs*. the ARS that remained bound on the column after elution when using (A) 0.1% formic acid, (B) 100% acetonitrile, and (C) 0.1% formic acid + 50% acetonitrile as the elution solution.

As a proof-of-concept, columns were prepared in IC scaffolds, rinsed with MeOH, and then allowed to dry overnight. Pieces of Teflon tubing were loaded with 20 µL 0.5 mM dopamine (another cis-diol-containing analyte) in loading buffer (20 mM $NaHCO_3$ at pH 7.5) and then connected to the column and loaded onto the column via perfusion with loading buffer. The column was connected at the inlet to a syringe pump containing elution buffer (0.1% formic acid/50% acetonitrile pH 2.0) and the outlet was connected to an ESI source (Figure 7.18). Eluent was then injected into the MS at 100 uL/min in positive ionization mode. Prior to infusion from the column, the ionization temperature and declustering potential were both optimized to achieve optimal dopamine signal at *m/z* 154. A peak at *m/z* 154 was observed growing once the column perfusion began; however, other contaminant peaks were much more prominent in the mass spectrum (Figure 7.19). This contaminant peak was tentatively identified as urethane dimethacrylate, a common component in dental resins that is likely present in the 3D printed scaffold, based on the adducts formed and MS/MS data obtained.

Similar results to those shown in Figure 7.19 were obtained using ARS as the analyte in negative ionization mode. Although the analyte of interest was observed eluting from the column with the elution buffer, the presence of the contaminant likely results in ionization suppression of the analytes and made extensive cleaning protocols necessary to eliminate that contaminant peak for future runs. These drawbacks indicate that MS will not be able to provide the low LODs necessary for quantitative interpretation of experimental results unless this contaminant peak is eliminated.

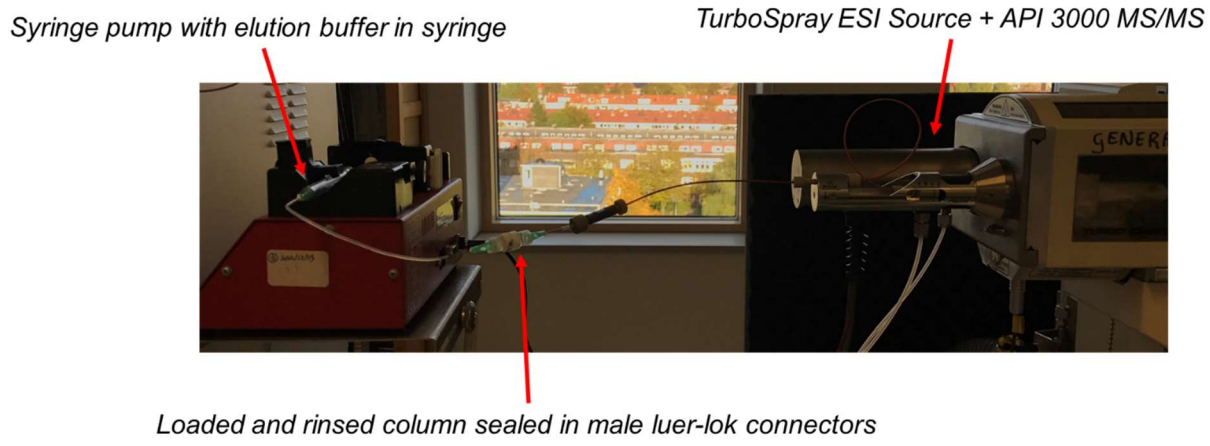

Figure 7.18. Integration of column with mass spectrometer.

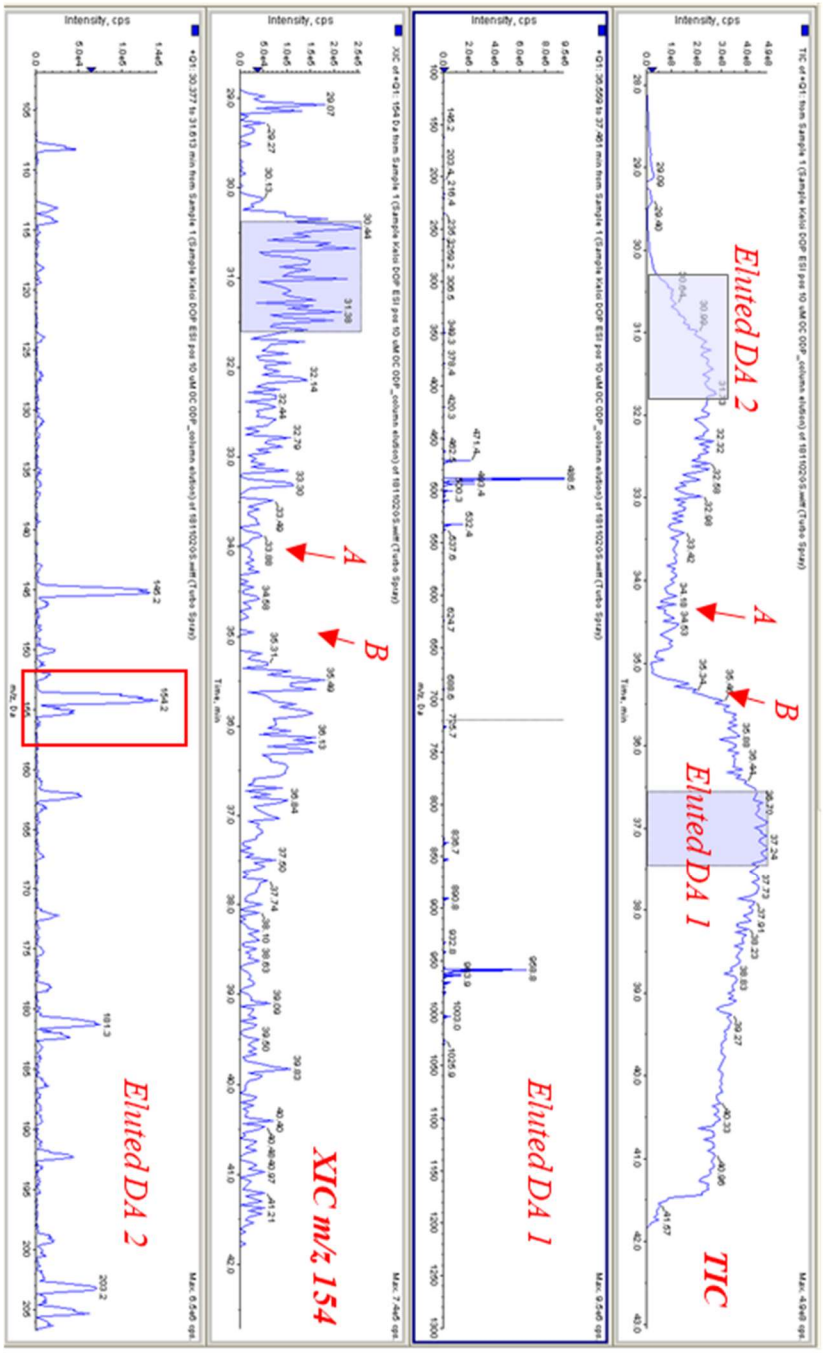

Figure 7.19. MS data obtained when a boronated column was loaded with DA and rinsed off-line and then perfused with elution buffer directly into the instrument as shown in Figure 7.18. (A) Total ion chromatogram during elution from column; (B) sample mass spectrum during elution in region 1; (C) extracted ion chromatogram at dopamine's m/z 154; (D) zoomed in mass spectrum during elution in region 2. “A” indicates a point when perfusion was paused and “B” indicates the point when perfusion was restarted.

Because the leaching of the contaminant from the 3D printed scaffold into the eluent was a concern for integration with mass spectrometry, the column was then integrated with a conventional LC UV detector (Figure 7.20B). In this configuration, the bottom of the IC scaffold was modified so that a piece of LC tubing could be inserted directly into the scaffold outlet for a tight seal with decreased dead volume (Figure 7.20A). Additionally, a Uniswitch device was obtained that enabled uninterrupted switching between the syringes containing analyte, loading/rinsing buffer, and elution buffer. As solution is flowed through the column at 50 – 100 μL/min, the eluent is directed into the flow cell and the absorbance is monitored at the λ_{max} for the analyte of interest, resulting in a shift in the background absorbance measured as analyte passes through the detector. While this method has been used to produce calibration curves for both dopamine and ARS, it is prone to shifts in the absolute signal over time (*e.g.* 10 μM analyte produces a different response at 10 min vs 40 min) even as the relative changes with concentration remain constant (*e.g.* 20 μM analyte would produce double the signal of 10 μM at both 10 min and 40 min into the experiment) (Figure 7.21A). Some preliminary data demonstrating the basic concept behind these experiments is shown in Figure 7.21. The hypothesis is that when a known amount of analyte is passed through boronated versus nonboronated columns, the nonboronated should result in a greater baseline shift as analyte is not trapped on the column. Then, when the low pH elution buffer is flowed through the system, the boronated should experience a greater baseline shift as that bound analyte is eluted. In comparing the traces from the two columns, conclusions should be able to be drawn about the efficacy of the columns. Current work is focused on accounting for differences in the baseline of the loading and elution buffers and minimizing the dead volume for faster response time when the concentration changes. Ultimately, this configuration will be used to monitor the trapping and elution of model analytes.

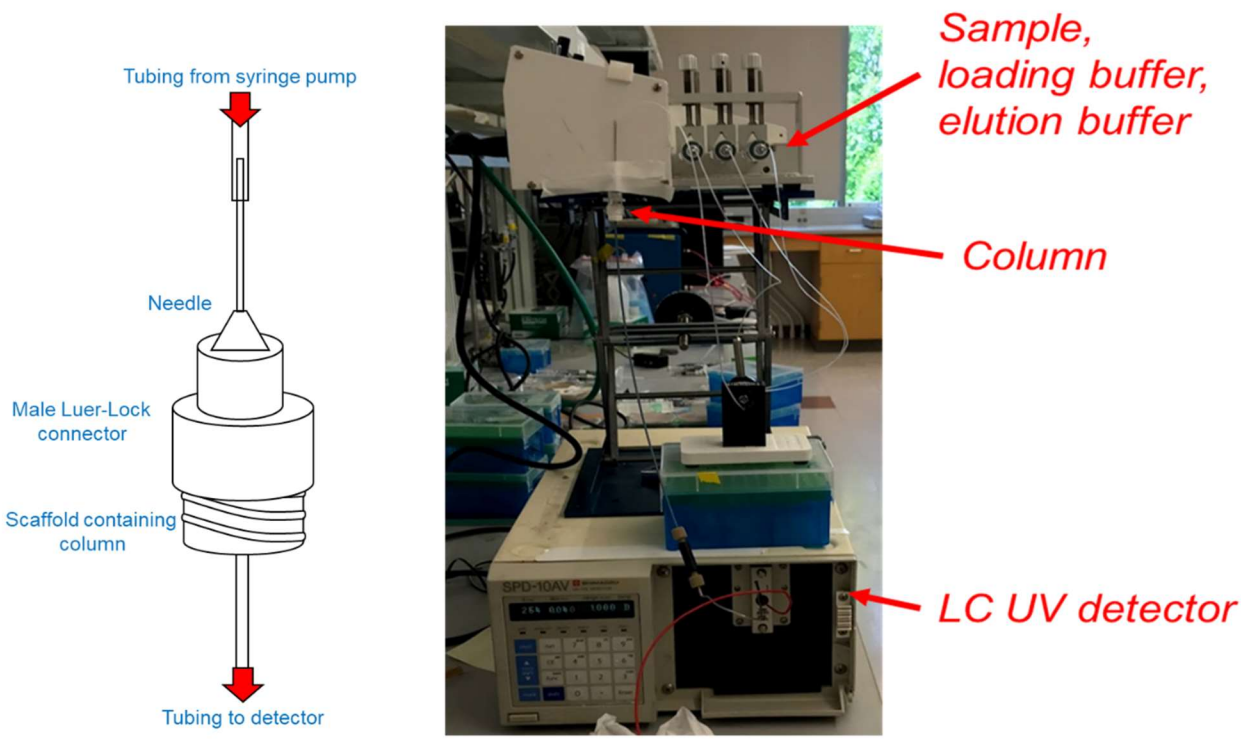

Figure 7.20. Integration of column with UV detector using a syringe pump and Uniswitch device.

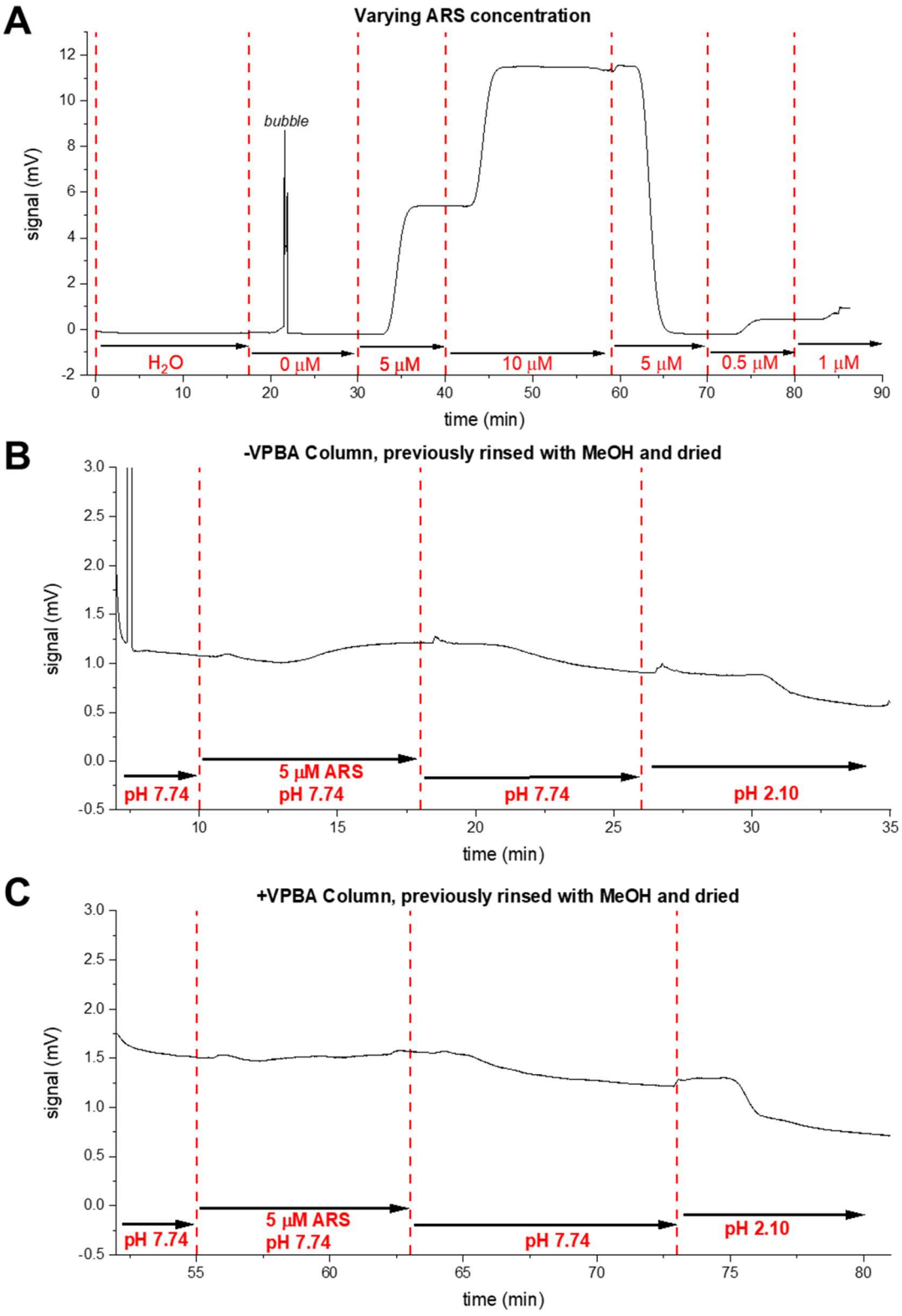

Figure 7.21. Sample preliminary data using LC UV detector for (A) calibration with ARS; (B) loading/rinsing/eluting ARS on a non-boronated column; (C) the same experiment on a boronated column.

7.4 Conclusions and outlook for 3D printing in relation to this work

In this chapter, progress towards a 3D printed scaffold for boronate affinity enrichment of derivatized nitrated peptides was described. Several scaffold designs were produced and evaluated to result in an optimal design that enabled *in situ* polymerization of a boronate monolith as well as perfusion and integration with other modules on both ends. The polymerization conditions were optimized and a protocol for loading and elution of model analyte Alizarin Red S was developed. Several methods were evaluated to monitor the concentration of analyte in the eluent, including offline detection with a spectrophotometer, plate reader, or capillary electrophoresis (not shown) and online detection with mass spectrometry or a UV flow cell. Future work will focus on improving the capture efficiency of the column and the integration with online detection to enable quantitative monitoring of the contents of the eluent. Ultimately, this device will be integrated with other modules to enable simplified determination of protein nitration in blood saples.

7.5 References

1. Wang, L.; Pumera, M., Recent advances of 3D printing in analytical chemistry: focus on microfluidic, separation, and extraction devices. *TrAC, Trends Anal. Chem.* **2020**, 116151.
2. Kalsoom, U.; Nesterenko, P. N.; Paull, B., Current and future impact of 3D printing on the separation sciences. *TrAC, Trends Anal. Chem.* **2018,** *105*, 492-502.
3. Salentijn, G. I.; Oomen, P. E.; Grajewski, M.; Verpoorte, E., Fused deposition modeling 3D printing for (bio) analytical device fabrication: procedures, materials, and applications. *Anal. Chem.* **2017,** *89* (13), 7053-7061.
4. Gross, B.; Lockwood, S. Y.; Spence, D. M., Recent advances in analytical chemistry by 3D printing. *Anal. Chem.* **2017,** *89* (1), 57-70.
5. Nawada, S.; Dimartino, S.; Fee, C., Dispersion behavior of 3D-printed columns with homogeneous microstructures comprising differing element shapes. *Chem. Eng. Sci.* **2017,** *164*, 90-98.
6. Gupta, V.; Beirne, S.; Nesterenko, P. N.; Paull, B., Investigating the effect of column geometry on separation efficiency using 3D printed liquid chromatographic columns containing polymer monolithic phases. *Anal. Chem.* **2018,** *90* (2), 1186-1194.
7. Beauchamp, M. J.; Nielsen, A. V.; Gong, H.; Nordin, G. P.; Woolley, A. T., 3D printed microfluidic devices for microchip electrophoresis of preterm birth biomarkers. *Anal. Chem.* **2019,** *91* (11), 7418-7425.
8. Parker, E. K.; Nielsen, A. V.; Beauchamp, M. J.; Almughamsi, H. M.; Nielsen, J. B.; Sonker, M.; Gong, H.; Nordin, G. P.; Woolley, A. T., 3D printed microfluidic devices with

immunoaffinity monoliths for extraction of preterm birth biomarkers. *Anal. Bioanal. Chem.* **2019,** *411* (21), 5405-5413.
9. Bickham, A. V.; Pang, C.; George, B. Q.; Topham, D. J.; Nielsen, J. B.; Nordin, G. P.; Woolley, A. T., 3D Printed Microfluidic Devices for Solid-Phase Extraction and On-Chip Fluorescent Labeling of Preterm Birth Risk Biomarkers. *Anal. Chem.* **2020,** *92* (18), 12322-12329.
10. Castiaux, A. D.; Currens, E. R.; Martin, R. S., Direct embedding and versatile placement of electrodes in 3D printed microfluidic-devices. *Analyst* **2020,** *145* (9), 3274-3282.

11. Castiaux, A. D.; Pinger, C.; Hayter, E. A.; Bunn, M. E.; Martin, R. S.; Spence, D. M., PolyJet 3D-Printed Enclosed Microfluidic Channels without Photocurable Supports. *Anal. Chem.* **2019,** *91* (10, 6910-6917.
12. Francisco, K. J. M.; do Lago, C. L., Improving thermal control of capillary electrophoresis with mass spectrometry and capacitively coupled contactless conductivity detection by using 3D printed cartridges. *Talanta* **2018,** *185*, 37-41.
13. Salentijn, G. I.; Permentier, H. P.; Verpoorte, E., 3D-printed paper spray ionization cartridge with fast wetting and continuous solvent supply features. *Anal. Chem.* **2014,** *86* (23), 11657-11665.
14. Casto, L. D.; Do, K. B.; Baker, C. A., A Miniature 3D Printed LED-Induced Fluorescence Detector for Capillary Electrophoresis and Dual-Detector Taylor Dispersion Analysis. *Anal. Chem.* **2019,** *91* (15), 9451-9457.
15. Dremina, E. S.; Li, X.; Galeva, N. A.; Sharov, V. S.; Stobaugh, J. F.; Schöneich, C., A methodology for simultaneous fluorogenic derivatization and boronate affinity enrichment of 3-nitrotyrosine-containing peptides. *Anal. Biochem.* **2011,** *418* (2), 184-196.
16. Cakal, C.; Ferrance, J. P.; Landers, J. P.; Caglar, P., Microchip extraction of catecholamines using a boronic acid functional affinity monolith. *Anal. Chim. Acta* **2011,** *690* (1), 94-100.
17. Springsteen, G.; Wang, B., Alizarin Red S. as a general optical reporter for studying the binding of boronic acids with carbohydrates. *Chem. Commun.* **2001,** (17), 1608-1609.

Chapter 8

Summary and Future Directions

8 Chapter 8: Summary and Future Directions

8.1 Summary

The overall goal of this dissertation was to develop a suite of analytical methods to monitor nitrosative and oxidative stress in biological samples. First, an improved microchip electrophoresis method with electrochemical detection was developed for the detection of nitrite in the bulk cell lysates of macrophage cells. Nitrite is a metabolite of nitric oxide that can be detected as a more stable indicator of the production of nitric oxide under conditions of stress. The concentration of tetradecyltrimethylammonium chloride (TTAC) in the run buffer was increased until the optimal separation of nitrite, azide (interferent from cell filters), ascorbic acid (antioxidant) and hydrogen peroxide (product of oxidative stress and neutral marker) was achieved in a buffer of 10 mM borate at pH 10 with 5.5 mM TTAC. Then the concentration of sodium chloride in the run buffer relative to the sample matrix was increased to induce transient isotachophoresis stacking of the nitrite peak, resulting in a much more efficient peak and a decrease of the limit of detection for nitrite from 2.5 μM to less than 500 nM. Then, a procedure to integrate a Pt black modification on a Pt band microelectrode integrated with microchip electrophoresis was developed, resulting in a 2-fold increase in sensitivity for nitrite. This method was then used to detect nitrite in native macrophage cells and cells stimulated with lipopolysaccharide to induce a proinflammatory response.

Next, capillary electrophoresis with diode array detection was used to detect both the RNOS peroxynitrite and its products with tyrosine. A separation of several tyrosine-containing peptides and modified tyrosine species was optimized in a background electrolyte of 20 mM borate at pH 8.2 with 5 mM SDS. Peroxynitrite was synthesized from the reaction of nitrite and acidified hydrogen peroxide and tyrosine was added to the reaction mixture at designated timepoints after synthesis. The products were then separated using the optimal CE method. The production of 3-nitrotyrosine was monitored, as well as the production of two primary byproducts. The conditions

necessary for the formation of these byproducts were determined and the electropherograms were monitored at several wavelengths in order to aid in tentative peak identification.

Dual electrode ME-EC was then applied to the selective detection of 3-nitrotyrosine. Attempts were made to develop a reproducible method; however, this proved difficult. Factors such as the effect of electrode material, electrode alignment relative to the separation field, and buffer composition and pH on the detector response are discussed. The source of a system peak in the reduction electropherogram of the dual electrode system was identified and a second peak was tentatively identified as resulting from the reduction of 3-nitrotyrosine, with a corresponding peak observed in the oxidation electropherogram. This identification was based on comparison to sample blanks and similarity to the electrochemistry of other nitrotyrosine-containing species as well as the investigation of the hydrodynamic voltammograms and calibration curves of these peaks. Finally, initial efforts to better understand the effect of electrode alignment on a dual electrode ME-EC system were presented using dopamine as a model analyte.

In the last chapter, the focus was again on development of a method to detect tyrosine nitration. However, instead of using electrophoretic separations, the goal of this project was to develop a 3D printed scaffold for a boronate affinity monolith. This monolith will be used for the selective trapping and elution of derivatized, nitrated peptides from the blood of Alzheimer's patients. The scaffold design and polymerization conditions were optimized and effective loading and elution conditions were determined. Then, several efforts to couple the scaffold with detection, both off-line and on-line, are discussed.

8.2 Future directions

8.2.1 Electrophoretic separations for the analysis of 3-nitrotyrosine in biological systems

In Chapters 5 and 6, two different electrophoretic methods for the detection of 3-nitrotyrosine are presented. Immediately, there is more work to be done in improving the

reproducibility of the dual electrode ME-EC method and lowering the limits of detection. As discussed in Chapter 6, much of the irreproducibility likely stems from inconsistencies in the positioning of the electrodes in the waste reservoir, as well as the configuration of these electrodes themselves. In order to improve upon this method, the two key innovations that must be addressed are the development of an effective electrode holder and the incorporation of a decoupler into the microchip.

Initial efforts to design an electrode holder were discussed in the chapter; however, these holders were not able to position the ground and counter electrodes close enough to one another without any risk of them touching. Additionally, the holder itself was not very stable and would need to be taped down in order to maintain the correct positioning, which is in itself not very reproducible since tension on the electrodes can vary during an experiment, especially when rinsing the bottom well. Current designs for a more effective electrode holder would feature the counter and ground electrodes fixed permanently into the holder with only a small distance above the well free to minimize the chance of them bending. The holder would also have magnets or another reversible adhesive mechanism on either side that would line up with the other half of the adhesive on the chip stage. This would enable reproducible, stable positioning of the electrode holder for each experiment. Additionally, while 3D printing does enable rapid prototyping, it would be best if theoretical simulations or modeling would be able to aid in determining some optimal positioning guidelines.

The necessity of a decoupler was not discussed at length in the chapter; however, it appears to be essential for achieving success in the dual electrode detection of 3-nitrotyrosine. A decoupler placed in the separation channel ahead of the working electrode would enable the separation field to be grounded prior to reaching the electrode, therefore reducing its impact on the background current stability and system peak intensities. Additionally, it would enable both working electrodes

to be aligned completely in-channel for reduced band broadening at the second working electrode for more sensitive detection. Decouplers have been microfabricated using palladium or platinum; however, they have not been fabricated in an all-PDMS microchip containing carbon fiber working electrodes, which were found to be optimal for the detection of these organic molecules. In order to design an electrode substrate that would be optimal for this analysis, it will be necessary to develop a fabrication protocol for the combination of metal and carbon electrodes on a single substrate. The size of the generator electrode could then be increased and it could be fabricated in a material such as gold mercury amalgam that is known for being a good electrode for reductions. All of these electrode modifications would result in a more stable electrochemical background and increased collection efficiency.

Once the dual electrode ME-EC system is improved upon, it can be used in combination with the CE-DAD method to study other nitration and oxidation reactions beyond those presented in Chapter 5. The ability to analyze these reactions by a combination of CE-DAD and ME-EC would provide a wealth of information about any products observed, all without the use of conventional structural characterization techniques. In Chapter 5, rather extreme reaction conditions were used as an initial proof-of-concept, including highly acidic conditions with large concentrations of oxidants. In the future, it would be desirable to tone down these conditions to more accurately emulate physiological conditions through use of a more moderate pH and minimal oxidant concentrations so that the true selectivity of these reactions could be observed. Additionally, a variety of RNOS donors could be evaluated, such as SIN-1 and PROLI-NONOate, to observe how different nitration and oxidation agents affect the products formed. These systems could then be used to observe how different oxidation and nitration conditions as well as different additives affect the redox balance of a biological system.

8.2.2 Development of a modular, 3D-printed device to detect protein nitration in the blood

As discussed in Chapter 7, efforts have been underway in our group to design a modular miniaturized system for the total sample preparation, enrichment, and detection of derivatized, nitrated peptides. We have envisioned several different modules that could be integrated to accomplish the entire analytical method with minimal opportunities for sample loss or human error, the key issues our collaborators have with their current, centrifugation-heavy approaches. In Chapter 7, the boronate affinity enrichment step was addressed. In order to apply this module to the enrichment of derivatized, nitrated peptides, it must be integrated with either mass spectrometry or fluorescence detection. Based on the preliminary experiments described in Chapter 7, it seems necessary to work to further minimize the dead volume of the system in order to achieve enrichment on the column, as opposed to it functioning instead to merely eliminate interfering species without actually enriching the analyte of interest. Once this is achieved, the hope is that it could be integrated downstream with a fluorescence flow cell detector that would enable the monitoring of the fluorescent, cis-diol-containing peptides. Once the detection system is functional, the loading and elution and polymerization conditions can be further optimized to a finer degree of resolution than was possible without integrated detection.

Efforts have also been focused on another module in the system, a cell lysis device that would be capable of lysing white blood cells without damaging their mitochondria. This is desirable so that the mitochondria would then be able to be effectively separated from other cellular organelles prior to protein digestion, as mitochondrial proteins are the ones of greatest interest to our collaborators. Different methods of cell lysis, both using a mechanical homogenizer and Triton-X for chemical lysis, were evaluated on bulk Jurkat cells and the mechanical homogenizer resulted in more consistent lysis of the cell samples. Because of this, we began designing a 3D printed cell lysis module that was based upon these principles.

The mechanical homogenizer used for these experiments consisted of a stainless-steel channel into which a ball bearing was placed. Cells were drawn up into a syringe and then forced through the channel, coming out at the outlet which was connected to a second syringe (Figure 8.1A). After several iterations of designing, printing, and evaluating, the device shown in Figure 8.1B was produced. This module can be interfaced with syringes on either end and contains a chamber that can fit a ball with a similar clearance to that at which optimal cell lysis occurred using the mechanical homogenizer. While this device has not yet been tested with cell samples, it is anticipated that with further developments such as potentially incorporating glass beads for lysis instead of a single 3D printed or metal ball and adapting the connectors, several of these could be connected in series to allow the cells to go through a controlled number of passages before reaching the next module.

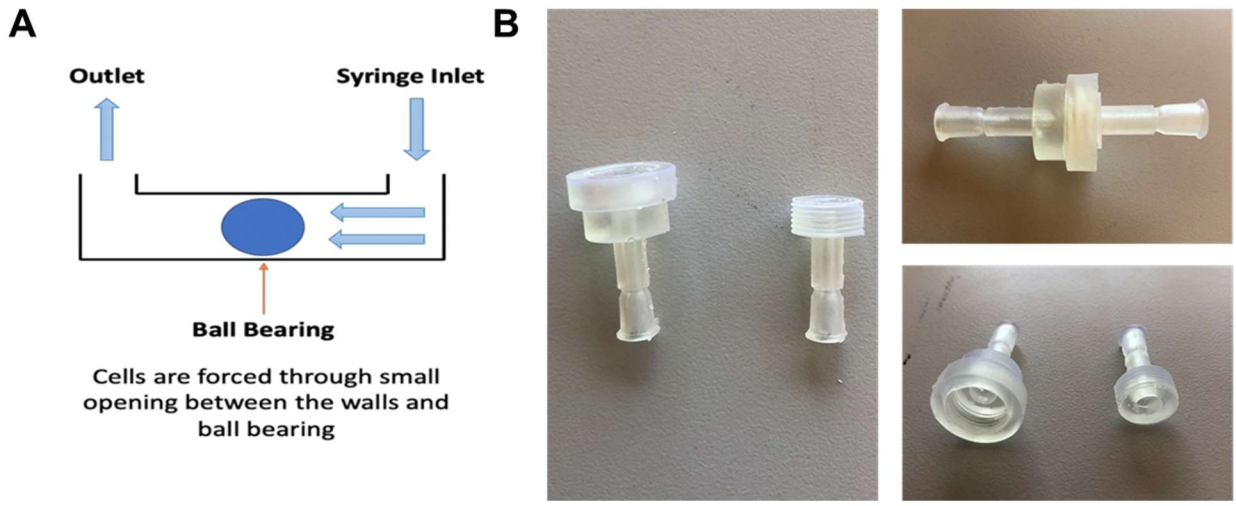

Figure 8.1. (A) Schematic of the mechanical homogenizer that was used for bulk cell lysis; (B) Photographs of a 3D printed version of this homogenizer in development.

Ultimately, the 3D printed modular devices in development by our group will be used to guide the development of the final, integrated device. This device will have endless applications, not only for the specific application of detection of nitrated peptides, but also for sample handling

and preparation in a variety of biological assays. If 3D printing and miniaturization can ultimately produce an integrated system that has less opportunity for user error or sample loss, this will result in more efficient analyses in clinical trials where every sample needs to go a long way.